UNIVERSITI TEKNOLOGI MARA

CHARACTERIZATION OF MICROSTRUCTURE, MECHANICAL BEHAVIOR AND PLC EFFECT IN WAAM-FORGED ER5356 ALUMINIUM ALLOY

NORNISAADILA BINTI MUSA

PhD

August 2026

UNIVERSITI TEKNOLOGI MARA

CHARACTERIZATION OF MICROSTRUCTURE, MECHANICAL BEHAVIOR AND PLC EFFECT IN WAAM-FORGED ER5356 ALUMINIUM ALLOY

NORNISAADILA BINTI MUSA

Thesis submitted in fulfilment
of the requirements for the degree of
Doctor of Philosophy
(Mechanical Engineering)

Faculty of Mechanical Engineering

August 2026

CONFIRMATION BY PANEL OF EXAMINERS

I certify that a Panel of Examiners has met on 20th May 2026 to conduct the final examination of Nornisaadila binti Musa on her Doctor of Philosophy thesis entitled "Characterization of Microstructure, Mechanical Behavior and PLC Effect in WAAM-Forged ER5356 Aluminium Alloy" in accordance with Universiti Teknologi MARA Act 1976 (Akta 173). The Panel of Examiners recommends that the student be awarded the relevant degree. The Panel of Examiners was as follows:

Mohd Faizal Hamzah, PhD
Associate Professor
Faculty of Mechanical Engineering
Universiti Teknologi MARA
(Chairman)

Alias Mohd Saman, PhD
Senior Lecturer
Faculty of Mechanical Engineering
Universiti Teknologi MARA
(Internal Examiner)

Mohd Sayuti Ab Karim, PhD
Associate Professor
Faculty of Engineering
University Malaya
(External Examiner)

PROF DR HJH ZURAEDA IBRAHIM
Dean
Institute of Postgraduate Studies
Universiti Teknologi MARA

Date: 28 August 2026

AUTHOR'S DECLARATION

I declare that the work in this thesis was carried out in accordance with the regulations of Universiti Teknologi MARA. It is original and is the result of my own work, unless otherwise indicated or acknowledged as referenced work. This thesis has not been submitted to any other academic institution or non-academic institution for any degree or qualification.

I, hereby, acknowledge that I have been supplied with the Academic Rules and Regulations for Postgraduate, Universiti Teknologi MARA, regulating the conduct of my study and research.

Name of Student	:	Nornisaadila binti Musa
Student ID. No.	:	2020873452
Programme	:	Doctor of Philosophy (Mechanical Engineering) – EM950
Faculty	:	Mechanical Engineering
Thesis Title	:	Characterization of Microstructure, Mechanical Behavior and PLC Effect in WAAM-Forged ER5356 Aluminium Alloy
Signature of Student	:	
Date	:	August 2026

ABSTRACT

WAAM of aluminium alloys presents a promising route for producing large-scale components with near-net-shape capabilities. However, WAAM processes inherently suffer from microstructural defects, residual stresses, and inconsistent mechanical performance due to rapid solidification and thermal cycling. This research addresses these limitations by evaluating the surface integrity and mechanical properties of WAAM and WAAM-forged aluminium alloy using simulation and experimentation, analyzing the effect of strain rate on the compressive strain hardening behavior of WAAM-forged Al-Mg alloy and developing a strain hardening relationship model between the stress-drop amplitude and strain rate. The continuous process chain for GMAW and CMT were compared in terms of thermal behavior, distortion, residual stress, effective plastic strain and contact pressure using Simufact.Welding and Simufact.Forming including experimental validation. Thermal behavior revealed that GMAW generated higher interpass temperatures of 795.6 °C and greater distortion compared to CMT which was verified through thin wall fabrication and 3D scanning. The height deviations were -24.93% for GMAW and -6.67% for CMT in the as-deposited condition, while post-processing of forging deviations were -26.62% and -19.46%, respectively with overall dimensional error ranging from -33.00% to +3.60%. Porosity analysis showed higher percentages in GMAW about 5.114% compared to CMT, which directly influence the density and tensile performance. The tensile strength at different orientations demonstrated anisotropic behavior with superior strength along the deposition direction. The CMT process consistently outperformed GMAW in ultimate tensile strength, yield strength and elongation due to reduced defect density. Compressive testing at different strain rates revealed strain-rate-dependent and Portevin-Le Chatelier (PLC) effects in WAAM and WAAM-forged samples. Higher strain rates reduced the amplitude of stress drop, while lower strain rates promoted pronounced serrated flow behavior. A new empirical correlation, named Musa Equation, is proposed to quantify PLC severity through the slope of the stress-drop amplitude vs log strain rate relationship. In conclusion, the hybrid WAAM-forging significantly enhances the surface and mechanical integrity of Al-Mg alloys, promoting a robust solution to overcome conventional WAAM limitations for high-performance applications.

ACKNOWLEDGEMENT

Alhamdulillah, thank you Allah SWT, the Most Gracious and Most Merciful, for granting me the strength, perseverance and clarity of mind to undertake and complete this research. I would like to express sincere appreciation to my main supervisor, Prof. Madya Dr. Mohd Shahriman Adenan of Faculty of Mechanical Engineering, Universiti Teknologi MARA (UiTM) Shah Alam, for his guidance, critical insights, and consistent encouragement in shaping the direction and substance of this research project.

I am also sincerely thankful to my co-supervisors: Prof. Madya Dr. Juri Saedon (Faculty of Mechanical Engineering, UiTM Shah Alam), Prof. Ir. Dr. Farazila binti Yusof (Department of Mechanical Engineering, Universiti Malaya), and Prof. Dr. Nur Izan Shahriah binti Hussein (Faculty of Industrial and Manufacturing Engineering, Universiti Teknikal Malaysia Melaka) for their professional input and academic mentorship in refining the technical depth and analytical rigor of this work.

A special note of appreciation to Prof. Dr. Daolun Chen from the Department of Mechanical, Industrial, and Mechatronics Engineering, Toronto Metropolitan University (TMU), Canada, for facilitating access to advanced laboratory facilities including research knowledge that significantly enriched the scientific scope and international relevance of this study.

I would like to acknowledge the support from the Ministry of Higher Education (MOHE) for funding under the Geran Konsortium Kecemerlangan Penyelidikan 600-RMC/KKP 5/3 (003/2021) to complete this research.

Special thanks to TSIS Welding Solutions Sdn Bhd, Klang Selangor for their invaluable guidance and support in the sample preparation process. I would like to extend my gratitude to all academic staff Faculty of Mechanical Engineering UiTM Shah Alam, Metal Forming Research Lab USM Nibong Tebal and Faculty of Industrial and Manufacturing Engineering UTEM for their continuous support and technical assistance, particularly in the areas of material preparation, robotic welding operations, and simulation infrastructure that were essential for the successful execution of both experimental and simulation phases of this research.

To all technical personnel and collaborators who have contributed directly or indirectly towards the completion of this thesis, I extend my sincere thanks for their guidance and assistance throughout this research. Your assistance is sincerely appreciated.

My deepest appreciation goes to my husband, parents, and family members, thank you for the love, support, patience, sacrifices, and encouragement. The moral and emotional support has been the anchor in my storm to complete this journey.

Lastly, to myself, thanks for the perseverance to endure long hours of experimentation and writing, for the courage to confront challenges with determination and steadfast belief that growth lies beyond comfort. This accomplishment stands as a reflection of dedication and strength to keep moving forward despite the odds.

TABLE OF CONTENTS

		Page
CONFIRMATION BY PANEL OF EXAMINERS		**ii**
AUTHOR'S DECLARATION		**iii**
ABSTRACT		**iv**
ACKNOWLEDGEMENT		**v**
TABLE OF CONTENTS		**vi**
LIST OF TABLES		**ix**
LIST OF FIGURES		**xi**
LIST OF SYMBOLS		**xx**
LIST OF ABBREVIATIONS		**xxi**
CHAPTER 1 INTRODUCTION		**1**
1.1	Research Background	1
1.2	Problem Statement	3
1.3	Research Objectives	4
1.4	Research Scope	5
1.5	Significance of Study	7
CHAPTER 2 LITERATURE REVIEW		**9**
2.1	Introduction	9
2.2	Current Status and Perspective of Wire Arc Additive Manufacturing (WAAM)	10
	2.2.1 Principles and Current Status of WAAM	10
	2.2.2 Influence of Process Parameters and Heat Input on Deposits Geometry	17
	2.2.3 Simulation Based Prediction of Process Parameter	26
2.3	Aluminium Alloys in WAAM	32
	2.3.1 Classification of Aluminium and Its Alloys	32
	2.3.2 Surface Integrity and Limitation	39

2.3.3 Grain Structure Development 45
2.3.4 Residual Stress Performance and Tensile Properties 47
2.4 Hybrid Manufacturing of WAAM Process 56
2.4.1 Current Progress of Hybrid WAAM-Forging Process 56
2.4.2 Forging of Aluminium Alloy 64
2.4.3 Compressive Behavior of Cold Forging Aluminium Alloy 69
2.4.4 Overview of Portevin-Le Chatelier (PLC) Effect 74
2.5 Summary of Literature Review 81

CHAPTER 3 RESEARCH METHODOLOGY 86
3.1 Introduction 86
3.2 Material 88
3.3 Numerical Modeling of Distortion and Residual Stress in WAAM and Process Chain WAAM-Forming Process 89
3.3.1 Formation Analysis using Simufact.Welding (SW) 89
3.3.2 Forming Behavior and Stress Analysis using Simufact.Forming (SF) 95
3.4 Sample Preparation 98
3.4.1 Morphological for Scanning Electron Microscopy (SEM) Analysis 99
3.4.2 Microstructural for Electron Backscatter Diffraction (EBSD) Analysis 103
3.5 Experimental Verification of WAAM and WAAM-Forging Process 104
3.5.1 Gas Metal Arc Welding (GMAW) Process 104
3.5.2 CMT Process 106
3.5.3 Wire Arc Additive Manufacturing-Forging (WAAM-Forging) Process 108
3.6 Deformation Behavior and Mechanical Properties Analysis in WAAM and WAAM-Forging Process 109
3.6.1 Distortion and Deformation Analysis 109
3.6.2 Surface Morphological Analysis 113
3.6.3 Tensile Behavior and Performance Analysis 115
3.6.4 Residual Stress Analysis 116
3.6.5 Compressive Properties in WAAM and WAAM-Forging Process 117

CHAPTER 4 RESULTS ON SURFACE INTEGRITY AND MECHANICAL PERFORMANCE WAAM AND HYBRID WAAM-FORGING ER5356 THIN WALL **119**

4.1 Introduction 119

4.2 Comparative Deformation Analysis of WAAM and WAAM-Forging by Simulation and Experimental 120

4.2.1 Deformation Analysis by Simulation Process 120

4.2.2 Dimensional and Geometrical Behavior of Fabricated Wall 126

4.2.3 Porosity Formation 130

4.3 Mechanical Properties of WAAM and WAAM-Forging 134

4.3.1 Tensile Performance of Thin Wall 134

4.3.2 Residual Stress Performance of Thin Wall 138

4.4 Microstructure Analysis of WAAM and WAAM-Forging of ER5356 143

4.5 Compressive Behavior of ER5356 WAAM and WAAM-Forging 145

4.5.1 Post Compression Texture 145

4.5.2 Compressive Properties 147

4.5.3 Strain Hardening Behavior 149

4.6 PLC Effect and Serrated Stress Flow 152

4.6.1 Amplitude of Stress Drop 156

CHAPTER 5 CONCLUSION **160**

5.1 Objective I: Surface Integrity and Mechanical Properties of Al-Mg using Simulation and Experiment 160

5.2 Objective II: Strain Hardening Behavior of Al-Mg WAAM and WAAM-Forging 162

5.3 Objective III: Strain Hardening Relationship Model of PLC Severity in Al-Mg WAAM and WAAM-Forging 163

5.4 Future Studies 165

REFERENCES **166**

APPENDICES **181**

AUTHOR'S PROFILE **185**

LIST OF TABLES

Tables	Title	Page
Table 2.1	Comparative of Common Materials on WAAM Application	12
Table 2.2	Comparative Analysis of GMAW and CMT for WAAM	16
Table 2.3	Influence of Process Parameters and Heat Input on Aluminium Alloy	20
Table 2.4	Aluminium Alloy Series for WAAM (Fang et al., 2021; Langelandsvik et al., 2021; Rathod, 2025)	35
Table 2.5	WAAM Research on Aluminium Alloys	37
Table 2.6	Comparative Shielding Gases on Porosity of Aluminium in WAAM	43
Table 2.7	The Anisotropy Behavior for Different Orientation (Building to Deposition Direction)	55
Table 2.8	Recent Studies Hybrid Manufacturing of WAAM for Various Alloys	58
Table 2.9	Recent Research Hybrid Manufacturing of WAAM on Aluminium Alloy	63
Table 2.10	Cold Forging Effects on Aluminium Alloys	68
Table 2.11	Types of Serration Flow (Lee et al., 2023)	78
Table 2.12	Summary of recent research (2023-2025) on WAAM-Hybrid and PLC Effect	84
Table 3.1	The Chemical Composition of ER5356 and Al6061	89
Table 3.2	The Mechanical and Physical of ER5356 and Al6061	89
Table 3.3	The Geometry Dimension for Different Welding Type	93
Table 3.4	The Welding Parameters Assigned in SW	93
Table 3.5	Goldak Heat Source Dimensions Used in SW	95
Table 3.6	The Forging Parameters Assigned in SF	97
Table 3.7	The Damage Model Parameters Setup in SF	97
Table 3.8	The Sample Preparation Process for WAAM and WAAM-Cold Forging Sample	103
Table 3.9	Data of Actual WAAM-GMAW Process	106

Table 3.10	Data of Actual WAAM-CMT Process	107
Table 3.11	Technical Data for GOM Scan 1 (200)	109
Table 3.12	Sensor Configuration for GOM Scan 1 (200)	111
Table 4.1	Dimensional of WAAM and WAAM-Forging using Simulation and Experimental	127
Table 4.2	Tensile Strength of WAAM and WAAM-Forging	135
Table 4.3	Strain Hardening Sensitivity of WAAM and WAAM-Forging	151
Table 4.4	Amplitude of Stress Drops at Different Strain Rates	157

LIST OF FIGURES

Figures	Title	Page
Figure 2.1	AM for Metal Classification (Treutler & Wesling, 2021)	10
Figure 2.2	Comparison between Wire-Based and Powder Bed Based AM (Rodrigues et al., 2019)	11
Figure 2.3	Advantages of WAAM and other AM process (Shah et al., 2023)	12
Figure 2.4	Schematic of GMAW Process (Bambach et al., 2020)	13
Figure 2.5	Principle of Operation of CMT Welding Technique (Truppel et al., 2019; Vazquez et al., 2023)	15
Figure 2.6	Thin Wall of Al5356 using Different Heat Input (a) 87.5 J/mm (b) 120.0 J/mm (c) 154.2 J/mm (d) 190.0 J/mm (Zuo et al., 2025)	18
Figure 2.7	SEM Micrograph Showing Cross-Section for Standard (a-b) GMAW process, (c-d) CMT process (Oliveira et al., 2021)	19
Figure 2.8	Cross-Section of Thin Wall Prepared by GMAW using Different Combination of Heat Input (a) ER5356 (b) Al 4047 (Chen et al., 2023; Greebmalai & Warinsiriruk, 2020)	22
Figure 2.9	Surface Structure Defects (a) Humping (b) Material Overflow (Shah et al., 2023)	22
Figure 2.10	Path Strategy for Material Deposition (a) Bidirectional, (b) Unidirectional, (c) Triangle (d) Spiral (Arana et al., 2022; Shah et al., 2023)	23
Figure 2.11	Aluminium alloy under Different Deposition Path using (a-b) Al-Mg (c-d) Bimetallic ER4043 and ER5356 (e-f) Al5356 (K. Derekar et al., 2019; Kesarwani et al., 2024; Y. Liu et al., 2022)	23
Figure 2.12	5356 Aluminium Microstructure on Bottom, Middle, and Top Region after WAAM of Different Proportions of Gases (S. Li et al., 2021)	25

Figure 2.23	(a) Schematic of the Gas Flow Rate on Solidification and Pore Behavior (b) Cross-Section of AlSi5 Wall using Varieties Flow Rate (Hauser et al., 2021)	42
Figure 2.24	Porosity in AA5356 wall with (a) Argon Gas (b) Stargold Gas (Arana et al., 2021)	44
Figure 2.25	Cracks Formation in AA7075 (a) Hot Cracks (b) Initiation of Cracks due to Porosity (Altıparmak et al., 2021)	44
Figure 2.26	Locations of liquation cracking in welded aluminium (Albannai & Albannai, 2022)	45
Figure 2.27	EBSD of Al-Mg under Different Process Parameter by CMT Process (a) 90A (b) 130A (c) 400 mm/min (d) 12.5 L/min (e) 1 min interlayer residence time (f) Sample Positioning (Y. Liu et al., 2022)	46
Figure 2.28	Scanning location and inverse pole figure (IPF) maps by EBSD of Al-5.0 Mg; (a) region A (b) IPF maps of region A, (c) region B, and (d) IPF maps of region B (Geng et al., 2022)	46
Figure 2.29	Visualization of Braggs' Equation (Harrington & Santiso, 2021)	48
Figure 2.30	Distribution of Longitudinal Residual Stress (a) Along Line 1 (b) Along Line 2 (c) Color Contour (Sun et al., 2021)	49
Figure 2.31	XRD Pattern Al-Mg of WAAM (a) Phase of Al-5.0 Mg (b) ER5556 (Geng et al., 2022; Y. Liu et al., 2022)	50
Figure 2.32	Tensile Specimen Orientation of Series 5 Aluminium Alloy Fabricated by GMAW (a) and (b) ER5356 wall (Arana et al., 2022; Köhler et al., 2020) (c) AA 5083 (Tonelli et al., 2021)	52
Figure 2.33	Stress-strain Curves for WAAM Aluminium Alloy on Different Orientation using (a-b) ER5356 (c) AA5083 (Köhler et al., 2019; L. Liu et al., 2023; Tonelli et al., 2021)	54
Figure 2.34	Geometry of Forged and Followed by WAAM (b) Microstructure of Ti-6Al-4V WAAM-Hot Forming (Bambach et al., 2020)	57
Figure 2.35	Hybrid WAAM-Milling of Steel (a) Process Procedure (b) Comparison of Mechanical Properties after Hybrid and WAAM (c) Tensile Properties (Karlina et al., 2024)	57

Figure 2.36	(a) Schematic Diagram of HR-WAAM Process (b) Temperature Distribution (c) WAAM Pore Size (d) HR-WAAM Pore Size (e-f) Tensile Properties of WAAM and HR-WAAM (J. Huang et al., 2024)	59
Figure 2.37	(a) Experiment Setup for WAAM-Hammering of Series 5 Aluminium Alloy (b) Hammering Process (c) OM Images of Pores and Porosity (d) EBSD IPF and Grain Size Distributions (Zhou et al., 2022)	60
Figure 2.38	Hybrid Manufacturing WAAM-UNSM Al5356 on Different Static Load (a) Experiment Setup (b) Hardness Analysis (c) Observation of Pores Through Optical Microscope (W. Li et al., 2023)	61
Figure 2.39	Hybrid Manufacturing WAAM-UIT ER2319 (a) Experiment Setup (b) Tensile Properties (c) Porosity Observation (d) IPF Maps (C. Wang et al., 2022)	61
Figure 2.40	Influence of Cold Forging on Al 6082 Microstructure (a) KAM Map (b) Grain Boundary Map (Bouquerel et al., 2014)	64
Figure 2.41	EBSD of Forging 7075 Aluminium Alloy of Various Press (a and c) 1% (b and d) 5% (H. Li et al., 2023)	65
Figure 2.42	(a) Geometry of a Forged-AM sample (b) Position for Tensile Test (c-d) Tensile Strength Forged and Welded (FW) (Hirtler et al., 2020)	67
Figure 2.43	Effect of Strain Rate on (a) YS (b) UCS (c) Hardening Capacity (Tahreen et al., 2014)	70
Figure 2.44	Strain Hardening Exponent on cast Mg (a) AZ31 (b) AZ61 (c) AZ91D (Tahreen et al., 2014)	71
Figure 2.45	Typical Strain Rate Sensitivity Plot using (a) Common Approach (b) Lindholm Approach (c-d) Simulated Mechanical Threshold Stress (MTS) Model (Tahreen et al., 2014; J. Xu et al., 2022)	72
Figure 2.46	Strain Rate Sensitivity using (a) Common Approach (b) Lindholm (Tahreen et al., 2014)	73

Figure 2.47	Typical Stress-Strain Curve of Al-Mg for Different Mechanical Tests (a) Tensile Strength (b) Compression (Uvarov & Efremov, 2019; J. Wang et al., 2021)	74
Figure 2.48	Type of Serrated Flow (a) Type A (b) Type B (c) Type C (d) Schematic Illustration for Mobile Atom Dislocation of Type A Serration (W. H. Wang et al., 2016)	76
Figure 2.49	Schematic Illustration for Three Types of PLC Bands Propagation Corresponding Serration Behavior (Lee et al., 2023)	76
Figure 2.50	(a) Schematic of the Stress Amplitude and Waiting Time (b) Definition of Stress Drop and Reloading Time (c) Schematic Illustration for the Quantitative Method of Serrated Flow (Bakare et al., 2023; C. Guo et al., 2025; Lee et al., 2023)	77
Figure 2.51	Serrated Stress-Strain Curves of Al-Mg at Different wt% (a) 2.3% (b) 4.57% (c) 1 – 4.5% (d) 2.86 – 9.41% (Ait-Amokhtar et al., 2015; Cai et al., 2017; Tian et al., 2024)	79
Figure 2.52	Stress-Strain Curves of AA5182 at Different Strain Rates and Temperature (J. Xu et al., 2022)	80
Figure 2.53	Overview of Research Trends in WAAM and Hybrid Manufacturing Studies (2015-2025)	83
Figure 3.1	Overview of the Research Methodology	87
Figure 3.2	(a) ER5356 Wire Filler on Workpiece Stage (b) Uncleaned (Left) and Cleaned (Right) of Al6061 Substrate	88
Figure 3.3	Detailed Flowchart of Welding Process using SW	90
Figure 3.4	Investigated Mesh Sizes using 4 mm, 5 mm, 7 mm and 8 mm with Refinement Mesh of 2 mm on Bead Formation Surface	91
Figure 3.5	Mesh Sensitivity Study of Substrate in SW	91
Figure 3.6	Geometry Setup in SW; (a) GMAW, (b) CMT	92
Figure 3.7	Clamping (a) Four Cylindrical Clamps of GMAW (b) Two Cuboidal Clamps of CMT	92
Figure 3.8	(a) WAAM Multi-layers in Directional Movement-Based Deposition (b) Arc Path and Pause in WAAM	93
Figure 3.9	(a) Heat Source Modeling in CMT Geometry (b) Goldak's Double Ellipsoidal Heat Source Model (Fisher et al., 2021)	94

Figure 3.10	Simulation Environment with Boundary Condition in SW	94
Figure 3.11	Geometry Setup in SF (a) Dimension of Geometry Part in SF (b) Deformation Defects Resulted from SW	95
Figure 3.12	(a) Geometry Setup in SF at x-z axis Position (b) Schematic of Geometry Setup (c) Geometry Position after 6% Reduction	96
Figure 3.13	Substrate Removal Process (a) MASTIKA Horizontal Band Saw Cutter Machine (b) Process of Substrate Removal	99
Figure 3.14	(a) MASTIKA Milling Machine (b) Milling Process Procedure	99
Figure 3.15	Sample Cutting using Waterjet (a) Equipment Set Up (b) Cutting Sample Process	100
Figure 3.16	Hot Mounting Set Up and Equipment (a) Phenolic Powder Mounting Compound in Black (b) Automatic Mounting Press Machine Model Simplimet 2000 (c) Sample Placement (d) Mounted Sample	101
Figure 3.17	(a) Grinder Model Buehler Metasarv 2000 (b) Mounted Sample after Hot Mounting Process (c) Mounted Sample after Grinding Process	101
Figure 3.18	(a) Polisher Model Imptech 10V and Polishing Solution (b) Mirror-image Sample	102
Figure 3.19	Etching Setup (a) Fume Hood for Etching Process (b) Mounted Sample Immersed in Keller's Reagent	102
Figure 3.20	Surface Observation Setup (a) Optical Microscope (b) Mounted Sample Observed under x50 Magnification before Undergoing SEM Analysis	102
Figure 3.21	(a) Microvoid Compound (b) Polished (P) sample and electrolyte polished (EP) sample (c) Electrolyte Polishing Setup	104
Figure 3.22	(a) GMAW Process Equipment Setup (b) GMAW Thin Wall Formation	105
Figure 3.23	(a) CMT Process Equipment Setup (b) CMT Thin Wall Formation	107
Figure 3.24	(a) Press forging Machine (b) Forging setup for WAAM-Forging Process	108

Figure 3.25	Equipment Set Up for 3D Scanning Process, (a) Front View of GOM Scan 1 Sensor	110
Figure 3.26	Camera Position and Projection View Towards the Measuring Volume	110
Figure 3.27	3D Scanning Procedure Steps	111
Figure 3.28	CPA30/210 3D Calibration Panel	111
Figure 3.29	Uncoded White Reference Stickers, (b) Uncoded White Reference Stickers at Unsystematic Positions	112
Figure 3.30	White Stickers Detected before Image was Captured	112
Figure 3.31	(a) Scanning Image of Raw Data of CMT Sample (b-c) Scanning Image of Mesh Data of CMT Sample	113
Figure 3.32	(a) Mounted Specimen in Chamber (b) Positioning of Mounted Specimen (c) Scanning Electron Microscope	114
Figure 3.33	(a) Mounted Specimen in Chamber (b) Positioning of Mounted Specimen (c) Scanning Electron Microscope	114
Figure 3.34	(a) Cut Plate using Waterjet, (b) Tensile Sheet Plate Dimension of ASTM E8M Standard, (c) Tensile Sheet Plate	116
Figure 3.35	(a) Tensile Sample Placement in Cross Head, (b) Tensile Machine	116
Figure 3.36	(a) XRD machine (b) XRD experimental setup	117
Figure 3.37	Compression Testing Equipment Setup (a) Sample Placement on the Compression Plate before the Test (b) Sample after 50% Compression Loading along z-axis (c) United STM-50kN Testing Machine	118
Figure 4.1	Interpass Temperature of Thin Wall Fabricated by ER5356 in SW (a-b) GMAW (c-d) CMT	121
Figure 4.2	Equivalent Stress using SW (a) GMAW (b) CMT	122
Figure 4.3	Total Displacement using SW Simulation for (a) GMAW (b) CMT	123
Figure 4.4	Contact Pressure using SF Simulation for (a) GMAW (b) CMT	125
Figure 4.5	Effective Plastic Strain using SF Simulation for (a) GMAW (b) CMT	126

Figure 4.6	Actual and 3D-Scanned Geometries of (a-b) GMAW (c-d) CMT WAAM Walls	128
Figure 4.7	Actual and 3D-Scanned Geometries of (a-b) GMAW-Forging (c-d) CMT-Forging	129
Figure 4.8	Porosity Formation at Different Position of (a) GMAW (b) GMAW-Forging (c) CMT (d) CMT-Forging	131
Figure 4.9	Density-Porosity Relationship of Different Process (a) WAAM (b) WAAM-Forging (c) WAAM Wall Observation Position	132
Figure 4.10	Chemical Composition Analysis of Different WAAM Modes (a) GMAW (b) CMT	134
Figure 4.11	Typical Stress-Strain Relationship at Different Orientation (a) Tensile Specimen Orientation (b) GMAW (c) GMAW-Forging (d) CMT (e) CMT-Forging	136
Figure 4.12	Yield Strength, Ultimate Tensile Strength and Elongation for (a) WAAM (b) WAAM-Forging Processes	137
Figure 4.13	Longitudinal and Transverse Residual Stress by XRD Analysis (a-b) WAAM (c-d) WAAM-Forging	139
Figure 4.14	Schematic Diagram of Stress in WAAM Thin Wall (a) Contraction and Shrinkage Phenomenon (b)	140
Figure 4.15	XRD pattern of ER5356 sample fabricated by different process (a) WAAM (b) WAAM-forged	142
Figure 4.16	Inverse Pole Figure (IPF) maps for ER5356 (a) Scanning Location for on Cross Section (b and d) WAAM (c and e) WAAM-Forging	143
Figure 4.17	Kernel Average Misorientation (KAM) Maps Orientation of ER5356 (a) WAAM (b) WAAM-Forging (c) Frequency Distribution of Local Misorientation	144
Figure 4.18	Polar Diagram of Al-Mg on Different Planes and Strain Rate (a) Base Metal, (b) $0.0001s-1$, (c) $0.1s-1$	146
Figure 4.19	Compressive Behavior of WAAM and WAAM-Forging (a and d) Yield Stress (b and d) UCS (c and f) Hardening Capacity	148
Figure 4.20	Typical Plots Used to Evaluate the Strain Rate Sensitivity at Different True Strain of WAAM and WAAM-Forging via (a-	

	b) Common Approach (c-d) Lindholm's Approach (e-f) Strain Rate Sensitivity	150
Figure 4.21	(a) Stress-Strain Curves of WAAM at Different Strain Rates (b) Magnified Images of Box Segment (c) $10-1s-1$ Curve (d) $10-2s-1$ Curve (e) $10-4s-1$ Curve (d) $10-4s-1$ Curve	153
Figure 4.22	(a) Stress-Strain Curves of WAAM-Forging at Different Strain Rates (b) Magnified Images of Box Segment (c) $10-1s-1$ Curve (d) $10-2s-1$ Curve (e) $10-4s-1$ Curve (d) $10-4s-1$ Curve	154
Figure 4.23	Type of Serration in PLC Effect (a) Type A (b) Type B (c) Type C (d) Amplitude of Stress Drop Measurement	155
Figure 4.24	Illustrated Cyclic Pinning-Unpinning Mechanism (a-b) Initial Dislocation Motion (c) Pinning Phase (d) Unpinning Phase	155
Figure 4.25	Linear Regression between Amplitude of Stress Drop up to 50% True Strain for (a) WAAM (b) WAAM-Forging	158

LIST OF SYMBOLS

Symbols

a_f	Front Width
a_r	Rear Width
b_f	Front Depth
b_r	Rear Depth
c_f	Front Length
c_r	Rear Length
f_f	Fraction of Heat in Front Quadrant
f_r	Fraction of Heat in Rear Quadrant
I	Welding Current
η	Heat Input Efficiency
Q	Heat Input or Energy Input Rate
q_f	Front Quadrant
t	Increment
τ	Lag Factor
U	Welding Voltage
V	Travel Speed

LIST OF ABBREVIATIONS

Abbreviations

AM	Additive Manufacturing
BJ	Binder Jetting
DED	Direct Energy Deposition
EBSD	Electron Backscatter Diffraction
EDX	Energy-Dispersive X-Ray
FEM	Finite Element Method
GMAW	Gas Metal Arc Welding
GTAW	Gas Tungsten Arc Welding
KAM	Kernel Average Misorientation
MIG	Metal Inert Gas
PAW	Plasma Arc Welding
PBF	Powder Bed Fusion
SEM	Scanning Electron Microscopy
SF	Simufact.Forming
SL	Sheet Lamination
SW	Simufact.Welding
TS	Travel Speed
UTS	Ultimate Tensile Strength

WAAM	Wire Arc Additive Manufacturing
WFS	Wire Feed Speed

CHAPTER 1
INTRODUCTION

1.1 Research Background

Additive manufacturing (AM) has developed as a transformative advanced manufacturing, enabling the layer-by-layer fabrication of complex structures. Among the various metal AM techniques, wire arc additive manufacturing (WAAM) has increasingly attracted industrial and academic interest due to its high deposition rates, low material wastage, and scalability for large structural components. The WAAM process uses arc welding to melt metal as feedstock is advantageous for producing medium to large parts in aerospace, marine, and structural applications. Compared to powder-based AM technologies, WAAM promotes cost-effectiveness and operational advantages, including better material utilization, lower equipment costs, and higher build rates.

However, when WAAM is applied to aluminium alloy, the process experiences challenges and limitations. Aluminium alloy presents unique issues during arc-based deposition such as porosity, coarse columnar grain structures, and residual stress accumulation due to aluminium's high thermal conductivity, rapid solidification rate, and strong hydrogen solubility differential between the liquid and solid phases during the solidification process. Instability of melt pool during the WAAM process exhibits lower performance of mechanical properties, microstructural inhomogeneity, and geometric distortion. These challenges are critical limitations for WAAM structural applications.

To tackle these challenges, various strategies have been studied in recent literature including arc mode optimization, interpass rolling, heat treatment and hybrid manufacturing. Advanced WAAM modes, from gas metal arc welding (GMAW) to cold metal transfer (CMT) process has been shown to improve WAAM process stability for aluminium alloy. CMT achieves lower and more controlled heat input through synchronized wire retraction and controlled droplet detachment, which reduces the risk of porosity and improving bead quality. However, even with CMT, WAAM components may still produce microstructures and internal defects due to the absence of post-solidification mechanical densification mechanisms. Therefore, the

combination of WAAM with cold forging represents a novel hybrid manufacturing that proposes to implement the geometric flexibility of additive processes with the microstructural refinement capabilities of deformation process. Cold forging is a well-established thermomechanical process that capable of enhancing the material density, reduce voids, and improve mechanical properties via work hardening and dislocation rearrangement. The integration of WAAM with cold forging process can refine grain structures, redistribute residual stresses, and potentially initiate recrystallization, depends on the strain and temperature. Therefore, the hybrid manufacturing process offers a promising route to overcome WAAM limitations particularly in aluminium alloy performance.

As the process parameters are validated by the experimental findings, finite element method (FEM) simulation using tools such as Simufact.Welding (SW) and Simufact.Forming (SF) are employed in this research prior to the experiments to model thermal histories, residual stress evolution, and deformation mechanics. These simulations provide predictive insight and help to optimize process parameters by correlating thermal and mechanical histories with microstructural and mechanical outcomes. Next, according to recent literature, the systematic studies of WAAM-forged aluminium alloys are scarce where the research lacks detailed insights into the microstructural evolution, mechanical anisotropy, and strain-rate dependent deformation behavior in hybrid WAAM components, especially under quasi-static conditions where dynamic strain aging and the Portevin-Le Chatelier (PLC) effect may be activated especially Al-Mg alloys. The PLC effect commonly observed in Al-Mg alloys at specific temperatures, Mg contents, and strain rates as serrated flow in stress-strain response due to interactions between mobile dislocations and diffusing solute atoms. It is essential to have a comprehensive understanding of the influence of PLC effect on WAAM and forging in predicting the performance under low-strain-rate and quasi-static loading conditions.

Moreover, the strain rate sensitivity and strain hardening behavior remain insufficiently described in WAAM aluminium alloy. Incorporating models such as Lindholm's strain rate sensitivity, as well as strain hardening laws (Holloman, Ludwik, Swift, and Afrin) provides a more complete understanding of the material's post-yield behavior and deformation mechanism. In summary, the background of this research is founded on addressing the fundamental barriers of WAAM aluminium alloy such as microstructural defects, mechanical anisotropy, and stress related deformation behavior

through hybrid WAAM-forging approach. By combining the numerical and experimental investigations, this research seeks to fill a critical gap in the current body of knowledge and contribute to the development of a more robust and performance-oriented hybrid manufacturing framework for aluminium alloy components.

1.2 Problem Statement

WAAM has experienced increasing acceptance as a high deposition rate, cost-effective technique for fabricating large-scale metal components. However, the application of aluminium alloys, specifically Al-Mg remain fundamentally limited by several process challenges such as formation of porosity, pronounced anisotropic grain structures, high residual stress, and weak mechanical properties. These defects originate from the cyclic thermal history, rapid solidification dynamics, and arc instability inherent in WAAM, which affect the structural integrity and dimensional accuracy of fabricated aluminium. Hybrid WAAM-forging has emerged as one of potential solutions to improve material integrity by refining grains and redistributing residual stresses. The effectiveness of cold forging on aluminium WAAM especially low reduction ratios to avoid cracking remains underexplored. Furthermore, there are limited studies on couple experimental observations with FEM simulations to optimize process parameters across both WAAM and forging stages.

The adoption of arc control of CMT over GMAW process has demonstrated improved deposition stability and reduced heat input. This modification improved metallurgical and mechanical performance. Moreover, the post-processing applied in conventional manufacturing such as heat treatment or machining are often ineffective or economically infeasible when applied in WAAM especially for thin wall structures. Additionally, a critical knowledge gap exists regarding deformation behavior and dynamic strain aging phenomena, such as PLC effect in WAAM-fabricated aluminium alloy.

The influence of hybrid WAAM-forging of Al-Mg on such deformation behaviors due to solute dislocation interactions has not been thoroughly investigated. The serrated flow and its dependence on microstructural state of WAAM and WAAM-forged remains underexplored. Therefore, a comprehensive study of the mechanical response, microstructural evolution, and residual stress behavior in WAAM and

WAAM-forged aluminium alloys remains limited especially when validated through integrated FEM simulations using platforms such as SW and SF.

There is also limited literature on the integration of plastic deformation process of cold forging as a post-processing strategy of hybrid manufacturing WAAM-forged to overcome these challenges in WAAM. The cold forging process's tendency to reduce porosity, enhance microstructure, redistribute residual stresses, and suppress the severity of the PLC effect has not been systematically evaluated for WAAM aluminium alloys. The absence of comprehensive simulation and experimental-based studies on hybrid WAAM-forged approaches represents a significant research gap. Therefore, this study is motivated by the need to explore the following critical problems:

a) The persistence of microstructural and mechanical deficiencies in WAAM of aluminium alloys, despite process optimization.
b) The lack of PLC effect understanding in additive manufactured Al-Mg alloys under varying strain rates.
c) The absence of validated hybrid manufacturing frameworks that combine WAAM with cold forging to produce mechanically reliable aluminium components.

Hence, this research seeks to overcome these problems through a combined numerical and experimental investigation of the surface integrity, microstructure, mechanical behavior, and residual stress evolution in WAAM and WAAM-forged ER5356 aluminium components with respect to deformation instability and dynamic strain aging phenomena.

1.3 Research Objectives

This study aims to investigate the potential of cold forging as a hybrid post-processing method for WAAM ER5356 to address the limitations of WAAM-fabricated aluminium components and identify gaps related to microstructural instability, residual stress accumulation, and mechanical behavior. Thus, the objectives of this research are outlined as follows:

a) To evaluate the surface integrity and mechanical properties of WAAM and WAAM-forged aluminium alloy using simulation and experimentation.
b) To analyze the strain rate on the compressive strain hardening behavior of Al-Mg WAAM-forged.
c) To develop a strain hardening relationship model between stress-drop amplitude and strain rate for evaluating the Portevin–Le Chatelier (PLC) effect in WAAM and WAAM-forged ER5356 aluminium alloy.

1.4 Research Scope

This research studies the integration of WAAM with cold forging to improve the microstructural and mechanical performance of aluminium alloy ER5356 thin wall. The limitation of WAAM studies focuses on the porosity, residual stress accumulation, and mechanical performance by incorporating a hybrid manufacturing to enhance the structural and functional reliability of additively manufactured parts. In WAAM, the research specifically employs two process modes, which are GMAW and CMT. The heat input strategies are constant heat input of 2970.51 J/cm for GMAW, while a multi-range heat input of 2962.40 – 2924.69 J/cm used for CMT where these values were selected based on a combination of thermal simulations and preliminary deposition experiments in maintaining deposition stability.

The material for WAAM process comprises ER5356 (Al-Mg based alloy) as the filler wire and Al6061 as the substrate material. The combination of filler wire and substrate is relevant in structural application as ER5356 offers superior weldability, good corrosion resistance, hence making it a preferred choice for WAAM. In contrast, Al6061 provides a heat-treatable frequently used in aerospace and automotive. The pairing of these aluminium alloys allows the investigation to remain industry relevant besides capturing the metallurgical interactions of WAAM deposited aluminium categories.

After the deposition, the thin wall is subjected to cold upset forging in the build direction (z-axis) with the height reduction of 6 mm. The forging process was constrained within 6% reduction to avoid cracking and geometric instability. The post-process aims to reduce porosity, refine microstructure, and redistribute the residual stress through plastic deformation, hence improving the final component quality. FEM simulations using SW and SF are employed to model thermal history, stress evolution,

and deformation behavior during the WAAM and forging processes. These simulations serve to validate experimental results and offer predictive capabilities for optimizing hybrid manufacturing routes. Further analysis includes 3D scanning to assess the dimensional stability.

To evaluate the efficiency of the hybrid process, a multi-characterization is applied. The microstructural analysis was performed using scanning electron microscopy (SEM) and electron backscatter diffraction (EBSD), focusing on the surface integrity and microstructure including the porosity distribution, inverse pole figure (IPF) maps, grain boundaries, kernel average misorientation (KAM) of grain refinement and crystallographic texture following the cold forging process. In addition, energy-dispersive X-ray spectroscopy (EDX) was utilized to determine the elemental composition of aluminium alloy in WAAM and forging during processing.

The investigation on microstructural and chemical analysis enables comprehensive study on the material integrity and performance. The mechanical behavior is assessed via tensile testing at three build orientations, parallel (0°), diagonal (45°), and perpendicular (90°) to the deposition path specifically for WAAM samples. To complement the mechanical and microstructural data, x-ray diffraction (XRD) was employed to evaluate the residual stress distributions of WAAM and WAAM-forged processes.

To investigate the strain-rate sensitivity and analyze the PLC effect on WAAM-forged sample, compression testing was also conducted. The compression testing was conducted at different strain rates (0.1, 0.01, 0.001, and 0.0001 s^{-1}). The occurrence of serrated flow is characterized in terms of stress-drop amplitude and frequency, where a new equation is proposed to relate the stress amplitude to the strain rate, providing a novel insight into dynamic strain ageing behavior in Al-Mg alloys via WAAM and cold forging. The strain rate sensitivity is quantified using both Lindholm's method and common approach, enabling comparative analysis across different models and deformation regimes. Next, the strain hardening exponent is evaluated from compression data using four models; Ludwik, Holloman, Swift, and Afrin to understand the post-yield behavior and work hardening of the material in the deposited condition and post-processing, WAAM vs WAAM-forged.

This research involves synthesis, post-processing, advanced characterization, and simulation of ER5356 aluminium alloy via WAAM and WAAM-forging. The research contributes to a comprehensive understanding of post-process deformation to

mitigate the WAAM defects, improve structural performance and advancing the understanding of deformation instability with PLC phenomenon of additively manufactured Al-Mg alloys. These findings have direct implications for the design of reliable, high performance aluminium structures in complex applications.

1.5 Significance of Study

This study promotes significant value in advancing the hybrid manufacturing methodologies for aluminium alloys, particularly through the WAAM and cold forging. Although WAAM has been considered a cost-efficient technique for fabricating large-scale metallic structures, the application in aluminium alloys, ER5356, is constrained by fundamental metallurgical challenges, including the formation of porosity, the development of coarse grain structures, the accumulation of residual stress, tensile stresses, and resulting limitations in mechanical performance. The application of cold forging process following WAAM deposition introduces a novel and strategic approach to address these deficiencies. The application of controlled plastic deformation, the cold forging facilitates material densification, which promotes microstructural refinement via dynamic recrystallization and enables relaxation of residual stress thereby enhancing the structural integrity of WAAM aluminium structures.

One major aspect is the systematic investigation of microstructural evolution in WAAM and WAAM-forged aluminium alloy components by using characterization techniques such as SEM and EBSD provides the mechanisms of grain refinement, dislocation rearrangement, and local misorientation redistribution following post-process forging. The surface integrity analysis provides insight into the enhancement of microstructural uniformity through controlled plastic deformation of additive manufactured aluminium parts.

Another significant factor is the research studies contribute to the mechanical understanding of strain rate sensitivity and dynamic deformation behavior in WAAM-fabricated Al-Mg alloys, through the PLC effect. While PLC phenomenon has been studied in wrought Al-Mg alloys, its manifestation in WAAM and WAAM-forged conditions under low strain rates is underexplored. By quantifying serrated flow characteristics and proposing a new model linking stress-drop amplitude to strain rate, this study advances fundamental knowledge on dynamic strain aging in the context of hybrid manufacturing WAAM-forging process.

A further aspect is the research work employs advanced process simulation via FEM to model thermal cycles, stress distributions, and deformation mechanics in both WAAM and cold forging. The simulation and experimental framework validates physical observations and also as predictive control of process structure property relationships. As a result, the findings have direct relevance to industrial-scale implementation where hybrid manufacturing approaches must balance the performance enhancement with process feasibility.

From a holistic perspective, the outcomes of this research are expected to bridge the gap between additive manufacturing and conventional metal forming, offering a practical solution in enhancement of structural and mechanical reliability of aluminium alloy components fabricated via WAAM. In addition, this study ensures high industrial relevance since the combination of ER5356 and Al6061 widely employed in aerospace, marine, and structural applications. Thus, this study provides a strong foundation for further innovations in hybrid manufacturing strategies for lightweight structural metals.

CHAPTER 2
LITERATURE REVIEW

2.1 Introduction

Wire arc additive manufacturing (WAAM) has emerged as a promising metal additive manufacturing technique due to the suitability for fabrication of large-scale metallic structures, high deposition rates, and cost efficiency. Among the various WAAM approaches, gas metal arc welding (GMAW) and cold metal transfer (CMT) processes widely adopted for aluminium due to their stable arc control and ease of integration. The literature review provide comprehensive review of the status of WAAM, including its fundamental principles, process parameters, heat input considerations, and their influence on the geometry accuracy including the mechanical properties. Advanced simulation tools are increasingly utilized to predict thermal profiles, residual stress development, and geometrical deformation.

Furthermore, to overcome WAAM limitations such as porosity, post-processing strategies involving hybrid manufacturing approaches that combine WAAM with forming has been reported. However, studies focusing on hybrid WAAM-forging of aluminium alloys concerning mechanical response and the Portevin-Le Chatelier (PLC) effect remain limited, thereby necessitating further investigation. Compression testing of aluminium offers quantitative insight into its mechanical response, facilitating the evaluation of strain hardening behavior and its correlation with the PLC effect. The PLC effect is manifested in the stress–strain response and is associated with the underlying deformation mechanisms and microstructural evolution induced by the hybrid WAAM-forging process. Therefore, this chapter presents an overview of WAAM-forging of aluminium alloys, establishing a systematic relationship between processing conditions, microstructural characteristics, and mechanical behavior.

2.2 Current Status and Perspective of Wire Arc Additive Manufacturing (WAAM)

2.2.1 Principles and Current Status of WAAM

Additive manufacturing (AM) technology or 3D printing produces complex geometry through layer-by-layer deposition (K. S. Derekar, 2018). It is highly demanded in industries due to its versatility in processing various materials and manufacturing near-net-shape parts with high accuracy (Y. Li et al., 2022). Metal AM technologies are generally classified into powder bed fusion (PBF), directed energy deposition (DED), binder jetting (BJ), and sheet lamination (SL), as illustrated in Figure 2.1. The two categories that are most frequently utilized in industry are PBF and DED (Treutler & Wesling, 2021). Compared with PBF, which relies on metal powders and controlled environments, DED offers greater material efficiency and lower raw material costs, making it more suitable for the fabrication of large-scale metallic components (Treutler & Wesling, 2021). In addition, DED processes typically employ either wire or powder and utilize heat sources such as lasers, electron beams, or electric arcs to melt metal wire, forming molten droplets on the substrate layer.

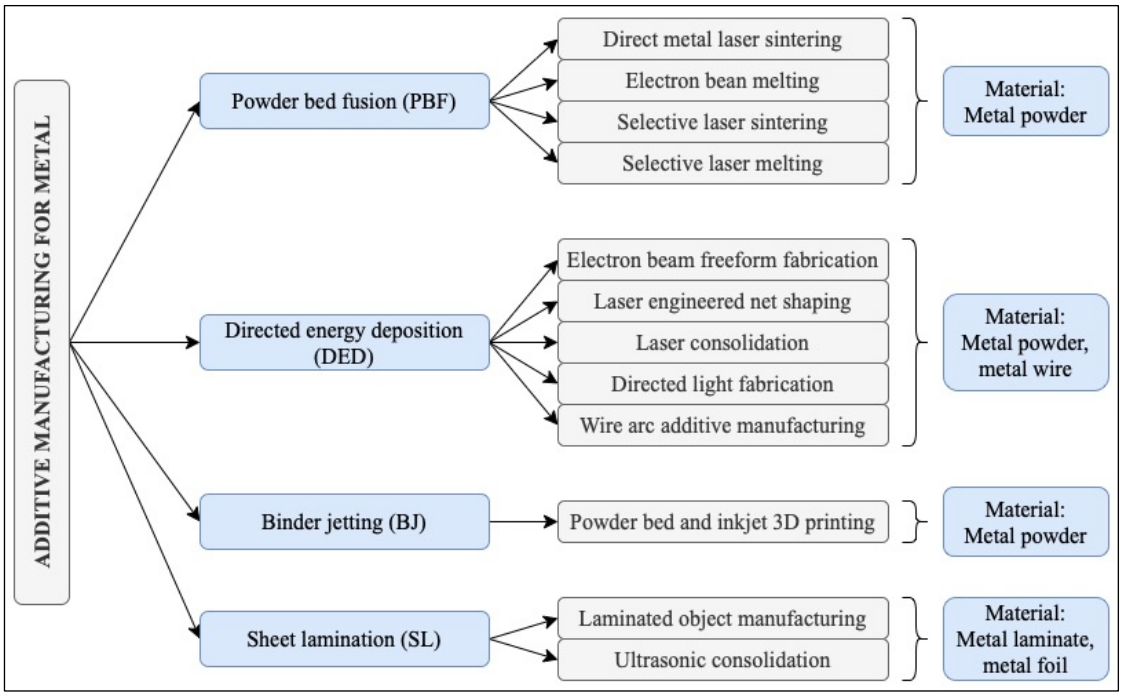

Figure 2.1 AM for Metal Classification (Treutler & Wesling, 2021)

As shown in Figure 2.2, wire-based DED achieves higher deposition rates and can fabricate complex parts than powder bed-based (Rodrigues et al., 2019). When an

electric arc and solid wire are combined, this process is known as wire arc additive manufacturing (WAAM) as defined by ASTM F2792-12a (S. R. Singh & Khanna, 2020). The process involves melting the wire to form a molten pool on the substrate, followed by successive layer deposition to build the component geometry. Basically, WAAM comprises the arc generation, wire feed system, and substrate for the desired deposition, where the process is controlled by a robotic arm system machine (Panchenko et al., 2019). Due to its efficiency, cost-effectiveness, and suitability in large-scale industrial production, WAAM has wide applicability to various metals and their alloys (Treutler & Wesling, 2021). Therefore, WAAM is being embraced by both academia and industry owing to the advantages of the technique (S. R. Singh & Khanna, 2020).

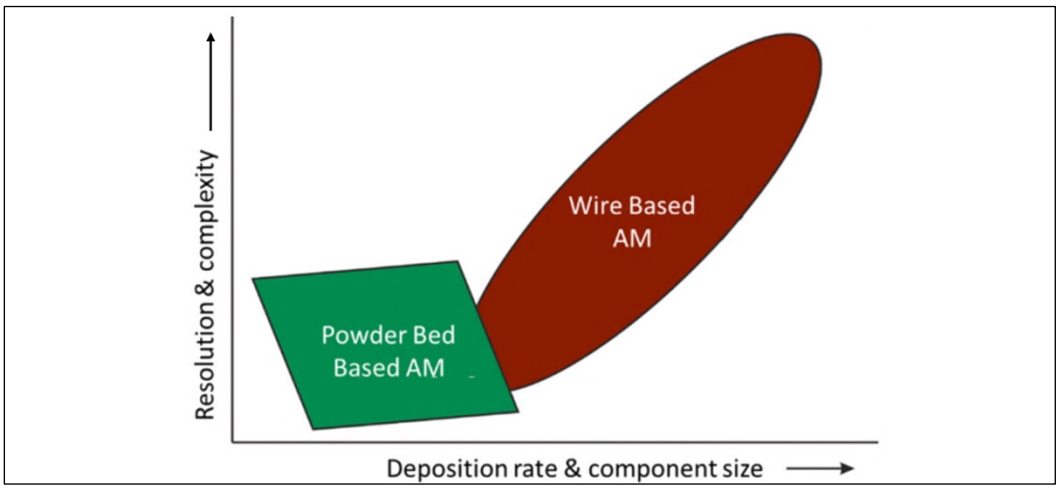

Figure 2.2 Comparison between Wire-Based and Powder Bed Based AM (Rodrigues et al., 2019)

WAAM is particularly promising for expensive materials like titanium, stainless steel, refractory nickel alloys, and high-strength aluminium alloy due to its greater flexibility, mechanical properties, material utilization, and economic efficiency compared to the other AM process as presented in Figure 2.3 (Shah et al., 2023). Table 2.1 listed the advantages and limitations of common materials employed in WAAM. According to the lists, aluminium alloys have received increasing attention due to their strength-to-weight ratio and cost efficiency for complex components (Srivastava et al., 2023). Aerospace applications including STELIA Aerospace's fuselage panels and large-scale components demonstrate aluminium's superior cost-to-performance ratio compared to expensive titanium alternative (Bambach et al., 2020; Kesarwani, Yuvaraj, & Niranjan, 2024). Thus, scholars and researchers are actively exploring methods to

improve weldability and mechanical properties of aluminium alloy, including the deposition strategy (Vimal et al., 2019).

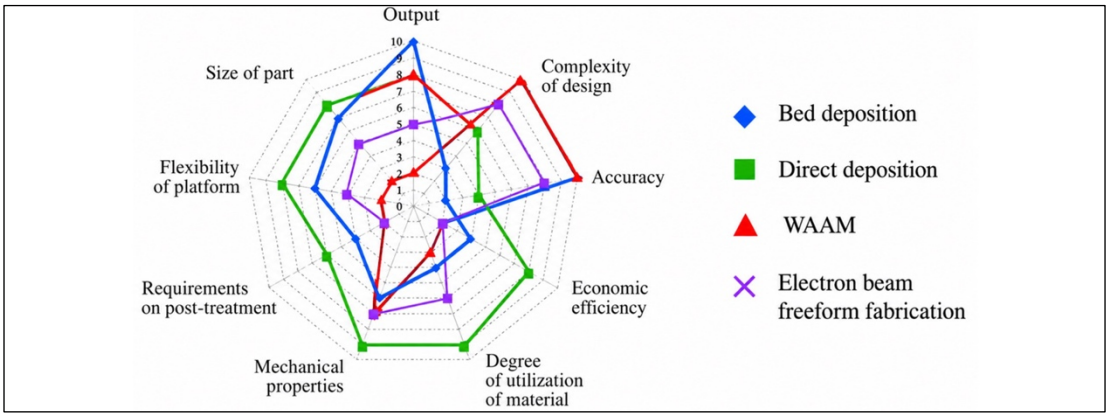

Figure 2.3 Advantages of WAAM and other AM process (Shah et al., 2023)

Table 2.1
Comparative of Common Materials on WAAM Application

Alloy	Advantages	Limitations	WAAM Relevance
Aluminium (Bambach et al., 2020; Oliveira et al., 2021; Srivastava et al., 2023)	Lightweight, good thermal and electrical conductivity, cost effective, excellent weldability, lower equipment cost	Lower melting point, porosity susceptibility, oxide layer formation, anisotropic properties, limited heat treatability some series	Widely studied for aerospace or automotive, balance of properties and affordability makes it ideal, WAAM enables complex part fabrication
Steel (Rodrigues et al., 2019; S. R. Singh & Khanna, 2020)	High strength and toughness, excellent durability, cost effective, wide availability	Higher density, significant residual stress development, weldability challenges in some alloys	Used for heavy duty applications, but has limits aerospace application compared with aluminium
Titanium (S. R. Singh & Khanna, 2020; Srivastava et al., 2023)	Exceptional strength-to-weight ratio, superior corrosion resistance, high temperature performance,	Very expensive, complex weldability, lower thermal conductivity, requires specialized equipment	High-value aerospace application, research ongoing but cost and complexity limit broader study compare Al
Nickel-based (S. R. Singh & Khanna, 2020; Srivastava et al., 2023)	High-temperature strength, superior creep resistance, high fatigue strength, oxidation resistance	Extremely costly, difficult to machine, high reactivity, complex processing requirements	Narrow high-temperature applications only, cost limits in WAAM, Al remains preferred for industrial

Most WAAM processes rely on the automated welding fundamental concepts such as gas metal arc welding (GMAW), plasma arc welding (PAW), and gas tungsten arc welding (GTAW) (S. R. Singh & Khanna, 2020). Among these, GMAW is the most used in the world due to its high productivity and possibility of automation since its development in the 1950s (Srivastava et al., 2023). GMAW, also known as metal inert gas (MIG) welding, establishes an arc between a wire electrode and the workpiece under inert gas shielding, which minimizes oxidation and contamination. A schematic of the GMAW process is shown in Figure 2.4. GMAW utilizes several metal transfer modes, each with distinct characteristics related to welding current, equipment, and electrode type (Oliveira et al., 2021). For aluminium alloys, the spray transfer mode is commonly preferred as it provides stable deposition and improved bead morphology (Oliveira et al., 2021).

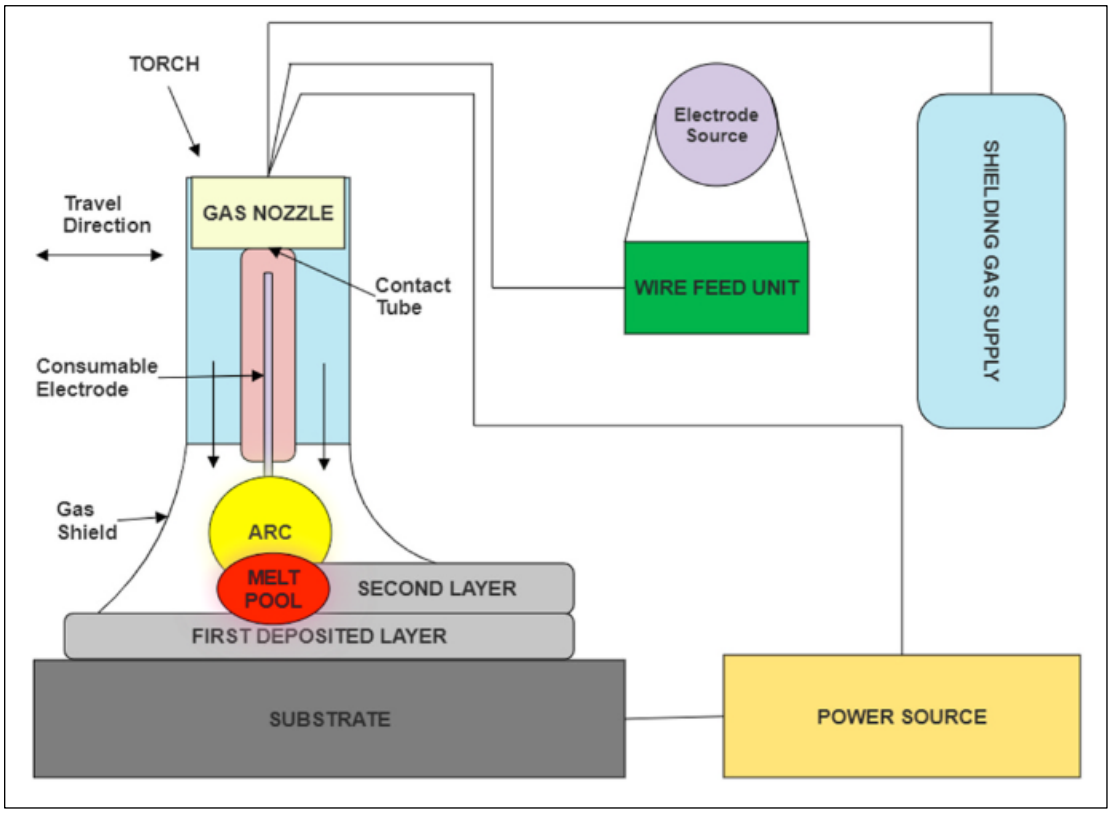

Figure 2.4 Schematic of GMAW Process (Bambach et al., 2020)

GMAW is commonly adopted in WAAM due to its high deposition rates of 15 to 16 g/min compared to PAW and GTAW, which makes it well-suited for large-scale part production in a shorter timeframe (S. R. Singh & Khanna, 2020; Srivastava et al., 2023). Besides that, GMAW is characterized by low-cost equipment, ease of operation, and versatile for a wide range of metals and alloys including aluminium, copper, steel, titanium, brass, and nickel alloys (Gokul KA & Jose MJ, 2022; Oliveira et al., 2021).

However, the relatively high heat input associated with GMAW leads to coarser microstructures, increased porosity, thermal distortion, and spatter formation especially on aluminium parts that can affect component tolerance and potentially lead to premature failure (Aldalur et al., 2021; Oliveira et al., 2021). Despite these limitations, GMAW is still widely used across various industries for manufacturing and repairing metal parts especially in automotive, aerospace, shipbuilding and marine industries, construction and general manufacturing due to its cost effectiveness and versatility for broad range of industrial manufacturing needs (Gokul KA & Jose MJ, 2022; Y. Zhao et al., 2022).

To enhance process stability and deposition quality, an advanced variant of GMAW known as cold metal transfer (CMT) was developed by Fronius International GmbH (S. R. Singh & Khanna, 2020). The CMT setup is generally similar to the conventional GMAW-based WAAM system in terms of using a consumable wire electrode, shielding gas, arc heat source, substrate, and robotic movement. However, CMT employs a controlled short-circuit metal transfer mechanism with synchronized wire retraction, significantly reduces heat input and enhances arc stability. This process enables finer microstructures, improved interlayer bonding, and minimal spatter, making it more suitable for WAAM applications where precision and microstructural control are critical (S. R. Singh & Khanna, 2020). This process employs a controlled push-and-pull electromechanical system to regulate droplet transfer. When the wire tip touches the molten pool, it triggers a retraction, causing the droplet to detach and transfer to the weld pool, thereby minimizing heat generation (Oliveira et al., 2021). This controlled droplet transfer contributes to a more stable arc and a refined weld bead.

Figure 2.5 illustrates the operating principle of the CMT welding technique. In GMAW, the process relies on spray or globular transfer driven by magnetic forces which create large droplets that escape the weld pool and generate noticeable spatter. In terms of setup, the CMT setup uses a controlled push–pull wire feeding system, where the wire is retracted when it touches the molten pool, allowing the droplet to detach at a lower current level. This reduces heat input and stabilises the molten pool during deposition. Therefore, compared with GMAW, the CMT setup provides better control of droplet transfer, lower thermal accumulation, reduced spatter, and improved bead formation, which makes it more suitable for WAAM of aluminium alloy where porosity, distortion, and heat accumulation are critical concerns.

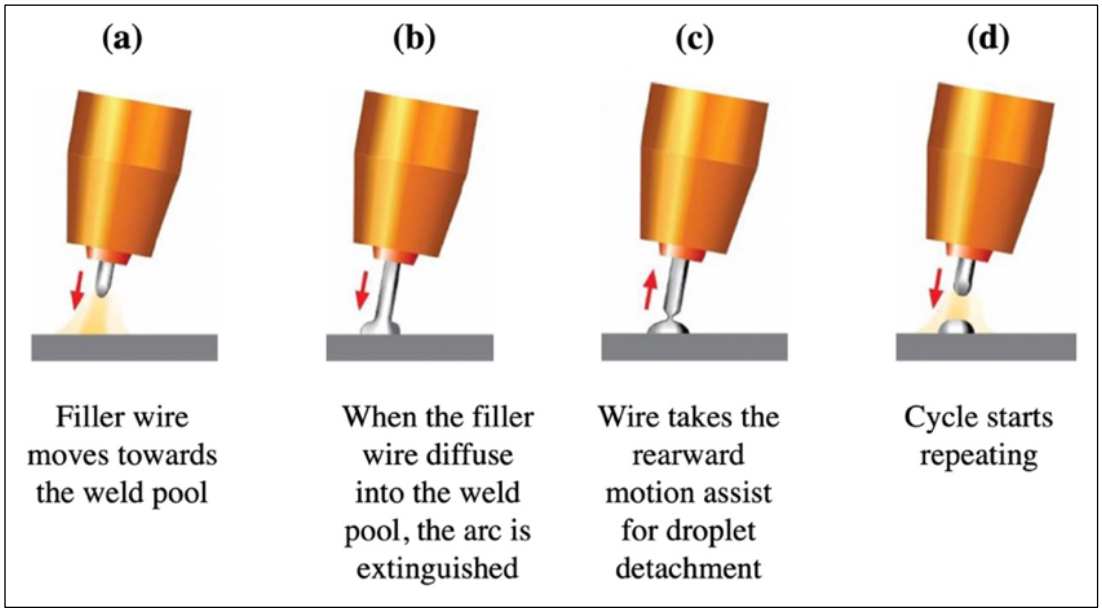

Figure 2.5 Principle of Operation of CMT Welding Technique (Truppel et al., 2019; Vazquez et al., 2023)

A comparison between GMAW and CMT processes is summarised in Table 2.2. CMT technology is particularly suitable for WAAM of aluminium alloy due to low heat input, which minimise the defects like porosity, hot cracking, and distortion since aluminium alloy have high thermal conductivity and narrow solidification range (Gu et al., 2020). The control solidification in CMT promotes finer grain structures and more uniform microstructures (Köhler et al., 2019). Despite the reduced heat input, CMT can achieve high deposition rates, which is crucial for the efficient manufacturing of large components (Singla et al., 2024).

Therefore, CMT-based WAAM has been increasingly adopted in aerospace, automotive, and customised components due to the flexibility and precision to add features to existing components (Wieczorowski et al., 2023). In conclusion, GMAW and CMT are important variations of the WAAM process. GMAW offers its simplicity and industrial maturity, making it a practical option for bulk deposition. However, its high heat input pose challenges such as porosity formation. In contrast, CMT offers better deposition control, reduced heat input, and increased process stability all of which are essential for raising the microstructural quality.

Table 2.2
Comparative Analysis of GMAW and CMT for WAAM

Feature	GMAW	CMT	Justification
Heat input	Higher, can lead to distortion and defects (Barath Kumar & Manikandan, 2022; Gu et al., 2020)	Lower, reduces distortion and defects (Barath Kumar & Manikandan, 2022; Gu et al., 2020)	CMT uses controlled short-circuit transfer reducing thermal energy. Proven through thermal gradient, GMAW peak temperatures ~1090 ℃ vs ~930 ℃ (Gokul KA & Jose MJ, 2022)
Metal transfer	Spray or globular transfer via magnetic forces	Mechanical droplet detachment with wire retraction	CMT's robotic wire movement provides precise control, eliminating spatter (Arana et al., 2021; Gokul KA & Jose MJ, 2022; Gu et al., 2020)
Porosity	More prone to porosity, especially with high heat input	Reduced porosity due to controlled solidification	CMT reduces hydrogen entrapment through lower thermal cycles. Pulsed-AC mode further reduces porosity compared to GMAW (Shanker & Wattal, 2023; Y. Zhao et al., 2022)
Deposition rate	Generally high (3-4 kg/h)	Lower compared GMAW (2-3 kg/h)	GMAW prioritizes speed, CMT prioritizes quality (Arana et al., 2021; Bambach et al., 2020; Srivastava et al., 2023)
Mechanical properties	Lower ductility	7 – 17% elongation	CMT achieves superior hardness refinement and reduced anisotropy (Oliveira et al., 2021; Y. Zhang et al., 2022)
Surface quality	Spatter significant	Almost zero spatter	CMT's low heat input produces better bead geometry (Chen et al., 2023)
Process stability	Unstable arc, sensitive to parameters	Highly stable, wide parameter	CMT shows constant short-circuit frequency via digital control (Gokul KA & Jose MJ, 2022)
Suitability materials	Steels, stainless steel, limited aluminium	Al alloys, Mg alloys, dissimilar metals	CMT's thermal control prevents hot cracking in heat-treatable alloys (Oliveira et al., 2021; Y. Zhang et al., 2022)
Cost	Lower equipment cost	Higher equipment cost (Fronius)	GMAW economical for production, CMT better for quality-critical aerospace parts (Bambach et al., 2020; Srivastava et al., 2023)

2.2.2 Influence of Process Parameters and Heat Input on Deposits Geometry

The selection and control of WAAM process parameters that associated heat input are critical determinants of the resulting bead geometry and wall formation quality (Srivastava et al., 2023). Heat input is defined as the specific energy transferred to the weld per unit length, calculated using the fundamental relationship using equation in (2.1), where Q is the heat input, U is the welding voltage, I is the welding current, V is the travel speed, and η is the heat input efficiency (Rosli et al., 2021). According to M. Wieczorowski et al. (Wieczorowski et al., 2023), the process efficiency has been reported to range between 0.8 and 0.9, with 0.8 being the commonly applied value for the WAAM thin wall geometry formation. The relationship allows to predict and control thermal distribution between deposition layers, thereby directly influencing geometry stability and dimensional accuracy of thin wall structures (Zuo et al., 2025).

$$Q = \frac{U \cdot I \cdot \eta}{V} \tag{2.1}$$

Recent studies in Table 2.3 confirm that optimizing heat input through welding current, voltage and travel speed can control porosity, grain refinement and phase distribution in WAAM aluminium components either GMAW or CMT processes. The application of lower heat input is consistently aligned with refined microstructure and enhanced in mechanical performance, for instance studies by J. Singla et al. (Singla et al., 2024) found that lowering heat input (95.4 J/mm) resulted reduced kernel average misorientation (KAM) and improved ultimate tensile strength (UTS) which exceeding 230.0 MPa for Al5356, compared to higher heat input of 208.5 J/mm. According to the literature, the optimal heat input range reported varies considerably. This is because M. Kohler et al. (Köhler et al., 2019) observed smooth, uniform waviness and fine porosity of Al5356 below 100.0 J/mm, whereas X. Zuo et al. (Zuo et al., 2025) identified formation for achieving stable thin wall formation approximately 120.0 J/mm.

These variations indicate that single heat input cannot be universally defined as optimal and applicable for the same types of material because the heat input sensitivity also influenced geometry and thermal accumulation during layers deposition. This is further evidenced by the findings of X. Zuo et al. (Zuo et al., 2025) were increasing the heat input within the low range of 87.5 J/mm to 190.0 J/mm on Al5356 resulted in wall width changes with an increment of 3.7 mm, refer to Figure 2.6 (Zuo et al., 2025).

Higher heat input promotes greater melting and material fluidity, resulting in increased wall width and penetration depth, concurrent with a decreased layer height due to molten pool spreading and prolonged the liquid state duration (Chandra et al., 2023; Zuo et al., 2025). These findings suggested that heat input selection is strongly dependent on types of material due to different manufacturer, component geometry, build orientation and thermal accumulation during WAAM deposition.

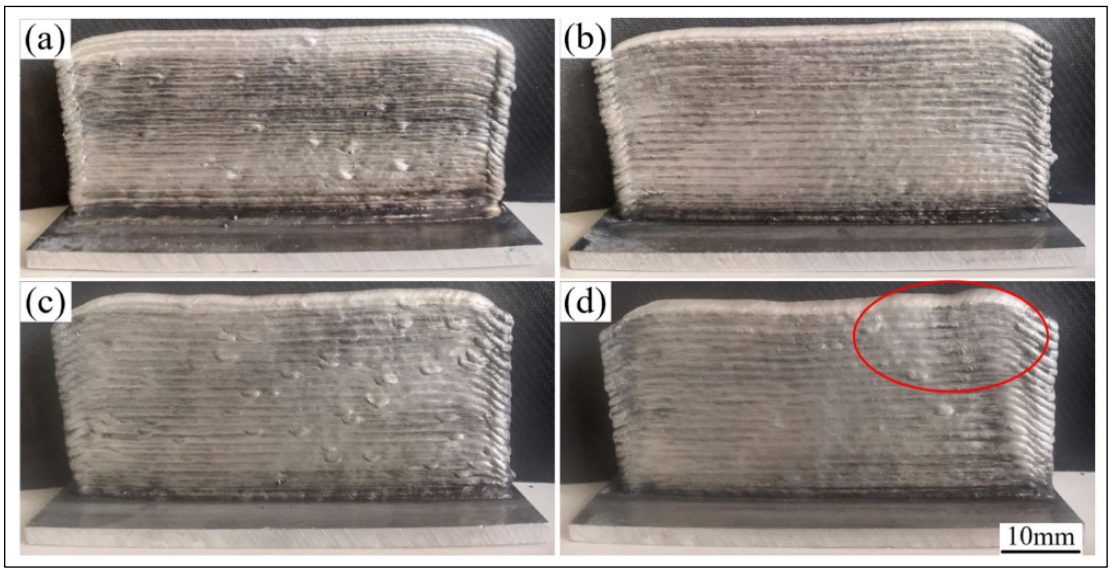

Figure 2.6 Thin Wall of Al5356 using Different Heat Input (a) 87.5 J/mm (b) 120.0 J/mm (c) 154.2 J/mm (d) 190.0 J/mm (Zuo et al., 2025)

The choice of welding technology plays a decisive role in governing the heat input magnitude and thermal distribution during deposition. As stated in 2.2.1, as compared with CMT, GMAW generates higher heat input due to its continuous metal transfer mode, which resulting more thermal energy to the substrate, consequently, produces higher peak temperature. This trend supported by A. Oliveira et al. (Oliveira et al., 2021) where the research found that the peak temperature for GMAW approximately 1090°C compared to the CMT process, 930°C. While the higher thermal input in GMAW leads to more open arc configuration, lower wetting angles and greater penetration depth, it increases excessive of heat accumulation in thin wall geometries (Oliveira et al., 2021).

In contrast, the reduced heat input in CMT provides greater control over geometry stability, making process selection critical for dimensional accuracy of thin wall deposition, as displayed in Figure 2.7. Therefore, the selection of welding technology inherently involves a trade-off between the speed and penetration efficiency offered by GMAW versus the superior thermal management and resultant quality

provided by CMT for WAAM application as justified in Table 2.2. Optimal process selection must align the welding technology with the component's geometry and specific heat accumulation constraints, rather than relying on deposition rate or penetration capability (Rodrigues et al., 2019).

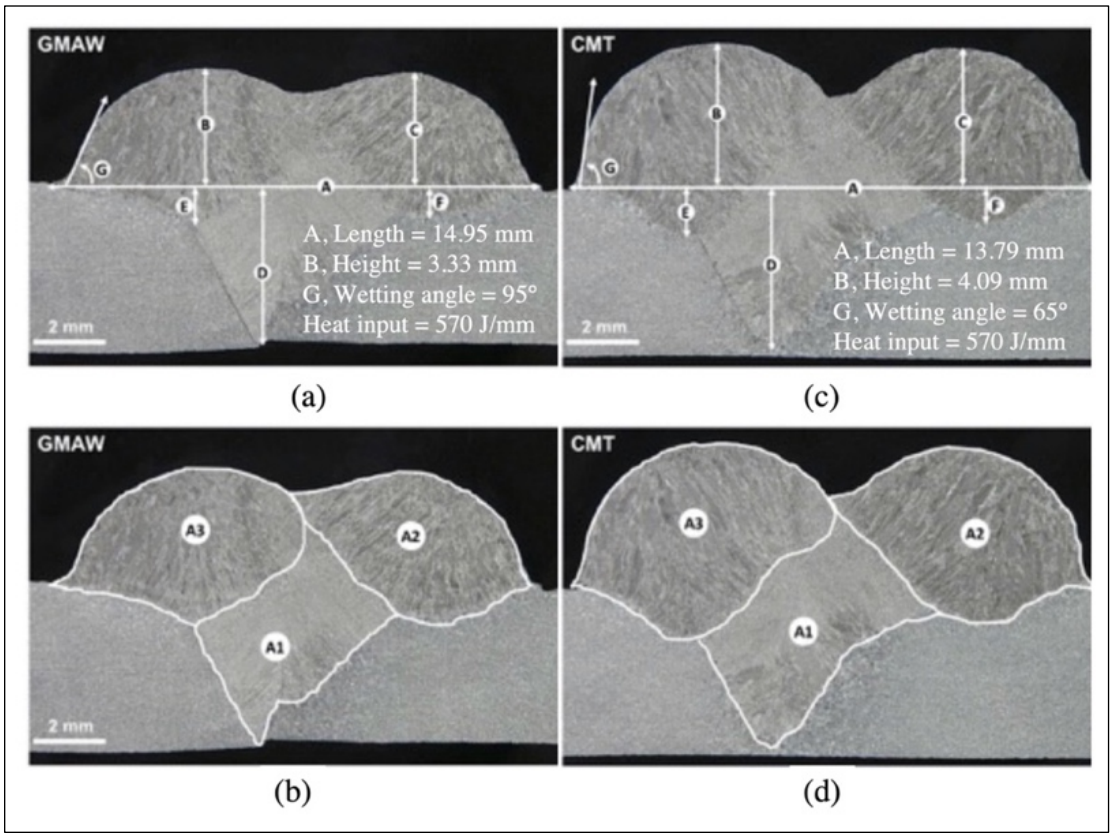

Figure 2.7 SEM Micrograph Showing Cross-Section for Standard (a-b) GMAW process, (c-d) CMT process (Oliveira et al., 2021)

Moreover, single and multi-heat input strategies produce distinctly different thin wall formation in WAAM, reflecting the cumulative nature of multi-layer thermal history, as presented in Figure 2.8. Recent research by C. Gen et al. (Greebmalai & Warinsiriruk, 2020) demonstrated that multi heat input approaches by combining current reduction with increased travel speed generates lower heat input, resulting in narrower, taller walls with improved height uniformity. Conversely, single condition current reduction produces cumulative heat accumulation, creating fan-shaped wall as shown in Figure 2.8(a). Notably, even when the total heat input remains constant as in Figure 2.8(b), variations in current reduction significantly influence the wall geometry across multiple layers. Therefore, the studies highlighting the importance of parameters interaction rather than individual parameter control.

Table 2.3
Influence of Process Parameters and Heat Input on Aluminium Alloy

Alloy / Reference	Arc Welding	Heat Input (J/mm)	Voltage (V)	Current (A)	Travel Speed (mm/s)	Macrostructure / Geometry	Microstructure	Mechanical Properties (Horizontal/Longitudinal: 0° deposition Vertical/Transverse: 90° deposition)
Al 5356 (Singla et al., 2024)	CMT	95.4	13.7	87.0	6.7	Flawless microstructure, dimensional stability	Finer grains, minimal KAM	UTS longitudinal: ~230.0 MPa UTS transverse: ~110.0 MPa
Al 5356 (Singla et al., 2024)	CMT	208.5	14.6	119.0	6.7	Irregular beads and material flow, void	Coarse, elongated toward the top	UTS longitudinal: ~180.0 MPa UTS transverse: ~70.0 MPa
Al 5356 (Köhler et al., 2019)	CMT	109.0	15.0 – 15.5	91.0 – 92.0	10.0	Smooth, uniform wall surface, relatively narrow	Evenly dispersed fine porosity, diameter < 50 μm	YS horizontal: 114.9 ± 1.0 MPa YS vertical: 114.9 ± 2.7 MPa UTS horizontal: 267.6 ± 3.5 MPa UTS vertical: 254.0 ± 5.6 MPa
Al 5356 (Zuo et al., 2025)	CMT	87.5	17.5	30.0	6.0	Width 5.22 mm	Finer, dispersed $\beta(Al_3Mg_2)$	Average hardness: 69.4 HV UTS horizontal: 236.0 MPa UTS vertical: 231.0 MPa
Al 5356 (Zuo et al., 2025)	CMT	120.0	18.0	40.0	6.0	Optimal formation	Size of $\beta(Al_3Mg_2)$ increases, promoting full metallurgical	Average hardness: 76.0 HV UTS horizontal: 249.0 MPa UTS vertical: 237.0 MPa

Alloy / Reference	Arc Welding	Heat Input (J/mm)	Voltage (V)	Current (A)	Travel Speed (mm/s)	Macrostructure / Geometry	Microstructure	Mechanical Properties (Horizontal/Longitudinal: 0° deposition Vertical/Transverse: 90° deposition)
Al 5356 (Zuo et al., 2025)	CMT	154.2	18.5	50.0	6.0	N/A	$\beta(Al_3Mg_2)$ particles form a connected network structure	Average hardness: 78.0 HV UTS horizontal: 240.0 MPa UTS vertical: 236.0 MPa
Al 5356 (Zuo et al., 2025)	CMT	190.0	19.0	60.0	6.0	Width increases significantly to 8.87 mm	Size of $\beta(Al_3Mg_2)$ in maximum, pronounced structure	Average hardness: 74.0 HV UTS horizontal: 239.0 MPa UTS vertical: 234.0 MPa
Al 5356 (Chandra et al., 2023)	GMAW	N/A	19.5	45.0 – 50.0	4.0	Porosity, lack of fusion, mostly on top	Anisotropic behavior observed	UTS transverse: 288.7 MPa UTS longitudinal: 253.5 MPa
Al-Mg (Y. Liu et al., 2022)	CMT	N/A	90.0 – 130.0	N/A	6.7 – 13.3	Reciprocating path results in better	Decreased current or increased speed reduces	UTS maximum: 382.0 MPa UTS average: 310.0 MPa

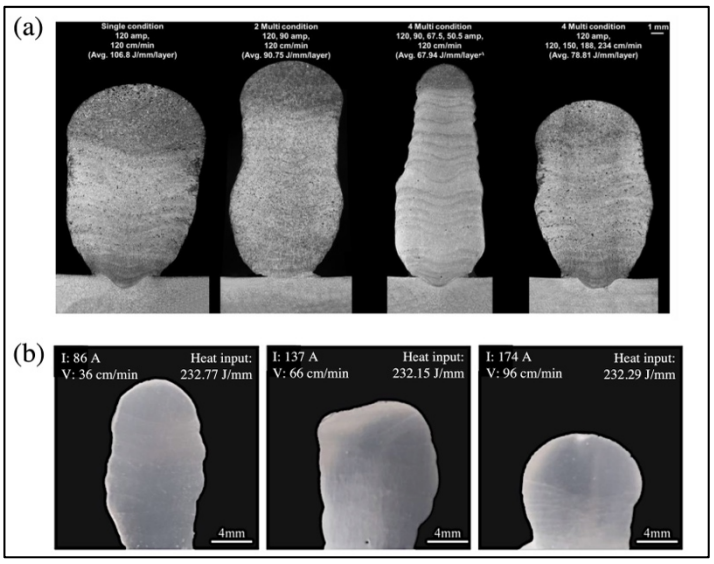

Figure 2.8 Cross-Section of Thin Wall Prepared by GMAW using Different Combination of Heat Input (a) ER5356 (b) Al 4047 (Chen et al., 2023; Greebmalai & Warinsiriruk, 2020)

However, excessive and insufficient heat input both present challenges in thin wall fabrication. Excessive heat input leads to geometrical defects including humping, wall waviness and molten pool overflow, which degrade structural integrity (Singla et al., 2024; Zuo et al., 2025). Although humping as shown in Figure 2.9 can be mitigate by controlling the wire feed speed to travel speed ratio (WFS/TS) to maintain molten weld pool shape (Shah et al., 2023). Conversely, insufficient heat input can result in incomplete fusion or lack of wettability between layers, potentially creating interlayer bonding defects (Zuo et al., 2025). Therefore, based on these findings, it suggests that effective thin wall fabrication requires coordinated multi parameter optimization rather than single parameter control.

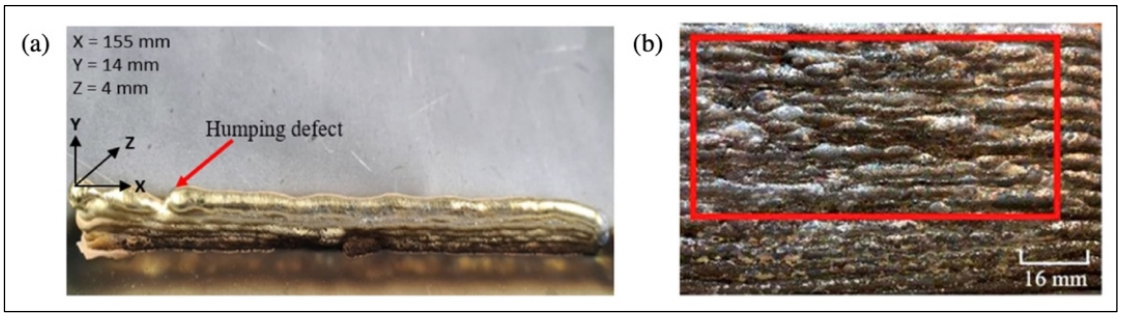

Figure 2.9 Surface Structure Defects (a) Humping (b) Material Overflow (Shah et al., 2023)

Other than heat input, deposition path strategies influences heat accumulation and wall quality. There are three deposition strategies of torch movement to consider in WAAM: unidirectional (straight direction), bidirectional (alternating direction) and weaving (oscillating torch path) (Arana et al., 2022; Shah et al., 2023). Unidirectional

strategy represents a straight weld bead without any weaving, while in contrast, weaving appear for overlap torch oscillation to generate triangle (zigzag) or circle travel direction as illustrated in Figure 2.10. Experimental studies consistently show that bidirectional and zigzag based deposition paths mitigate heat accumulation by alternating thermal loading between layers, thereby promoting more uniform heat dissipation and stabilised wall formation. M. Srivastava et al. (Srivastava et al., 2023) and M. Arana et al. (Arana et al., 2022) demonstrated that bidirectional path can help manage heat accumulation and improve surface stable deposited layers.

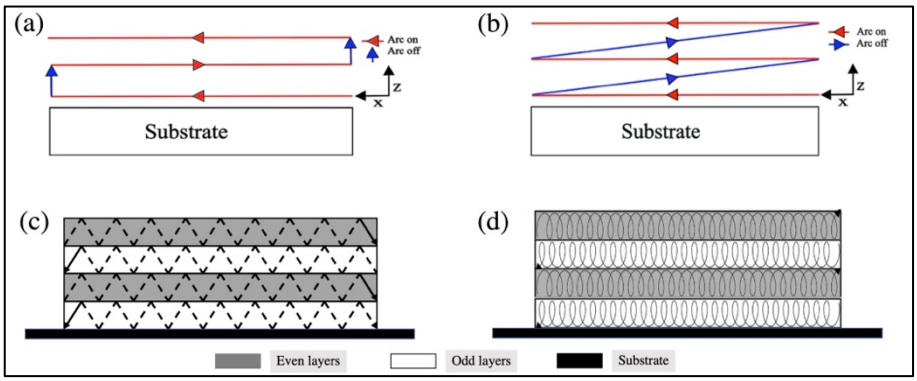

Figure 2.10 Path Strategy for Material Deposition (a) Bidirectional, (b) Unidirectional, (c) Triangle (d) Spiral (Arana et al., 2022; Shah et al., 2023)

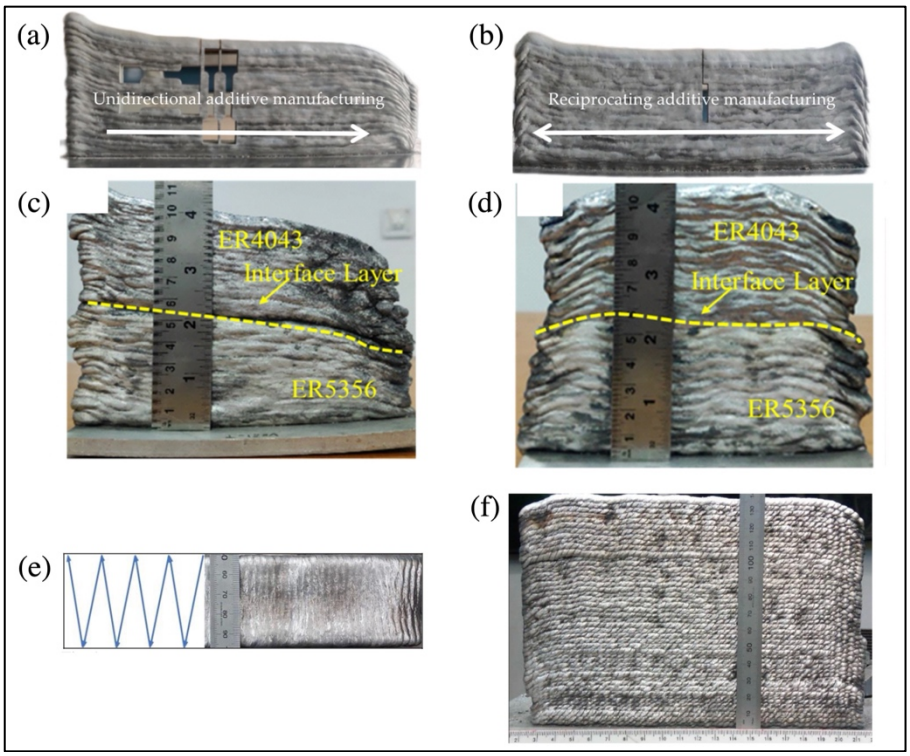

Figure 2.11 Aluminium alloy under Different Deposition Path using (a-b) Al-Mg (c-d) Bimetallic ER4043 and ER5356 (e-f) Al5356 (K. Derekar et al., 2019; Kesarwani et al., 2024; Y. Liu et al., 2022)

This observation aligns the bidirectional path strategy of Al-Mg thin wall compared to unidirectional as shown in Figure 2.11(a) and (b). The effectiveness of zigzag and bidirectional strategies able to ensure symmetric shapes and compensate for wall irregularities at weld start and end position, refer Figure 2.11(f) (Arana et al., 2022; Kesarwani et al., 2024). In addition, employing zigzag path able to increase the width of the wall (Figure 2.11(e)). Notably, these improvements are independent of filler material, indicating that deposition path strategy more influence on thermal and geometric stability than material composition variation. This is supported by the findings of S. Kersrwani et al. (Kesarwani et al., 2024), where bimetallic aluminium walls exhibited unstable and non-uniform formation, under unidirectional paths (Figure 2.11(c)), whereas bidirectional deposition consistently produced a stable and uniform aluminium thin wall (Figure 2.11(d)). This geometric stability is critical as it directly influences residual stresses and microstructural uniformity during WAAM fabrication.

Shielding gas composition also contributes as a critical parameter in WAAM aluminium processing as it directly influences arc stability and bead formation by protect the arc and weld pool from atmospheric contamination (Saravana Kumar et al., 2024). Welding of aluminium alloy mainly use argon and helium as shielding gas. These gasses mixtures provide higher arc energy and improved weld pool stability, resulting in deeper penetration and reduced porosity compared to pure argon. However, the high cost of helium limits its industrial application, leading to the predominant use of argon in manufacturing (Hauser et al., 2021). Based on the microstructure 5356 after WAAM by Li. S et al. (S. Li et al., 2021) as displayed in Figure 2.12, the application of 100% pure argon deposit does not have strip-like and flaky substances if compare with other proportions of gases used. This finding suggests that despite having lower arc energy compared to gas mixtures, for instance those containing oxygen, pure argon has been provided sufficient process stability for WAAM aluminium alloy with optimal gas flow rate. Therefore, the shielding gas effects are dependent on the interaction with deposition condition and the interaction with heat input.

Beyond shielding gas effects, WAAM component quality is governed by the interaction of multiple process parameter rather than isolated control variables. While heat input remains the dominant control variable, recent studies emphasize that current, transverse speed, heat accumulation phenomena and molten pool dynamics collectively determine final component quality (Saravana Kumar et al., 2024). It is crucial to acknowledge that the individual contributions of parameters like current and transverse

speed, as well as their interactions, play a significant role in determining the final forming quality, microstructure and, mechanical properties of WAAM components. Therefore, achieving stable and consistent geometry requires optimizing parameters to control heat input and deposition behavior.

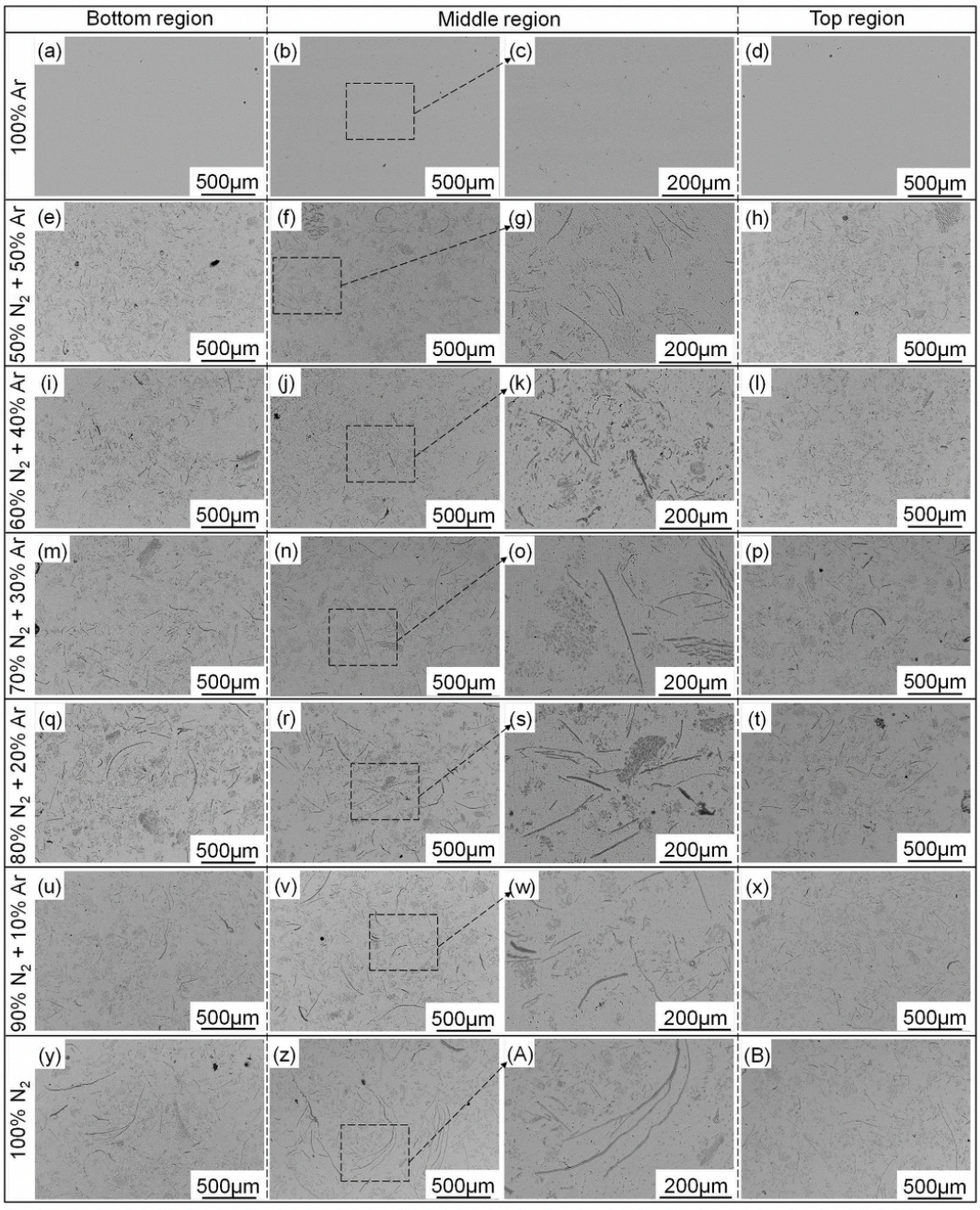

Figure 2.12 5356 Aluminium Microstructure on Bottom, Middle, and Top Region after WAAM of Different Proportions of Gases (S. Li et al., 2021)

In conclusion, WAAM thin wall fabrication relies on heat input and process parameter interactions rather than isolated parameter control. The literature collectively shows that heat input governs fundamental thermal mechanical phenomena affecting wall geometry, while other parameters such as deposition path, welding technology

selection, parameter sequencing and shielding gas composition enables precision control over dimensional accuracy, microstructural uniformity and defect minimization. Future work should prioritize multi parameter optimization frameworks that account for both induvial parameter effects and their interactive influences, moving beyond single variable towards integrated process design methodologies for reliable thin wall fabrication in aluminium alloy application. In this context, simulation-based approaches allow for the prediction of thermal cycles, heat accumulation, molten pool behavior, and geometry evolution before experimental validation. Numerical modeling frameworks such as finite element-based offer multi parameter interactions which are not effectively gained through experimental studies independently.

2.2.3 Simulation Based Prediction of Process Parameter

Simulation-based prediction serves as a vital modeling tool, which enables the analysis and control of thermal, mechanical and metallurgical phenomena prior to actual fabrication of WAAM to achieved optimized process parameters (Barath Kumar & Manikandan, 2022). Finite element method (FEM) is used to predict geometrical distortion and residual stresses in WAAM components (H. Huang et al., 2020; Manurung et al., 2021). However, the reliability of FEM based optimization is strongly dependent on mesh sensitivity which influences numerical accuracy and computational efficiency (Manurung et al., 2021; Prajadhiana et al., 2022). Finer meshes are prioritised in regions experiencing steep thermal gradients such as weld seam and heat-affected zone or any significant temperature gradient occurs to reduce the computational time (H. Guo et al., 2023).

For instance, Y. Manurung et al. (Manurung et al., 2021) identified 2528 elements (Figure 2.13(a)) which approximately 1 mm mesh size for an optimize rectangular wall. At this element number, the maximum temperature achieved stable value, which it is efficient to the application compared to larger meshes that only added calculation time. Similar conclusions were reported by M. Shahriman et al. (Adenan et al., 2023), where the welding-forming chain of S235 validated using Simufact.Welding (SW) and Simufact.Forming (SF) employed a model with 5984 total elements as optimal, refer Figure 2.13(b). The chosen of elements ensured the maximum temperature value stabilized while drastically reducing the wall time compared to significantly finer meshes. Simufact software typically employ a sequentially thermal

mechanical solution and provides specialised modules for AM and forming applications (Adenan et al., 2023; Manurung et al., 2021).

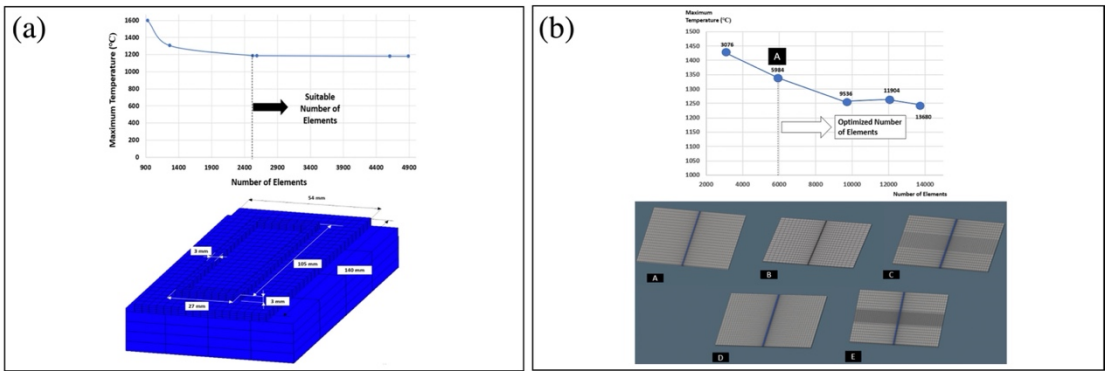

Figure 2.13 Mesh sensitivity analysis and graph maximum temperature (a) Wall SS316L (b) Butt Joint S235 (Adenan et al., 2023; Manurung et al., 2021)

In Simufact, SW software allows predictions based on mesh density, material properties, heat source configuration, and boundary conditions. Its predictive accuracy is further validated by a moving double ellipsoidal heat source, which accurately represents heat flow and distribution during welding, enhancing the reliability of predicted temperature gradients and stress distribution not only for small product applications but also for the shipbuilding industry (Bin et al., 2024). The Goldak double-ellipsoidal heat source model is widely adopted volumetric heat source model, which effective for simulating the intense moving heat flux characteristic of arc welding processes (Ahmad et al., 2020; Manurung et al., 2021). By dividing the heat source into two distinct front and rear ellipsoids (Figure 2.14), the power density distribution function for the front quadrant, q_f along z-axis is describes as in (2.2), where f_f is fraction of heat in front quadrant, Q is energy input rate (W), a_f, b_f, c_f are the characteristic radius (m) in x, y, z space at given time, t (s) increment.

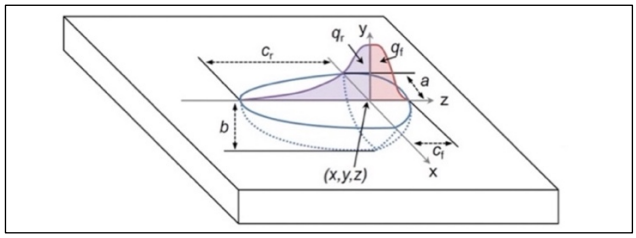

Figure 2.14 Schematic of Double-Ellipsoid Heat Source Model Showing the Gaussian Power Distribution (Fisher et al., 2021)

While v is travel speed and τ is lag factor needed to define heat source position at $t = 0$ (Fisher et al., 2021). According to (2.3), f_r is fraction of heat in the rear quadrant, and a_r, b_r, c_r are the characteristic radius (m) of the heat source for the rear quadrant with all other variables the same. It should be noted that $f_f + f_r = 2$ for the

Goldak heat source model. Based on Figure 2.14, the distribution function by semi-axes parameters which consists of width (a), depth (b), front length (c_f) and rear length (c_r) can be independently modified to match the observed weld pool geometry (Fisher et al., 2021).

$$q_f = \frac{6\sqrt{3f_f}Q}{a_f b_f c_f \pi\sqrt{\pi}} e^{-3x^2/a_f{}^2}\ e^{-3y^2/b_f{}^2}\ e^{-3[z-v(\tau-t)]^2/c_f{}^2} \tag{2.2}$$

$$q_r = \frac{6\sqrt{3f_r}Q}{a_r b_r c_r \pi\sqrt{\pi}} e^{-3x^2/a_r{}^2}\ e^{-3y^2/b_r{}^2}\ e^{-3[z-v(\tau-t)]^2/c_r{}^2} \tag{2.3}$$

The importance of calibration is further emphasized by Y. Manurung et al. (Manurung et al., 2021) where accurate reproduction of experimental peak temperatures and cooling slopes for each layer as presents in Figure 2.15(a), confirming that the Goldak double ellipsoid source combined with the calibrated coefficients accurately reproduces the real thermal history. According to S. Nursyahirah et al. (Ahmad et al., 2020) the heat source models for both rectangular and Goldak can be effectively implemented in SW. However, Goldak model remains widely preferred for WAAM because it accurately represents the asymmetric heat distribution characteristic of moving arc processes (Manurung et al., 2021). This asymmetry is relevant in WAAM because double ellipsoid model is advantageous as it considers heat flux in the thickness direction and accounts for the alteration of arc penetration including the temperature gradient distribution throughout the welding process (H. Guo et al., 2023).

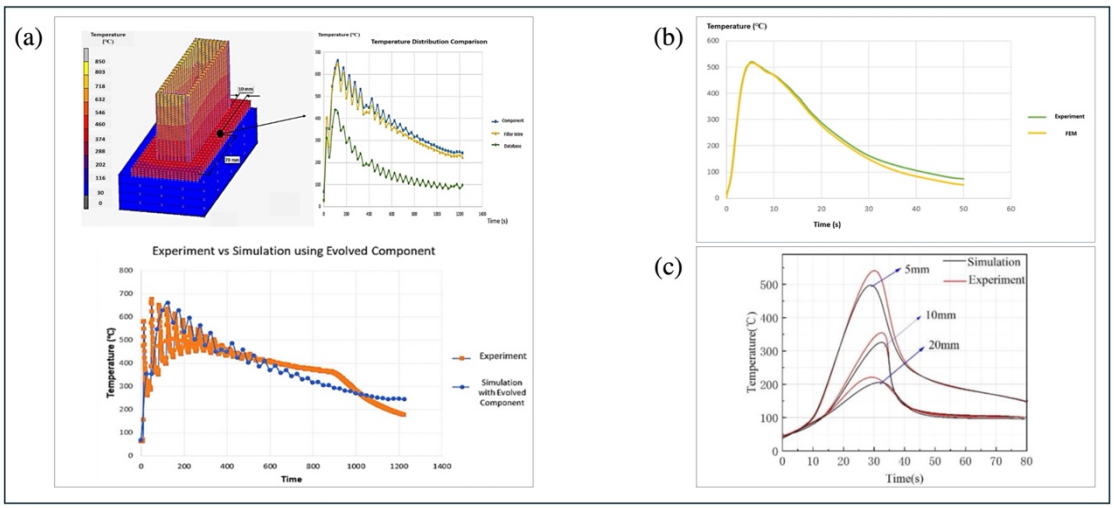

Figure 2.15 Simulative and Experimental Temperature Distribution using SW on Different Material and Components (a) Hollow Rectangular Wall SS316L and SS304 (b) Butt Joint S235 and G2Si (c) T-Joint 6063-T6 (Adenan et al., 2023; Manurung et al., 2021; X. Zhu, 2024)

Rather than just matching the peak temperature, SW able to captures the transient and cumulative thermal behavior inherent to multi-layer. According to the validation of previous research plotted in Figure 2.16, the simulated thermal histories resulted good agreement with the measurements of dimensions and fusion zones shape, reproducing both the peak magnitude and the cooling slope for all layers (Sun et al., 2021). This recent research resulted close agreement between the thermal prediction and experimental thermocouple data as illustrated in Figure 2.15(a) (Adenan et al., 2023). Similarly, X. Zhu (X. Zhu, 2024) reported that the 6063-T6 aluminium T-joint simulated temperature histories using thermocouples at several locations (Figure 2.15(b)) resulted less than 5% from experimental measurements, hence, consistently suggested SW predicts the spatial and temporal temperature distribution of real welds with thermocouple readings. This confirms that thermal accuracy in SW on temperature prediction is a realistic representation of melt pool geometry.

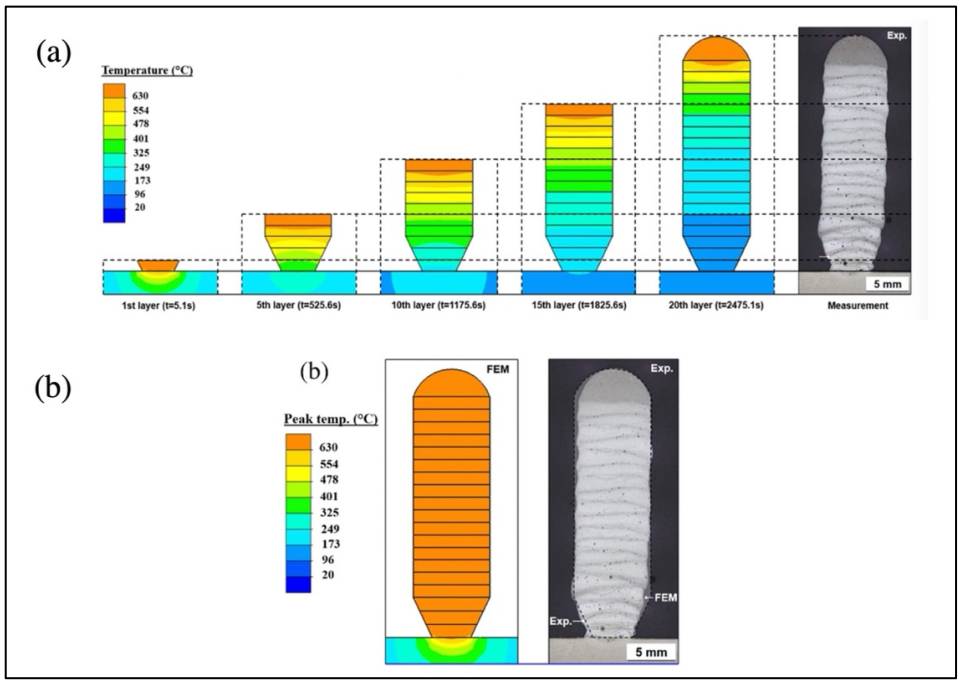

Figure 2.16 WAAM Micrograph Comparison of Al5356 and Al6082 (a) Temperature Distribution (b) Peak Temperature after WAAM Process (Sun et al., 2021)

Furthermore, based on J. Sun et al. (Sun et al., 2021), the peak temperature resulted at the uppermost layer of the wall because the top layers experience high heat accumulation and short cooling time, hence raising the temperature of last-added layer. For a built structure, according to M. Köhler et al. (Köhler et al., 2020) the substrate initially acts as an effective heat sink, rapidly cooling the first layers. However, as the build increases, the heat accumulation in the lower layers reduces the overall cooling rate. This leads to the substrate's temperature reaching a highest value at roughly mid-

height of the wall as shown in Figure 2.17, which it starts to decrease towards the top layers during the fabrication (Köhler et al., 2020).

In WAAM, higher preheat on substrate and interpass temperatures reduce residual stresses because the temperature difference between the deposited material and surrounding material decreases (Wu et al., 2020). According to Q. Wu et al. (Wu et al., 2020), arc power, scanning speed, substrate thickness and preheat temperature are significant parameters that affected the residual stress. Hence, when the solidus temperature of the alloy and the preheat temperature are close together, the resulting residual stress is smaller. This is because the conditions will reduce thermal contraction and expansion during cooling. Thus, lower thermal stresses develop during cooling cycle. Therefore, properly controlling workpiece temperature through higher interpass temperature will reduce residual stress and improve mechanical properties. In fact, substrate preheating is identified as most influential variable among process parameters for controlling residual stresses (Wu et al., 2020). Hence, the initial state of component able to predict the welding deformation that caused by thermal cycling and subsequent shrinkage during cooling as shown in Figure 2.18(a). The prediction is essential for assessing the geometrical accuracy before any post-wed processes occur.

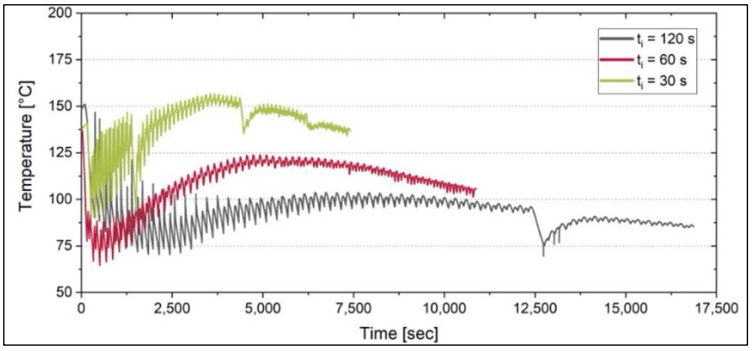

Figure 2.17 Temperature Distribution of the Substrate Al6082 for Fabrication of Al5356 Thin Wall (Köhler et al., 2020)

Specialised FEM software like SW, another FEM such as SYSWELD, and ANSYS are also widel(Ahmad et al., 2020; Barath Kumar & Manikandan, 2022)Barath Kumar & Manikandan, 2022). While SW effectively captures the thermal mechanical behavior during deposition, SF has been used to simulate plastic deformation, strain distribution and stress evolution during forming process. SF simulation allows the users to model various aspects of the manufacturing process, including cold extrusion, forging and bending. Hence, frequently used in the industry to analyze the process conditions, predict elastic deformation, evaluate project parameters under specific deformation conditions to reduce costs and development time (Silveira & Schaeffer, 2018).

Generally, the effective plastic strain directly showed the work hardening changes in yield stress. For instance, the effective plastic strain in muti-stage forging of thin wall tube superalloy is non-uniform where the heat section of forged thin wall tube showed higher effective strains up to 8.47 while the rod section up to 6.77 due to varied operation sequences (Tao et al., 2023). Based on the recent research by J. Bouquerel et al. (Bouquerel et al., 2014), effective plastic strain is correlated with the microstructure of the material as low plastic strain value that less 0.1 in 6082 alloy potentially leading to alloy hardening without significantly affecting grain size.

For cold forging applications, damage criteria selection is critical to accurate failure prediction and process optimization. There are few available damage models in SF such as Cockcroft-Latham, Johnson-Cook, Gurson, Lemaitre, Modified Mohr Coulomb, Oyane and Bonora, which perform different functionality and depends on process specification Recent studies by E. Abdullah and A. Jalil (Abdullah & Jalil, 2025) emphasize that for aluminium alloys like AA5754 and AA6061, appropriate damage criteria within FEM software significantly impacts prediction accuracy, where the choice depends on strain levels, deformation complexity and forming temperature. The Johnson-Cook damage model in SF through LS-DYNA integration, incorporates stress triaxiality as a fundamental parameter to predict fracture initiation under various loading condition (Mohamed et al., 2021). While the Gurson model based on void growth and coalescence mechanisms which provides micromechanics-based predictions that suitable for ductile materials and effective in capturing the effects of hydrostatic stress on material failure (Mohamed et al., 2021).

When integrated with SW, the software enables comprehensive analysis of coupled manufacturing processes, where results from the welding simulation, including temperature distribution, residual stress and deformation that are transferred to the forming simulation as initial boundary conditions (Adenan et al., 2023). In Figure 2.18(b) the chained simulation approach showed acceptable deformation error percentages of 4 – 12% across measurement points as presents in which demonstrates practical efficiency for predicting multi-step processes before physical manufacturing (Adenan et al., 2023). Consequently, the predictive potential of simulation for hybrid manufacturing has not been fully explored. Most studies treat SW and SF processes separately and limited work has integrated both simulations to represent the hybrid process. This gap highlights the lack in process chain based simulation framework in

which SW and SF combined to predict hybrid WAAM-forming processes particularly in aluminium alloy.

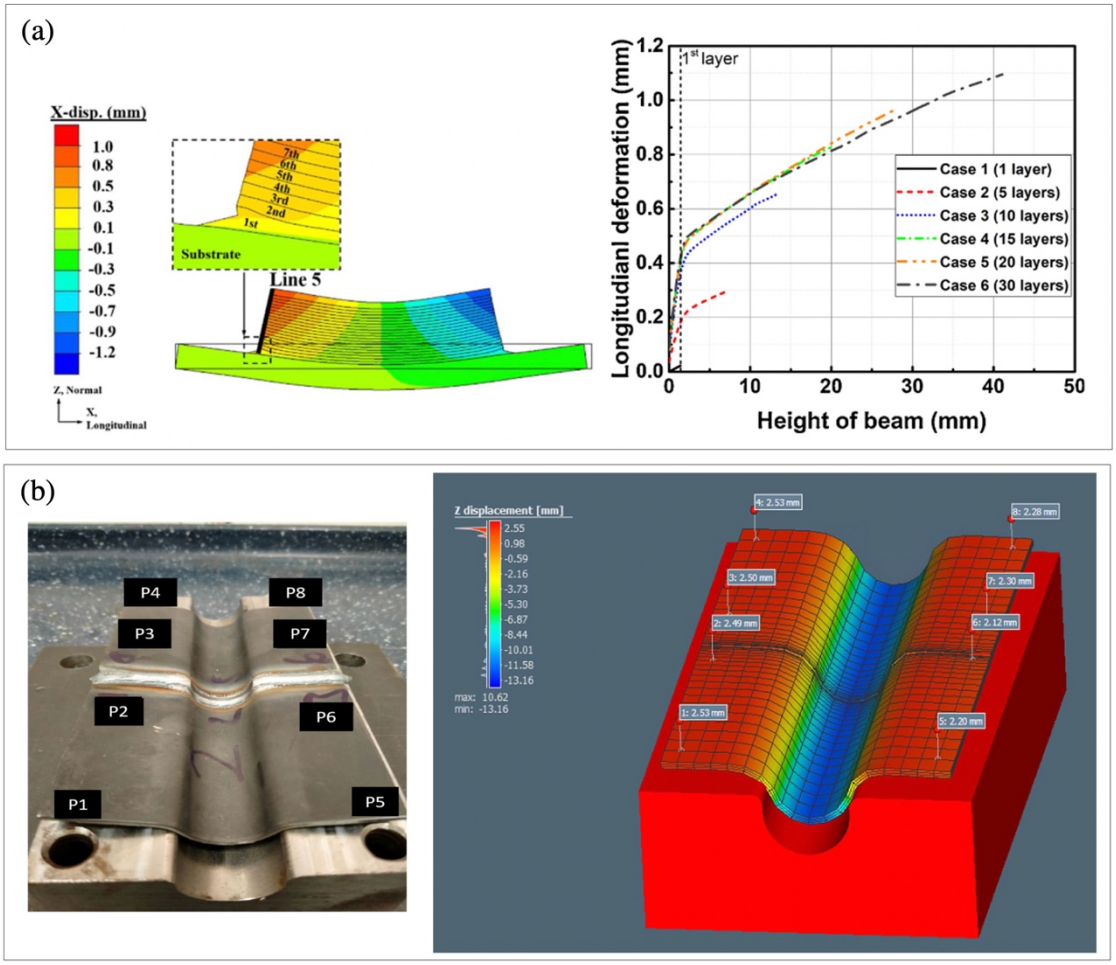

Figure 2.18 Displacement Analysis on Different Process (a) WAAM of Al5356 and Al6082 (b) Process Chain Welding-Forming of S235 and G2Si (Adenan et al., 2023; Sun et al., 2021)

2.3 Aluminium Alloys in WAAM

2.3.1 Classification of Aluminium and Its Alloys

Aluminium and its alloys are characterized by a relative low density of 2.7 g/cm^3, high electrical and thermal conductivities, good corrosion resistance in some common environment including at ambient atmosphere and high ductility due to their face centred cubic (FCC) crystal structure which reta(William D. Callister & David G. Rethwish, 2018)ister & David G. Rethwish, 2018). Hence, the low melting temperature of aluminium (600°C) limits high temperature applications. The mechanical strength of aluminium can be enhanced by cold work and alloying with

common alloying elements such as copper (Cu), manganese (Mn), silicon (Si), magnesium (Mg), zinc (Zn). However, in several alloys, precipitation hardening mechanisms occurred due to the precipitation of two elements to form an intermetallic compound such as $MgZn_2$, even both processes tend to decrease resistance to corrosion (William D. Callister & David G. Rethwish, 2018). According to ASTM standards, aluminium alloys can be divided as wrought alloys in four digits notation which can be classified into eight series and cast alloys as three digits notation followed by a decimal value (Manufacturing, 2021). Figure 2.19 illustrated the classification of wrought and cast aluminium alloy including the range ultimate tensile strength (Z. Zhu et al., 2023). Wrought alloys are mechanically known for their superior mechanical properties and structural integrity which primarily improved through rolling, extrusion, or forging (Haque et al., 2023).

Table 2.4 summarise the applicability of aluminium alloy series (1xxx-7xxx) for WAAM based on alloying elements, strengthening mechanism, heat treatability and weldability. The 1xxx series Al alloys are commonly referred as commercial pure aluminium exhibit excellent corrosion resistance but has no structural application for WAAM due to its softness and more suitable as cladding material (Manufacturing, 2021). Meanwhile, the 3xxx (Al-Mn) and 4xxx (A-Si) series offer intermediate strength levels and good formability, making 3xxx series more versatile and used as general-purpose alloys. While the 4xxx (Al-Si) series are mostly used for casting purposes due to excellent flowability and decreased thermal shrinkage especially in wrought application, welding and brazing applications (Rosli et al., 2021).

According to Figure 2.20(a), the Boeing 777 relies on aluminium with 70% material usage followed by others material (Altıparmak et al., 2021). This reflects that wrought aluminium alloys provide wide range of mechanical and functional properties. In contrast with other alloy series, 2xxx (Al-Cu) and 7xxx (Al-Zn-Mg-Cu) series are widely used as a structural alloy in the aerospace sector, especially in aircraft fuselage and wing primary structures as shown in Figure 2.20(b-c). These series are classified as high strength but suffer from poor corrosion resistance and solidification cracking, hence not available as commercial feedstock for WAAM (K. S. Derekar, 2018). Similarly, 6xxx (Al-Mg-Si) series are heat-treatable and high cracking during solidification makes these alloys difficult to process by AM even though have wide range of application as extruded profiles.

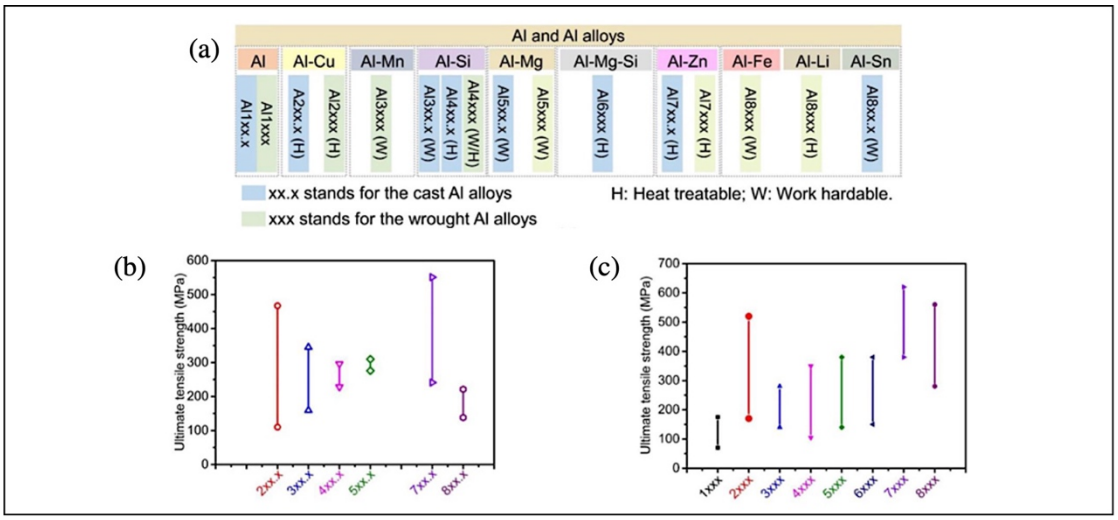

Figure 2.19 (a) Classification of Aluminum Alloy (b) Ultimate Tensile Strength of Wrought Aluminium Alloys, (c) Ultimate Tensile Strength of Wrought Aluminium Alloys (Z. Zhu et al., 2023)

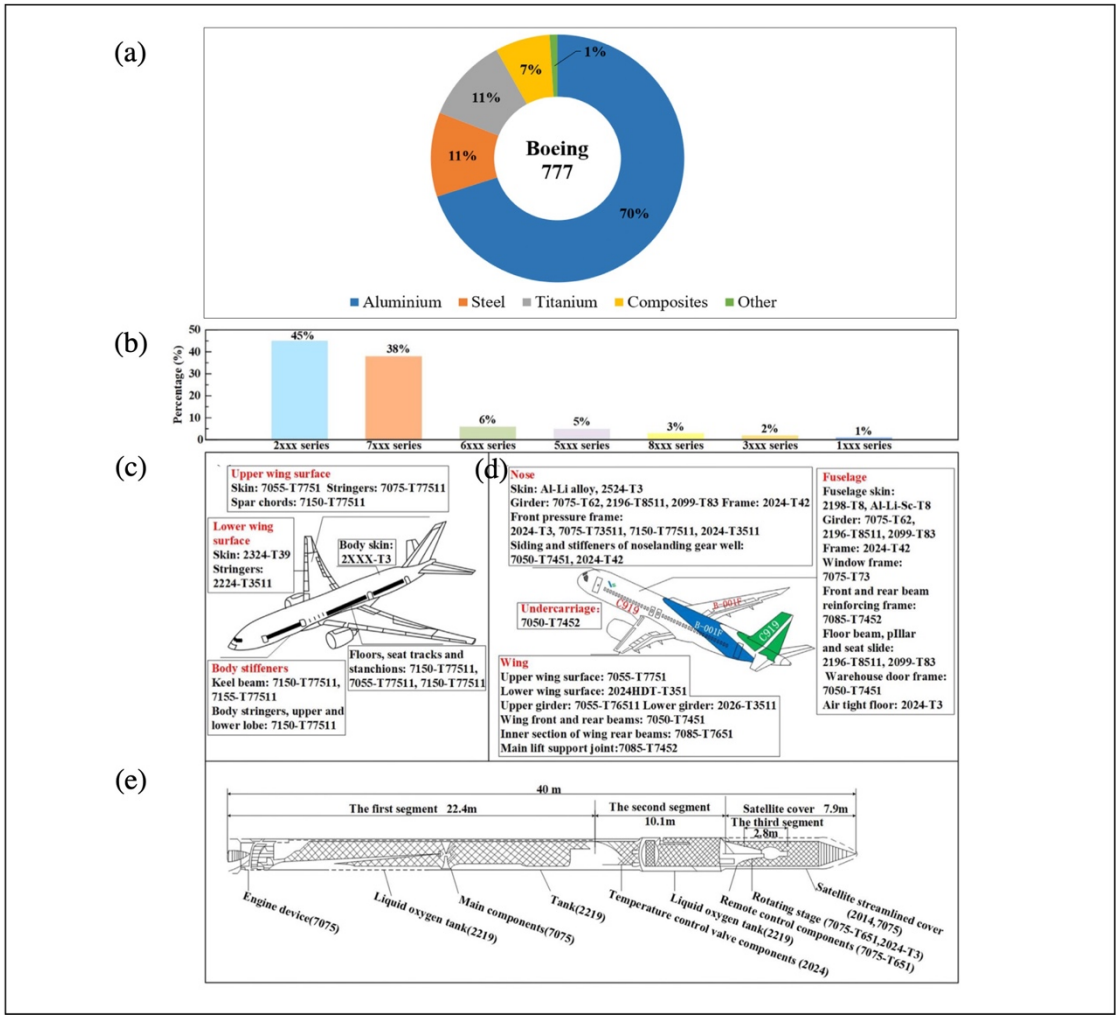

Figure 2.20 Application of Al in Aerospace (a) Material Usage for Boeing 777 (b) Al Alloys in Boeing 777 (c) Boeing 777 (d) Comac's C919 of China (e) Japanese H-1 Rocket (Altıparmak et al., 2021; S. S. Li et al., 2023)

Table 2.4
Aluminium Alloy Series for WAAM (Fang et al., 2021; Langelandsvik et al., 2021; Rathod, 2025)

Series	Common Alloy	Key Alloying Element (s)	Heat Treatable	Strengthening Mechanism	WAAM Applicability	Chemical Composition Benefits
1xxx	1100	≥99% Al	No	Work hardening	Limited	Exceptional corrosion resistance and electrical conductivity due to high purity. Rarely used in WAAM because of low strength
2xxx	2319, 2219, 2024	Cu, Mg, Mn	Yes	Heat treatment and aging	Challenging	High strength from Cu/Mg but suffers from hot cracking and poor weldability. Limited use in WAAM without modifies or special techniques
3xxx	3003	Mn	No	Work hardening	Feasible	Good corrosion resistance, moderate strength, improved weldability. Mn provides moderate strengthening without sacrificing formability
4xxx	4043	Si	Both	Varies	Common	High Si content reduces hot cracking, excellent weldability, preferred as filler for WAAM due to smooth operation and crack tolerance
5xxx	5083, 5356	Mg, Mn	No	Work hardening	Very common	Mg enhances strength and corrosion resistance. Good weldability, suitable for WAAM in marine and structural uses. Proven mechanical stability and favourable microstructure in as-built WAAM
6xxx	6061, 6063	Mg, Si	Yes	Heat treatment and aging	Feasible and aging	Offers good strength, toughness, and weldability. Mg-Si combination creates hardening phases, but 6xxx alloys may suffer hot cracking and require careful process control
7xxx	7075	Zn, Mg, Cu	Yes	Heat treatment and aging	Under development	Very high strength from Zn/Mg/Cu. Limited WAAM use due to hot cracking, porosity and evaporation issues with Zn but promising with advanced heat treatments. Suited for aerospace if defects can be managed

Among all series, the 5xxx (Al-Mg) alloys are the most suitable and widely adopted for WAAM because its non-heat treatable properties help to avoid metallurgical complexities that plague heat treatable series such as formation of oxide layer and solidification behavior. This alloy strengthened through Mg content where according to the review studies by C. R Song et al. (Song et al., 2024), the Mg content in the Al-Mg is in the range of 0.8% - 5.2%. The existence of Mg preferentially forms the anodic phase Al_3Mg_2 or Al_8Mg_5 in intergranular precipitation, which is beneficial to the formation of grain boundary cracks and stress corrosion (Song et al., 2024). However, a critical challenge in WAAM of Al-Mg is Mg evaporation (D. S. Zhao et al., 2022). Since Mg's boiling point 1107℃ is much lower than Al's (2519℃), Mg preferentially burns away during the high temperature arc process. Studies by Y. Liu et al. (Y. Liu et al., 2022) found that Mg content decreases from 4.9% to 4.68% during WAAM deposition. The loss of Mg slightly reduced when short circuit process of CMT is applied compared to GTAW (Y. Liu et al., 2022).

Based on Table 2.5, the reviewed WAAM studies on aluminium alloys have mainly focused on process parameters, deposition quality, microstructure, porosity formation, and mechanical performance due to complex thermal history and strength reduction. Heat accumulation, arc instability, oxidation and uneven elemental distribution are frequently reported especially in multilayer walls. Among the investigated aluminium alloy, ER5356 is widely recognized for their suitability in WAAM due to a combination of desirable properties such as high specific strength compared to heat treatable alloys (Singla et al., 2024). However, limited attention has been given to ER5356 aluminium alloy produced through different WAAM modes, particularly GMAW and CMT, besides its subsequent improvement through post-processing deformation. It requires integration of post-processing methods such as forming and adaptive cooling to achieve acceptable microstructural quality and strength characteristics (Vimal et al., 2019). Therefore, this study addresses this gap by comparing GMAW and CMT ER5356 WAAM thin walls and further investigating the effect of cold forging on surface integrity, residual stress, microstructural features, and mechanical performance.

Table 2.5
WAAM Research on Aluminium Alloys

Reference	Aluminium Series	WAAM Mode	Objective	Problem / Limitation	Future Research / Recommendation
(Köhler et al., 2019)	Al5356 (Al-5Mg), Al 4047 (Al-12Si)	CMT-Pulse (GMAW variant)	To evaluate buildup accuracy, mechanical behavior, and residual stress in WAAM Al	Poor geometry formation and surface waviness in Al 4047. Vertical elongation loss in Al 5356. Fine porosity in both alloys. High deviation in residual stress due to coarse grains	Optimize inter-pass temperature and heat input. Study porosity reduction strategies. Apply post-process deformation such as milling or casting to improve structure
(S. Li et al., 2020)	Al-Zn-Mg (7xxx)	GMAW / MIG	To investigate the influences of process parameters on single pass forming	Pores in the cross-section of weld beads under different parameters (reduced the strength and plasticity). The elements were unevenly distributed due to layer-by-layer deposition.	WAAM has great development potential for Al-Zn-Mg alloys due to their advantages in specific strength, stiffness, processability, and weldability, especially for aerospace applications.
(Gu et al., 2020)	AlCu4.3 Mg1.5, 2024-T351	CMT	To study Al-Cu-Mg alloy microstructure, defects, and mechanical properties	Micropores or microcavities. The WAAM alloy tensile, yield strength and elongation were lower in the vertical direction and fracture due to their smaller loading area and lower bearing capacity	Techniques to reduce microvoid formation, and grain growth during heat treatment need consideration. Optimising the composition of the filler material. Hybrid WAAM such as inter-layer rolling or laser shock peening are recommended

Reference	Aluminium Series	WAAM Mode	Objective	Problem / Limitation	Future Research / Recommendation
(M. Xu et al., 2023)	ER2319 (Al-Cu)	CMT	To understand the cracking behavior and mechanism in WAAM of Al-Cu alloys	Macrocracks. Coarse grains and high thermal stress due to high heat input. Lower tensile strength and elongation due to microcracks.	Investigate methods to control grain morphology to prevent crack. Optimize parameters to reduce thermal stress. Control of the solidification rate.
(Hu et al., 2023)	ER2319	CMT and TIG	To determine the deformation and damage mechanisms of WAAM-processed in the temperature from 77 K to 523 K	Heterogeneous microstructure due to complex thermal history in AM, lead to complex failure. Degraded tensile strengths at elevated temperatures due to dynamic recovery and dynamic recrystallization.	Modification measures in terms of alloy composition to reduce grain boundary segregation, texture intensity, porosity and to produce a homogeneous microstructure with refined equiaxed grains and higher dislocation density.
(Chandra et al., 2023)	Al 5356, Al 5083	GMAW	To investigate the mechanical properties of manufactured wall, focusing on tensile tests and fractography	Defects due to heat accumulation and inevitable conditions during automatic deposition, especially on top layers. Arc instability, spatter, and increase filler wire extension. Oxidation on top layers due to oxygen rich atmosphere near the melt pool	In-situ monitoring and feedback systems help control the mechanical properties of WAAM during continuous deposition. Adaptive control could be used to adjust contact tube to workpiece distance and ensure consistent bead formation
(Kumar et al., 2024)	Al 5356, Al6061	CMT	To investigate mechanical characteristics, microstructure, and optimize parameters for Al 5356 wall deposition	High heat input, residual stress, and porosity can pose challenges. Temperature gradients, cooling rates, and microstructural differences can reduce tensile strength. Achieving a balance between hardness, flexibility, and toughness is critical	Control heat input and inter-pass temperature. Optimize deposition rate, arc voltage, and wire feed rate to manage thermal gradients and cooling rates. Employ heat treatment methods

2.3.2 Surface Integrity and Limitation

When processing most aluminium alloys in WAAM process, manufacturers often face the general problem of porosity, which should avoid or keep as low as possible to minimize alterations to mechanical properties as tensile strength of the manufactured components (Hauser et al., 2021). The microstructure of aluminium alloy can be characterized using scanning electron microscope (SEM), where this analysis often combined with energy-dispersive X-ray spectroscopy (EDX) to observe phase distributions and analyze elemental compositions within the alloy microstructure. Microstructure analysis also correlated to the density of the material to observe the mechanical property behavior.

For metal density identification, Archimedes method is favoured primarily due to its simplicity, low cost, high accuracy, and repeatability when applied to standard specimen (Bruce et al., 2022). The Archimedes method is supported by ASTM standards, such as ASTM B962 and ASTM B311, which provide detailed procedures for its application in the industry (Bruce et al., 2022). The Archimedes method is utilized to measure density and its sensitivity to the changes caused by specimen thickness, post-processing conditions, and build location. Referring to the recent research on density by A. Nawaz and S. Rani (Nawaz & Rani, 2021) concluded that the density of the metal decreases as its porosity increases, which means the volume of the metal is occupied by pores or voids that filled with gas. The density of material is calculated as equation stated in (2.4), where ρ is density. As microstructure morphology is related to the formation of voids, porosity, and cracks on the material surfaces, hence, the percent porosity of material significantly influencing their characteristics and potential application. Porosity also linked to the reduction of metal alloys, making them lighter and suitable for desired application (Nawaz & Rani, 2021). The percent porosity is evaluated using the equation stated in (2.5).

$$Density, \rho(g/cm^3) = \frac{Mass, m\ (g)}{Volume, V\ (cm^3)} \tag{2.4}$$

$$Porosity\ (\%) = \frac{\rho_{initial} - \rho_{final}}{\rho_{initial}} \times 100 \tag{2.5}$$

Porosity resulted from the solidification process during the material deposited and form through four stages: gas pores nucleation, growth, separation from molten

pool wall, and escaping (J. Xu et al., 2023). The micrograph in Figure 2.21(b) shows the presence of pores, which appeared as dark spots against a lighter background using SEM analysis. The recent research of WAAM process on aluminium alloy in Figure 2.21 experience higher concentration of pores, particularly of medium and large sizes at different level of thin wall layers. This can be attributed to several reasons such as heat accumulation, molten pool dynamics, and solidification rate.

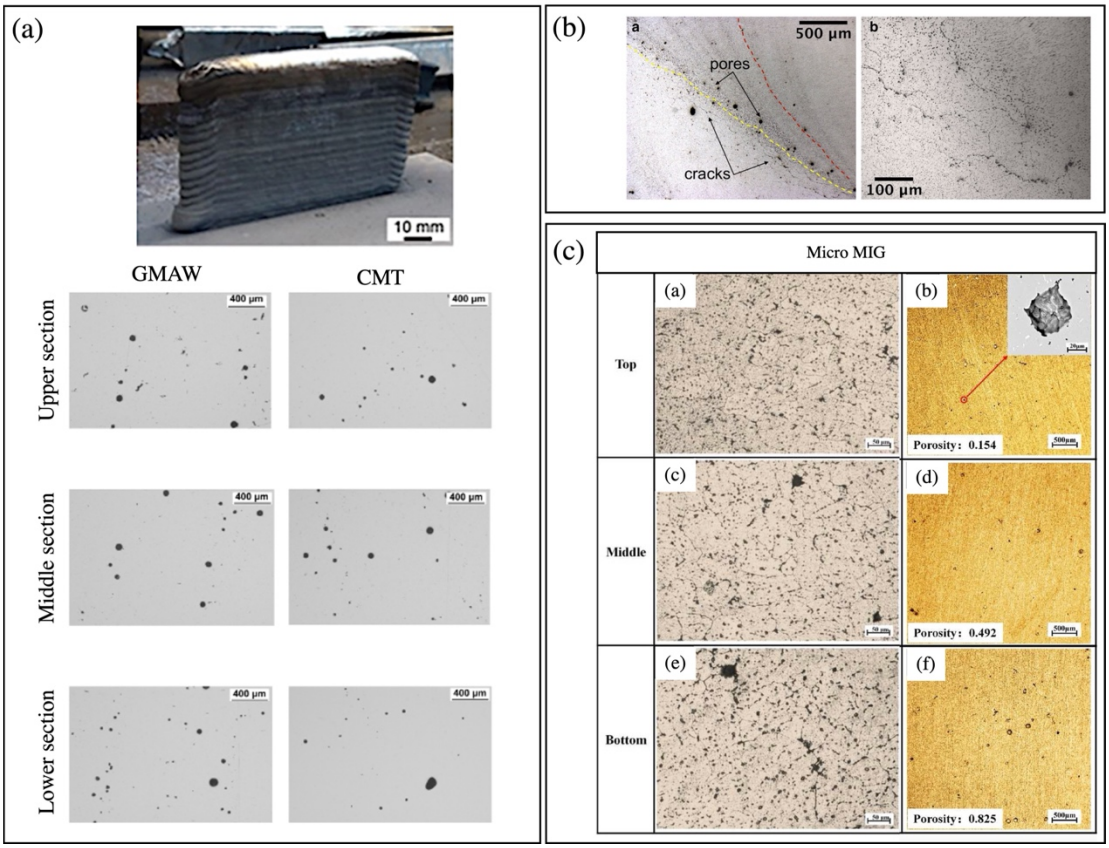

Figure 2.21 Distribution of Pores on SEM Micrograph of Thin Wall (a) GMAW of Al5356 Microstructure (b) Formation of Porosity and Crack AA5083 (c) ER5356 Microstructure (Aldalur et al., 2021; Jiangang et al., 2022; Tonelli et al., 2021)

According to P. Jiangang et al. (Jiangang et al., 2022), the microstructure in the thin wall of 5356 aluminium alloy fabricated using GMAW depending on the location within the wall. Referring to Figure 2.21(c), the porosity is generally higher at the bottom of the wall and decreases towards the top due to the heat accumulation effect. The bottom of the wall experiences a faster solidification rate because there is less heat accumulation initially, limiting the time for hydrogen to escape, thus resulting higher porosity. Conversely, as the wall height increases, more heat is accumulated, leading to a slower solidification rate and allowing more hydrogen to escape subsequently lower porosity at the top. These outcomes were equivalent to E. Aldalur et al. (Aldalur et al.,

2021) findings for GMAW and CMT WAAM modes, though CMT resulted less pores, refer to Figure 2.21(a).

Porosity in WAAM of aluminium alloys can be classified into small (homogenous distributed) hydrogen pores with the dimension up to 100 µm, and big (inhomogeneous distributed) process pores (Hauser et al., 2021). As shown in Figure 2.22(a-b), the highest number of pores occurs in the 0-100 µm diameter range for different travel speed tested, directly influences the microstructure. According to M. Sahul et al. (Sahul et al., 2024), the microstructure of Al-Mg alloys is strongly influenced by Mg loss during deposition. Mg evaporates when the molten pool temperature exceeds its boiling point (1107℃), especially at the top of the pool (D. S. Zhao et al., 2022). As reported by D. S Zhao et al. (D. S. Zhao et al., 2022), Mg depletion weakens the aluminium matrix surroundings and promotes larger equiaxed grains, which reduced material's ability to close the micro-voids during solidification. Hence the weakened zones are more prone to retain the bubbles created by Mg evaporation. This is consistent with the findings in Figure 2.21(c-d), where greater Mg loss subsequently increases pore formation which strongly correlated with higher heat input induced by lower travel speed or higher current.

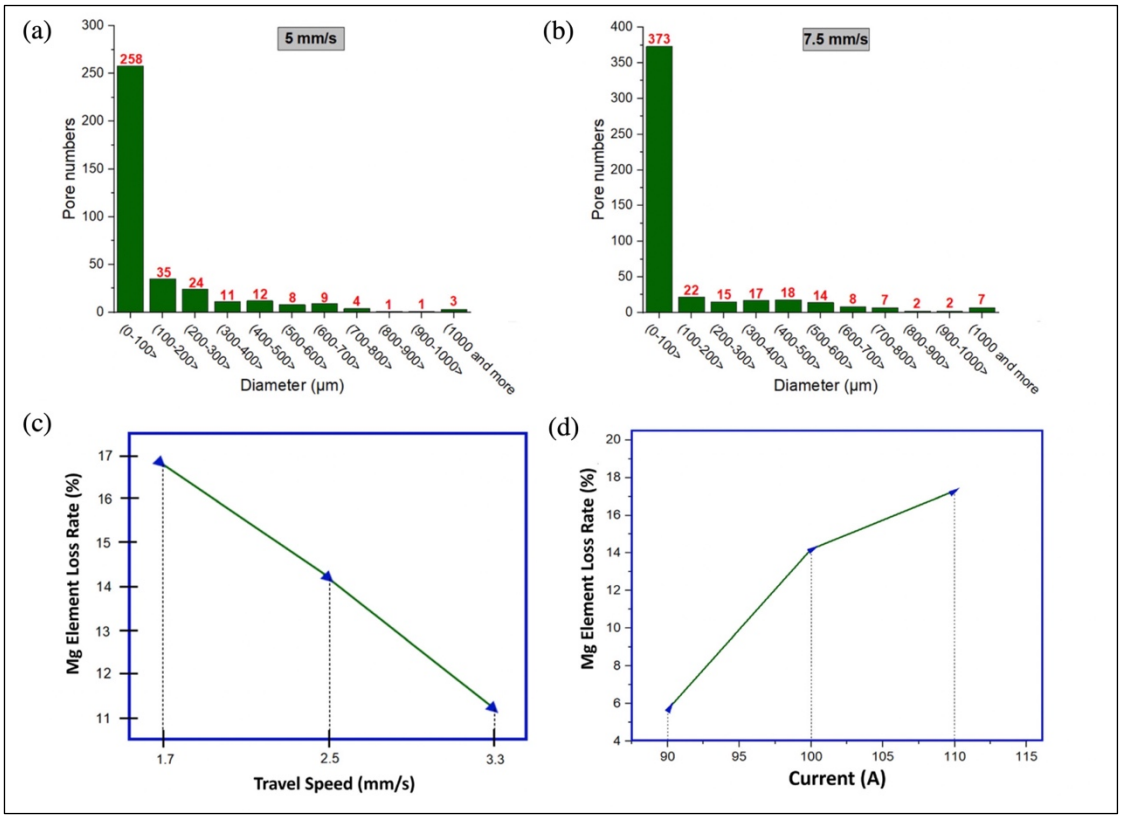

Figure 2.22 (a) Pore numbers at 5 mm/s (b) Pore numbers at 7.5 mm/s (c) Mg loss rate Porosity on Different Travel Speed (d) Mg loss rate Porosity on Different Current (Sahul et al., 2024)

In addition, the distribution of pores is more inhomogeneous, caused by the entrapment of shielding gas, air (oxygen and nitrogen), or other gases that cannot escape because the aluminium solidifies rapidly (Hauser et al., 2021). One of the major sources of hydrogen originates from the wire that contains moisture, grease, and hydrocarbon contaminants on its surface, which can vaporize in the arc and convert into atomic hydrogen (Ryan et al., 2018). Hence, the shielding gas is crucial for protecting the melt pool from atmospheric contamination, where excessive high flow rate leads to increased porosity due to enhancement cooling and solidification process (Hauser et al., 2021). This is aligned with the research by T. Hauser et al. (Hauser et al., 2021) where an increases in gas flow rate can lead to higher porosity levels due to enhanced melt pool turbulence and arc instabilities as illustrated in Figure 2.23(a). In contrast, a lower gas flow rate reduces convection effects, allowing the melt pool surface to remain liquid for a longer duration. Hence, it will extend liquid state facilitates better gas escape, thereby minimizing pore entrapment within the solidified structure. Figure 2.23(b) shows higher porosity formation as the gas flow rate increases based on longitudinal cross-sections of AlSi5 wall.

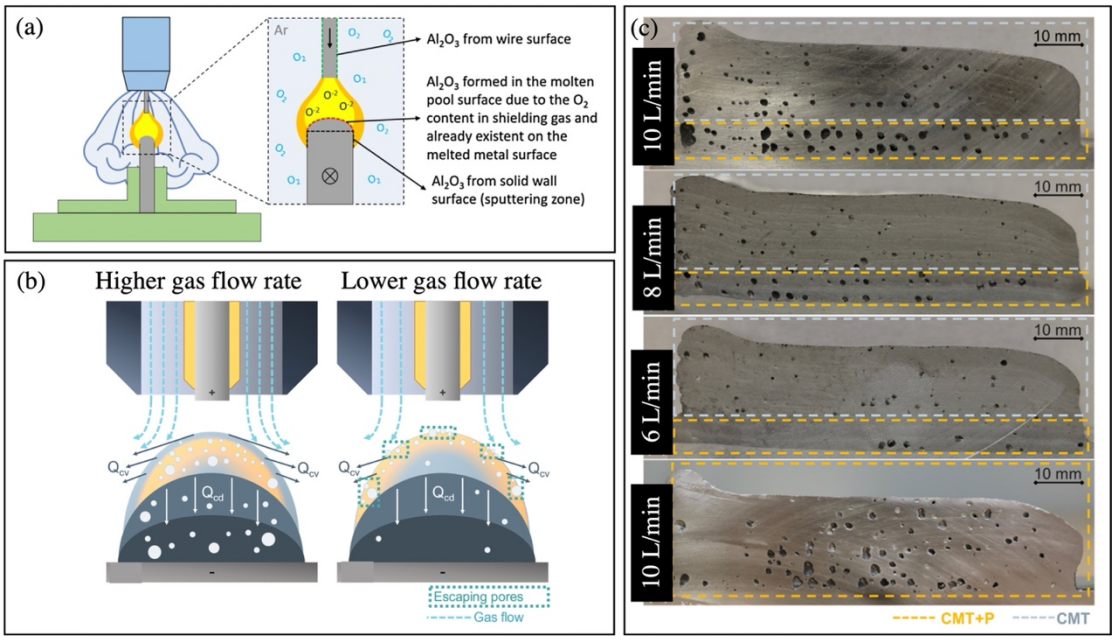

Figure 2.23 (a) Schematic of the Gas Flow Rate on Solidification and Pore Behavior (b) Cross-Section of AlSi5 Wall using Varieties Flow Rate (Hauser et al., 2021)

In Table 2.6, argon is the most suitable shielding gas for aluminium alloys. As specified in ISO 14175/l argon gas for welding process suggested to be 16 L/min and argon also produced better outcomes than nitrogen gas (Kumar et al., 2024). The formation of porosity using argon gas is less and reduced below 0.035% compared to

other gas as presents in Figure 2.24. For argon, 6-12 L/min achieves uniform, stable walls with minimum porosity referring to other condition and wall fabrication. Although previous studies have investigated porosity reduction through gas control and deposition parameter optimization, fewer studies have examined porosity improvement through mechanical post-processing such as cold forging. This indicates a research gap in understanding how post-deposition plastic deformation can reduce porosity and improve the surface and mechanical integrity of WAAM and WAAM-forged of aluminium alloy.

Table 2.6
Comparative Shielding Gases on Porosity of Aluminium in WAAM

Reference	Aluminium Type	Shielding Gas	Deposition Strategy	Gas Flow Rate	Porosity Percentage / Outcomes
(Sahul et al., 2025)	AA5087	Argon	Bidirectional	12 L/min	0.49%
(Kumar et al., 2024)	Al5356	Argon	Bidirectional	16 L/min	Highest porosity at top layers compared bottom
(Hauser et al., 2021)	AlSi5	Argon	Bidirectional	6 L/min	Lowest pores compared 8 -10 L/min
(Arana et al., 2021)	ER5356	Argon	Weaving (Circling)	25 – 30 L/min	0.056 – 0.162 %
(Arana et al., 2021)	ER5356	Argon + Oxygen + Nitrogen Oxide	Unidirectional	25 – 30 L/min	0.121 – 0.224 %
(S. Li, Zhang, Ning, Wang, Zhang, Zhang, Na, et al., 2020)	Al5356	Argon	Unidirectional	12 L/min	Fewer pores, stable arc, better droplet transfer
(S. Li, Zhang, Ning, Wang, Zhang, Zhang, Na, et al., 2020)	Al5356	Nitrogen	Unidirectional	12 L/min	Unstable droplet transfer

In addition, the presence of porosity initiates the crack formation in aluminium alloys during WAAM due to the combined effects of heating, thermal gradients and solidification. Figure 2.25 presents the SEM micrographs illustrating cracking in specifically focusing on hot cracking or liquation cracking and porosity in AA7075. Liquation cracking occurs in the heat affected zone, driven by localized melting in

alloys with high thermal conductivity and alloying content as shown in Figure 2.26. Based on the SEM in Figure 2.25, the micrograph shows the relationship between the porosity and crack initiation. This is because pores are voids within the material and act as stress concentrators. As the stress build up during the AM process due to thermal gradients and solidification shrinkage, these stress concentrators at pores can easily the cracks (Altıparmak et al., 2021).

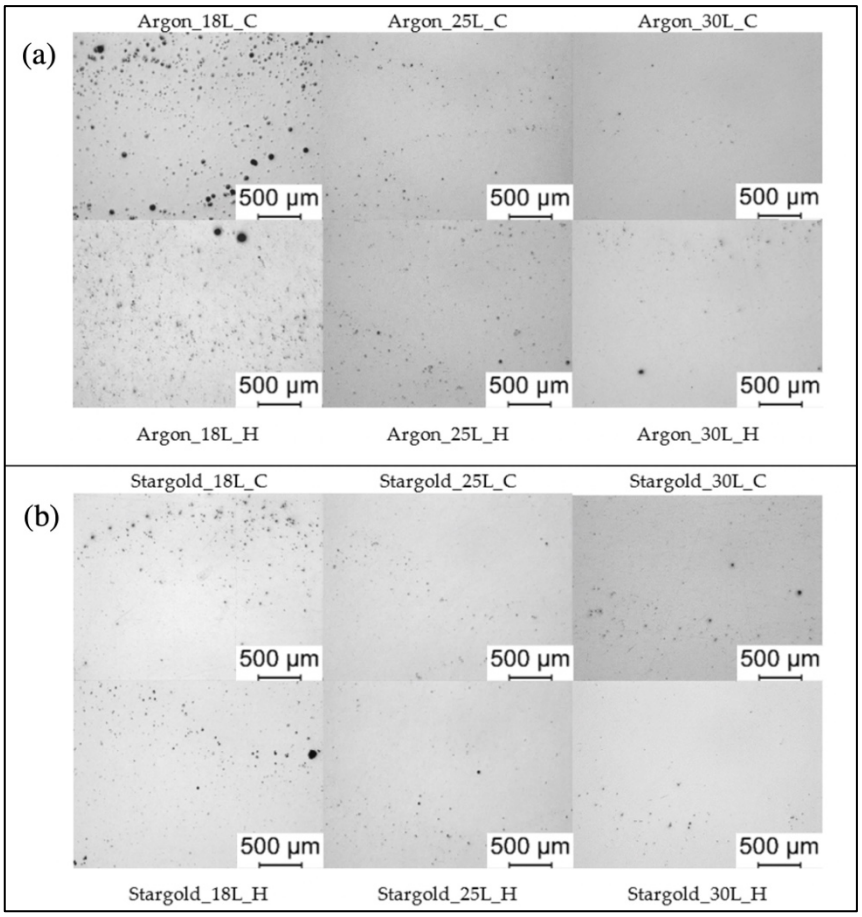

Figure 2.24 Porosity in AA5356 wall with (a) Argon Gas (b) Stargold Gas (Arana et al., 2021)

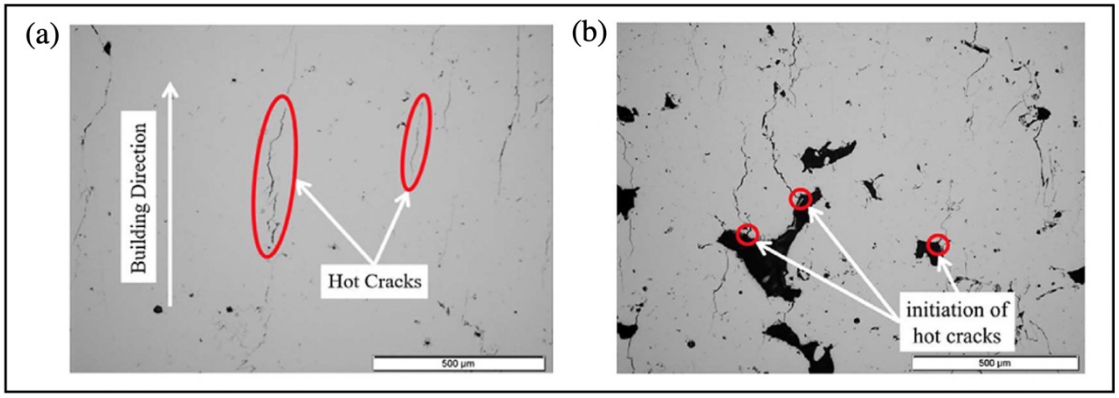

Figure 2.25 Cracks Formation in AA7075 (a) Hot Cracks (b) Initiation of Cracks due to Porosity (Altıparmak et al., 2021)

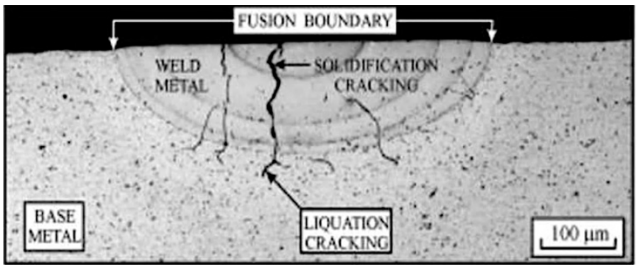

Figure 2.26 Locations of liquation cracking in welded aluminium (Albannai & Albannai, 2022)

In conclusion, surface integrity in WAAM of aluminium alloys is strongly influenced by porosity and associated defects, which are primary affected by shielding gas condition, heat input, and process stability as listed in Table 2.6. The formation of such defects also fundamentally controls the evolution of grain morphology, highlighting the need for a detailed understanding of microstructural development to optimize WAAM process parameters.

2.3.3 Grain Structure Development

WAAM aluminium alloys exhibit distinct grain morphologies dependent on thermal cycles and deposition layers. According to M. D. B. Kumar and M. Manikandan (Barath Kumar & Manikandan, 2022), typical as-deposited microstructures contain columnar grains near fusion lines and equiaxed grains in interlayer regions. Columnar grain growth due to steep temperature gradients during deposition, while equiaxed grains form in regions experiencing slower cooling rates (Barath Kumar & Manikandan, 2022). According to the findings in Figure 2.27, when the shielding gas flow is low, the grains become columnar, and the size distribution is uneven. By increasing the has flow rate from 12.5 L/min to 22.5 L/min, the weld bead formation is better which favors the formation of equiaxed grains and resulted more uniform microstructure. However, lower heat input by reducing welding current or increasing the welding speed also refined grains toward an equiaxed morphology. This finding aligns with observation by N. A. Rosli et al. (Rosli et al., 2021) in which by reducing heat input to 87.5 – 154.2 J/mm resulted finer equiaxed grain, which improves mechanical properties and reduces porosity.

Apart from the influence of process parameters, the microstructure within the deposited wall also found to result in variations of grain morphology. Y. Geng et. al (Geng et al., 2022) analyzed the microstructure of Al-5.0 Mg at two different regions at

the thin walled as depicted in Figure 2.28(a) and (c) found that the grain morphology of region A (cross section of the thin wall) composed homogenous equiaxed grain that mixed with fine and coarse grains, as shown in Figure 2.28(b) with average grain size of 33.69 µm and maximum grain size 257.89 µm. The formation of fine grain is affected by the formation of multi-layer heat input during the deformation up the height of the thin wall. However, the grain morphology of region B composed heterogenous columnar grains.

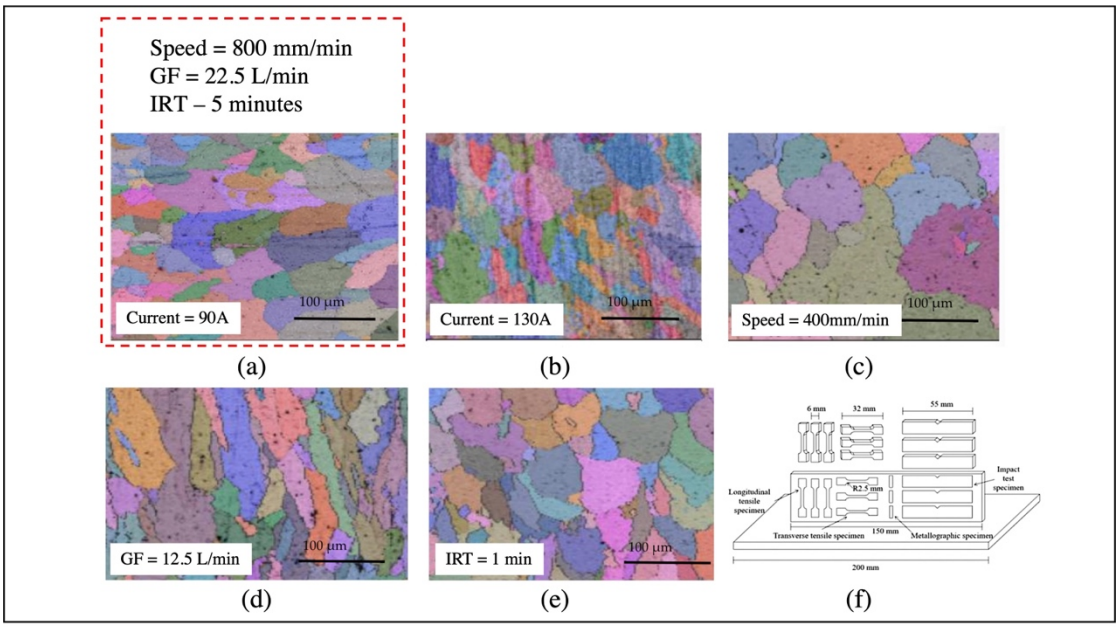

Figure 2.27 EBSD of Al-Mg under Different Process Parameter by CMT Process (a) 90A (b) 130A (c) 400 mm/min (d) 12.5 L/min (e) 1 min interlayer residence time (f) Sample Positioning (Y. Liu et al., 2022)

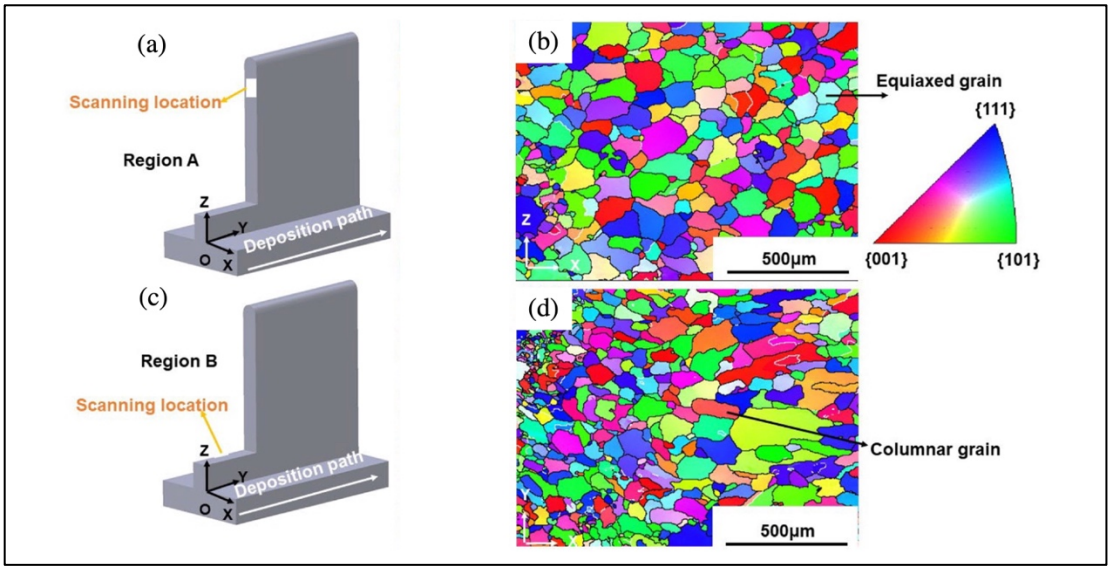

Figure 2.28 Scanning location and inverse pole figure (IPF) maps by EBSD of Al-5.0 Mg; (a) region A (b) IPF maps of region A, (c) region B, and (d) IPF maps of region B (Geng et al., 2022)

Similarly, the findings also proved in the research by C. Su et al (Su et al., 2019) on the same material fabricated by CMT where the decrement of travel speed delays the solidification and cooling of weld pool, which fasten the tendency of grain growth and refine the grain size. Mirroring this study, J. Xiong et. al (Xiong et al., 2018) stated that the relationship of the deposition current and wire feed speed increasing simultaneously in the application of GMAW process even though the research using different type of WAAM and materials, as stated in Figure 2.27. The optimal process parameter used in the research was 158 A for welding current, 16.8 V for the voltage, 7.0 m/min wire feed speed, 0.6 m/min travel speed, gas flow rate 20 L/min, which performed 212.352 J/m of heat input. Hence, it is related to the heat input theory where current, voltage, thermal efficiency, and travel speed are the main process parameters that affected the microstructure of WAAM manufactured.

Finally, the interlayer residence time also affected the grain size distribution. The slower the interlayer residence time form uniform grain size because the thermal accumulation improved and prolonging the holding time of grains to grow. Thus, the research concludes the better microstructure applied in this research are using 90 A welding current, 800 mm/min welding speed, 22.5 L/min gas flow rate and interlayer residence time 5 minutes as in the red box as depicted in Figure 2.27(a). The deposition path and the building axis of WAAM thin wall significantly impact the microstructure differently because the deposition path experiences rapid cooling and directional solidification. However, the building direction undergoes cumulative heat accumulation, slower cooling and grain coarsening due to repeated heating and cooling.

2.3.4 Residual Stress Performance and Tensile Properties

In WAAM, as the thin wall is repeatedly built up increasing the z-direction or build direction, each subsequent layer is deposited onto a previously cooled layer. Hence, the bottom layers and the tops layers experience different temperature regions and rapid cooling rates. Therefore, shrinkage of large pools of liquids during solidification and repeated cycles of heating and cooling result in high residual stress (Wu et al., 2020). For determining residual stress in WAAM-processes thin walls, X-ray diffraction (XRD) is a powerful and versatile technique for determining residual stresses in WAAM-processes aluminium thin walls because it offers a non-destructive

means of measuring the interatomic spacing in crystalline materials, which is directly related to the stress state (Monine et al., 2018).

Besides that, XRD technique also sensitive to stresses near the surface of the material, which is suitable for highest stresses that located in WAAM components. The principle relies on the interplanar atomic spacing in a crystalline material change under stress (Yelamasetti et al., 2022). Referring to Figure 2.29, when X-ray are directed onto a sample, they diffract at specific angles, as described by Bragg's Law (2.6) where λ is wavelength, θ_B is Bragg angle, and hkl subscript of the interplanar spacing, d, refers to the Miller indices of the crystallographic plane. n is an integer that refers as the order of the diffraction maxima, for instance, n=1 being the first order, and n=2 being the second order and so on (Harrington & Santiso, 2021).

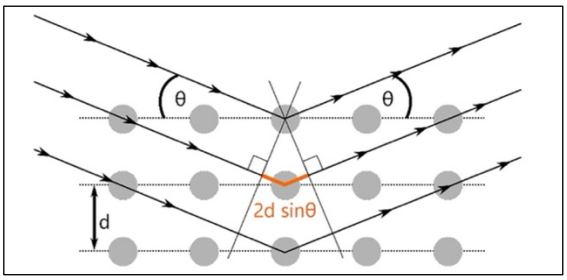

Figure 2.29 Visualization of Braggs' Equation (Harrington & Santiso, 2021)

$$n\lambda = 2d_{hkl}sin\theta_B \tag{2.6}$$

Residual stresses are significant concern in WAAM which leads to deformation, inaccurate shapes, potential fractures, and reduced fatigue performance (Barath Kumar & Manikandan, 2022). However, controlling process parameters and employing post-treatment can mitigate these issues (Barath Kumar & Manikandan, 2022). The research by Q. Wu et al. (Wu et al., 2020) identified that with higher preheat temperature on the substrate is the most influential variable in reducing residual stresses. This is because the longitudinal residual stress resulted maximum value near the substrate area. Residual stresses in WAAM are generally categorized into longitudinal and transverse according to their orientation to the deposition path. Longitudinal residual stress which is parallel to the deposition direction tends to be dominant component. According to the studies by J. Sun et al (Sun et al., 2021), it is generally tensile along most of the wall height especially near the top layer. Shrinkage in the longitudinal direction pulls against the substrate and previous layers which creating tension, while transverse shrinkage has minimal substrate interaction. At the higher height, the top surface longitudinal residual

stress may switch from tension to compression due to stress redistribution during cooling, refer to Figure 2.30 (c). In contrast, transverse residual stress that perpendicular to the deposition direction produced lower in magnitude.

Longitudinal stresses are typically higher than transverse stresses due to clamping and unclamping effect. The clamping positioned perpendicular to the welding direction further constrain longitudinal movement but not transverse. During building, clamps prevent the distortion and keep high longitudinal stress. However, after unclamping, bending distortion occurs and the residual stress redistributes. But the longitudinal components remain the largest contributor to the final stage and distortion (Boruah et al., 2023). Experiments and simulations on WAAM by J. Sun et al. (Sun et al., 2021) showed the substrate restraint strongly elevates longitudinal stresses in the build, while transverse stresses in the build are relatively insensitive to restraint, hence remained smaller.

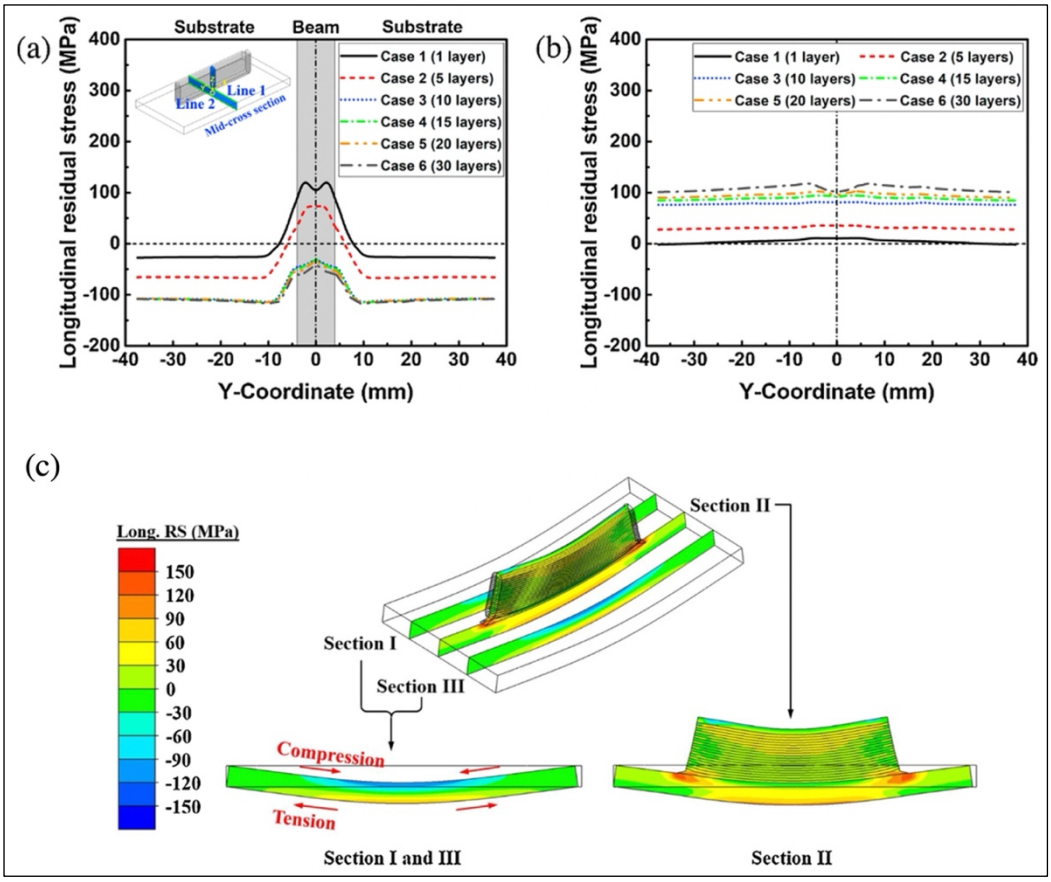

Figure 2.30 Distribution of Longitudinal Residual Stress (a) Along Line 1 (b) Along Line 2 (c) Color Contour (Sun et al., 2021)

During WAAM process, the thermal cycles and cooling rates plays a significant role in determining the resulting microstructure, material anisotropic and preferred grain orientation, also known as texture. As the process involves repeated melting and

solidification, the process leads to complex heat effects that influence grain growth (Geng et al., 2022). The specific cooling direction and the rate in different regions of deposited sample can lead to variations in grain morphology. After the cooling process, the molten pool will crystallize and precipitate on the substrate of subsequent layer. Hence, the temperature will reach between eutectic temperature and liquidus temperature, also known as eutectic reaction, make the material undergo intermetallic compounds (M. Xu et al., 2023).

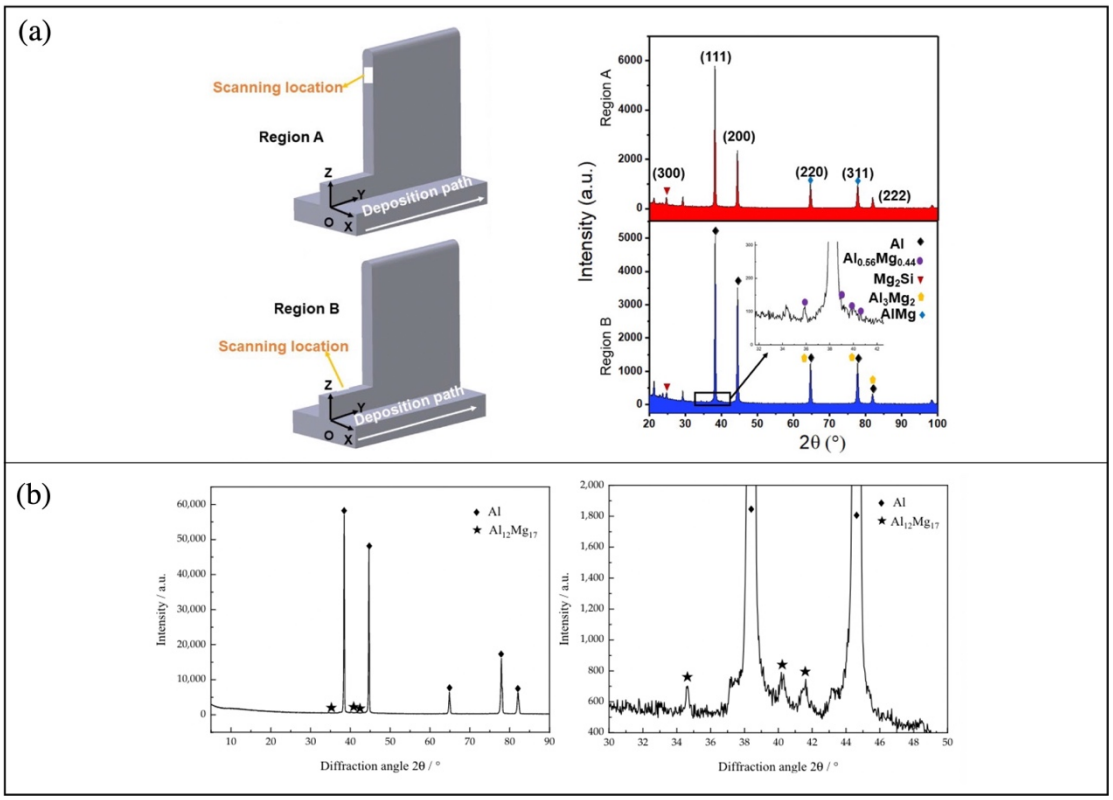

Figure 2.31 XRD Pattern Al-Mg of WAAM (a) Phase of Al-5.0 Mg (b) ER5556 (Geng et al., 2022; Y. Liu et al., 2022)

For instances, aluminium alloys predominantly contain α-Al matrix with secondary phases. In 5356 alloys, β-phase (Al_3Mg_2) precipitates along grain boundaries (Zuo et al., 2025). XRD can reveal the grains deposited material with desired crystallographic orientation (Geng et al., 2022). The XRD pattern in Figure 2.31 shows the presence of main phases in typical Al-Mg alloys which confirmed the existence of α-Al matrix and intermetallic compounds like Al_3Mg_2 or $Al_{12}Mg_{17}$ including the other of minor phases or precipitates that form due to alloying elements or process conditions (Geng et al., 2022; Y. Liu et al., 2022). The crystallographic orientation diffracted in specific planes. According to scholars, since aluminium is FCC structure, the (111) and (200) planes are most densely packed planes, often associated with the primary growth

direction due to lower surface energy. The presence of specific textures or orientations in additively manufactured Al-Mg alloy means that a greater proportion of grains are aligned with these crystallographic planes parallel to the sample surface or growth direction (Geng et al., 2022).

Phase identification and crystallography obtained from XRD analysis provide important insight into the strengthening mechanism. The tensile properties of aluminium walls fabricated using WAAM exhibit significant characteristics influenced by the process. For instance, the defects such as porosity, negatively impact the tensile properties. This defect can act as stress concentrators, reducing both strength and ductility (Tonelli et al., 2021). The strength of aluminium after WAAM process such as ultimate tensile strength (UTS), yield strength (YS), and elongation are crucial to predict the performance and understanding of failure mechanism (Greebmalai & Warinsiriruk, 2020; Y. Liu et al., 2022). The standards for tension testing of metallic materials widely refer to ASTM E8/E8M-16a or also known as “dog-bone” shaped that designated to ensure failure occurs within the gauge length (Tonelli et al., 2021).

Tensile tests revealed that the mechanical properties of WAAM aluminium alloy depending on the direction of testing relative to the build direction (Tonelli et al., 2021). Specifically, the specimens oriented longitudinal typically exhibit highest tensile properties including UTS and elongation because the fracture path tends to cut across the layers, minimizing the influence of inter-layer defects (Tonelli et al., 2021). In contrast, the research by M. Chandra et al. (Chandra et al., 2023) stated that the transverse (T) direction generally exhibits higher UTS, and elongation compared to the longitudinal (L) direction, in which the research was applied the same orientation but different term of explanation (Arana et al., 2022). Based on the recent research, the terms transverse, longitudinal, and diagonal of WAAM samples refer to the orientation to the deposited layers or build direction, as displayed in Figure 2.32(a). To make it fixed and clear, the longitudinal orientation specimen is aligning parallel which is 0° to the deposition layers that horizontally moving to build up the height of the wall. The transverse orientation will be perpendicular or 90° to the deposited layers, while the diagonal orientation is 45° relative to the deposition layers (Tonelli et al., 2021). Figure 2.32(c) illustrates the exact specimen orientation, which is used as the reference for the subsequent discussion.

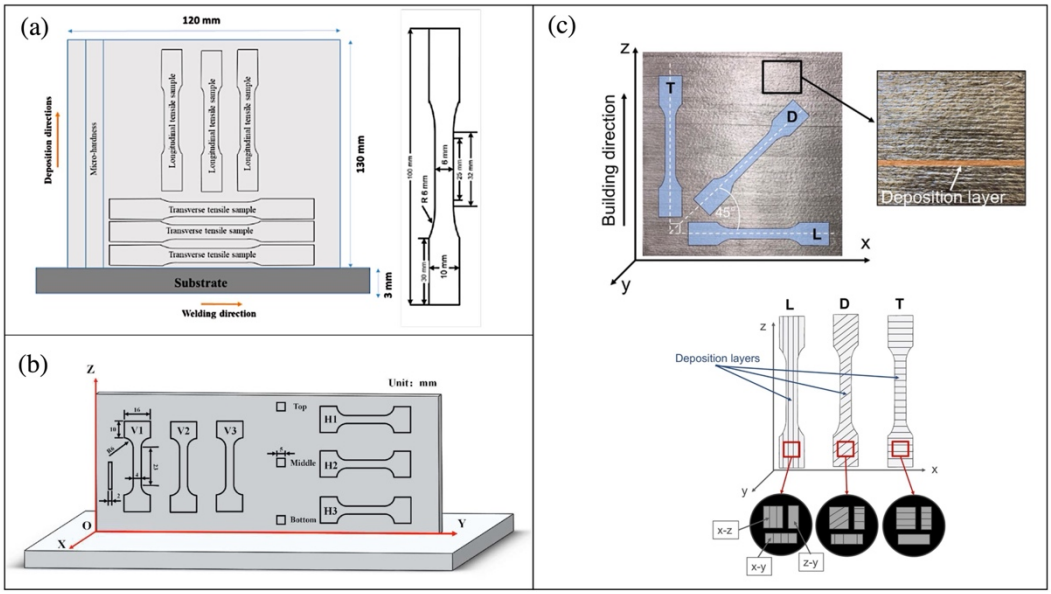

Figure 2.32 Tensile Specimen Orientation of Series 5 Aluminium Alloy Fabricated by GMAW (a) and (b) ER5356 wall (Arana et al., 2022; Köhler et al., 2020) (c) AA 5083 (Tonelli et al., 2021)

Regarding to L. Tonelli et al. (Tonelli et al., 2021), the L (0°) specimen consistently shows the highest UTS values, while in contrast, the T (90°) specimen displays the lowest UTS, with notable drop of approximately 27% compared to L (0°) specimens for AA5083. The D (45°) specimens display in line with slightly lower than standard requirements, where the L specimens reached up to 300 MPa, while T (90°) specimens had UTS around 200 MPa. Figure 2.33 shows the stress-strain curves of different orientation in the recent studies. A similar pattern for Al5356 by M. Kohler (Köhler et al., 2019) where the horizontal build direction (longitudinal) reaches UTS approximately 267 MPa, while the vertical direction (transverse) falls to 254 MPa (Köhler et al., 2019). The anisotropy is attributed to microstructural discontinuities such as pores and layer boundaries that align unfavourably to the loading axis. Similar to UTS trend, the longitudinal orientation tends to yield high YS values, and the transverse shows the lowest YS (Tonelli et al., 2021).

Regarding to L. Tonelli et al. (Tonelli et al., 2021), the L (0°) specimen consistently shows the highest UTS values, while in contrast, the T (90°) specimen displays the lowest UTS, with notable drop of approximately 27% compared to L (0°) specimens for AA5083. The D (45°) specimens display in line with slightly lower than standard requirements, where the L specimens reached up to 300 MPa, while T (90°) specimens had UTS around 200 MPa. Figure 2.33 shows the stress-strain curves of different orientation in the recent studies. A similar pattern for Al5356 by M. Kohler

(Köhler et al., 2019) where the horizontal build direction (longitudinal) reaches UTS approximately 267 MPa, while the vertical direction (transverse) falls to 254 MPa (Köhler et al., 2019). The anisotropy is attributed to microstructural discontinuities such as pores and layer boundaries that align unfavourably to the loading axis. Similar to UTS trend, the longitudinal orientation tends to yield high YS values, and the transverse shows the lowest YS (Tonelli et al., 2021).

The longitudinal orientation tends to generate higher UTS and YS because of the alignment of deposition layers is parallel to the tensile load which allows the material to utilize its strength more effectively across the layers. In addition, the characteristic of melt pool boundaries and solidification patterns is oriented to resist the fracture along the direction of loading. The parallel alignment of deposition layers and tensile load exert less stress concentration effect that can initiate the premature fracture compared to when they are perpendicular to the load. Hence, the transverse specimen breaks earlier and resulting lowest UTS and YS. In transverse specimen, the tensile load applied is perpendicular to the deposition layers, hence, the interlayer defects directly in the path of the applied stress, acting as critical stress risers that promote crack initiation and propagation. Thus, reducing UTS and YS (Tonelli et al., 2021).

According to the comparison across AA5083, AA5356 and another Al-Mg in Table 2.7, the alloys have variations in anisotropic behavior. AA5083 specimens consistently show the expected pattern with lowest transverse properties (215 MPa UTS, 7% elongation) while some AA5356 variants exhibit more complex behavior (Tonelli et al., 2021). This suggests that Mg content, intermetallic phase distribution and grain structure characteristics interact with the deposition induced microstructure to produce different anisotropy signatures. The observation that AA5356 robotic controlled GMAW produces higher transverse UTS (288.65 MPa) than longitudinal (253.50 MPa) challenges the common assumption, which means the process parameter control and heat management strategies can substantially influence degree and direction of anisotropy (Tonelli et al., 2021). This indicates that anisotropy is not an immutable characteristic but rather a consequence of process microstructure interactions that may be customised through parameter optimization.

Typical UTS values for the Al-Mg alloys in industrial practice fall within 250 – 300 MPa with YS of 125 – 150 MPa and elongation of 15 – 20% (Elka Mehr Kimiya, 2024). The data in Table 2.7 shows that WAAM-fabricated 5xxx alloys generally achieve tensile properties, particularly when tested in specified load direction. Based on

Table 2.3, recent studies demonstrate that process parameters including heat input, interaction temperature and deposition strategy directly influence the manifestation of anisotropy. Components fabricated under low heat input shows refined grain structures and reduced porosity, potentially moderating anisotropic effects. The thermal cycling inherent to multi-layer WAAM deposits creates a gradient in microstructural features from bottom to top of the component, contributing to additional mechanical property variations beyond simple orientation-based anisotropy. Therefore, in structural application, components should be designated where principal load paths aligned with favourable orientations, preferably longitudinal as there will be approximately 20% increment in strength (Tonelli et al., 2021).

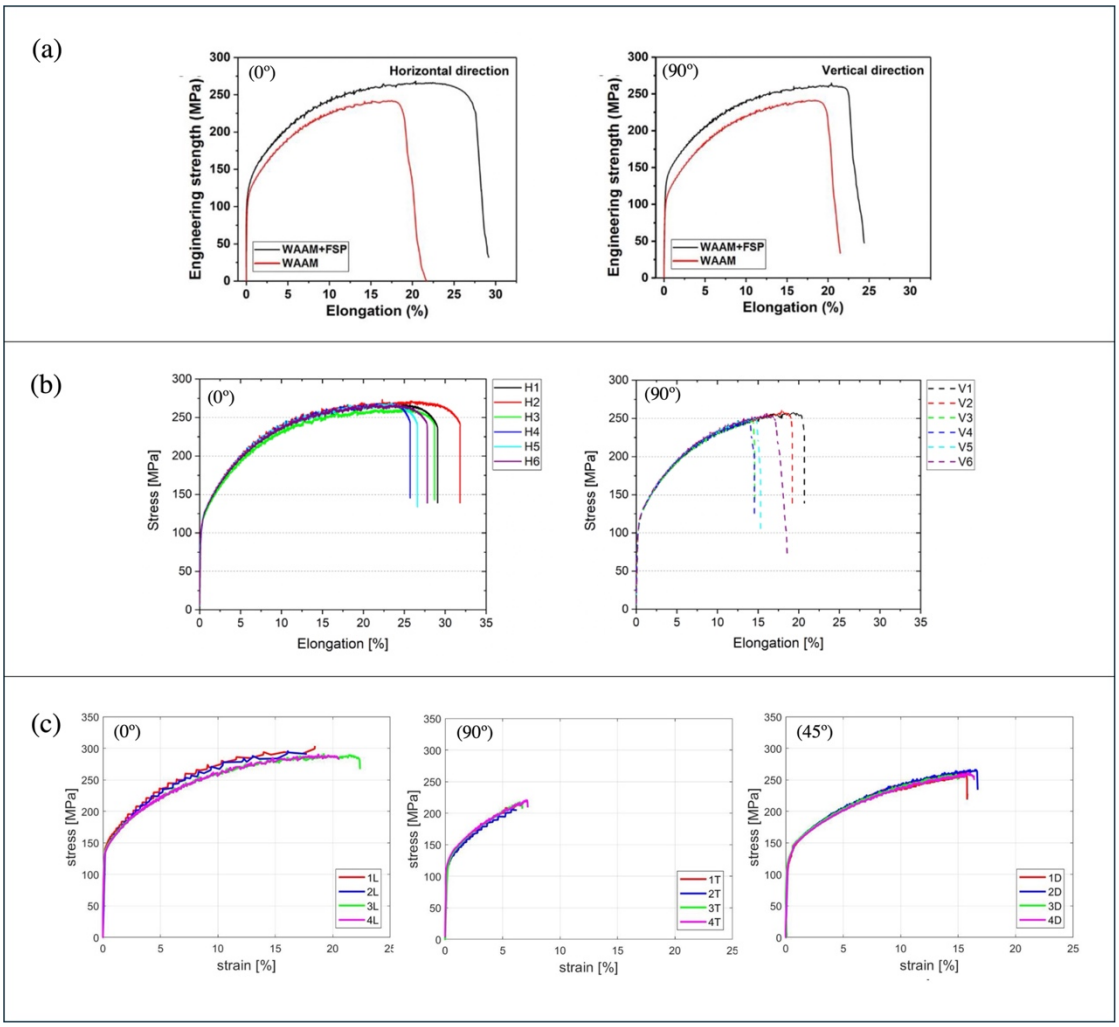

Figure 2.33 Stress-strain Curves for WAAM Aluminium Alloy on Different Orientation using (a-b) ER5356 (c) AA5083 (Köhler et al., 2019; L. Liu et al., 2023; Tonelli et al., 2021)

Table 2.7
The Anisotropy Behavior for Different Orientation (Building to Deposition Direction)

Aluminium Type	Purpose	Orientation / Angle	UTS (MPa)	YS (MPa)	Elongation to Failure (%)
AA5083 (Tonelli et al., 2021)	Specimen orientation	L: 0º D: 45º T: 90º	295.00 ± 5 263.00 ± 3 215.00 ± 6	143.00 ± 1 127.00 ± 7 123.00 ± 3	20.00 ± 2 16.00 ± 1 7.00 ± 15
Al5356 (Köhler et al., 2019)	Different Al type	L: 0º T: 90º	267.60 ± 3.5 254.00 ± 5.6	114.9 ± 1 114.9 ± 2.7	28.3 ± 2.1 17.1 ± 2.7
ER5356 (Wieczorowski et al., 2023)	Robotic GMAW	L: 0º T: 90º	253.50 288.65	123.35 134.34	19.62 34.12
AA5356 (D. S. Zhao et al., 2022)	Mg loss study	L: 0º T: 90º	236.70 267.60	N/A N/A	19.62 34.12
AA5356 (Zuo et al., 2025)	Low heat input	L: 0º T: 90º	245.88 236.00	N/A N/A	37.00 32.40
AA5356 (S. Li et al., 2021)	Argon protection	L: 0º T: 90º	280.00 275.00	127.00 126.00	29.00 27.00
Al5356 (Köhler et al., 2020)	Thermal cycling	L: 0º T: 90º	254.00-277.00 247.00-260.00	115.00-120.00 115.00-120.00	14.00-28.00 14.00-20.00

As summarised in Table 2.7, anisotropic behavior in WAAM components is commonly related to the deposition direction, build orientation, grain structure, and thermal history. Most existing studies focus on tensile properties at different orientations, while limited work has linked anisotropic mechanical response with post-forging deformation, residual stress redistribution, and subsequent compressive strain-hardening behavior. This gap is addressed in the present study by evaluating the mechanical performance of WAAM and WAAM-forged ER5356 aluminium alloy, including tensile behavior, residual stress condition, and strain-rate-dependent compression response.

2.4 Hybrid Manufacturing of WAAM Process

2.4.1 Current Progress of Hybrid WAAM-Forging Process

Hybrid manufacturing is the integration of additive manufacturing with one or more subtractive or forming processes in single work, enabling a structure within the same build cycle to overcome the limitations of singular processes while leveraging their respective strengths (Pragana et al., 2021). For instance, hybrid manufacturing integrates WAAM with mechanical deformation of forming processes such as rolling, forging and similar thermo-mechanical interventions to simultaneously build near net shape components. Recent studies on hybrid integration of WAAM have primarily emphasized pre-process, in-process and post-process approaches, where mechanical treatments are applied during or after deposition to enhance material properties especially in strength and microstructural characteristics depending on whether they are applied before, during, or after material deposition.

The summarise of effectiveness hybrid manufacturing strategies using several post-processing methods, including rolling, hammering, machining, and other deformation-assisted approaches to counter the limitations of the WAAM process for various material listed in Table 2.8. For stainless steel such as ER316LSi, in-process hot forging combined with WAAM successfully reduced porosity and refined the microstructure, leading to improved geometric accuracy and surface quality (Mendes et al., 2025). In Ti-6Al-4V, combining WAAM with forging whether as a pre-process or post process as displayed in Figure 2.34 led to benefits like grain refinement, dynamic recrystallization and tensile properties surpassing wrought material specification (Bambach et al., 2020; Meiners et al., 2020). Specifically, forging after WAAM resulted in refined equiaxed grains and reduced texture (Maurya et al., 2022). Furthermore, layer-by-layer grinding combined with WAAM for steel effectively reduced defects and increased tensile properties, as shown in Figure 2.35 (Karlina et al., 2024). Hybrid manufacturing using cold or warm rolling subsequent heat treatment on Inconel 718 converted coarse columnar dendrites intro finer equiaxed grains, significantly increasing microhardness and tensile performance after warm rolling (T. Zhang et al., 2022).

Similarly, the efficiency of mechanical post work such as cold forging, rolling and surface treatments in further improving density, hardness and wear or fatigue

resistance is worked for aluminium alloy. M. Azlin et al. (Azlin et al., 2024) applied cold forging to WAAM ER5356 showed visible densification near surfaces, reduced pore visibility and improvements in hardness and wear rate compared to as-built specimen. The hybrid process of forming on aluminium also able to increase dislocation density and grain growth based on the research by J. Huang et al. (J. Huang et al., 2023). The impact of hybrid manufacturing is evident in hot rolling-WAAM of Al-Si alloys, where porosity levels were reduced from 1.72% to 0.21% accompanied by an approximate 55% decrease in average pore size, particularly enhanced strength and ductility (J. Huang et al., 2023). Although various hybrid manufacturing strategies have been explored, the application of cold forging as a hybrid process in aluminium alloy remains underexplored.

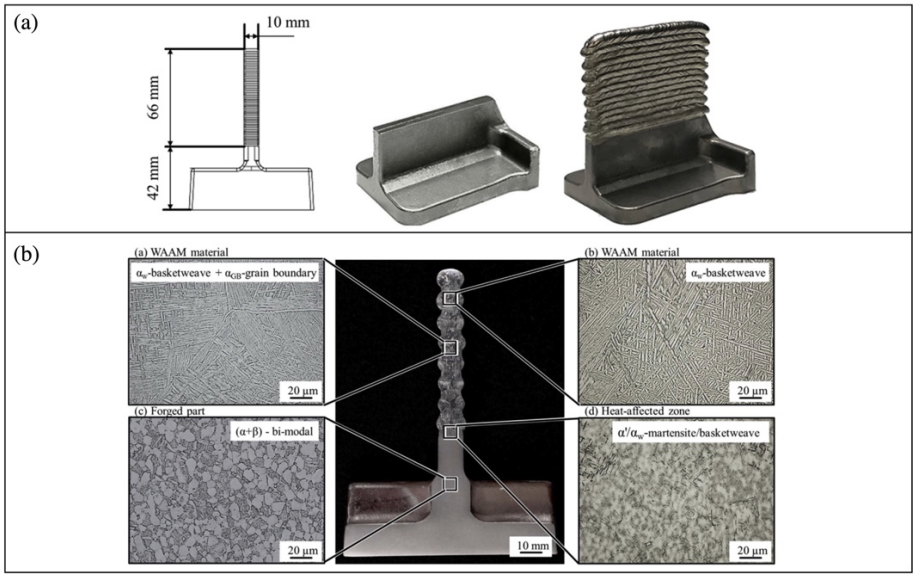

Figure 2.34 Geometry of Forged and Followed by WAAM (b) Microstructure of Ti-6Al-4V WAAM-Hot Forming (Bambach et al., 2020)

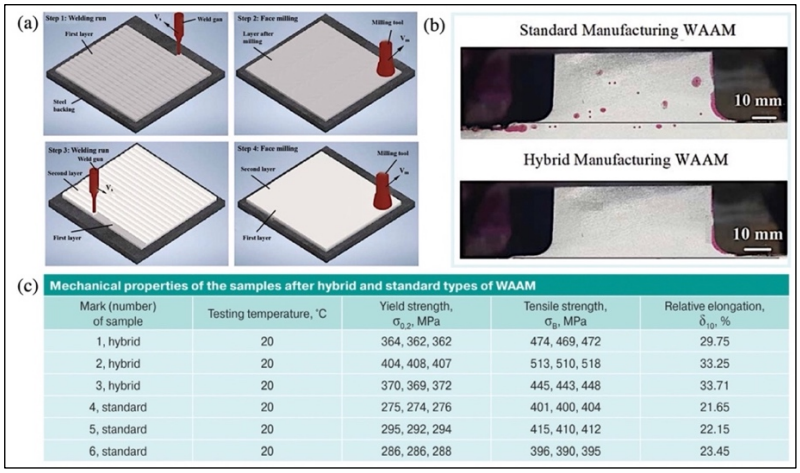

Mark (number) of sample	Testing temperature, °C	Yield strength, $\sigma_{0.2}$, MPa	Tensile strength, σ_B, MPa	Relative elongation, δ_{10}, %
1, hybrid	20	364, 362, 362	474, 469, 472	29.75
2, hybrid	20	404, 408, 407	513, 510, 518	33.25
3, hybrid	20	370, 369, 372	445, 443, 448	33.71
4, standard	20	275, 274, 276	401, 400, 404	21.65
5, standard	20	295, 292, 294	415, 410, 412	22.15
6, standard	20	286, 286, 288	396, 390, 395	23.45

Figure 2.35 Hybrid WAAM-Milling of Steel (a) Process Procedure (b) Comparison of Mechanical Properties after Hybrid and WAAM (c) Tensile Properties (Karlina et al., 2024)

Table 2.8
Recent Studies Hybrid Manufacturing of WAAM for Various Alloys

Reference	Material	Hybrid Process	Stage of Hybrid Integration	Improvements over Standard WAAM	Future Studies
(Mendes et al., 2025)	ER316LSi Stainless steel	Hot forging + WAAM	In-process	Porosity reduced, refined microstructure, improved geometric accuracy and surface quality, enhanced tensile	Complex geometries, and multi material application
(T. Zhang et al., 2022)	Inconel 718	WAAM + cold/warm rolling + heat treatment	In-process	Columnar dendrites transform to equiaxed grains, microhardness increase, tensile test after warm roll better	Apply warm rolling to aluminium with adapted loads
(Maurya et al., 2022)	Ti-6Al-4V	WAAM + Hot forging	Post-process	Dynamic recrystallization at 900-950 °C, strain more than $0.1s^{-1}$ refined equiaxed grains, strength and elongation increase, texture decrease	Extend deformation maps for aluminium alloy with WAAM conditions
(Karlina et al., 2024)	Steel	WAAM + layer by layer grinding	In-process	Porosity and defects reduced, tensile properties increase, improved surface integrity	Test the hybrid manufacturing – grinding for aluminium pore control
(Meiners et al., 2020)	Ti-6Al-4V	WAAM + Forging	Post-process	Heat treatments eliminated anisotropy, tensile properties better than ASTM specification, complex neat-net shape	Adapt forging and AM route to high strength aluminium alloy
(Bambach et al., 2020)	Ti-6Al-4V	Forming + WAAM	Pre-process	Form recrystallised particles, yield strength and elongation increase, strong interface bonding	Apply to aluminium with force-controlled interpass deformation

In addition, interlayer hot rolling integrated with WAAM on an Al-Mg also reported that HR-WAAM samples reduced the porosity from 1.89% to 0.56%, simultaneously achieved an UTS of ~338 MPa, yield strength of ~276 MPa, and elongation of 20.9% (J. Huang et al., 2024). These findings are corresponded to the increment of approximately 28.5%, 41.5% and 38.4% respectively compared with conventional WAAM without rolling, as shown in Figure 2.36. The combination of fewer pores and a refined grain reduces early crack nucleation while allowing the material to sustain larger plastic strain before failure.

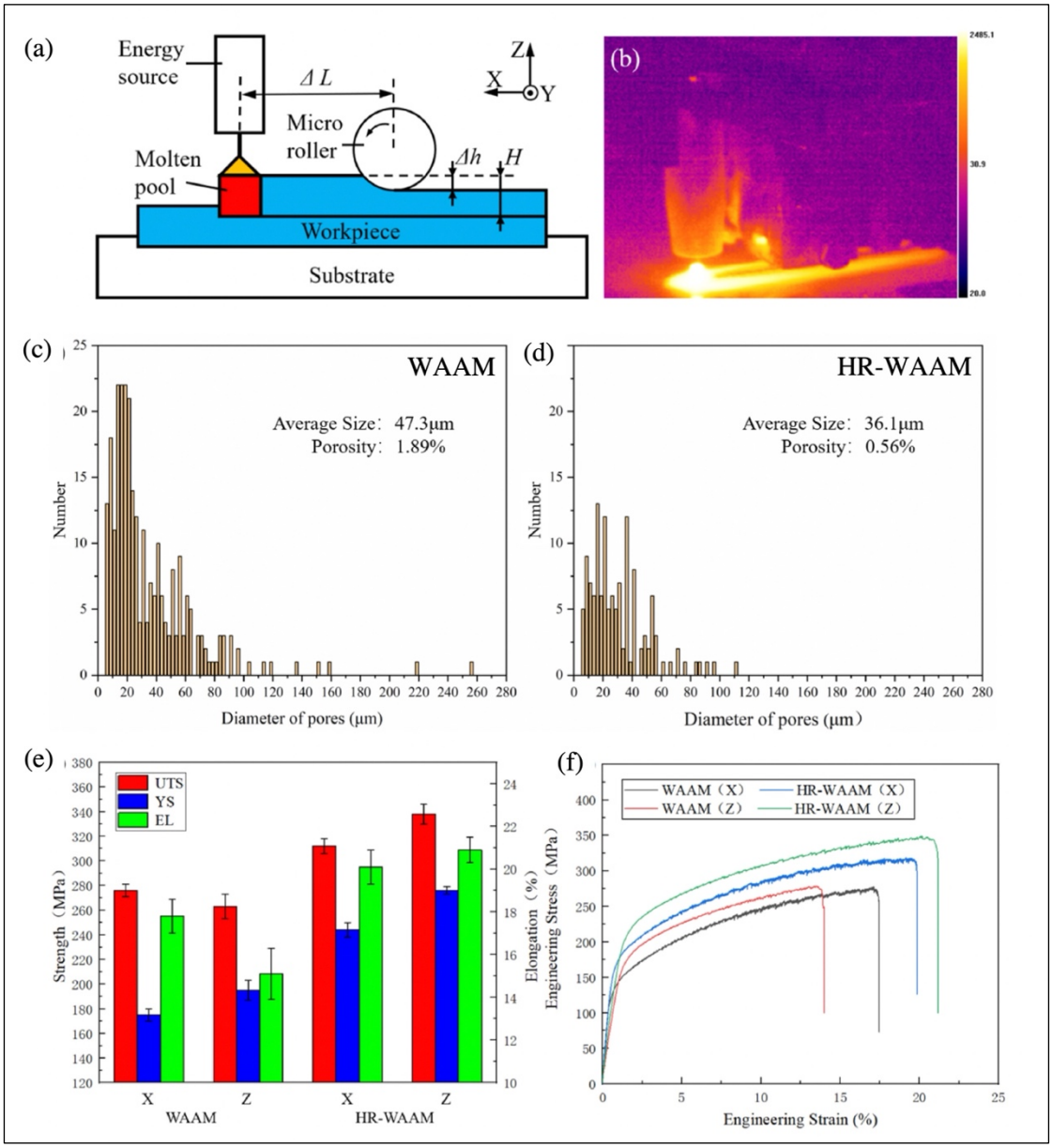

Figure 2.36 (a) Schematic Diagram of HR-WAAM Process (b) Temperature Distribution (c) WAAM Pore Size (d) HR-WAAM Pore Size (e-f) Tensile Properties of WAAM and HR-WAAM (J. Huang et al., 2024)

However, according to S. Zhou et al. (Zhou et al., 2022) studies, hammering is preferred instead of rolling for distributed because the process involves lower load deformation of layers. In the case of aluminium alloy, inter-layer hammering has been shown to transform round pores into flattened or sealed voids, while simultaneously trapping hydrogen within dislocations or vacancies, thereby preventing subsequent pores growth, as shown in Figure 3.37. The porosity percentage drop from 1.39% to 0.28% as the load of hammered increases. This method creates a periodic microstructure of work-hardened and recrystallized regions, leading to high strength of UTS up to 400 MPa and improved plasticity. Hence, the application of hybrid manufacturing works on aluminium WAAM.

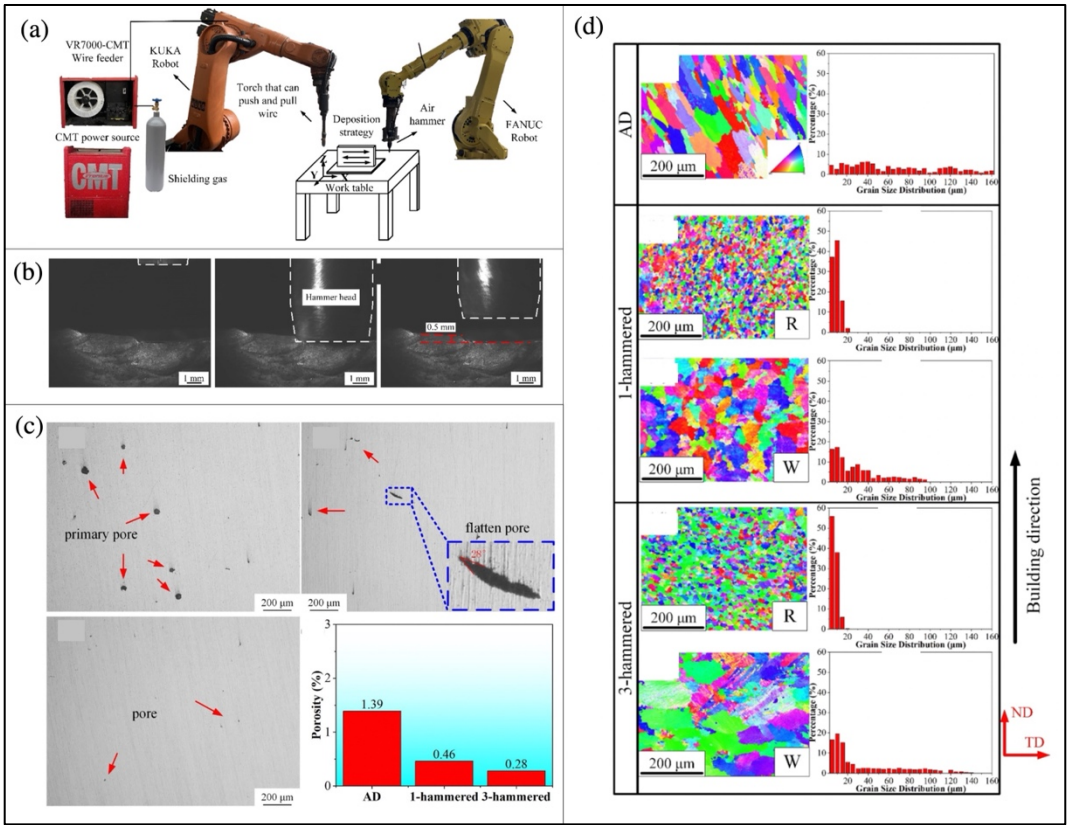

Figure 2.37 (a) Experiment Setup for WAAM-Hammering of Series 5 Aluminium Alloy (b) Hammering Process (c) OM Images of Pores and Porosity (d) EBSD IPF and Grain Size Distributions (Zhou et al., 2022)

The summarise of hybrid manufacturing on WAAM process for aluminium are listed in Table 2.9. Other hybrid manufacturing such as surface intensive methods, for instance ultrasonic nanocrystalline surface modification (UNSM) or ultrasonic impact treatment (UIT) also produce significant hardness and fatigue improvement in 5 series aluminium alloy as shown in Figure 2.38 and Figure 2.39. Although the precise percentage increase in UTS does not often give in these surface treatment studies, the

studies supported bulk porosity and deliver efficient improvements in wear resistance and fatigue performance (W. Li et al., 2023; C. Wang et al., 2022).

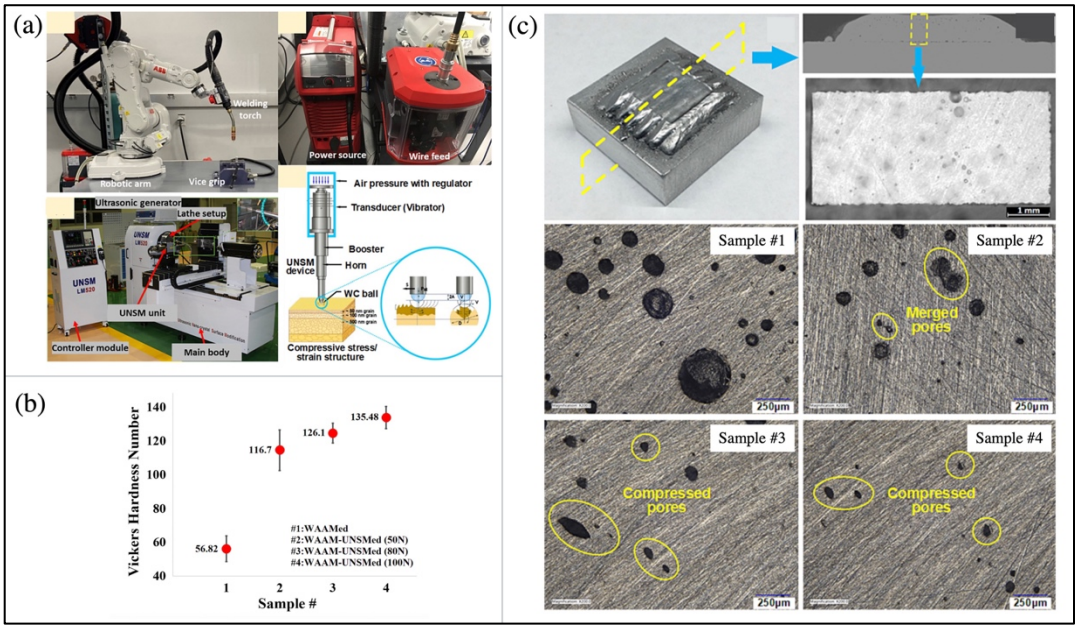

Figure 2.38 Hybrid Manufacturing WAAM-UNSM Al5356 on Different Static Load (a) Experiment Setup (b) Hardness Analysis (c) Observation of Pores Through Optical Microscope (W. Li et al., 2023)

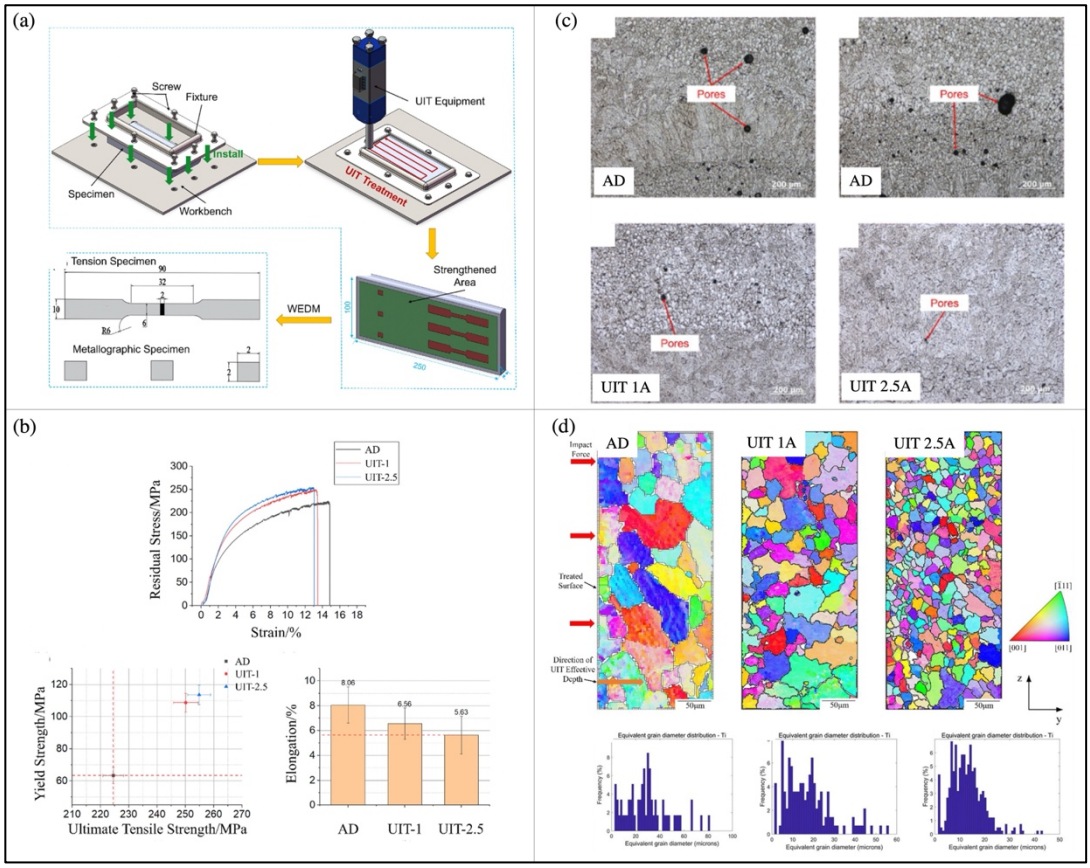

Figure 2.39 Hybrid Manufacturing WAAM-UIT ER2319 (a) Experiment Setup (b) Tensile Properties (c) Porosity Observation (d) IPF Maps (C. Wang et al., 2022)

The effectiveness of hybrid manufacturing processes on WAAM clearly reflected in the grain refinement in IPF. Hybrid plastic deformation such as UIT and hammering as presented in Figure 2.39 and Figure 2.37 resulted strain energy that drives recrystallization during subsequent thermal cycles, transforming these detrimental structures. For instance, after hammered, the microstructure generates recrystallization (R) regions and work hardening (W) regions, resulting in significantly refined, equiaxed grains and a weakened texture with average grain sizes reduced to as low as 5.2 μm in the R region for Al-Mg alloys (Zhou et al., 2022). Similarly, increasing the working current in UIT resulting refined grains as shown in Figure 2.39(d).

Hybrid manufacturing approaches must account for the properties of material, particularly in the case of aluminium alloys. Owing to their relatively soft nature, aluminium alloys are susceptible to damage under heavy deformation processes such as hot rolling or hot forging. To overcome this limitation, warm deformation and cold working preferred to improved grain structured and precipitation distribution, besides improving strength and hardness (T. Zhang et al., 2022). Alternatively, subtractive hybrid steps such as milling and grinding able to remove defects while avoiding excessive mechanical loading (S. Zhang et al., 2023). To prevent surface tearing in soft alloys, the application of hybrid process depends on precise control of process parameters such as applied force, temperature and deformation rate. It is proved by the existing studies, where combining WAAM of aluminium with controlled deformation or machining results in notable improvements in mechanical properties, surface quality and defect suppression. Hence, to fill the gap, this study focuses on cold forging of aluminium, since the studies remains limited in WAAM hybrid process application.

Table 2.9
Recent Research Hybrid Manufacturing of WAAM on Aluminium Alloy

Reference	Material	Post-Deposition Process	Porosity Percentage / Observation	Strength / Mechanical Observation	Efficiency on Post-Deposition Process
(J. Huang et al., 2023)	ER4043	In-situ hot rolling	Porosity reduced, refined Si phase, higher dislocation density, increase tensile strength, smother surface	Improvements of 13.0%, 37.9%, and 29.6% in the average tensile strength, YS and elongation for the HR-WAAM	Smaller grain size, fewer pores in the HR-WAAM facilitate a more uniform distribution of load stress
(J. Huang et al., 2024)	ER5087	Interlayer hot rolling	Interlayer hot rolling reduced pore size and number	Rolling improved bonding and reduced stress concentrators. Mechanical strength improved compared WAAM	Interlayer rolling adds process time and cost but delivers measurable strength and ductility
(Azlin et al., 2024)	ER5356	Cold deformation (Open die)	Porosity reduction near surface, fewer visible pores in micrographs after forging	Forged specimen showed lower specific wear rate, and lower coefficient of friction, improved wear resistance	Improvement in wear resistance, even the process adds extra steps and time, nut improves service life
(C. Wang et al., 2022)	ER2319	UIT (surface cold forging)	UIT reduced near-surface porosity and refined grains near surface	UIT produced surface hardening and improved fatigue and strength near surface	Good surface performance improvement, efficient for shallow defect improvement
(Eimer et al., 2023) 2023	AA2024	Interlayer cold rolling + heat treatment	Interlayer cold work and heat treatment produced high mechanical properties, low anisotropy and porosity reduced	Strength improved after interlayer cold work and heat treatment, which support cold deformation strategy for WAAM	Properties of 2024 improved by combining cold work and post-deposition heat treatment
(W. Li et al., 2023)	Al5356	UNSM	After UNSM, large pores eliminated, and medium pores reduced ~50%	Hardness and surface finish significantly improved, expected improvement in fatigue	Good improvement by possibly less cost and time

2.4.2 Forging of Aluminium Alloy

Forging is a manufacturing process that shapes metal through localised compressive forces, traditionally applied with hammer or a press, where the applied stress exceeds the material's yield strength, causing a permanent change in its shape and internal structure (Khan & Mohan, 2020; Prajadhiana et al., 2022). In aluminium alloys, the forging can be performed either as hot forging above the recrystallization temperature of about 370°C to 593°C, depending on the alloy, or as cold forging below recrystallization at room temperature. Cold forging allows precise, near-net-shape parts with excellent surface finishes and minimal material waste, commonly used for complex and detailed designs. Cold forging may require intermediate annealing to relive stresses and allow continued deformation without cracking (Khan & Mohan, 2020).

The quality of forged components is strongly influenced by process parameters including lubrication, material selection, die design and mechanical parameters such as strain and strain rate (Baygut et al., 2020; Bouquerel et al., 2014). The effective lubrication such as molybdenum bisulfide, graphite or mineral oil plays a critical role as it reduces friction, thereby, minimizes barrelling or bulging of the workpiece, prevents tool wear and improves surface finish while simultaneously reducing the required forging force (Bouquerel et al., 2014; Pop et al., 2023; Priyadarshini et al., 2018). In addition, forging processes also classified based on the die arrangement; open-die forging, closed-die forging and flashless forging where each approaches govern the microstructural refinement and mechanical performance of aluminium alloy.

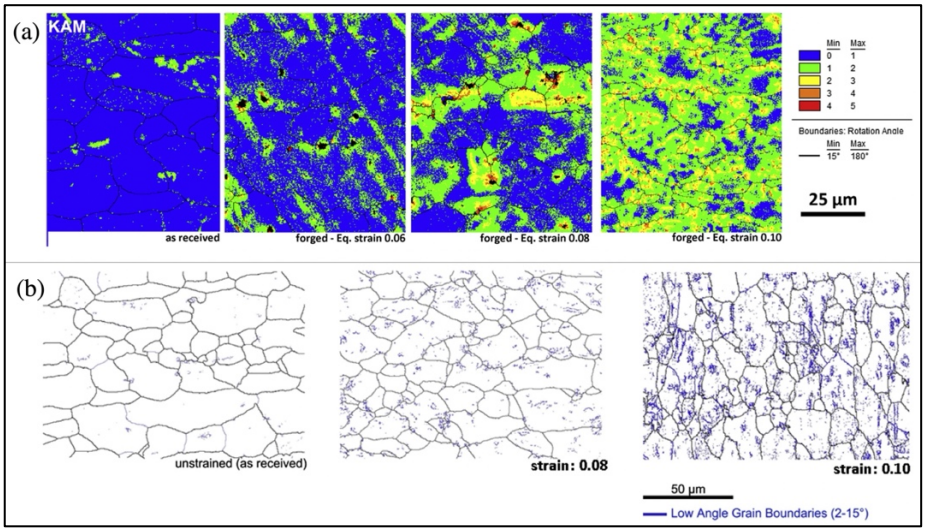

Figure 2.40 Influence of Cold Forging on Al 6082 Microstructure (a) KAM Map (b) Grain Boundary Map (Bouquerel et al., 2014)

For aluminium alloys, cold forging is particularly effective for producing high-strength, lightweight components with superior mechanical properties compared to cast parts (Song et al., 2024). This is also related to the microstructural response in cold forging process as it will mainly induces sub-structure formation via dislocations, rather than large-scale grain refinement (Bouquerel et al., 2014). The microstructural changes through severe plastic deformation at near room temperature leading to work hardening (Baygut et al., 2020). In addition, severe plastic deformation methods like multi-directional forging (MDF) are utilized when ultra-fine grain structures are specifically investigated (Manjunath et al., 2021).

Figure 2.40(a) shows the KAM maps of the as received and forged sample which explains as the nominal plastic strain increases, the KAM increases and is widespread inside the grains (Bouquerel et al., 2014). Research by J. Bouquerel et al. (Bouquerel et al., 2014) found that the microstructural alteration is the development of sub-structures which visible as new low-angle grain boundaries (LAGBs) within the grains as shown in Figure 2.40(b). The increments of LAGBs confirmed that a local strain increase and reflecting the nucleation of new dislocations. The existing grains often become elongated in the direction perpendicular to the forging axis (Kumar et al., 2018). However, in materials subjected to substantial deformation, the heightened dislocation density can lead to entanglement and the formation of dislocation cell structures (H. Li et al., 2023).

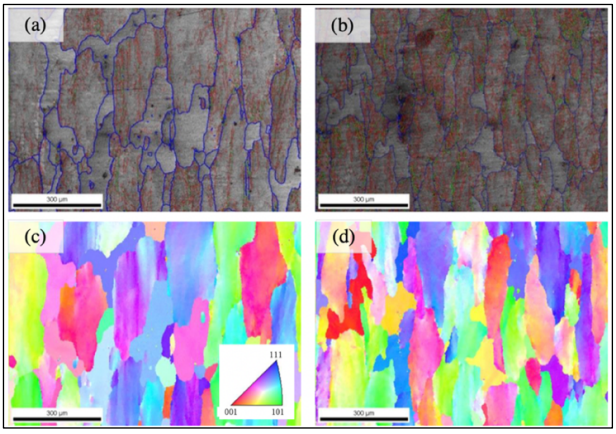

Figure 2.41 EBSD of Forging 7075 Aluminium Alloy of Various Press (a and c) 1% (b and d) 5% (H. Li et al., 2023)

Therefore, the increasing of strain enhanced the stored energy and dislocation density of the material (H. Li et al., 2023). Based on the EBSD results in Figure 2.41, the microstructure after cold compression displays a recrystallized crystal morphology. The recrystallization proportion was found to be higher at 1% compression strain

compared to 5% compression strain. This is because at 5% strain, the dislocation density becomes very large, forming tangled networks and promoting strain-induced precipitation that pin grain boundaries and enhance the nucleation, thus, exceeding the recrystallization and leaving many grains with high dislocation density. Consequently, the lower strain condition yields a greater recrystallized proportion.

Since cold forging in aluminium alloy undergoes dislocation rearrangement, the compressive stresses and plastic deformation mechanically close or flatten typical spherical hydrogen induced pores found in aluminium (Kumar et al., 2018). S. Kumar et al. (Kumar et al., 2018) found that increasing cold forging reduction to 75% in spray-formed Al-6Si drastically decreased porosity from 16% to 2% as compression forces minimizes remaining voids. Similarly, S. Cecchel and G. Cornacchia (Cecchel & Cornacchia, 2025) showed that low-pressure forging of Al-Si refines the microstructure and reduces typical casting defects such as voids, porosity, oxide films, inclusions, and coarse intermetallic. At moderate strains, recent cold forging studies and simulation indicate that the deformation strengthens the alloy and develops sub-grains without significantly change overall grain size in aluminium 6082 (Al-Mg-Si) (Bouquerel et al., 2014). J. Bouquerel et al. (Bouquerel et al., 2014) further demonstrated that higher strains or with additional processing such as rolling or severe plastic deformation, resulted significant grain refinement and altered phase distributions. This occurs because applied compressive stress contributes to work hardening, increasing yield strength and hardness due to the accumulation of dislocations (H. Li et al., 2023). In conclusion, the magnitude and direction of the applied pressure are important since it will increase with strain hardening. Optimized forging steps can minimize required force without compromising final mechanical properties (Baygut et al., 2020).

Table 2.10 summarizes cold forging effect across several aluminium alloys, primarily focusing on Al-Mg-Si alloys and Al-Mg subjected to upset or multi-stage forging. A consistent microstructural observation for the 6xxx alloys is that the Mg-Si strengthening precipitates remain stable, with no dissolution or recrystallization observed under cold forging conditions. The deformation is characterized by strain localization, leading to macro barrelling and surface hardening, which is a phenomenon that is reduced by applying effective lubricants (Priyadarshini et al., 2018). Based on Table 2.10, for AA5754, the strength increases due to dislocation storage with no phase change reported (Mohamed et al., 2021). Future studies are directed toward linking

internal strain patterns to selective precipitate redistribution and coupling FEM with precipitation prediction to better manage deformation processes (Ann et al., 2020).

Higher forging strain or press load during deformation introduces plastic strain, which leads to grain refinement that contributes to higher tensile strength. In the case of hybrid manufacturing, higher strain during WAAM-forging promotes grain refinement through grain subdivision and dislocation accumulation. In Figure 2.42(a) by M. Hirtler et al. (Hirtler et al., 2020), the base forged material softens. The tensile strength of 6082 base material drops to 155 MPa after the WAAM process, which is lower than the value for the original T6 temper material as presented in Figure 2.42(c). This is due to the heat influence and uncontrolled cooling conditions which cause the destruction of strength increasing particles and the precipitation of the material phase. The relationship between UTS and elongation is inverse as the strength increases, the elongation (ductility) decreases.

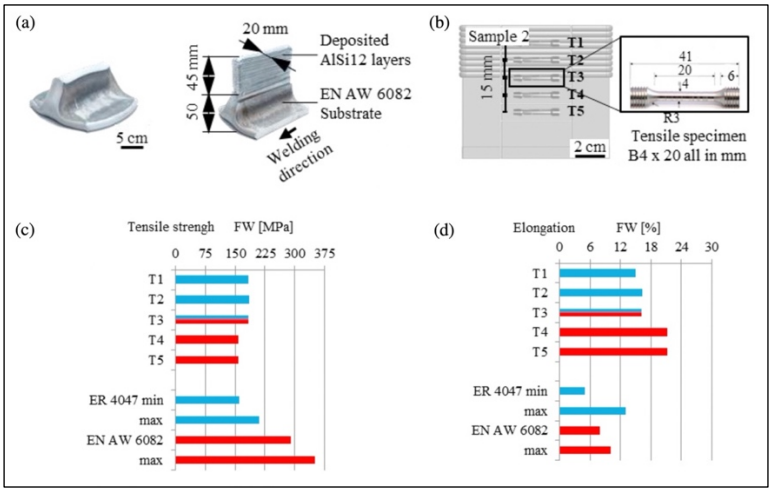

Figure 2.42 (a) Geometry of a Forged-AM sample (b) Position for Tensile Test (c-d) Tensile Strength Forged and Welded (FW) (Hirtler et al., 2020)

Based on the literature review, research on cold forging particularly for Al-Mg alloys remains limited. Consequently, hybrid process with WAAM has not been thoroughly investigated. Introducing cold forging in WAAM requires mechanical characterization, such as compression testing, to assess its effects on microstructure, porosity and overall material performance. Therefore, compression testing serves as a crucial tool to evaluate the effects of cold forging on the material's strength, ductility and residual stress which provides direct insight into the mechanical improvements through the hybrid WAAM-forging process. Hence, future study can address this gap by exploring the potential of WAAM-cold forging as a novel hybrid manufacturing approach.

Table 2.10
Cold Forging Effects on Aluminium Alloys

Ref / Year	Material	Process and Parameters	Observation in Phase	Microstructural Evidence	Impact on Properties	Future Studies
(Priyadarshini et al., 2018) 2018	AA 6082 (Al-Mg-Si)	Cold upset forging, aspect ratio 0.5-1, friction varied (dry, grease, mineral oil)	Mg-Si precipitates unaffected, strain localization differences	Macro barrelling, surface hardening	Improved uniformity with lube, phase stable	Connect strain patterns to selective precipitate distortion
(Ann et al., 2020) 2020	Al 6082 (Al-Mg-Si)	Multi-stage cold forging (6 stages), Cockcroft-Latham forming limit, axial loading, ring compression (friction m=0.05)	Mg-Si phase unchanged, no precipitate dissolution, no recrystallization	Precipitates stable, grain structure constant	Maintain properties, no over-strain damage	Explore deformation-induced beneficial redistribution
(Pop et al., 2023) 2023	AA 6088 (Al-Mg-Si)	Upset forging, ring compression (Coulomb friction model), axial press, hammer drop height variable	Stable Mg-Si precipitates	Less barrelling with low friction	Increase hardness and strength with graphite in oil	Study combined strain and thermal effects
(Priyadarshini et al., 2018) 2018	AA 6082 (Al-Mg-Si)	Cold upset forging, aspect ratio 0.5-1, friction varied (dry, grease, mineral oil)	Mg-precipitate unaffected, strain localization differences	Macro barrelling and surface hardening	Improved uniformity with lube, phase stable	Connect strain patterns to selective precipitate distortion
(Mohamed et al., 2021) 2021	AA5754 (Al-Mg)	Cross-die cold forging simulation and experiment	Al-Mg solid solution unaffected, no precipitate	Strain hotspots, no phase change	Strength increase via dislocation storage	Couple FEM with precipitation prediction

2.4.3 Compressive Behavior of Cold Forging Aluminium Alloy

Compression tests provide fundamental deformation including load needed to form the aluminium alloy without failure. The fundamental means to evaluate the load-bearing response of aluminium alloy under quasi-static conditions, for instance within strain rate range of $10^{-4}s^{-1}$ to $10^{-1}s^{-1}$ (Tahreen et al., 2014). Unlike torsion, which highlights ductility and fracture behavior, compression emphasize resistance to plastic instability, dislocation mobility and the strain hardening characteristics. The compression exerted on cold forging structure significantly enhances the compressive behavior of aluminium alloy, particularly the 5xxx series which rely on strain hardening and solid solidification strengthening from Mg by extensive plastic deformation that generates a high density of dislocations within the material structure (Song et al., 2024). Consequently, the intersect dislocation become tangled, severely impeding their movement and increasing the material's resistance to deformation.

This directly results in substantial increase in both yield strength (YS) and ultimate compressive stress (UCS) compared to the initial state (Baygut et al., 2020). In general, for metallic materials, the YS and UCS increase with increasing strain rate because plastic deformation requires time to accomplish and at higher rates, the deformation resistance is higher (Tahreen et al., 2014). Research by N. Tahreen et al. (Tahreen et al., 2014) in cast Mg-Al-Zn alloys compressed at room temperature revealed that an increase in the strain rate caused a slight increase in YS, although the hardening capacity decreased with increasing strain rates as shown in Figure 2.43. The overall hardening capacity is related to the material's ability to resist further plastic deformation, often measured as a ratio of UTS, σ_{UTS} to YS, σ_y of a material as stated in (2.7) (Tahreen et al., 2014). However, according to N. Tahreen et al. (Tahreen et al., 2014), in the case of compression, the UTS could be replaced by UCS, σ_{UCS} to estimate the hardening capacity of the material under compression as (2.8).

$$H_c = \frac{\sigma_{UTS} - \sigma_y}{\sigma_y} = \frac{\sigma_{UTS}}{\sigma_y} - 1 \tag{2.7}$$

$$H_c = \frac{\sigma_{UCS} - \sigma_y}{\sigma_y} = \frac{\sigma_{UCS}}{\sigma_y} - 1 \tag{2.8}$$

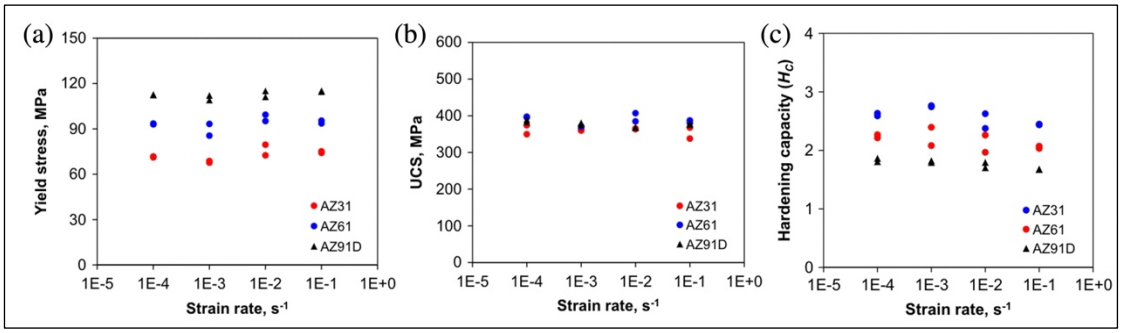

Figure 2.43 Effect of Strain Rate on (a) YS (b) UCS (c) Hardening Capacity (Tahreen et al., 2014)

According to recent research, to understand better on the deformation behavior of the material, strain hardening exponent at different strain rates should be evaluated (Tahreen et al., 2014). The strain hardening exponent is a quantitative parameter that reflects the strain hardening behavior more directly than other parameters such as flow stress and ultimate strength (Tahreen et al., 2014). Theoretically, the larger the magnitude of strain hardening exponent, the greater the strain hardening for a given amount of plastic strain (William D. Callister & David G. Rethwish, 2018). Several researchers have proposed different empirical equations to evaluate strain hardening exponent.

The first model was proposed in 1909 by P. Ludwik (P. Ludwik, 1909) by an empirical relationship as in (2.9) where n_1 is the strain hardening exponent and K_1 is the strength coefficient which represents the increment in strength due to strain hardening at $\varepsilon = 1$, σ is the true stress and ε is the true strain.

$$\sigma = \sigma_y + K_1 \varepsilon^{n_1} \tag{2.9}$$

After Ludwik's equation, Holloman (Bowen & Partridge, 1974) simplified the model by eliminating the parameter σ_y and giving the following two parameter, K and n expression as (2.10), where n is the strain hardening exponent and K is the strength coefficient.

$$\sigma = K\varepsilon^n \tag{2.10}$$

The other researchers, Swift. H (Swift, 1952) also proposed another power law equation as (2.11). The evolution of the model continued by N. Afrin et al. (Afrin et al., 2008), as they proposed the (2.12) equation, considering only the net flow stress and net plastic strain of the material after yielding. Regarding (2.12) equation, $n^*, \sigma, \varepsilon, \sigma_y$

and ε_y are the strain hardening exponent, true stress, true strain, yield strength and yield strain of the material, respectively. $K^*$is the strength coefficient which reflects the increment in strength due to strain hardening corresponding to $(\varepsilon - \varepsilon_y) = 1$.

$$\sigma = K_S(\varepsilon + \varepsilon_y)^{n_s} \tag{2.11}$$

$$\sigma - \sigma_y = K^*(\varepsilon - \varepsilon_y)^{n^*} \tag{2.12}$$

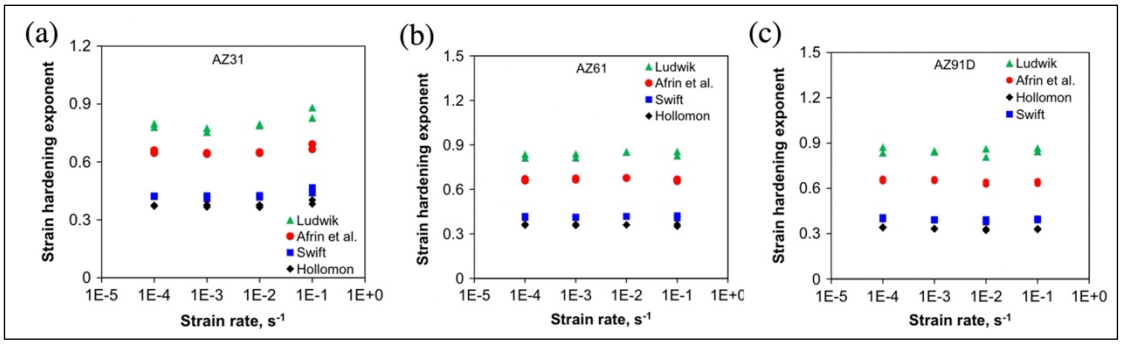

Figure 2.44 Strain Hardening Exponent on cast Mg (a) AZ31 (b) AZ61 (c) AZ91D (Tahreen et al., 2014)

According to recent studies on strain hardening exponent, the Holloman model is the most common model due to its simplicity, relying on two parameters, strength coefficient (K) and strain hardening exponent (n) (Bowen & Partridge, 1974; William D. Callister & David G. Rethwish, 2018). It is often acceptable for modeling uniform plastic deformation in bulk metals (Kwesi Nutor, 2017). However, in 2021, research by A. Lavakumar et al. (Lavakumar et al., 2021) stated that Holloman and Ludwik equation could not explain strain hardening characteristics of the experimental of steel over entire strain range satisfactory. This is because the parameters K and n are calculated using the Hollomon model, especially at strains below 1% can be inaccurate since the stress parameter, σ_y is eliminated (Bowen & Partridge, 1974; Tahreen et al., 2014). For instance, the Hollomon model provided a better fit for aluminium than for steel, suggesting that material composition and yield phenomena influence its reliability (Kwesi Nutor, 2017).

For materials conforming to the Hollomon equation, maximum strength and strain hardening capacity require large K values and n values between 0.1 and 0.3. This explains why N. Tahreen et al. (Tahreen et al., 2014) stated that models derived from Ludwik, such as Swift's model or the Afrin's equation are generally more reliable for capturing actual strain hardening behavior as they incorporate a consideration for strain that occurs prior to or only the net flow after yielding. Hence, the choice of model should

be ultimately reflecting the best statistical correlation with experimental data for the specific material being studied (Kwesi Nutor, 2017).

While the strain hardening exponent characterizes the material's ability to strengthen with plastic deformation, the strain rate sensitivity (SRS) is a critical parameter in material that quantifies material's flow stress (σ) changes in response to variations in the applied strain rate ($\dot{\varepsilon}$) (Tahreen et al., 2014; J. Xu et al., 2022). This property is closely linked to the phenomena like dynamic strain aging (DSA) and the Portevin-Le-Chatelier (PLC) effect, particularly in aluminium and magnesium alloys (Cho et al., 2020; Tahreen et al., 2014). There are two types of strain rate sensitivity; positive SRS and negative SRS (nSRS). Positive SRS is a normal behavior that the flow stress increases with increasing strain rate, refer Figure 2.45(a) (Knapek et al., 2017). This typical for most metallic materials outside the DSA regime (J. Xu et al., 2022). While nSRS is an abnormal behavior that show the decrement of flow stress with increasing strain rate (Ait-Amokhtar et al., 2015; J. Xu et al., 2022). For instance, Figure 2.45(b) shows nSRS for 15% 12% true strain, similarly in Figure 2.45(c) and (d) for the strain rate $10^{-4}s^{-1}$ – $10^{-2}s^{-1}$ and 230 – 300 K, respectively.

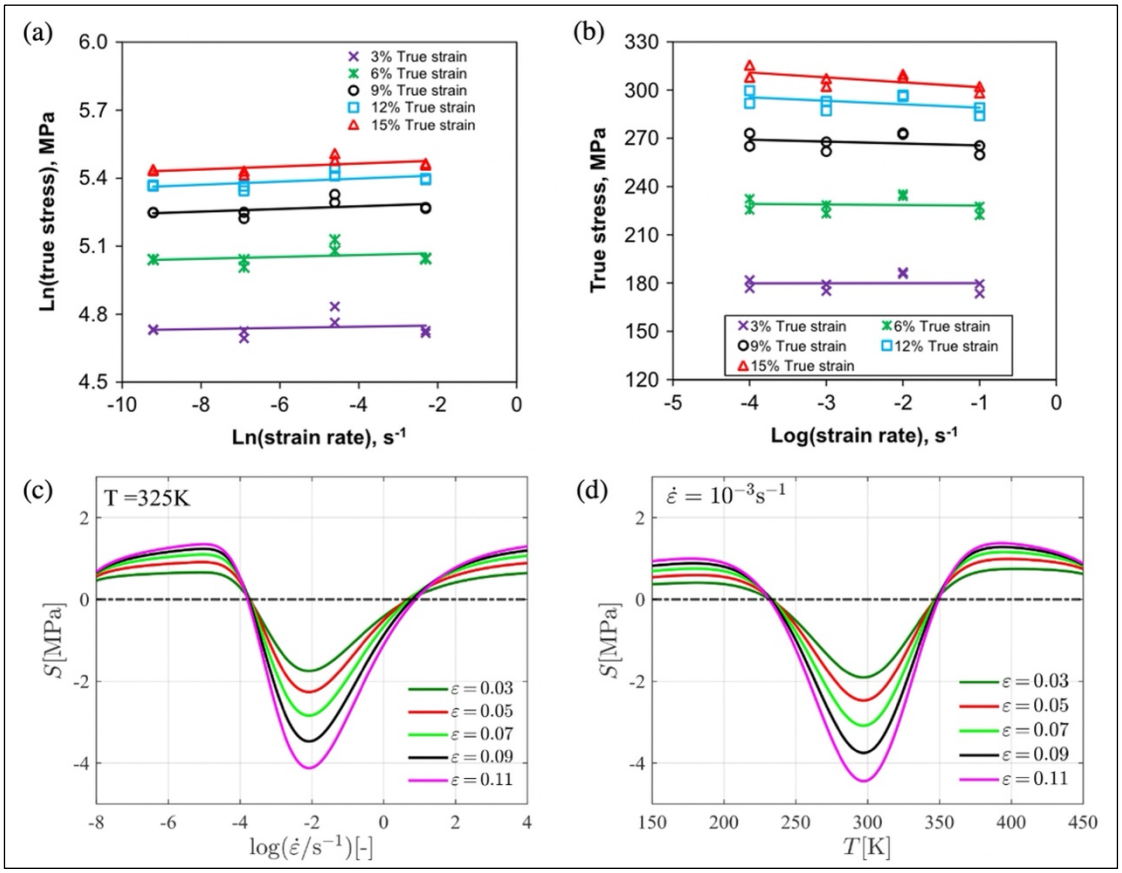

Figure 2.45 Typical Strain Rate Sensitivity Plot using (a) Common Approach (b) Lindholm Approach (c-d) Simulated Mechanical Threshold Stress (MTS) Model (Tahreen et al., 2014; J. Xu et al., 2022)

The SRS of a material can be evaluated using various experimental techniques and subsequent analytical approaches, primarily aimed at determining the exponent of sensitivity. Firstly, common power law approach relies on modeling the flow stress (σ) as the power law function of the strain rate ($\dot{\varepsilon}$) typically expressed as (2.13) or logarithmically as (2.14), where σ is the flow stress, C is a constant and m is the SRS (Tahreen et al., 2014).

$$\sigma = C\dot{\varepsilon}^m \tag{2.13}$$

$$\ln \sigma = m \ln \dot{\varepsilon} + \ln C \tag{2.14}$$

This common approach method is widely used particularly describing the effect of strain rate on flow properties of Mg alloys (Tahreen et al., 2014). The SRS of the alloys could also be evaluated using Lindholm approach that uses a single logarithmic form to relate the flow of stress to the strain rate which derived from thermal activation theory models for the drag of dislocations (Tahreen et al., 2014). The Lindholm approach shows in (2.15), where σ is the flow stress, σ_o is the reference stress (constant) and m_L is the SRS.

$$\sigma = \sigma_o + m_L log\dot{\varepsilon} \tag{2.15}$$

Based on recent research in evaluating cast Mg alloys by N. Tahreen et al. (Tahreen et al., 2014), both common approach and Lindholm approach showed similar trends when evaluating. However, the Lindholm approach appeared to be more sensitive, yielding much larger absolute values for SRS, refer to Figure 2.46.

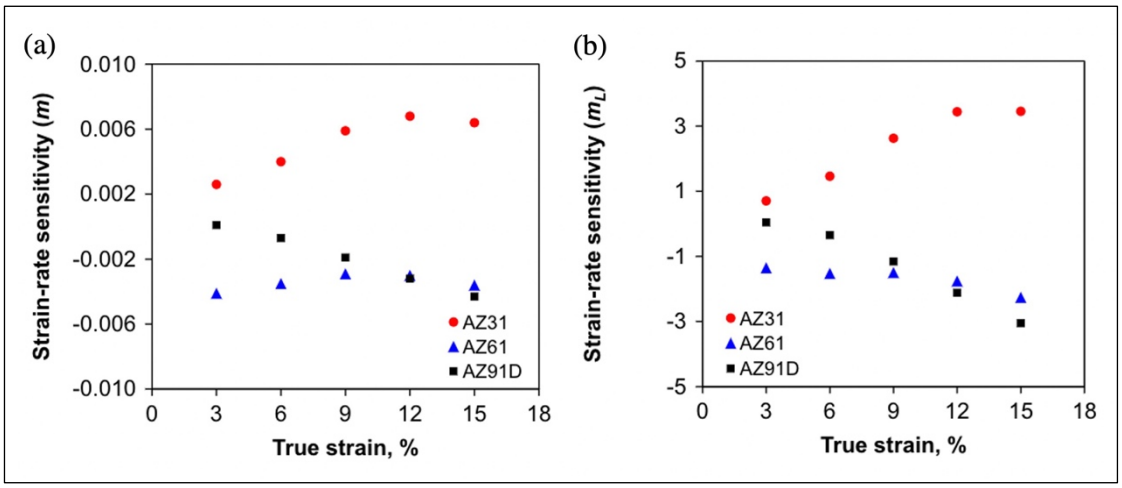

Figure 2.46 Strain Rate Sensitivity using (a) Common Approach (b) Lindholm (Tahreen et al., 2014)

As stated earlier, the understanding of SRS provides a crucial discussion of serrated flow behavior which commonly referred as PLC. This effect manifests as discontinuous yielding or stress oscillations during plastic deformation, particularly within specific ranges of strain rate and temperature. Thus, having established fundamental deformation response through YS, UCS, strain hardening, and SRS becomes essential to further explore the PLC effect stress flow.

2.4.4 Overview of Portevin-Le Chatelier (PLC) Effect

According to the literature by N. Tian et al. (Tian et al., 2024a) the serrated oscillation with increase of the flow strain during plastic deformation including the tensile, compression and torsion at specific temperature and strain rate appeared for metallic materials such as aluminium alloy, nickel-based high temperature alloys, steel, high entropy alloy and magnesium alloys. At lower strain rates, serrations on the stress-strain curve of Al-Mg tend to show larger amplitudes but less frequent, reflecting more time for solute Mg atoms to interact with mobile dislocations. However, at higher strain rates, serrations typically become finer and more frequent, while the overall flow stress increases due to reduced solute diffusion time.

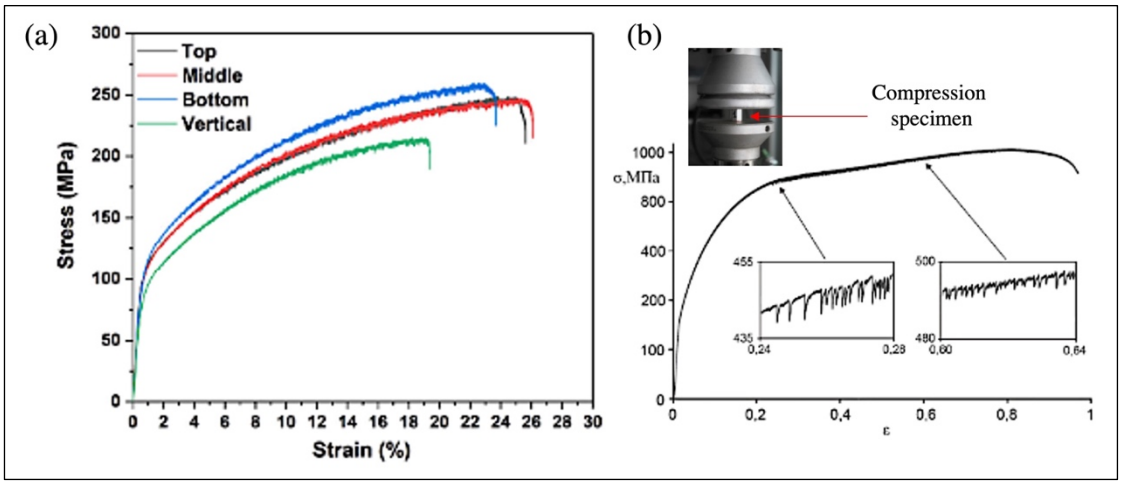

Figure 2.47 Typical Stress-Strain Curve of Al-Mg for Different Mechanical Tests (a) Tensile Strength (b) Compression (Uvarov & Efremov, 2019; J. Wang et al., 2021)

The PLC effect is a phenomenon observed in alloys during plastic deformation, characterized by repetitive yielding or serrations in the stress-strain curve, and localised deformation bands on the sample surface. Referring to the typical stress-strain curves of aluminium alloy in Figure 2.47(a), there are serrated yielding or repetitive stress

increase and decrease throughout the curves that indicates as fluctuation in the plastic deformation region (Bakare et al., 2023). It is a material phenomenon that occurs when the rate at which solute atoms diffuse to mobile dislocations and matches the rate of dislocations move under an applied stress, also refer as dynamic strain aging (DSA). DSA is a mechanism that synchronise to a characteristic form of plastic instability known as PLC effect (Bakare et al., 2023). The cyclical process involving pinning and unpinning of solute atoms in the alloys like magnesium (Mg) in series 5 aluminium alloy. The pinning causes the stress required for continued deformation to increase while unpinning happened when the applied stress reaches a certain threshold, the dislocation manage to break free from the solute atmosphere (Bakare et al., 2023). Figure 2.47(b) shows the repeated cycle of pinning and unpinning manifests as the serrated or jerky flow observed in stress-strain curves after compression on Al-Mg alloy (Cai et al., 2017).

The PLC effect is observed in both tensile and compression tests when the underlying conditions for DSA are met (Uvarov & Efremov, 2019). The fundamental mechanism of solute atom interaction with dislocations remains the same, regardless of the mode of deformation. Similarly to tensile deformation, the same DSA mechanism can operate. For instance, in aluminium foam, the PLC effect has been observed under compression, attributed to the sudden, collective deformation of numerous struts, leading to a chain-like propagation of strain bursts across the material (Knapek et al., 2017). The serrations in compression tests also indicate localized yielding events driven by the pinning and unpinning of dislocations by solute atoms (Uvarov & Efremov, 2019). When dislocations are pinned, the material's resistance to deformation increases, causing a rise in stress. Eventually, dislocations overcome the pinning obstacles, leading to a sudden release of strain and a drop in stress. The schematic illustration of pinning-unpinning formation shown in Figure 2.48.

The type of classification of serrated flows is displayed in Figure 2.49, corresponding to the description of serration in Table 2.11. The serrated flow is classified in terms of ratio of stress, $R_{\Delta\sigma}$, of magnitude of stress peak, $\Delta_{\sigma_{peak}}$ against $\Delta\sigma$ just before stress peak, as schematically illustrated in Figure 2.50. In addition, the PLC effect in tensile tests often show more distinct serration patterns due to localized necking, whereas in compression, the stress drops may be less sharp due to homogenous

strain distribution and absence of necking. The PLC effect occurs in materials with Mg content which alloying element in many aluminium alloy (Cai et al., 2017).

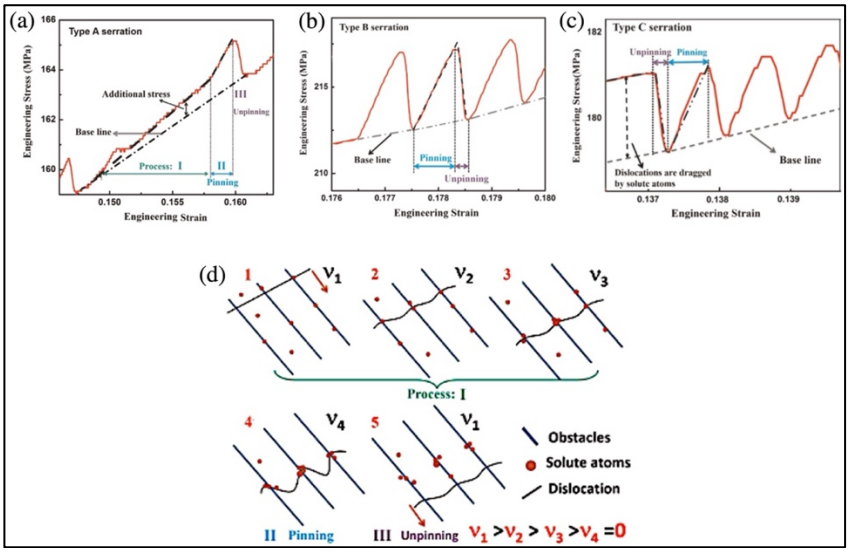

Figure 2.48 Type of Serrated Flow (a) Type A (b) Type B (c) Type C (d) Schematic Illustration for Mobile Atom Dislocation of Type A Serration (W. H. Wang et al., 2016)

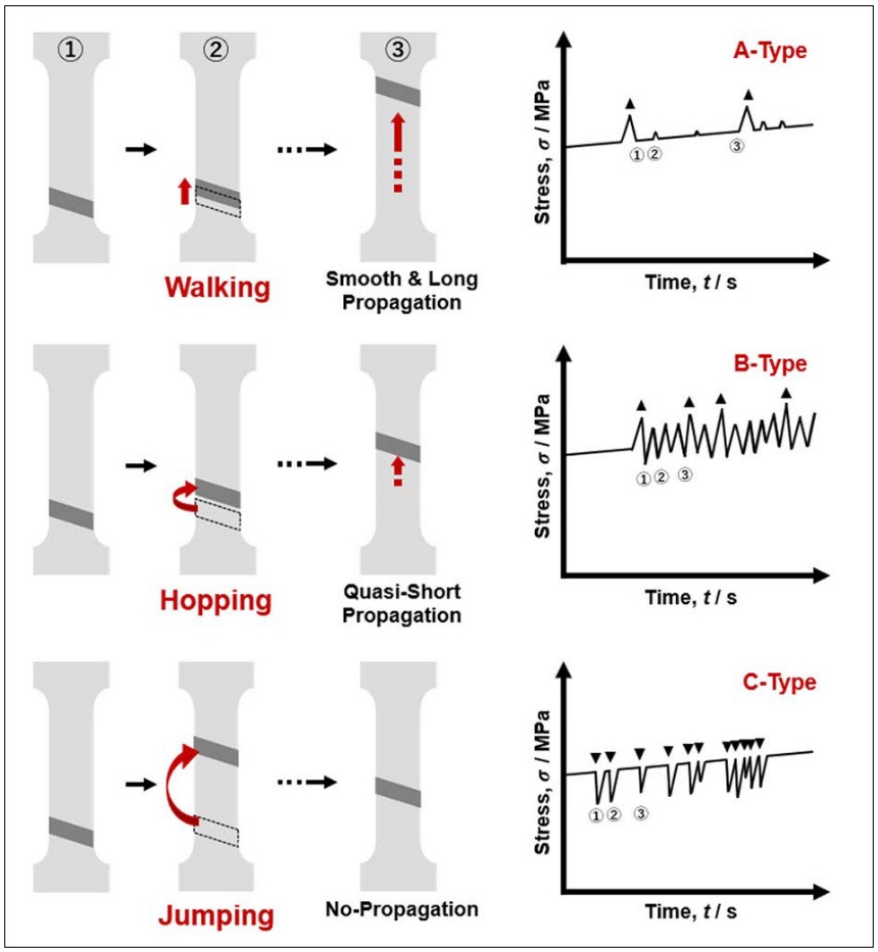

Figure 2.49 Schematic Illustration for Three Types of PLC Bands Propagation Corresponding Serration Behavior (Lee et al., 2023)

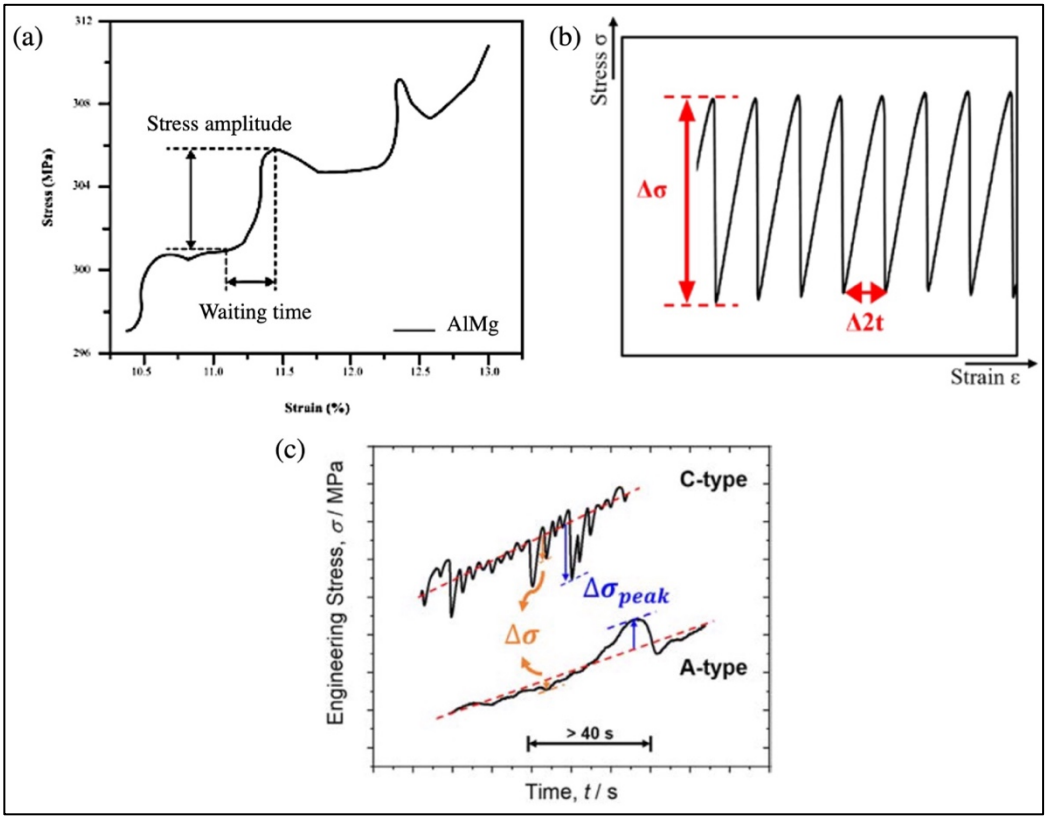

Figure 2.50 (a) Schematic of the Stress Amplitude and Waiting Time (b) Definition of Stress Drop and Reloading Time (c) Schematic Illustration for the Quantitative Method of Serrated Flow (Bakare et al., 2023; C. Guo et al., 2025; Lee et al., 2023)

In Al-Mg alloys, the Mg diffuse within the aluminium lattice and segregate to dislocations, where the segregation strengthens the pinning effect on dislocations. This is the key to PLC effect, hence, higher Mg concentration generally led to more pronounced DSA effects and more significant serrations (Cai et al., 2017). For instance, the studies in Figure 2.51 show the increment of Mg content generally amplifies the PLC effect by increasing the stress-drop amplitude and modifying strain periods. In addition, the clustering of Mg atoms and the formation of intermetallic particles, for instance, Mg_2Al_3 become more significant (Uvarov & Efremov, 2019). These factors enhance the pinning effect on dislocations, leading to larger stress-drop amplitude and increase in critical strain required for PLC effect to initiate (Tian et al., 2024). This means that higher Mg concentrations generally promote a more pronounced PLC effect, occurring over a wider range of strains. In addition, the Mg content can also influence the type of PLC deformation bands, in which higher Mg content leads to stronger DSA and increased waiting times for dislocations, favours a switch in band propagation from continuous (Type A) to hopping (Type B) (Ait-Amokhtar et al., 2015).

Table 2.11
Types of Serration Flow (Lee et al., 2023)

Type	Descriptions	Stress ratio, $R_{\Delta\sigma}$
A	Characterized by periodic stress peaks followed by a drop to a general level of the stress-strain curve. In terms of PLC behavior, band nucleates at one end of the gauge part and propagates smoothly to the opposite end. The smooth propagation results in a large stress peak upon nucleation, followed by smaller stress fluctuations during propagation.	≥ 2.5
A + B	Intermediate condition between type A and type B. Characterized by stress fluctuations that are irregular, with a higher amplitude than A-type but less dense than B-type serrations. In PLC behavior, the propagation is also intermediate, described as 'quasi-propagation'. The PLC band nucleation is narrow spacing, and the stress fluctuations are mix of the larger peaks seen in A-type and the oscillation in B-type.	≥ 1.5
B	Characterized by stress oscillations around the general level of stress. Observed under intermediate conditions of strain rate and temperature. The PLC band behavior involves hopping propagation, where PLC bands nucleate in isolated regions near previous band, leading to discontinuous propagation. Results in relatively large stress peaks with smaller, denser stress fluctuations between them.	≥ -1.5
B + C	Transition phases involve characteristics of both B-type (humping) and C-type (jumping) mechanism. Possibly with the band starting to nucleate more randomly as the transition towards C-type progresses.	≥ -2.5
C	Characterized by an initial drop in stress, followed by a rise to the general level of stress. Tends to appear at lower strain rates or higher temperatures. The PLC bands nucleate randomly within the gauge part in a jumping manner without a significant propagation. Leads to jump-down simultaneous nucleation of localized PLC bands.	< -2.5

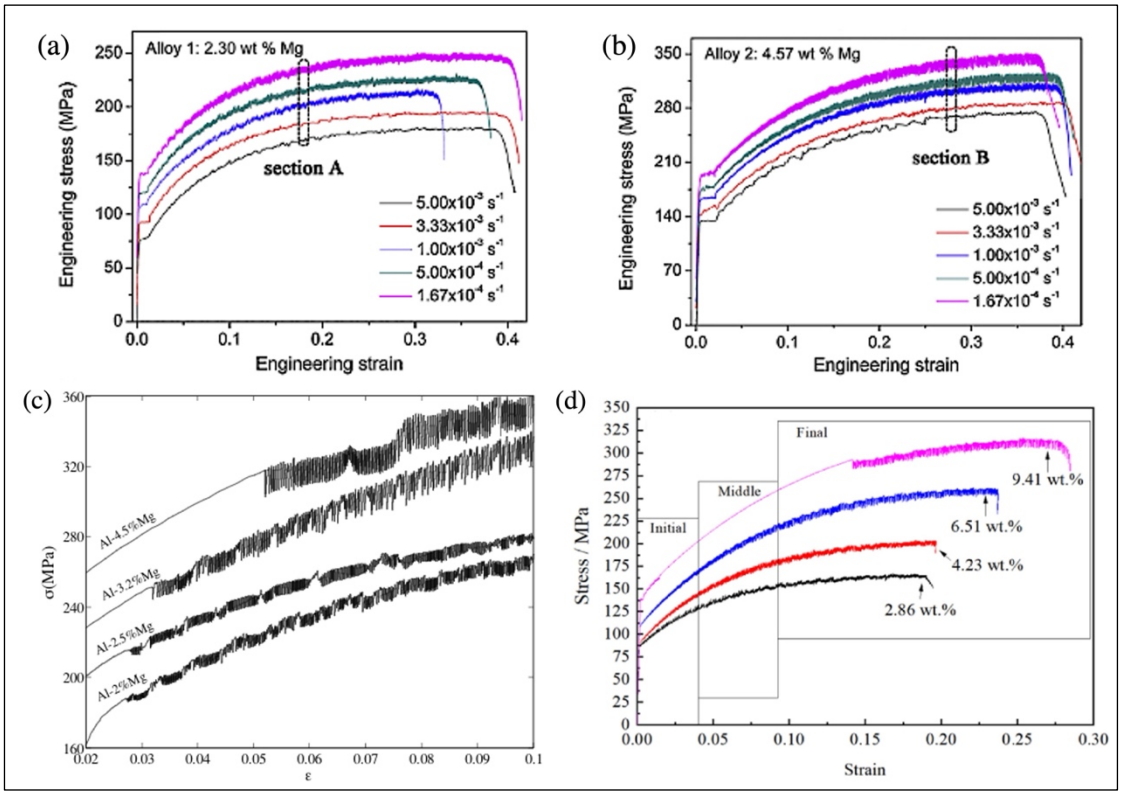

Figure 2.51 Serrated Stress-Strain Curves of Al-Mg at Different wt% (a) 2.3% (b) 4.57% (c) 1 – 4.5% (d) 2.86 – 9.41% (Ait-Amokhtar et al., 2015; Cai et al., 2017; Tian et al., 2024)

There is another factor that influenced PLC effects in Al-Mg alloys. Temperature significantly affects the diffusion rate of solute atoms. At higher temperature, solute atoms diffuse more rapidly, which can either promote or inhibit the PLC effect depending on the strain rate and the specific stage of DSA, refer Figure 2.52 (J. Xu et al., 2022). Besides that, the type of serration observed (A, B, and C) is strongly dependent on temperature. As the temperature increases, the tendency of serration types to transition from A to B and then C, in decreases in strain rate (W. H. Wang et al., 2016). At elevated temperatures, the DSA process which causes the PLC effect can lead to embrittlement in Al-Mg alloys, characterized by reduced elongation and (Niu, Kou, Zhang, Wang, & Li, 2017). Strain rate is another factor that affects the PLC effect in Al-Mg. Strain rate directly influences the mobility of dislocations and the time available for solute atom diffusion. The PLC effect occurs when the rates of these two processes become comparable (Tian et al., 2024b). Similar to temperature, strain rate also dictates the type of serrations observed. Higher strain rates generally favour Type A serrations, while lower strain tend to produce Type C serrations, with Type B in between (Tian et al., 2024b).

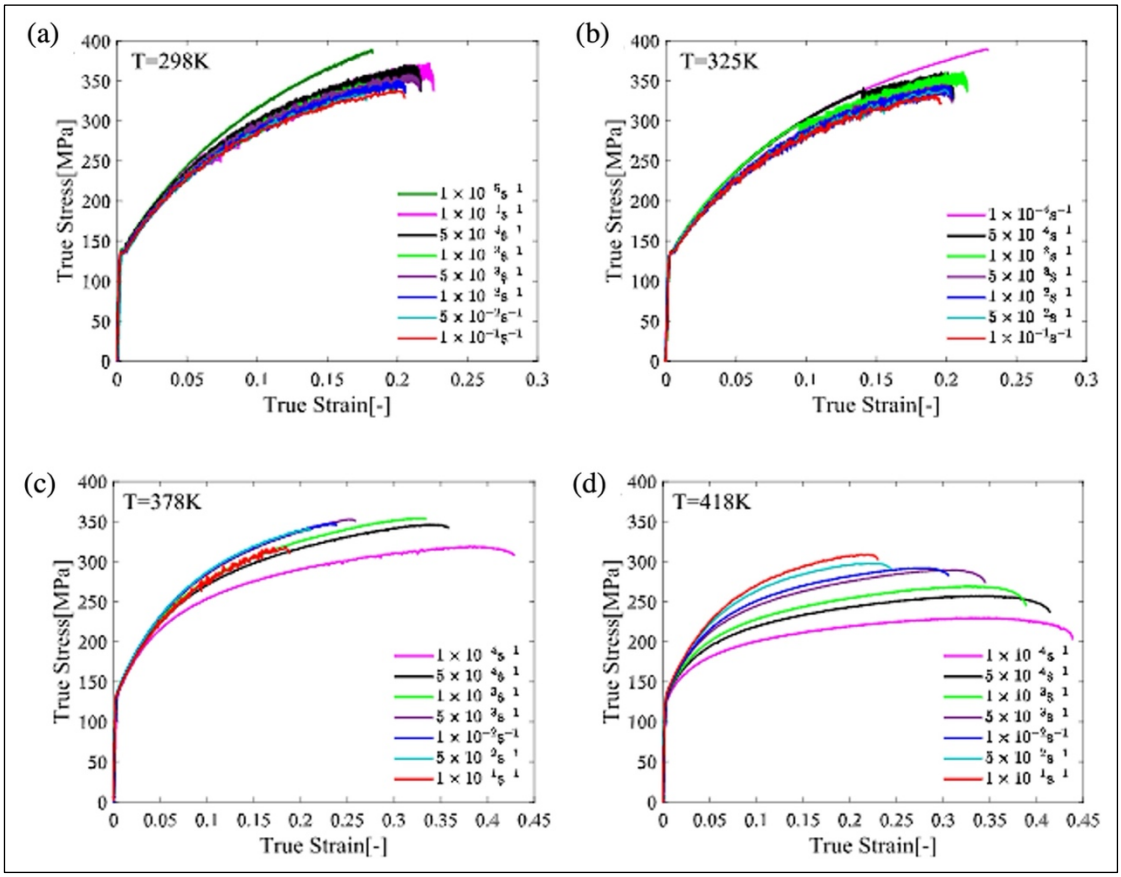

Figure 2.52 Stress-Strain Curves of AA5182 at Different Strain Rates and Temperature (J. Xu et al., 2022)

To identify severity of PLC effect, can be characterized primarily by the amplitude of stress drops and the number of stress drops (frequency) along the strain (Y. Wang et al., 2022). However, the amplitude of stress drops correlates more directly with the magnitude of localised strain burst and energy release during PLC effects, reflecting the intensity of severity of individual serrations (Barannikova & Nadezhkin, 2021). The amplitude of stress drops directly quantifies the magnitude of jerky-flow in localised regions (Tian et al., 2024a). Larger amplitude of stress drops implies greater localised plastic instability and a more significant deviation from uniform deformation. This directly affects the work hardening capacity and can lead to earlier necking or fracture (Tian et al., 2024a). Higher amplitude of stress drops also associated with stronger interactions between solute atoms and dislocations also become greater for pinning precipitate, which are the fundamental drivers of the PLC effect. In addition, the amplitude of stress drops can cause more pronounced surface defects and reduce overall formability of the material, where higher amplitude of stress drops means a large sudden release strain and lead to localised failure. Hence, to describe and define the PLC severity, the amplitude of stress drops is more indicative of the severity and

instability, while the frequency of stress drops indicates repetition of the PLC effect during the deformation (Tian et al., 2024a).

The PLC effect in Al-Mg alloys generally results in a negative feedback mechanism in terms of mechanical properties, though the relationship can be complex. Since PLC effect is characterized by jerky flow and localised deformation bands, which are forms of plastic stability, the instability leads to a reduction in ductility and an increase in surface roughness, where can be undesirable for manufacturing processes (Tian et al., 2024b). The serrations, particularly the stress drops, indicate a loss of strain hardening capacity in localised regions (Tian et al., 2024b). This means that instead of uniformity hardening, the material undergoes localized yielding, which can prematurely lead to failure or reduced overall formability. The PLC effect appears on stress-strain curves due to several factors: serrated yielding, stress amplitude, waiting time and direct observation. Theoretically, reducing the severity of the PLC effect in series 5 aluminium alloy (Al-Mg) leads to decrease in magnitude and number of stress drops. It also associated with an improvement in surface quality of the aluminium alloy (Bakare et al., 2023).

2.5 Summary of Literature Review

Based on Figure 2.53, although aluminium WAAM has been widely studied, existing research mainly focus on isolated manufacturing process with investigation on microstructure or basic mechanical properties, which hybrid of WAAM remains underexplored. As listed in Table 2.12 the study of WAAM that incorporate with post deposition cold forging remains limited. Based on the mapping, majority of the existing studies rely on experimental investigation, whereas fewer work incorporates numerical simulation approaches. Moreover, most of FEM-based focus on deposition process, without considering the influence of subsequent deformation behavior after cold forging. As a result, the combined effects of WAAM and cold forging on porosity, residual stress redistribution and mechanical response on aluminium remain limited investigation. This gap highlights the need for a systematic evaluation of surface integrity and mechanical properties of WAAM and WAAM-forged aluminium using coupled numerical simulation and experimental validation.

To address this limitation, the incomplete understanding of surface integrity evolution also restricts insight on WAAM-forged aluminium responds under mechanical loading. Table 2.12 indicates that mechanical characterization in WAAM related studies is focus to tensile testing that conducted at a single or limited strain rate. While compression behavior directly reflects the deformation mode during cold forging is seldom examined. In WAAM, the microstructure produced are further modified by cold forging, suggesting that strain hardening behavior may differ from conventionally processed alloys. However, the influence of strain rate on compressive strain hardening in WAAM-forged Al-Mg alloys has not been systematically investigated, leaving a critical gap in understanding the deformation mechanisms governing hybrid WAAM-forging processes.

This unresolved issue of strain-rate-dependent mechanical insights further limits the PLC effect which is increasing reported in aluminium studies. While previous research identifies stress serration during plastic deformation, their analysis remains largely qualitative, which focusing on occurrence rather than quantification. Therefore, without a clear understanding of influence of strain rate governs strain hardening behavior, it is not possible to robust relationship between stress drop characteristics and deformation conditions of WAAM-forged aluminium. Hence, the combination as highlighted in blue color of Table 2.12 are not done yet by other researchers.

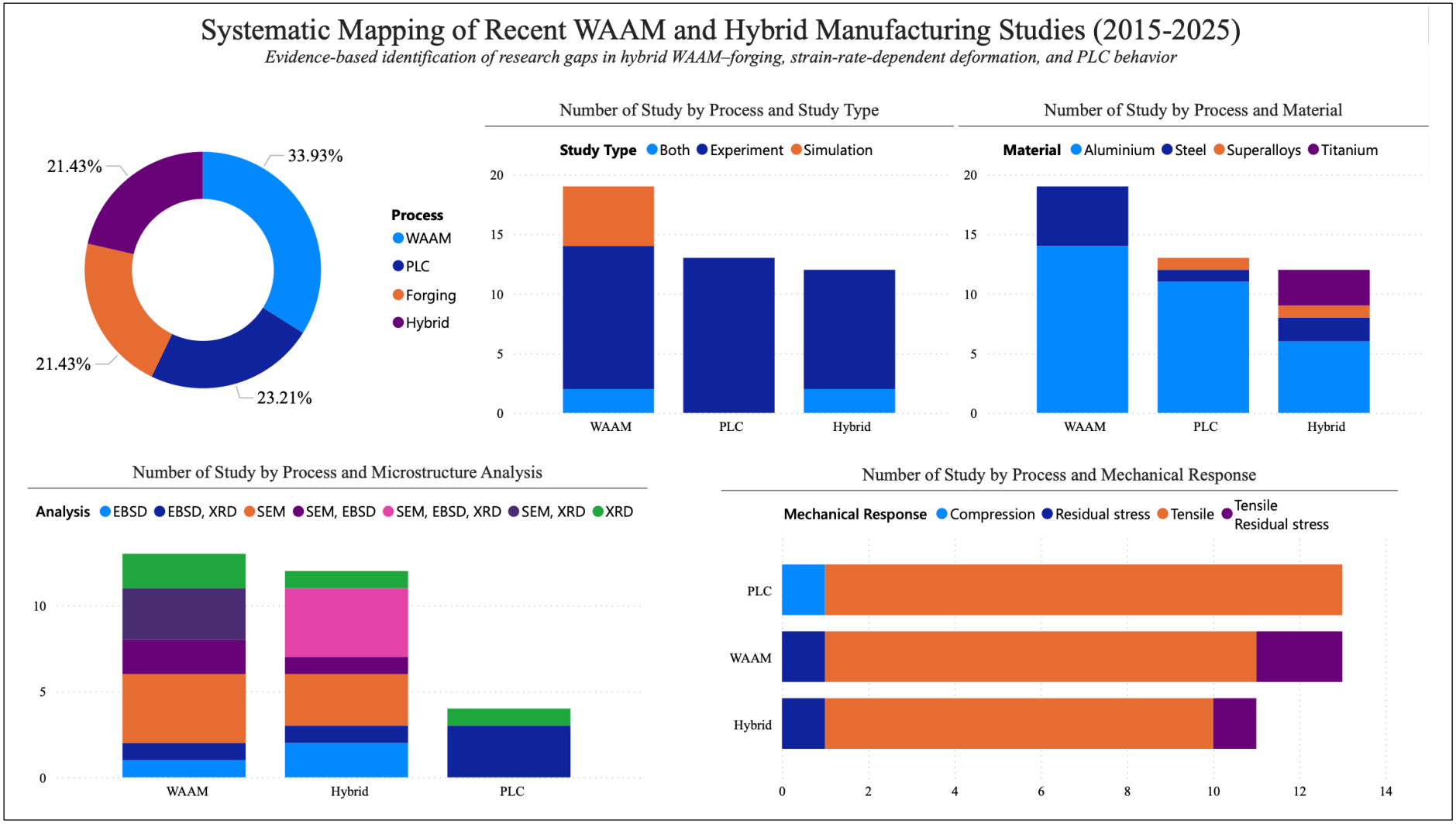

Figure 2.53 Overview of Research Trends in WAAM and Hybrid Manufacturing Studies (2015-2025)

Table 2.12
Summary of recent research (2023-2025) on WAAM-Hybrid and PLC Effect

Material			Process			FEM			Forging			Microstructure			Mechanical Performance				PLC	
Aluminium	Steel	Superalloy	WAAM	Hybrid	Thermal	Distortion	Residual stress	SW	Cold	Hot	SF	Porosity	Grain	Texture	Phase	UTS	YS	Elongation	Residual stress	Stress drop
(Zuo et al., 2025)																				
/			/												/	/	/	/		
(Sahul et al., 2025)																				
/			/									/								
(Kesarwani et al., 2024)																				
/			/									/	/		/	/	/		/	
(Singla et al., 2024)																				
/			/										/	/	/	/		/		
(Saravana Kumar et al., 2024)																				
/			/									/				/				
(K. Zhu et al., 2024)																				
/			/									/	/			/	/	/		
(Hu et al., 2023)																				
/			/										/			/	/	/		
(Wieczorowski et al., 2023)																				
/			/									/				/	/	/		
(Chandra et al., 2023)																				
/			/									/			/	/	/	/		
(J. Huang et al., 2024)																				
/				/								/	/	/	/	/	/	/		
(J. Huang et al., 2023)																				
/				/								/	/		/	/	/	/		
(Karlina et al., 2024)																				
	/			/								/				/	/	/		
(W. Li et al., 2023)																				
/				/								/							/	

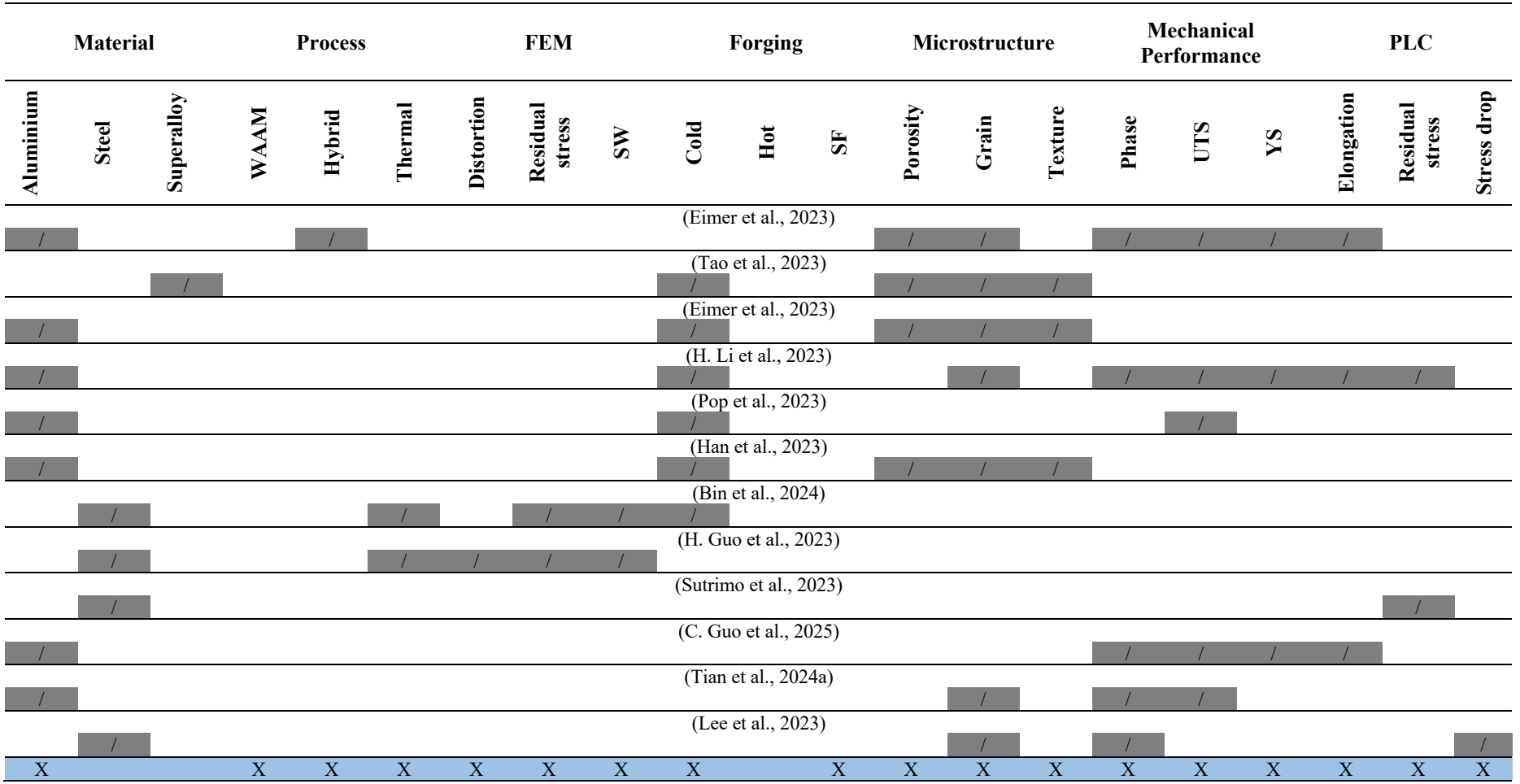
Material
Process
FEM
Forging
Microstructure
Mechanical Performance
PLC
Aluminium
Steel
Superalloy
WAAM
Hybrid
Thermal
Distortion
Residual stress
SW
Cold
Hot
SF
Porosity
Grain
Texture
Phase
UTS
YS
Elongation
Residual stress
Stress drop
(Eimer et al., 2023)
(Tao et al., 2023)
(Eimer et al., 2023)
(H. Li et al., 2023)
(Pop et al., 2023)
(Han et al., 2023)
(Bin et al., 2024)
(H. Guo et al., 2023)
(Sutrimo et al., 2023)
(C. Guo et al., 2025)
(Tian et al., 2024a)
(Lee et al., 2023)

CHAPTER 3
RESEARCH METHODOLOGY

3.1 Introduction

This chapter presents the structured research method used for fabrication, processing, and characterization of WAAM and hybrid manufacturing WAAM-forged samples. The analysis incorporates the GMAW and CMT processes for the AM of ER5356 aluminium alloy onto Al6061 alloy substrate. A full description of the fabrication parameters such as material and sample preparation, heat input control, and deposition strategy is provided to ensure the consistency of the processes. The parameters of WAAM and WAAM-forged were simulated using finite element method of Simufact software. The process chain parameters involving SW and SF. After performing WAAM, the deposited thin wall structures were subjected to an upsetting cold forging process to enhance material density, microstructural uniformity, and mechanical properties. The forging was carried out using 6% height reduction with a contact pressure of 390.65 MPa from a 1000 kN punching power press machine. The specific range of contact pressure was chosen to control excessive deformation, bending and cracking of the samples while still maintaining structural integrity.

To evaluate the impact of WAAM and hybrid WAAM-forging on the Al-Mg alloy, scanning electron microscopy (SEM) and electron backscatter diffraction (EBSD) are used for microstructural analysis and deformation, XRD for residual stress and phase identification including comprehensive mechanical properties were carried out. The evaluation was made with compressive tests at several strain rates at $0.0001s^{-1}$ to $0.1s^{-1}$. These investigations were conducted with the purpose of designing adaptable and overall performance of WAAM as-built and WAAM-forged Al-Mg aluminium alloy samples. This chapter provide a step-by-step description of the WAAM and WAAM-forging. Figure 3.1 illustrated the overview process flow of the research methodology involved in the study.

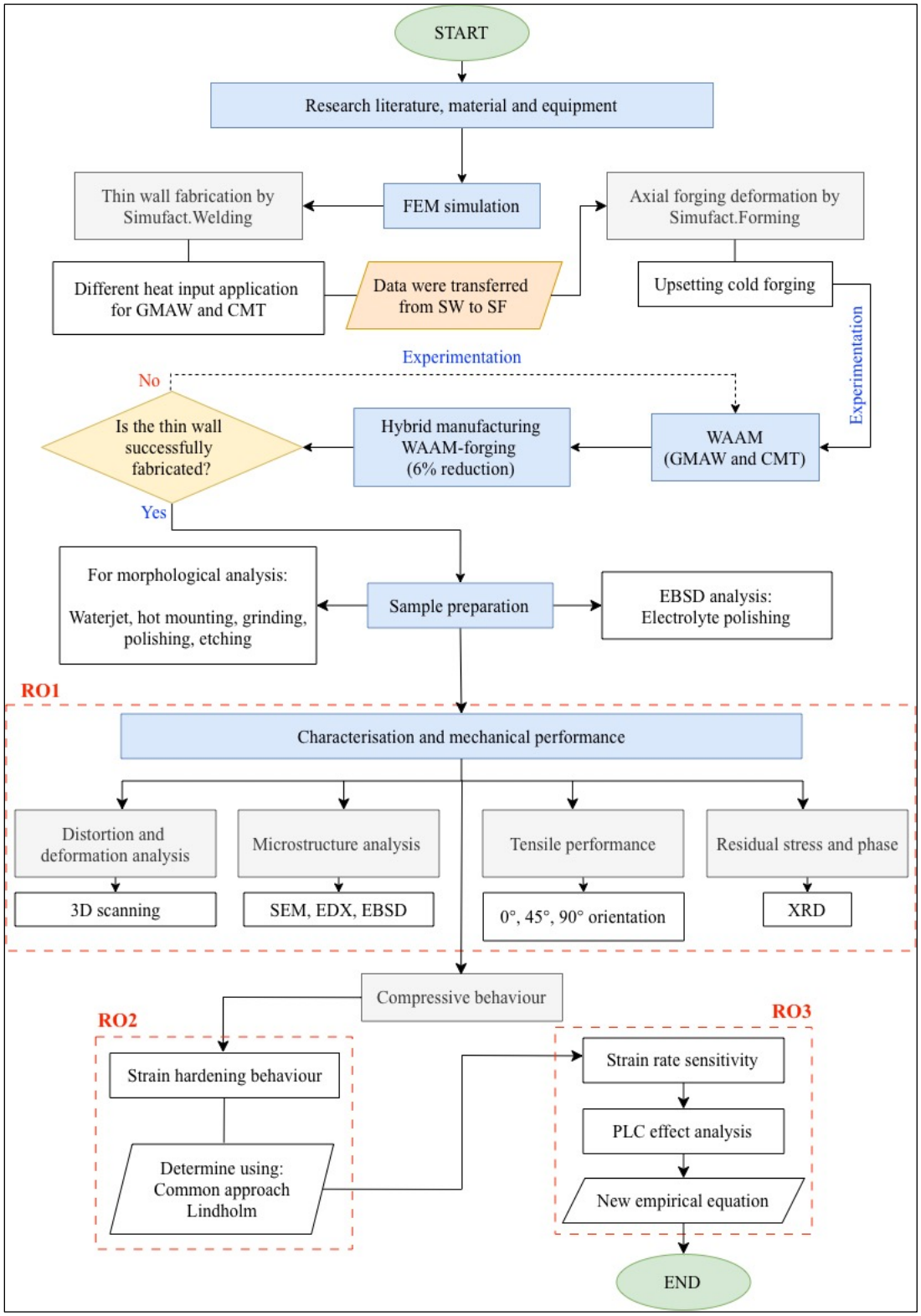

Figure 3.1 Overview of the Research Methodology

3.2 Material

The material employed in the research work is the series 5 and series 6 aluminium alloy, ER5356 and Al6061. The wire filler ER5356 used was 1.2 mm diameter and Al6061 substrate plate with 130 mm x 60 mm x 25.4 mm (L x W x H) dimension. ER5356 is a solid wire for GMAW that consisting of up 5% Mg. Compared with other aluminium alloys, the Mg element act as crucial strengthening element, improves the strength and the corrosion of Al-Mg alloys (Y. Liu et al., 2022). It is classified general-purpose filler alloy due to the presence of various properties such as ductility, corrosion resistant, formability, recyclability, and high electrical conductivity (Vijayakumar et al., 2020). In addition, the material of 5356 aluminium alloy provides good weldability and corrosion resistance which widely used in automotive, ship building, aeronautical engineering and additive manufacturing (Wieczorowski et al., 2023).

Table 3.1 gives the above elemental compositions of the wire and substrate accordingly to the standards EN ISO 18273:04 while Table 3.2 shows the mechanical and physical properties for all processes. The substrate of series 6 aluminium was chosen as a typical aluminium alloy to ensure good weldability and thermal conductivity (Köhler et al., 2020). The intermetallic compound in 6061 aluminium alloy generally well-controlled during heat treatment which making it eligible for high deposition rate process in WAAM structural application (Doumenc et al., 2022). The chemical composition analysis was examined by using energy-dispersive X-ray (EDX) using Team™ EDS Software Suite at Material Science Lab, Faculty of Mechanical Engineering, UiTM Shah Alam. Figure 3.2 shows the wire filler and substrate used in the research work.

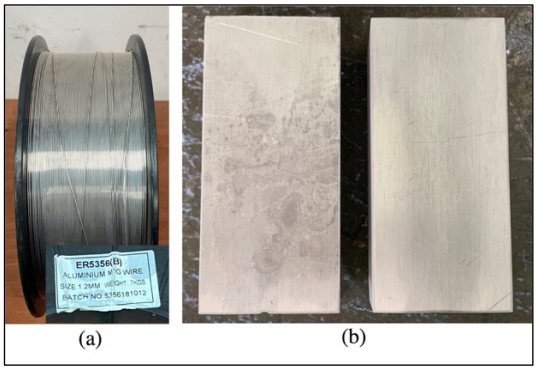

Figure 3.2 (a) ER5356 Wire Filler on Workpiece Stage (b) Uncleaned (Left) and Cleaned (Right) of Al6061 Substrate

Table 3.1
The Chemical Composition of ER5356 and Al6061

Element	Si	Fe	Cu	Mn	Mg	Cr	Zn	Ti	Al
ER5356	0.62	0.36	0.81	0.29	5.12	0.64	0.77	0.31	Bal.
Al6061	0.10	0.20	0.30	0.10	5.00	0.70	0.20	-	Bal.

Table 3.2
The Mechanical and Physical of ER5356 and Al6061

Tensile Strength	Yield Strength	Elongation	Melting Range	Density
270 MPa	120 MPa	25 ($L_o = 5d_o$)	575 – 633 ($°C$)	2.640 (kg/m^3)

3.3 Numerical Modeling of Distortion and Residual Stress in WAAM and Process Chain WAAM-Forming Process

3.3.1 Formation Analysis using Simufact.Welding (SW)

SW is a finite element-based software for welding simulation that suitable for modeling the elastic, plastic and hardening material. Hence, SW can simulate the welding structures. SW was designated to predict welding distortions through standard implementation of predefined materials and material model. Figure 3.3 shows the overall process flow for welding simulation using SW. The first stage of the simulation was geometrical design using MSC Marc Mentat 2022.1 software version. Five sizes of meshes were investigated on the bead surface formation; refer Figure 3.4. The substrate was an adapted form of the refinement mesh, and the meshes on the substrate were paired with a constant hexahedral element in the thin wall. According to the plot reported in Figure 3.5, high meshing smoothness and fine-quality meshing produced more accurate results for the simulation process. However, the simulation takes longer computational time to complete the analysis. The highest computational time is observed on 4 mm nodes mesh achieved 3.47 mm total displacement with 2.25 hours' time, while 8 mm nodes mesh achieved 4.38 mm total displacement in 1 hour simulation time.

The mesh refinement was stopped at 4 mm because further refinement was expected to increase computational cost and convergence difficulty without providing a proportional improvement in the predicted thermal–mechanical response. The 5 mm mesh size was selected instead of the 4 mm mesh because it provided a more stable and efficient numerical solution for the subsequent welding simulations. Although a finer 4

mm mesh may provide higher spatial discretisation, it also increases the computational demand and may lead to longer solving time without producing a significant improvement in the overall simulation response. In this study, the 5 mm mesh with 936 nodes was able to achieve better iterative convergence within 1.58 hours, while still providing sufficient mesh refinement to capture the thermal–mechanical response of the WAAM thin wall. Therefore, the 5 mm mesh was considered the optimum compromise between computational efficiency, solution stability, and modeling accuracy.

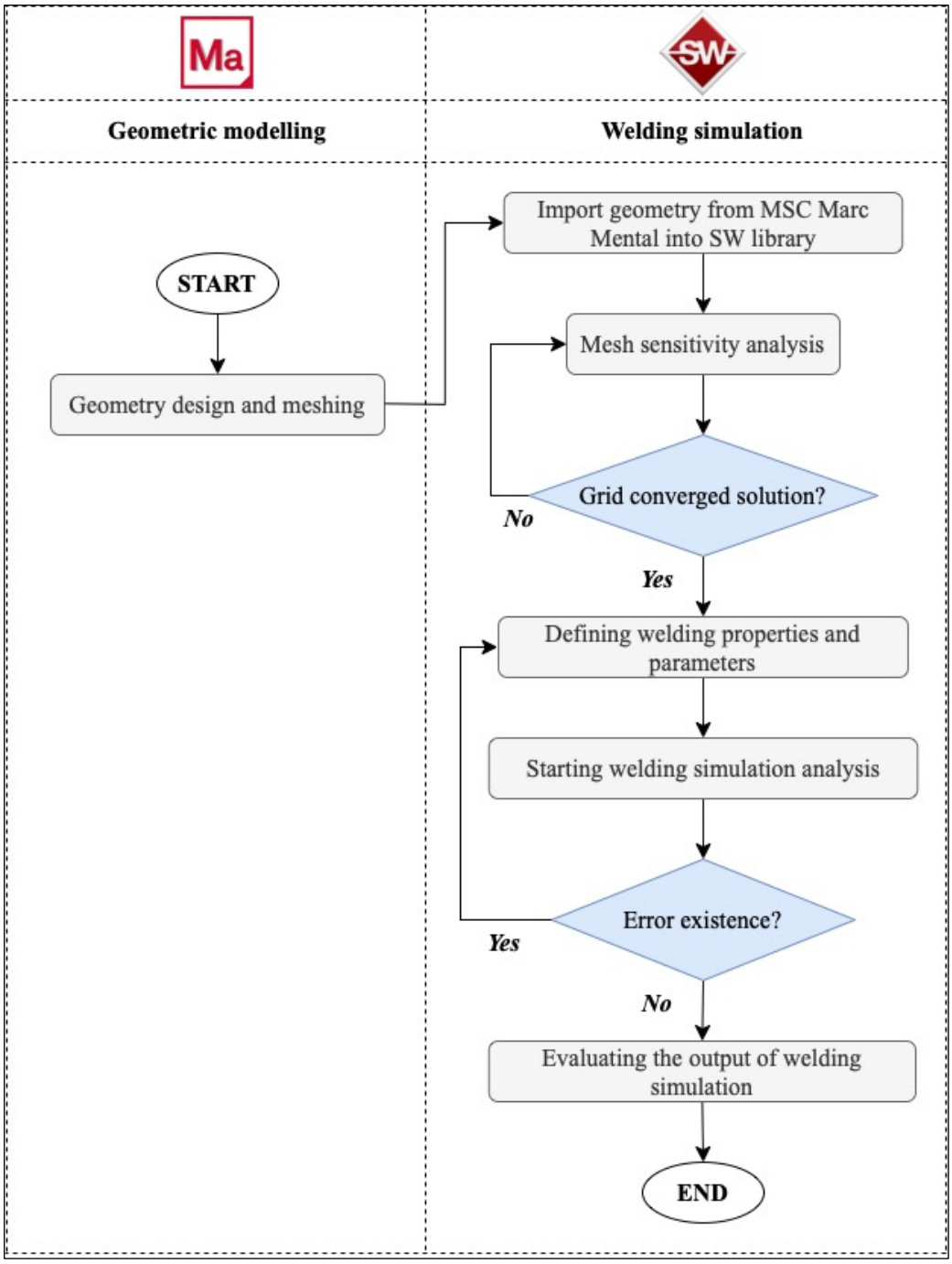

Figure 3.3 Detailed Flowchart of Welding Process using SW

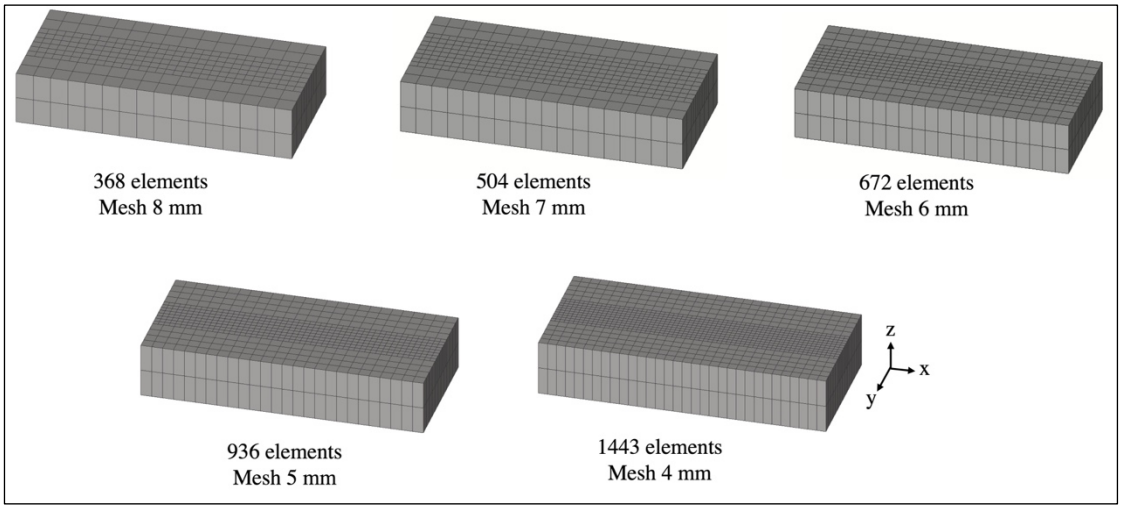

Figure 3.4 Investigated Mesh Sizes using 4 mm, 5 mm, 7 mm and 8 mm with Refinement Mesh of 2 mm on Bead Formation Surface

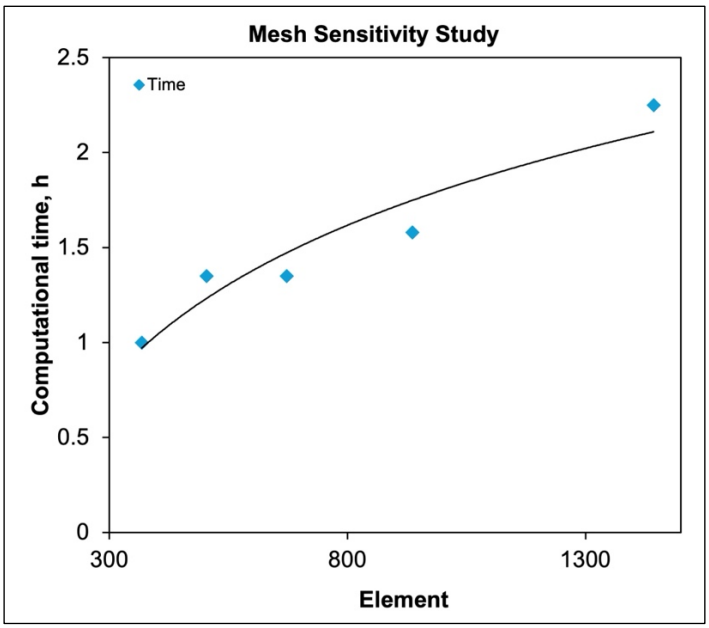

Figure 3.5 Mesh Sensitivity Study of Substrate in SW

Two different modeling setups were assigned for GMAW and CMT to reflect their actual experimental configurations, particularly in terms of clamping condition, heat input strategy, and process-specific arc behavior, ensuring that the simulated deformation and stress responses represent the physical WAAM conditions more accurately. Although CMT has been reported in the literature to offer superior thermal control and deposition stability compared to GMAW, both processes were investigated in this study to establish an experimental and simulation-based baseline comparison under the specific ER5356 WAAM condition, thereby providing a clear justification for selecting CMT for the subsequent hybrid WAAM-forging process.

The completed assembled models in SW shown in Figure 3.6 were set up for the bead geometry modeling. The bearing and clamping were designated in two dimensions for different WAAM processes; GMAW and CMT, based on actual experimental equipment. Hence, there are two types of clamping involved in this research work: cylindrical and cuboidal clamps. The clamping was set up as in Figure 3.7. Each assembled model was designated with the inclusions of bearing, substrate, clamping and multi-layer weld bead formation.

The wire filler is being deposited using bidirectional strategies; see Figure 3.8. This deposition strategy helps in settling the weld beads in the previous layer, which results in better surface equity and less warping as the deposition is completed (S. Singh et al., 2021). The interlayer waiting time takes 4 seconds before starting with a new layer deposition to ensure stable growth of formation during the welding process (Arana et al., 2021). The material selected for the welding simulation was same as in Table 3.1, where the thermochemical material properties used are based on SW databases material library. While Table 3.3 and Table 3.4 present the geometry dimension in SW includes the process parameters applied.

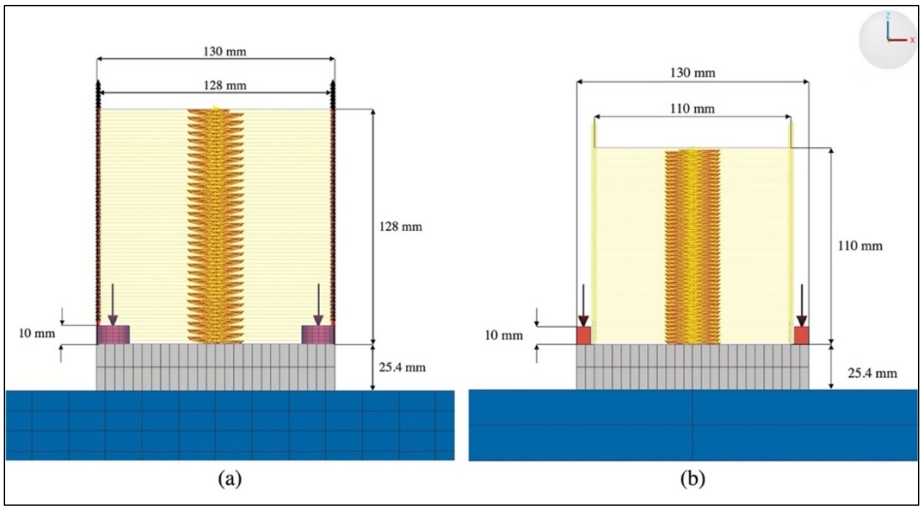

Figure 3.6 Geometry Setup in SW; (a) GMAW, (b) CMT

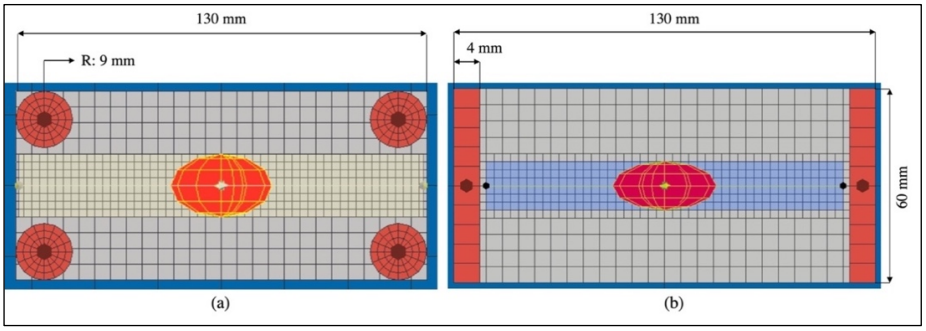

Figure 3.7 Clamping (a) Four Cylindrical Clamps of GMAW (b) Two Cuboidal Clamps of CMT

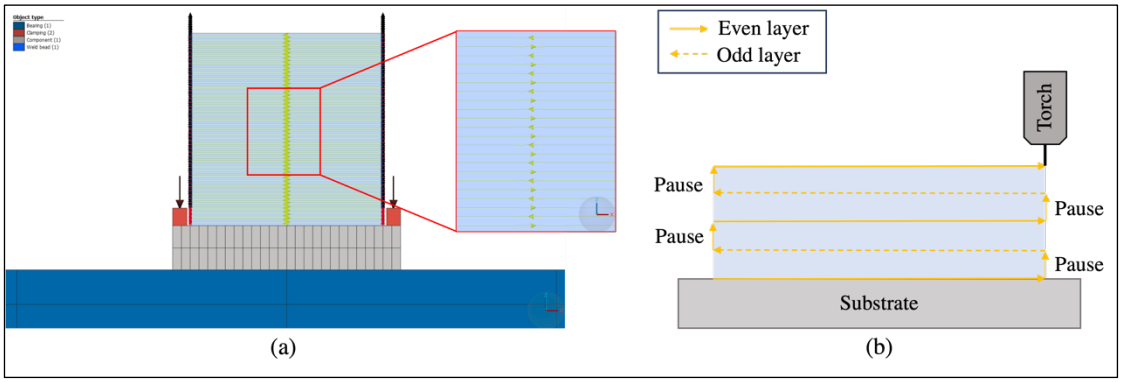

Figure 3.8 (a) WAAM Multi-layers in Directional Movement-Based Deposition (b) Arc Path and Pause in WAAM

Table 3.3
The Geometry Dimension for Different Welding Type

Properties	GMAW	CMT
Substrate, mm	130 x 60 x 25.4 (L x W x H)	
Thin wall, mm	128 x 20 x 128 (L x W x H)	110 x 15 x 110 (L x W x H)
Clamping, mm	Cylindrical: 10 (H), 9 (R)	Cuboidal: 4 x 60 x 10 (L x W x H)
Bearing, mm	600 x 500 x 44 (L x W x H)	900 x 1400 x 35 (L x W x H)
Number of layers	100	65

Table 3.4
The Welding Parameters Assigned in SW

WAAM	Clamping	Layer	Heat Input	Electrical Parameter			
				Velocity	Current	Voltage	Efficiency
GMAW	4	1 – 65	2970.51 J/cm	7 mm/s	152.0 A	17.1 V	0.8
CMT	2	1 – 33	2962.40 J/cm	7 mm/s	161.0 A	16.1 V	0.8
		34 – 66	2961.94 J/cm	7 mm/s	159.0 A	16.3 V	0.8
		67 – 99	2924.69 J/cm	7 mm/s	157.0 A	16.3 V	0.8

To investigate the thermal behavior and temperature distribution during the fabrication of thin wall structures, two different deposition processes were simulated to reflect the experimental conditions. Thus, to accurately represent the heat input and its effect on thermal field, the heat flux distribution in the melt pool using Goldak's double

ellipsoidal, which depicts the heat power density from an electric arc penetrating the existing surface, is analyzed for deep penetration welds. The model could replicate the realistic three-dimensional heat distribution in and around the weld pool; refer to Figure 3.9. The Goldak's model simulates the movement of the heat source along the deposition path, accounting for spatial and temporal temperature variations in the thin wall component during and after each layer is deposited. A summary of the parameters used for both GMAW and CMT process simulations is presented in Table 3.5. These values define the shape and intensity of the heat source used in the simulation, enabling the prediction of the melt pool behavior, cooling rates, and thermal cycles during the WAAM process. Figure 3.10 shows overall parts with boundary condition simulated in SW.

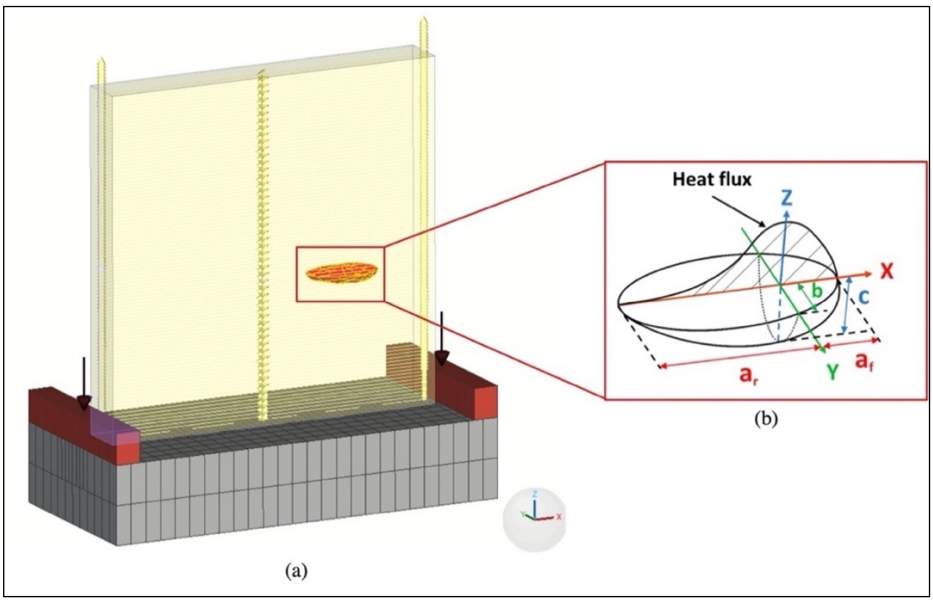

Figure 3.9 (a) Heat Source Modeling in CMT Geometry (b) Goldak's Double Ellipsoidal Heat Source Model (Fisher et al., 2021)

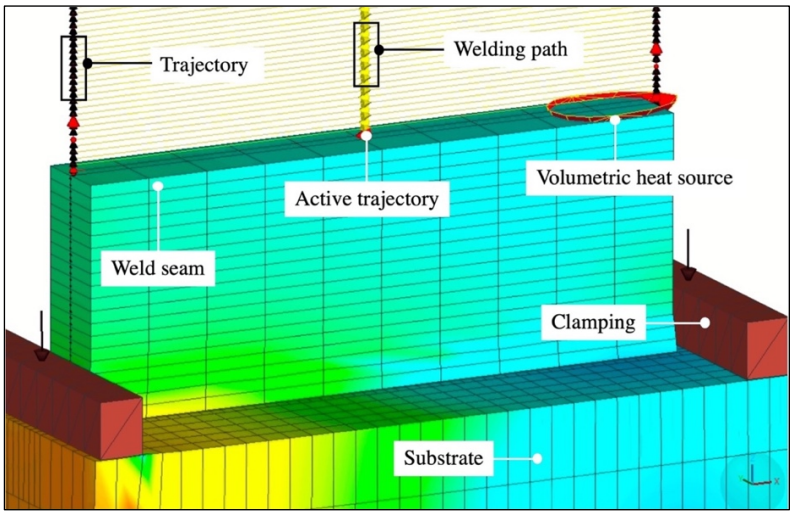

Figure 3.10 Simulation Environment with Boundary Condition in SW

Table 3.5
Goldak Heat Source Dimensions Used in SW

Process	Front length, a_f (mm)	Rear length, a_r (mm)	Width, b (mm)	Depth, c (mm)	Gaussian parameter (mm)	Heat front scaling factor
GMAW	8.0	16.0	10.0	4.0	3.0	0.67
CMT	8.0	16.0	7.5	4.0	3.0	0.67

3.3.2 Forming Behavior and Stress Analysis using Simufact.Forming (SF)

Figure 3.11 shows geometry setup in SF using upsetting cold forging process. Following the thermal simulation of the WAAM process using SW, the resulting temperature field, wall deformation, and residual stress distribution were exported and used as input for a subsequent mechanical forming simulation in SF. As presented in Figure 3.11(b), the deformation defect resulted from the as-deposited thin wall simulation using SW were transferred into SF. SF, a FEM-based virtual manufacturing program, was chosen and performed numerical model of the actual cold forging process in this research (Adenan et al., 2023). This is because the SF employs similar real-world manufacturing as the software provides a selection of the well-known forming machines for controlling tool movement (Rajesh et al., 2021).

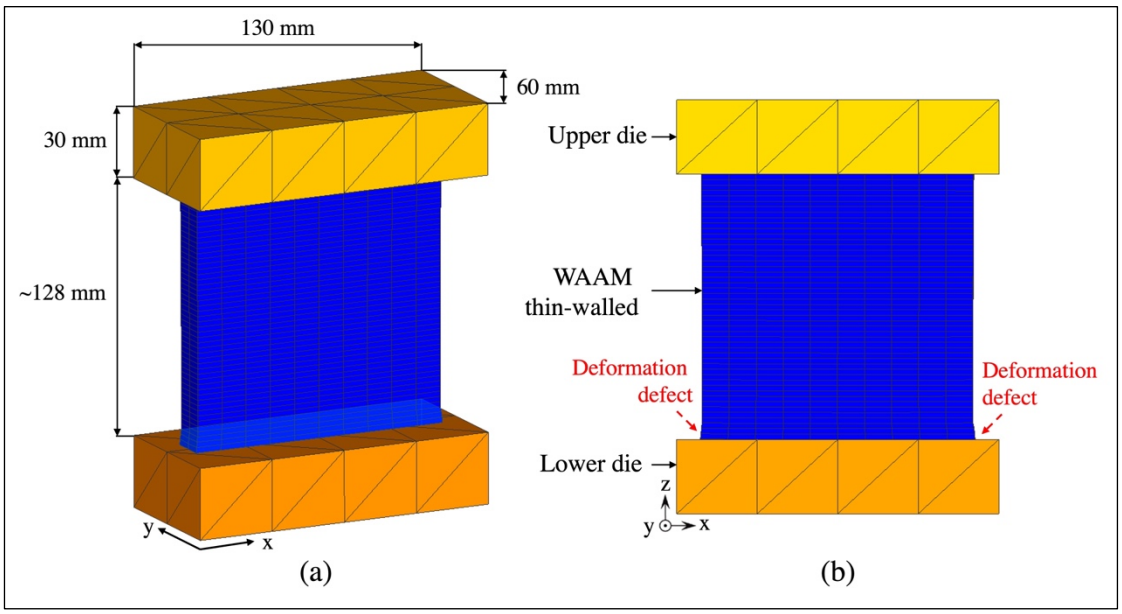

Figure 3.11 Geometry Setup in SF (a) Dimension of Geometry Part in SF (b) Deformation Defects Resulted from SW

The cold forging process was simulated on the as-deposited thin wall structure. The forging process is carried out along the z-axis, with the 6% height reduction of thin wall to study the plastic deformation applied after the forging process as illustrated in Figure 3.12. The reduction ratio was selected based on experimental limitations, ensuring deformation without excessive bending or cracking. The simulation was conducted in ambient conditions to reflect actual cold forging process used in hybrid WAAM-forged. There was no thermal input was applied. The friction conditions between the tool and workpiece were assumed to follow Gurson friction laws with calibrated coefficients based on experimental setups. Table 3.6 presents the forging parameters assigned in SF.

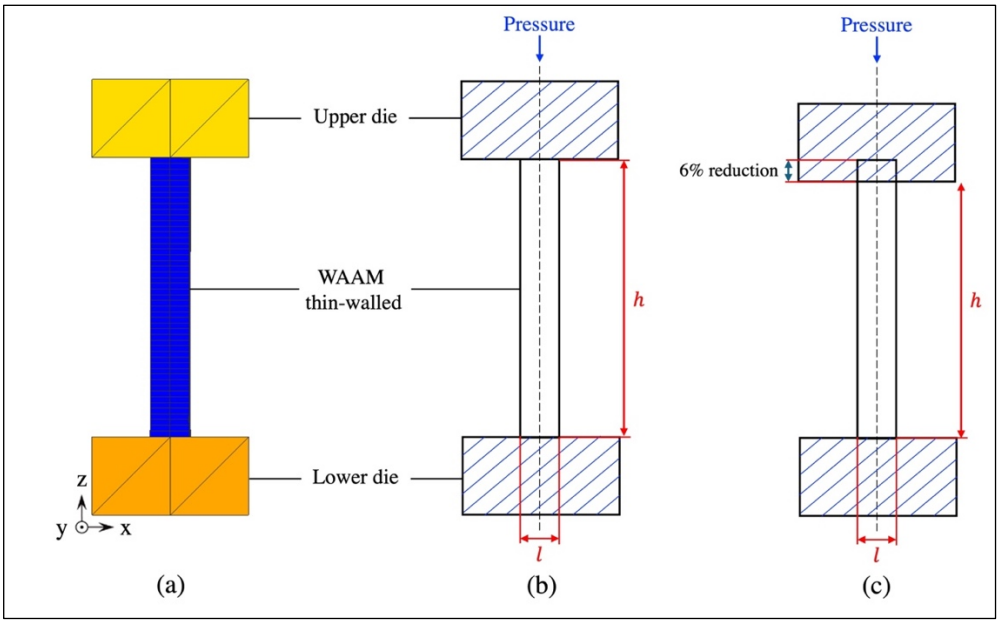

Figure 3.12 (a) Geometry Setup in SF at x-z axis Position (b) Schematic of Geometry Setup (c) Geometry Position after 6% Reduction

The Gurson plasticity model is particularly well-suited for simulating void growth, nucleation, and collapse during plastic deformation, making it highly appropriate for assessing the effectiveness of the cold forging process in reducing porosity. In addition, the Gurson model introduces a damage variable that evolves based on the porosity of the materials by simulating the void closure and densification of WAAM microstructure under compressive load. The damage parameters setup in SF is in Table 3.7, By incorporating this model, the simulation could realistically predict that forging could improve mechanical integrity in hybrid WAAM-forged components. The simulation outputs include strain and stress distribution, changes in residual stress and microstructural deformation after the forging process, which can be validated using experimental works.

Table 3.6
The Forging Parameters Assigned in SF

Process type	Damage model	Press	Temperature	Stroke
Upsetting	Gurson	Crank press Crank radius: 70 mm Rod length: 30 mm Revolution: 100 rpm	Ambient, 20℃	6%

Table 3.7
The Damage Model Parameters Setup in SF

Constant	Parameter	Value
First yield surface multiplier	q_1	1.5
Second yield multiplier	q_2	1.0
Initial void volume fraction	f	0.02
Critical void volume fraction	f_c	0.08
Failure void volume fraction	f_f	0.15
Volume fraction for void nucleation	f_N	0.03
Mean strain for nucleation	ε_n	0.2
Standard deviation	S	0.15

The selection of material and damage model parameters in the FEM simulation was based on the requirement to represent the thermal–mechanical response of ER5356 during WAAM deposition and subsequent cold forging. In SW, the assigned material properties control the predicted thermal history, heat accumulation, deformation, and residual stress development during the layer-by-layer deposition process. In SF, the Gurson damage model was selected because it is suitable for representing void nucleation, void growth, and void closure during plastic deformation, which is relevant to the porosity reduction and densification behavior expected during cold forging of WAAM aluminium alloy. The parameters listed in Table 3.7, including the initial void volume fraction, critical void volume fraction, failure void volume fraction, and nucleation parameters, influence the predicted damage evolution, effective plastic strain, contact pressure response, and local deformation behavior. Therefore, the simulation results should be interpreted as process-level predictions that support the experimental observations rather than as absolute material constants. The use of these

modeling assumptions enables comparison between GMAW, CMT, GMAW-forged, and CMT-forged conditions under consistent numerical settings.

3.4 Sample Preparation

The quality and accuracy of microstructural and mechanical analyzes depend on proper sample preparation. In this study, the WAAM and WAAM-forged fabricated ER5356 thin wall samples underwent a series of preparation steps to ensure consistency, minimize surface irregularities, and enhance measurement reliability. The preparation process included machining, milling and surface finishing to achieve stable and uniform surfaces for characterization. For each WAAM mode, one wall was kept in the as-deposited condition, while another wall was subjected to cold forging, resulting in four main sample conditions; GMAW, CMT, GMAW-forged, and CMT-forged. The specimens were then extracted from these thin walls according to the required testing geometry to verify and compare the simulation outcomes, surface integrity, microstructural characteristics, and mechanical behavior of each processing condition. This approach reduced the need for excessive sample repetition while maintaining sufficient experimental evidence to support the simulation-assisted analysis. In addition, the number of specimens was also constrained by the available thin-wall geometry after sectioning for multiple analyzes, including microstructural observation, tensile testing, residual stress measurement, and compression testing.

Basic machinability for WAAM parts is derived from a model for an acceptable surface waviness (Treutler & Wesling, 2021). To ensure the quality is met, the minimum amount of material needed to be removed where the combination of additive manufacturing and machining allow the achievement of the desired surface (Fuchs et al., 2020). The process started with substrate removal and cutting the sample to an effective shape and dimension using the MASTIKA UE-916A 9” horizontal band saw machine as shown in Figure 3.13(a). Figure 3.13(b) shows almost half of the substrate is perpendicular, separated from the wall to produce a flat and stable surface.

As the surface of the WAAM process results in geometrical variation and influences uniform deformations across the profile, the surface is removed by milling using the MASTIKA B-3V (2005) milling machine as shown in Figure 3.14(a) on its side and top surfaces. End milling was performed on the side surfaces to remove irregularities, while face milling was applied to the bottom surface to achieve flatness

and parallelism. Flat plates of 3.0 mm nominal thickness are produced to analyze the mechanical properties and surface morphology of ER5356 and Al6061 after WAAM and the hybrid process of WAAM-forged. Figure 3.14(b) was essential for preparing the sample with consistent surface conditions and showing the flat plate that resulted after the milling process. Both machines are located at the Faculty of Mechanical Engineering, UiTM Shah Alam.

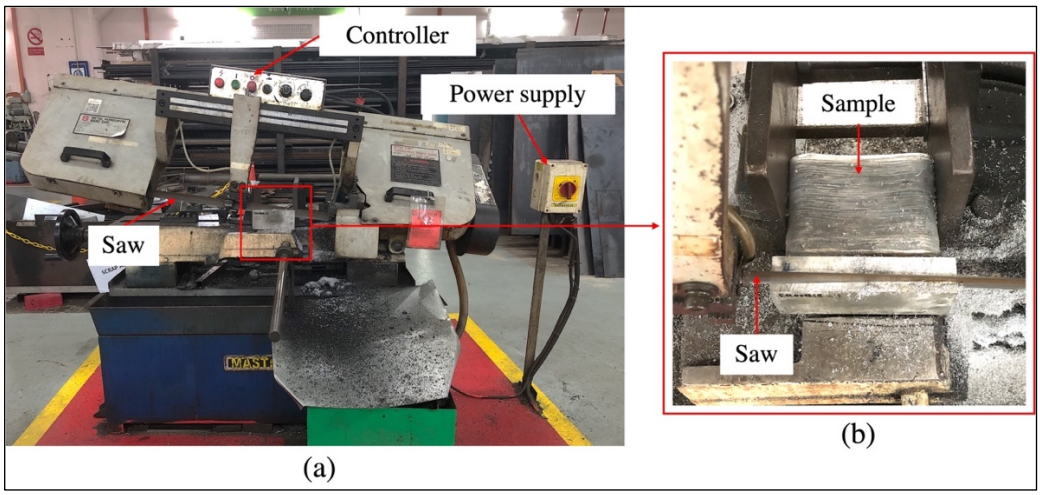

Figure 3.13 Substrate Removal Process (a) MASTIKA Horizontal Band Saw Cutter Machine (b) Process of Substrate Removal

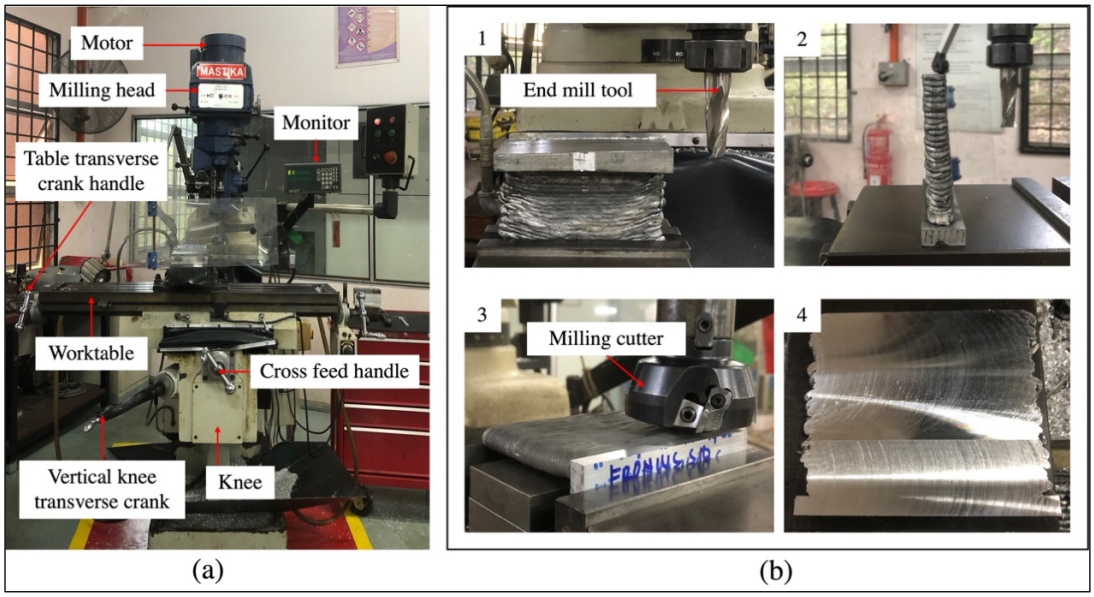

Figure 3.14 (a) MASTIKA Milling Machine (b) Milling Process Procedure

3.4.1 Morphological for Scanning Electron Microscopy (SEM) Analysis

The high-quality surface observation resulted from proper sample preparation especially when using a scanning electron microscope. Sample preparation helps to

detect features on surface such as distribution of porosities, cavities and cracks. The process started with waterjet cutting to obtain smaller specimen from positions of WAAM and WAAM-forged samples. The cutting process used Mach 100 Flow abrasive waterjet machine technology as shown in Figure 3.15. The abrasive waterjet is added by garnet abrasive into the cutting head and mixed with the pure waterjet steam to cut into small specimens; see Figure 3.15(b). The waterjet process takes nearly 15 minutes per sample to complete all specimens cutting. A small amount of the flat plate is removed with the tip of a grain sand in a size of 2 mm at extremely high-speed using a supersonic erosion process. The process involved little heat generated that is not enough to change the heat on the plate. Hence, there the specimen retaining its original properties.

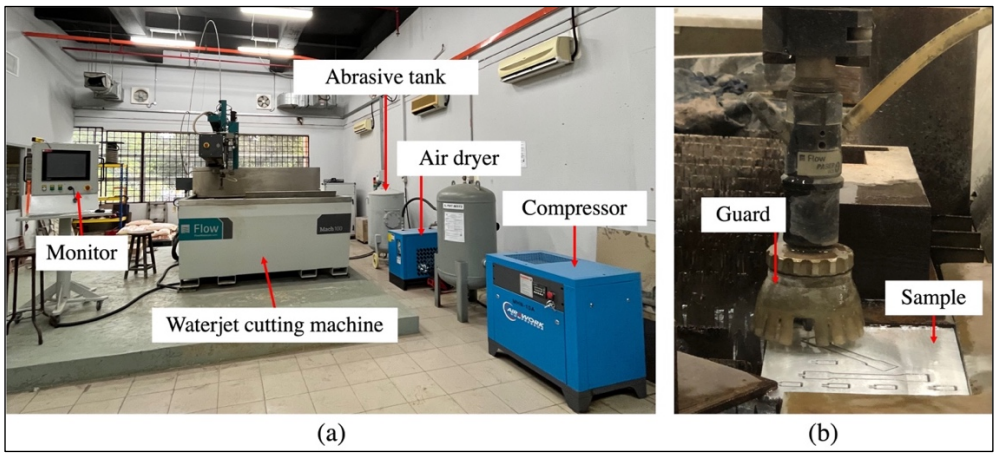

Figure 3.15 Sample Cutting using Waterjet (a) Equipment Set Up (b) Cutting Sample Process

The surface morphology and mechanical properties of WAAM and WAAM-forged must be prepared for the hot mounting process. The equipment and setup involved are shown in Figure 3.16. The sample must be prepared by hot mounting by using phenolic powder mounting compound, refer to Figure 3.16(a). The mounting machine, Simplimet 200 automatic mounting press is set to the temperature of 180°C and heats up in 10 minutes, while the cooling time is set to 8 minutes. The top plate is pressed by the hydraulic until the mould surface is visible purposely to place the sample on it. The pressure is released to put on the phenolic powder. The top plate is closed by pressing the machine until the pressure reaches and is maintained at 200 bar. As the hot mounting finished, the sample was taken out and ready for a grinding process to remove the layers on the sample surface.

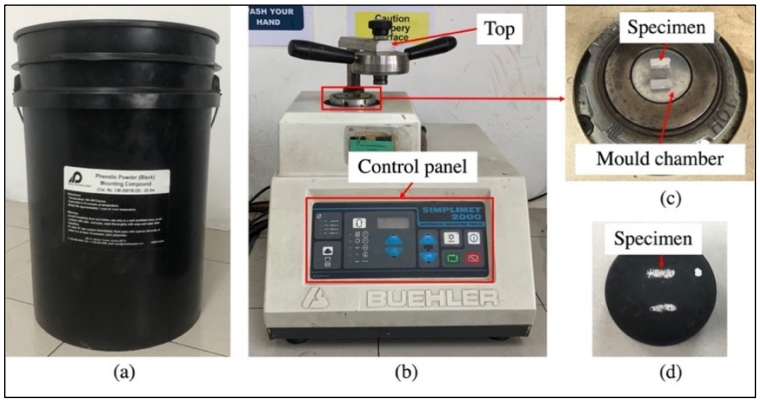

Figure 3.16 Hot Mounting Set Up and Equipment (a) Phenolic Powder Mounting Compound in Black (b) Automatic Mounting Press Machine Model Simplimet 2000 (c) Sample Placement (d) Mounted Sample

Figure 3.17 shows a grinding machine using silicon carbide sandpaper. The sample proceeds with the polishing and etching process. Figure 3.18 shows a polishing machine used to get a mirror-image surface on the mounted surface by using alumina powder, see Figure 3.18(a). To ensure the existence of scratchers, porosities, and other defects on the mounted surface to be seen clearer, the mounted sample is etched using Keller's reagent before being observed under the optical microscope. The mounted sample is immersed for 20 seconds in Keller's reagent and immediately immersed in warm water as shown in Figure 3.19 . The Keller's reagent consists of 95 ml distilled water, 2.5 ml HNO_3, 1.5 ml HCl and 1 ml HF. Table 3.8 shows the procedure of the sample preparation method. The mounted sample is observed under x50 magnification using an OLYMPUS model optical microscope, as seen in Figure 3.20(b), to verify the surface deformation after WAAM and the hybrid process.

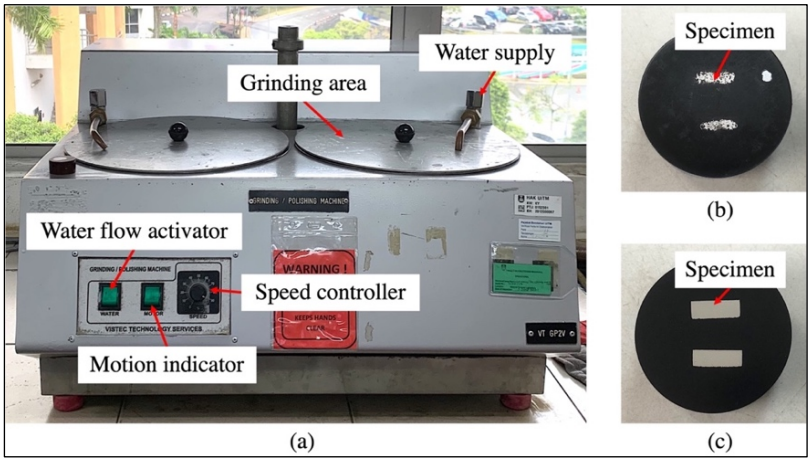

Figure 3.17 (a) Grinder Model Buehler Metasarv 2000 (b) Mounted Sample after Hot Mounting Process (c) Mounted Sample after Grinding Process

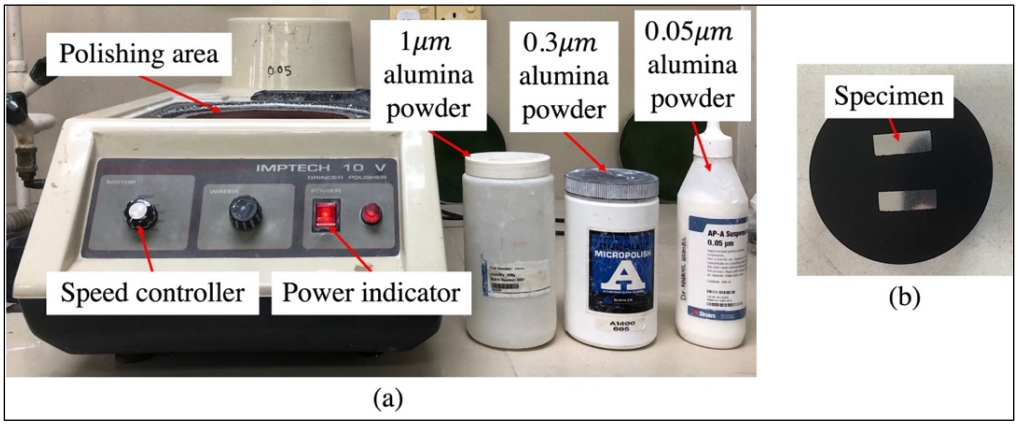

Figure 3.18 (a) Polisher Model Imptech 10V and Polishing Solution (b) Mirror-image Sample

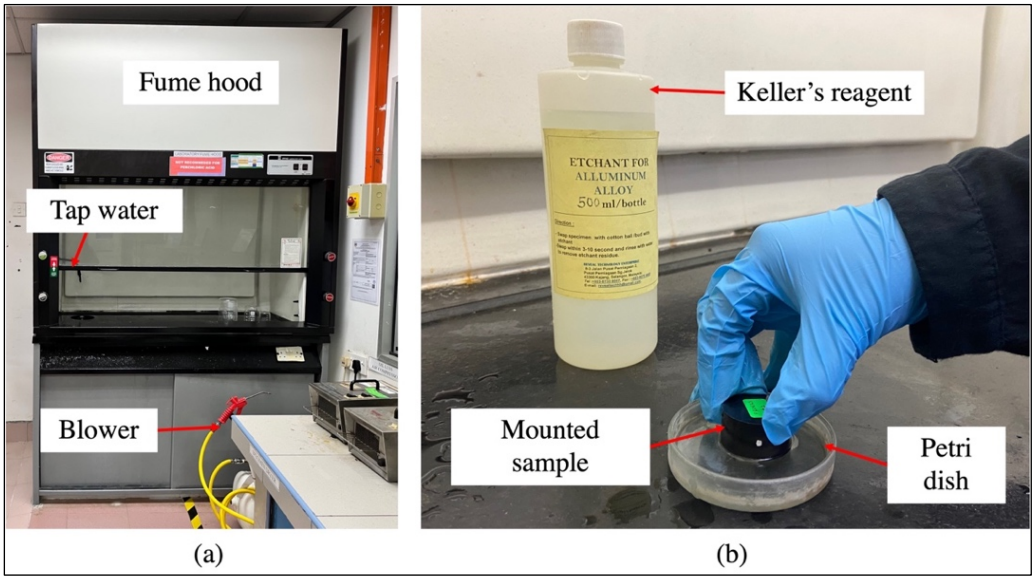

Figure 3.19 Etching Setup (a) Fume Hood for Etching Process (b) Mounted Sample Immersed in Keller's Reagent

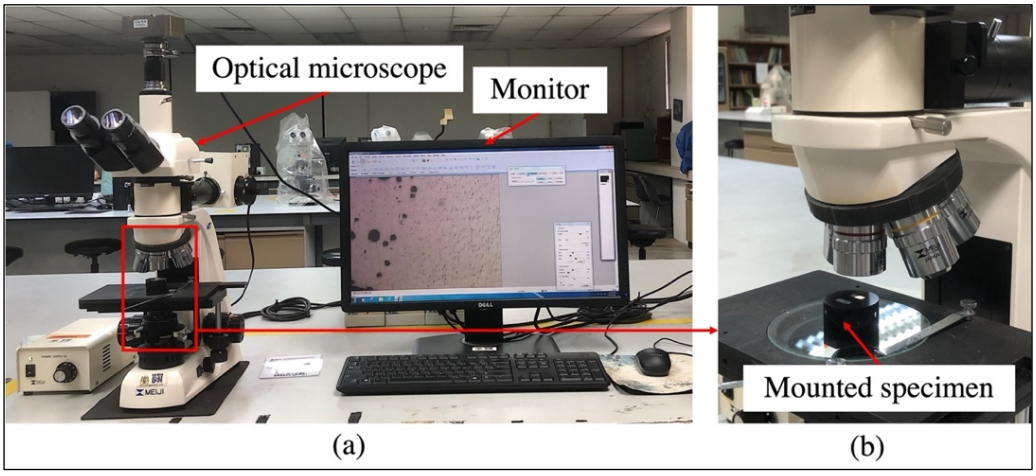

Figure 3.20 Surface Observation Setup (a) Optical Microscope (b) Mounted Sample Observed under x50 Magnification before Undergoing SEM Analysis

Table 3.8
The Sample Preparation Process for WAAM and WAAM-Cold Forging Sample

Operation	Abrasive	Speed	Load	Time	Rotation Direction
Cutting	Horizontal band saw	-	-	-	-
	End milling	-	-	-	-
	Water jet (Orifice diameter: 0.254mm, High water pressure: 379 MPa, Low water pressure 103 MPa, Abrasive flow rate: 0.31759 kg/min)	200 %	-	-	-
Grinding	SiC sandpaper (400 grid)	400 rpm	6 N	900 s	Counter
	SiC sandpaper (600 grid)	400 rpm	6 N	900 s	Counter
	SiC sandpaper (1200 grid)	400 rpm	6 N	900 s	Counter
	SiC sandpaper (2400 grid)	400 rpm	6 N	900 s	Counter
Polishing	1 μm alumina powder	400 rpm	6 N	900 s	Counter
	0.3 μm alumina powder	400 rpm	6 N	900 s	Counter
	0.05 μm alumina powder	400 rpm	6 N	900 s	Complimentary
Etching	Keller's reagent (95 ml distilled water, 2.5 ml HNO_3, 1.5 ml HCl and 1 ml HF)	-	-	20 s	-

3.4.2 Microstructural for Electron Backscatter Diffraction (EBSD) Analysis

To ensure optimal surface quality with the least amount of deformation, grinding, polishing, and an electrolyte polishing process were performed before been analyzed using Electron Backscatter Diffraction (EBSD) procedure. For grinding process, finer silicon carbide (SiC) papers were used in the following the grit sizes: 600 grit, 1200 grit, and 2000 grit. Each grinding step was carried out at a fixed load to prevent overheating and surface damage. The samples were thoroughly cleaned with ethanol between each stage to remove any residual debris. Following grinding, the samples undergo polishing to achieve a deformation-free surface using Leco microvoid compound with a 6-micron diamond suspension, refer to Figure 3.21(a), combined with a diamond extender to facilitate uniform material removal and improve the surface quality from scratches.

The final surface polishing was conducted at the Mechanical, Industrial, and Mechatronics Engineering department of Toronto Metropolitan University, Canada. The sample was immersed in a solution consisting of 90 ml of ethanol and 10 ml of

perchloric acid using Buehler Electromet 4 electropolisher power supply and electrolyte polishing at a voltage of 30V for 20 seconds, see Figure 3.21(c). Therefore, any residue deformation layers were removed, revealing the surface as smooth and free of strain concentration, which is crucial for high-quality EBSD patterns. Figure 3.21(b) shows the surface differences between normal polished (P) and electrolyte polished (EP) samples.

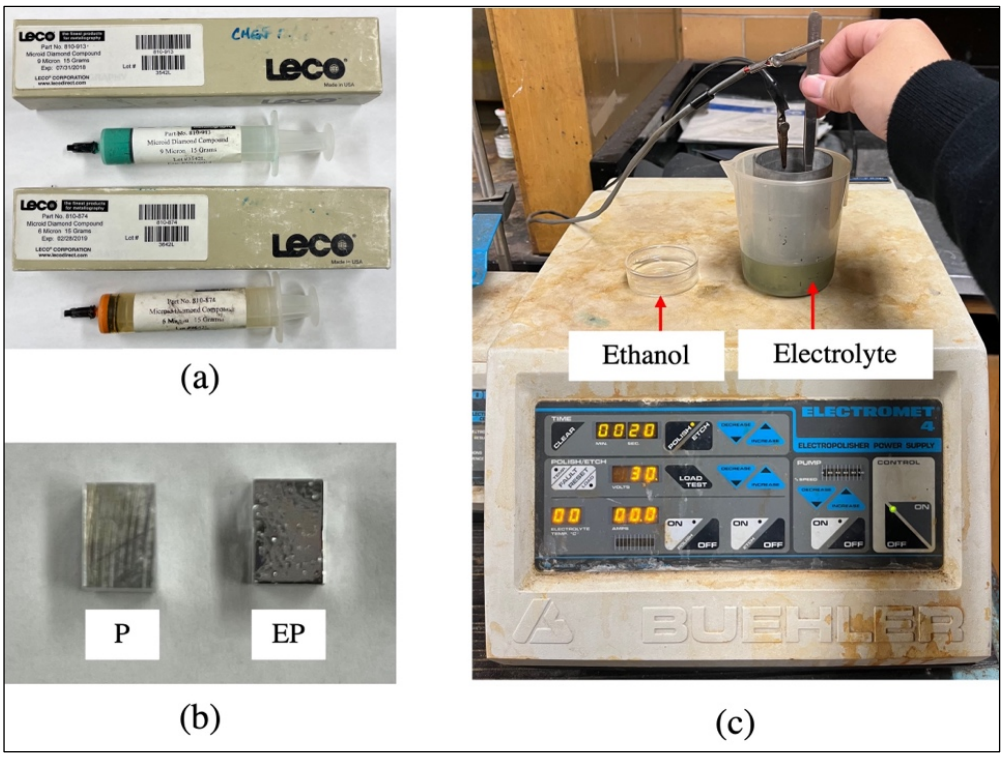

Figure 3.21 (a) Microvoid Compound (b) Polished (P) sample and electrolyte polished (EP) sample (c) Electrolyte Polishing Setup

3.5 Experimental Verification of WAAM and WAAM-Forging Process

3.5.1 Gas Metal Arc Welding (GMAW) Process

The GMAW process is used to fabricate a thin wall structure using ER5356 aluminium alloy wire on an Al6061 substrate. The substrate used for the deposition process was Al6061 aluminium alloy with dimensions of 130 mm x 60 mm x 25.4 mm. As the pre-processing of WAAM, all substrates were cleaned by mechanical polishing using a steel brush to remove any contaminants, oil stains and oxidation film, then wiped clean with acetone, while the wire filler was kept dry. Preheating was not applied, as the controlled interlayer cooling time was sufficient to regulate thermal accumulation. The interlayer cooling time between successive layers was 30 seconds to

prevent excessive heat accumulation with an arc length of 15 mm and a 2 mm offset for all layers. However, for the GMAW process, each layer needed to have extra cooling time because the process applied high heat input. Hence, air blowing is needed to increase the cooling time for the next layer formation. The welding process was carried out using a GMAW system, which consisted of an EWM Titan XQ R 500 Pulse D power source as shown in Figure 3.22(a), compatible with a 6-axis FANUC Robot Arc Mate 100iD at the Faculty of Mechanical Engineering, UiTM Shah Alam. Pure argon gas was used as a shielding gas at a flow rate of 15.0 – 20.0 L/min. The experimental parameters are based on the simulation analysis as shown in Table 3.9.

As shown in Figure 3.22(b), the GMAW torch was placed perpendicular to the substrate before starting the deposition process. The initial weld bead was deposited with controlled penetration to ensure good adhesion to the substrate. While the width of the bead was monitored to maintain consistent layer thickness. The deposition strategy is bidirectional and the travelling direction is changed from odd layers to even layers to provide more stable building. After the deposition of each layer, the cooling time was applied before the next layer, as it helped in minimizing residual stresses and preventing grain coarsening. The deposition continued sequentially following a linear torch path to maintain uniform bead placement. A total of 65 layers were deposited to achieve an approximate wall height of 100 mm.

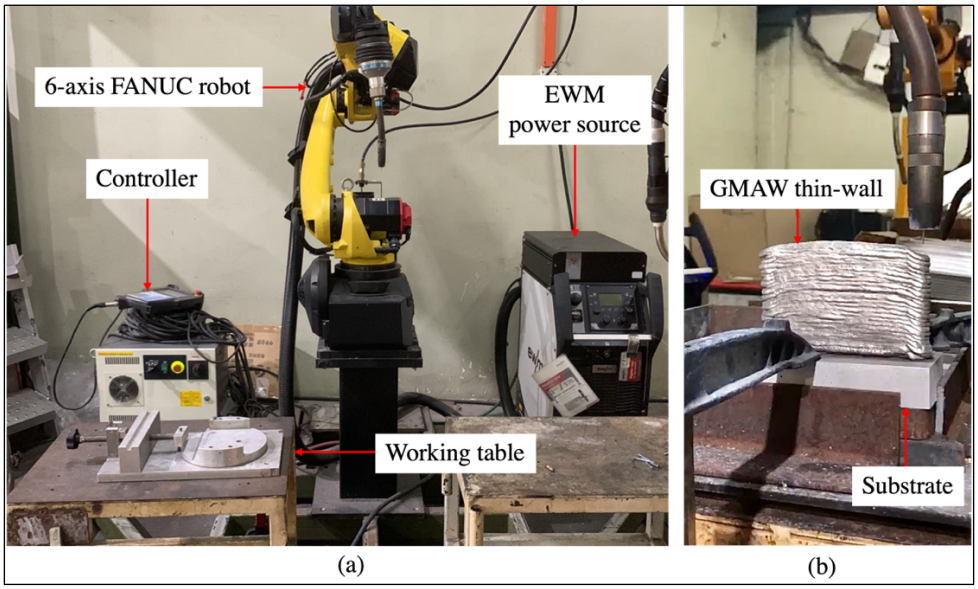

Figure 3.22 (a) GMAW Process Equipment Setup (b) GMAW Thin Wall Formation

Table 3.9
Data of Actual WAAM-GMAW Process

Parameters	WAAM-GMAW
Wire feed speed, m/min	9.2
Travel speed, mm/s	7.0
Current range, A	152.0
Arc voltage, V	19.2
Voltage correction, V	1.5
Heat input, J/mm	307.5
Robot	6-axis FANUC Robot Arc Mate 100iD
Power source	EWM Titan XQ R 500 Pulse D
Shielding gas	Argon
Gas flow rate, L/min	15.0 – 20.0

3.5.2 CMT Process

Unlike the GMAW process, which utilized a constant heat input during the deposition, the CMT process was performed using a multi-heat input range of 115.52 to 217.57 J/mm. This approach was due to the nature of the CMT process. The GMAW process operates at higher energy levels and requires a stable heat input to ensure a complete fusion, while the CMT process involves controlled droplet transfer with lower energy, requiring dynamic heat adjustments to maintain uniform deformation. The material and dimension of the substrate and wire filler used are the same, ER5356 and Al6061, respectively. The substrate was prepared using the same method for the GMAW process. The type of shielding gas and gas flow rate are kept constant for both processes. However, the interlayer cooling was 4.5 seconds before the deposition of the next layer. It is also an essential step to prevent excessive heat buildup and maintain a stable deposition process.

The layer deposited by the CMT process was 96 layers to achieve a thin wall with approximately 100 mm height. The CMT process is started by an arc length of

approximately 12.0 mm with an offset of 2.0 mm. However, the arc length increases 0.4 mm when achieving 60 layers because of the heat accumulated along the wall formation. The travel speed is kept constant at 10.0 mm/s, whereas the wire feed speed varies at 7.0 m/min, as shown in Table 3.10. A visual inspection was conducted to examine the thin wall structure to verify the dimensions and layer uniformity. The details of experiment setup are displayed in Figure 3.23.

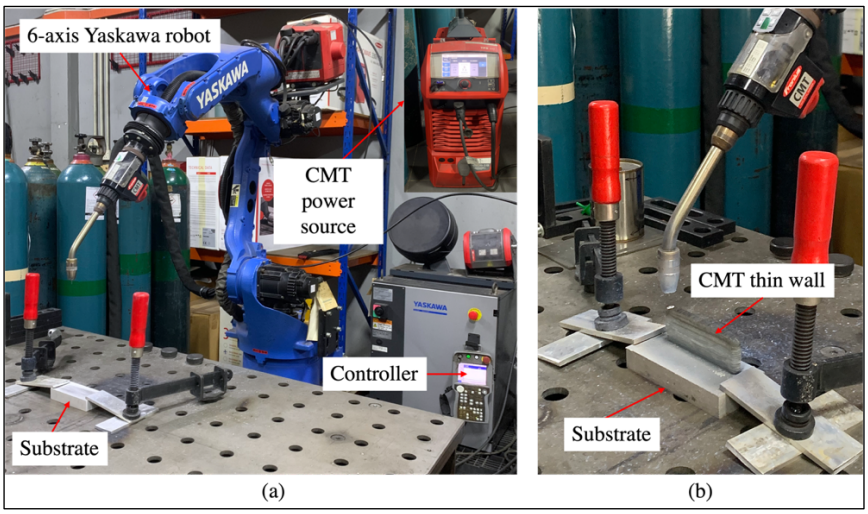

Figure 3.23 (a) CMT Process Equipment Setup (b) CMT Thin Wall Formation

Table 3.10
Data of Actual WAAM-CMT Process

Parameters	WAAM-CMT
Wire feed speed, m/min	5.3 – 10.9
Travel speed, mm/s	10.0
Current range, A	95 – 147
Arc voltage, V	15.2 – 18.5
Voltage correction, V	0.0
Heat input, J/mm	115.5 – 217.6
Robot	6-axis Yaskawa Motoman MA1440
Power source	Fronius TPS 500i Pulse
Shielding gas	Argon
Gas flow rate, L/min	15.0 – 20.0

3.5.3 Wire Arc Additive Manufacturing-Forging (WAAM-Forging) Process

The combination of additive manufacturing and the forming process was aimed at improving the shape of deposited material by deformation, besides improving the properties of the material (Pragana et al., 2021). The forging was performed using axial upsetting along the z-axis, with incremental height reductions of 6 mm (6%). The maximum reduction height was limited to 6 mm, as further reduction up to 9 mm led to excessive deformation, resulting in bending and cracking in the thin wall. Moreover, axial upsetting was employed over multi-axial forging to reduce tooling complexity and preserving for accurate comparison with the as-built WAAM thin wall. The forging process proceeded after the WAAM process by using a J23-100 1000 kN tonne punching power press machine, which can deliver the required force for controlled deformation.

The machine and forging setup for CMT wall as shown in Figure 3.24. The sample was placed on the spacer made of SKH55 (AISI M35) material with hardness 65 HRC. The set forging speed is 25 mm/min. The bed of the universal tester was moved upward until the load became the set load value and kept at that position for 1 second. The set load value is 1000 kN, which provides the contact pressure of 390.65 MPa on the specimen surface. The pressing process undergoes a value reduction of 6 mm for WAAM-forged walls.

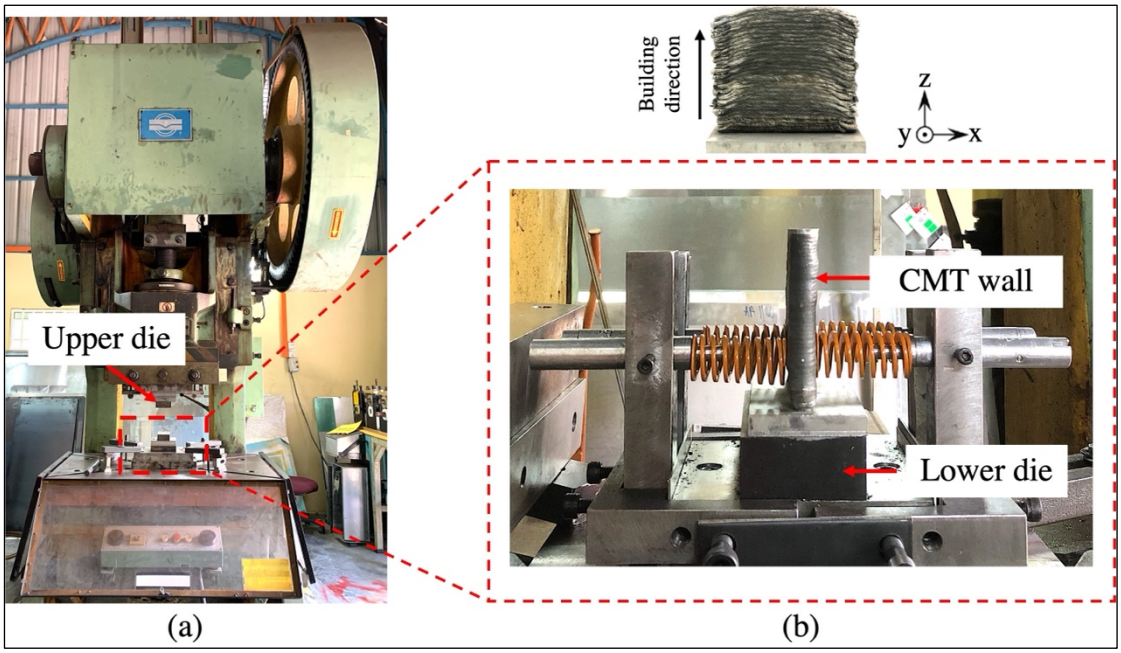

Figure 3.24 (a) Press forging Machine (b) Forging setup for WAAM-Forging Process

3.6 Deformation Behavior and Mechanical Properties Analysis in WAAM and WAAM-Forging Process

3.6.1 Distortion and Deformation Analysis

3D scanning is a technology that obtains information about the geometry of a physical object by using a contact or non-contact digitization system to inspect the surface of a workpiece by virtual computer space through the network of points (x, y, z) in the form of a 3D graphic representation (Afteni et al., 2022). 3D digitizing or digitization provides 3D coordinates of scanned surfaces. These 3D coordinates or cloud of points connected via polygonization, result in a polygonal mesh. Figure 3.25(a) shows equipment set up for the 3D scanning process at First Metrology Sdn. Bhd. Selangor. The technical data for GOM Scan 1 is shown in Table 3.11.

Table 3.11
Technical Data for GOM Scan 1 (200)

Type	GOM Scan 1 (200)
Light source	LED
Projector light	Artificial optical radiation; blue 440-465 nm (Medium risk according to DIN EN 62471, issue March 2009, condition when looking into the light source)
Measuring area (mm^2)	$200\ x\ 125\ mm^2$
Point distance (mm)	0.060 mm
Working distance (mm)	450 mm
Weight (kg)	Approximate 2.5 kg
Dimension (mm^2)	$290\ x\ 215\ x\ 80\ mm^2$
Cable length	5 m
Operating system	Windows 10
Software	GOM Inspect 2022

The 3D scanning process involves meshing editing functions with the aid of GOM Inspects 2022 software. The software firstly determines the geometrical parameters and image characteristics of the camera lens chip based on the recorded camera images. To have a view and understanding of 3D scanning captured images, Figure 3.26 shows the camera position and projection view towards the measuring volume, while the sensor configuration of the camera scanner is shown in Table 3.12.

In addition, the GOM Inspect software computes 2D calibration points to 3D coordinates points. The process was carried out by the optical fringe projection scanner GOM Scan 1 in the MV 200 version, as in Figure 3.25(b). MV refers to measuring volume. Therefore, the optical scanner is convenient to define the sample that is less than 200 mm in all axes. The scanner captures the complete surface of the part with blue fringe projection. It delivers detailed resolution in no time.

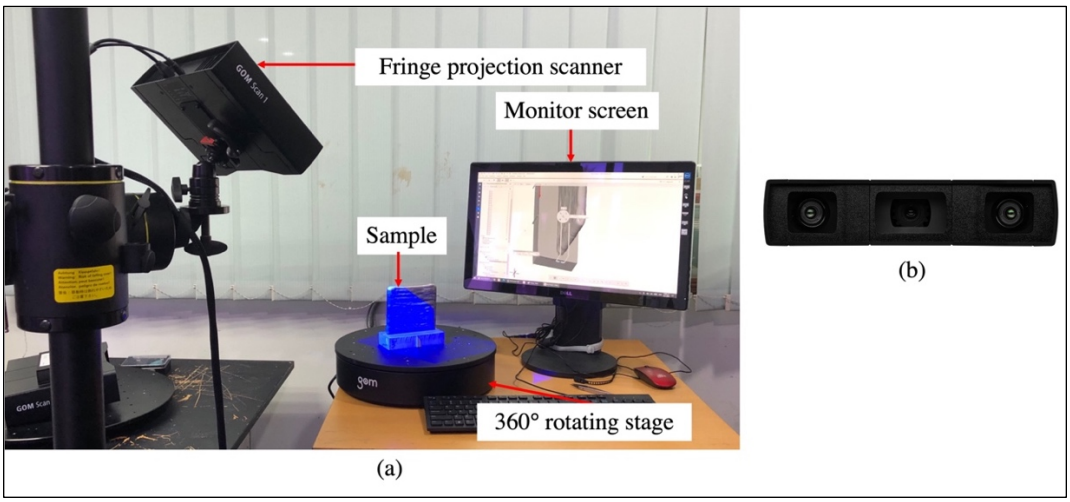

Figure 3.25 Equipment Set Up for 3D Scanning Process, (a) Front View of GOM Scan 1 Sensor

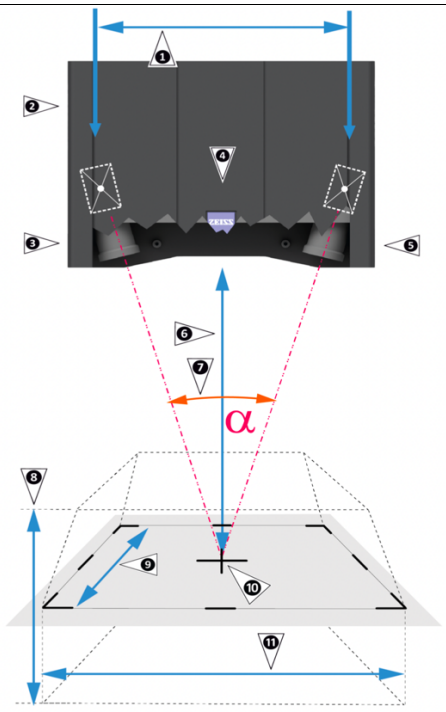

1. Camera position (Approximate distance)
2. GOM Scan 1 sensor
3. Right camera lens, R
4. Projector lens, P
5. Left camera lens, L
6. Measuring distance, from front edge of housing to the center of measuring volume
7. Camera angle
8. Height of the measuring volume, H
9. Width of the measuring volume, W
10. Center of the measuring volume
11. Length of the measuring volume, L

Figure 3.26 Camera Position and Projection View Towards the Measuring Volume

Table 3.12
Sensor Configuration for GOM Scan 1 (200)

Measuring volume (MV)	200 mm (l) x 125 mm (w) x 150 mm (h)
Measuring point distance	0.060 mm
Recommended reference points	Ø 1.5mm
Measuring distance	450 mm
Standard calibration objects	CPA30/210

Figure 3.27 shows 3D scanning procedure steps. The process begins with the calibration of the sensor by using a 3D calibration panel, CPA30/210, see Figure 3.28. The measuring system is adjusted to ensure the dimensional consistency. The approximation of camera position distance affected the view of the intersection point on the calibrated panel. During the process, the calibration panel is ensured to be in the center of the measuring volume. Based on the projected blue light, 18 positions are detected to be scanned. The software guides by providing instructions either by rotating or tilting the calibration panel to achieve the desired position, see Appendix 1 (a). This step is repeated to gain optimum calibration results by showing a green icon. As the calibration process completed, the results show general and calibration details data. Appendix 1 (c) shows the calibration result.

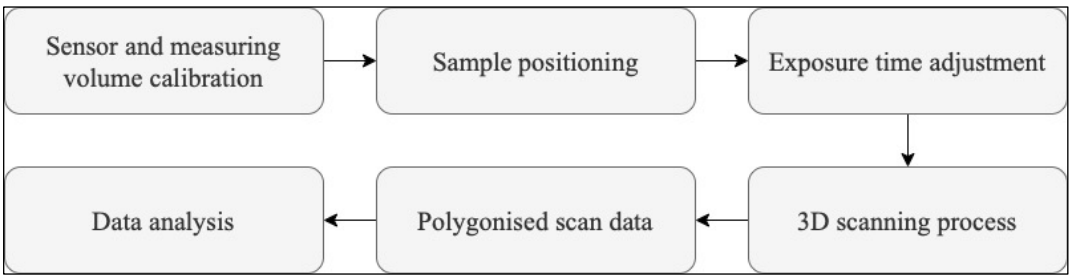

Figure 3.27 3D Scanning Procedure Steps

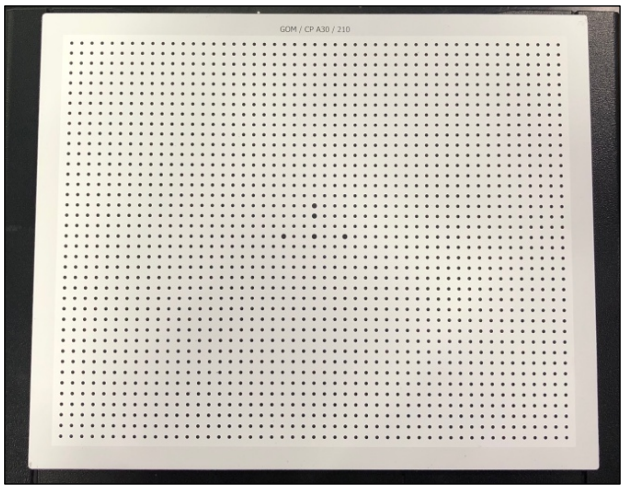

Figure 3.28 CPA30/210 3D Calibration Panel

The next step is the positioning of the sample. The sample is placed on the worktable. According to Figure 3.25(a), the camera position adjusted to be at the optimum position with the center of the measuring volume. An uncoded white sticker in 1.5 mm diameter was unsymmetrically placed on the worktable and sample before the scanning image was captured. The position of the reference points resulted in the reference point deviation. Reference point deviation is referred to as intersection error. The sensor detects reference points by the stickers. Figure 3.29(a) shows the example of uncoded white reference stickers while Figure 3.29(b) shows the stickers placement on the sample. As the image has been captured, the white stickers are detected in red, as shown in Figure 3.30.

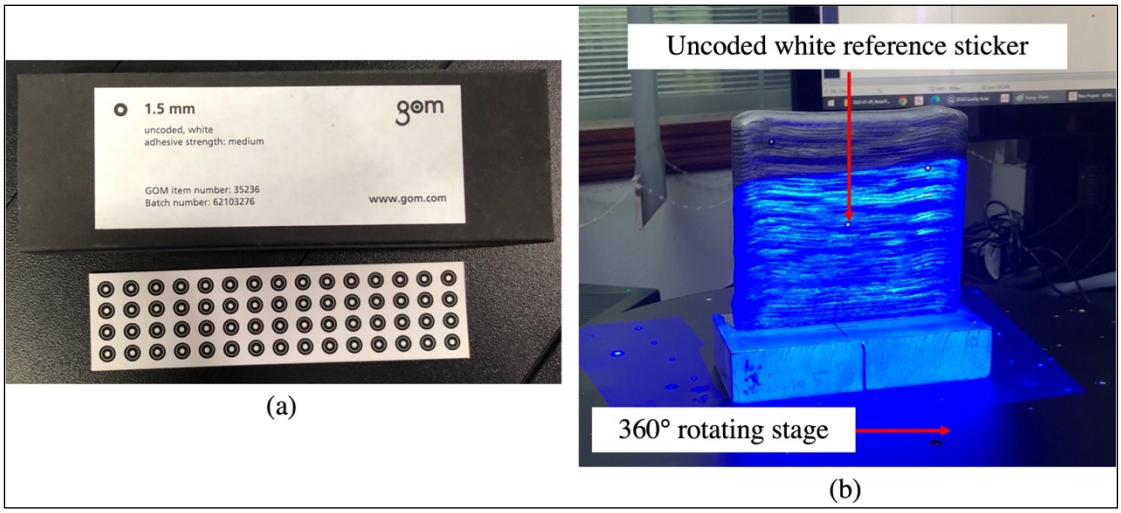

Figure 3.29 Uncoded White Reference Stickers, (b) Uncoded White Reference Stickers at Unsystematic Positions

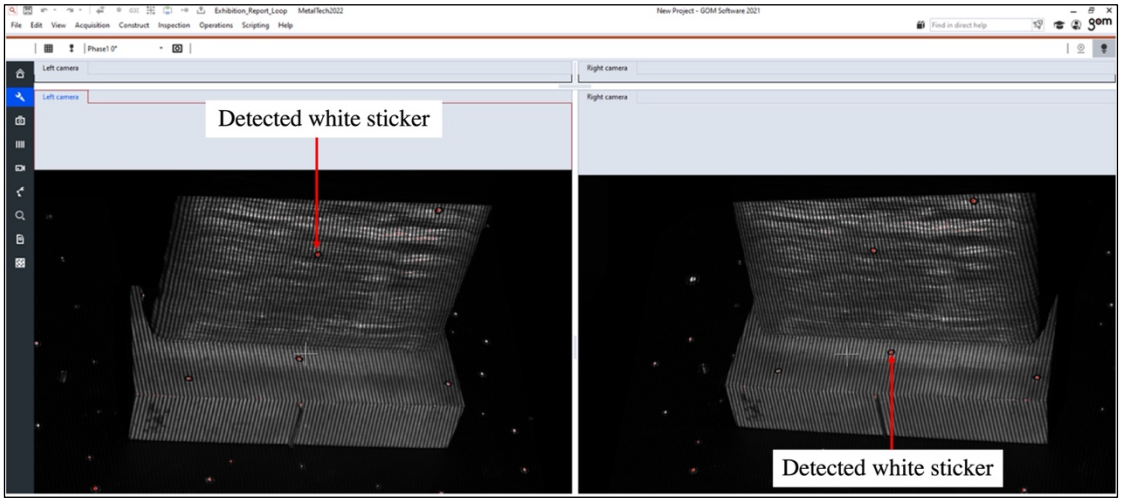

Figure 3.30 White Stickers Detected before Image was Captured

Besides the calibration, exposure time needs to be automatically adjusted. This is to avoid overexposed areas, as no image will be captured in the software later and

leave empty spaces. Red overexposed areas on the calibration plate result in an empty image in the software. Appendix 1 (d) shows some outside areas which are considered as overexposed areas. The scanning process is done automatically. The scanning process started from a few coded points. The coded points refer to sticker reference points. The number of captures can be assigned according to the complexity of the part. In this case, 20 captures are assigned.

Manual scanning proceeds to the empty scan through the sample. It is to manually add new reference points so that a large area can be captured. Noted that during the scanning process, no vibration or any disturbances through the worktable, as it will stop the scanning process. If the captured image is not being captured in the system box, the worktable position can be adjusted by rotating or moving to another position, not the part position, as it has been calibrated. Removing the part position causes the user to do the calibration again. The following step is connecting all the cloud points of the polygonised scan data to form mesh. Appendix 1 (e) shows the points assembled. The raw and mesh data can be seen to observe the whole scanning part; see Figure 3.31 . Next, the data is analyzed, such as flatness and dimension. The data can be compared with nominal and actual data.

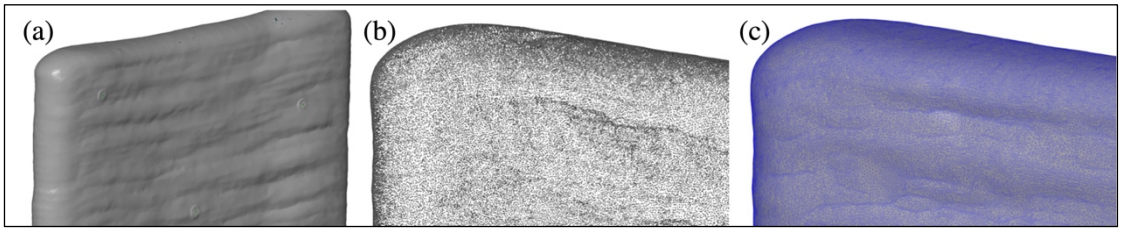

Figure 3.31 (a) Scanning Image of Raw Data of CMT Sample (b-c) Scanning Image of Mesh Data of CMT Sample

3.6.2 Surface Morphological Analysis

The microstructure analysis includes SEM and EDX analysis. To characterize the deformation surface, a Hitachi Scanning Electron Microscope (SEM) Model SU3500 is used as shown in Figure 3.32. The SEM can characterize the defects on the WAAM deformation and observe the existence of aluminium defects after the WAAM process, such as porosities and cracks. The SEM analysis needs to be handled at low pressure inside the vacuum chamber. Figure 3.32(a) shows the mounted sample position on the sample stage in the chamber. As the aluminium alloy is a block specimen, it had to be observed under the magnification of x1000 or lower. The quality of the observed image is based on the conductivity of the materials in the vacuum chamber.

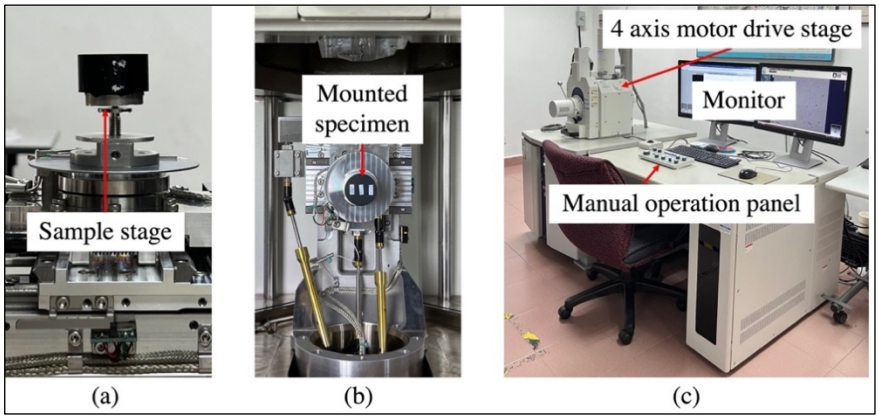

Figure 3.32 (a) Mounted Specimen in Chamber (b) Positioning of Mounted Specimen (c) Scanning Electron Microscope

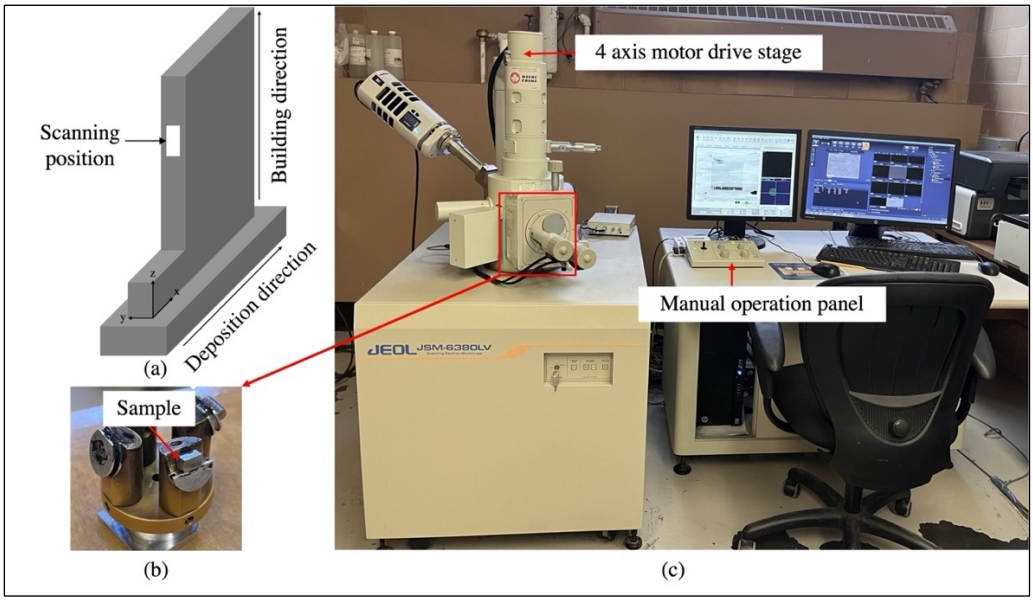

Figure 3.33 (a) Mounted Specimen in Chamber (b) Positioning of Mounted Specimen (c) Scanning Electron Microscope

Continuing from SEM, the energy-dispersive X-ray (EDX) analysis can be done by using TEAM™ EDS Suite software right after the images are captured. The elementary analysis proceeds to make a comparison of the chemical composition of aluminium alloy before and after the WAAM and WAAM-forging processes. Certain spots on the surface are chosen to identify the weight percentage of the elements that exist. All sample preparation processes for surface observation for SEM analysis are proceeded at the Faculty of Mechanical Engineering, UiTM Shah Alam. The EBSD examination was performed at the WAAM and WAAM-forging samples to observe for accurate crystallographic details. The step of the morphological examination was 1.2 µm, and the magnification was 200x, done at the Mechanical, Industrial, and Mechatronics Engineering department of Toronto Metropolitan University, Canada, using a Jeol JSM-6380LV scanning electron microscope. The detailed analysis of

microstructural features of WAAM and WAAM-forging samples such as grain size, porosity, crystallographic orientation, grain structure and misorientation within the material are examined for understanding material's mechanical properties. Figure 3.33 presents the machine and set up for EBSD analysis.

3.6.3 Tensile Behavior and Performance Analysis

The tensile sheet plate specimens were extracted perpendicular (90°), diagonal (45°), and parallel (0°) to the deposition layer, as shown in Figure 3.34(a), for WAAM specimens and WAAM-forging specimens using waterjet with an orifice diameter of 0.254 mm to evaluate the mechanical properties such as tensile strength, yield strength, and elongation, which including the deformation characteristic of WAAM and WAAM-forging ER5356 aluminium alloy. Due to space and material limitations, only one specimen per orientation was tested. Although this limits statistical analysis, the results provide initial insights into the directional mechanical behavior. Table 3.8 shows the setup of the cutting process using a waterjet machine. According to the ASTM E8M standard, the tensile sheet plate specimens are represented in Figure 3.34(b). The final thickness of the tensile samples was 3 mm.

Tensile tests were performed in a Shimadzu Servopulser universal testing machine as shown in Figure 3.35(b), model of EHF-EV101K1-020-0A at the Faculty of Mechanical Engineering, UiTM Shah Alam. The test started by placing the sheet plate in the machine's crosshead to hold it rigidly; see Figure 3.35(a). One of the crossheads is kept fixed while the other crosshead is moved at a predetermined load speed, which is 2.0 mm/min using an extensometer with a gauge length of 2 mm. Hence, the specimen is extended, and the maximum load capacity of the machine is 98 kN. The specimen is pulled by moving the crosshead until it fractures, and a load-extension plot is extracted. The raw data from the tensile test is processed to get the engineering stress-strain curve and true stress-strain curve by Servo 4830 Shimadzu software, besides identifying other mechanical properties such as Young's Modulus or stiffness, proportional limit, elastic limit, yield strength, ultimate tensile strength, true fracture strength, uniform elongation or elongation until necking, total elongation before fracture, strain hardening coefficient, reduction in area, resilience and tensile toughness.

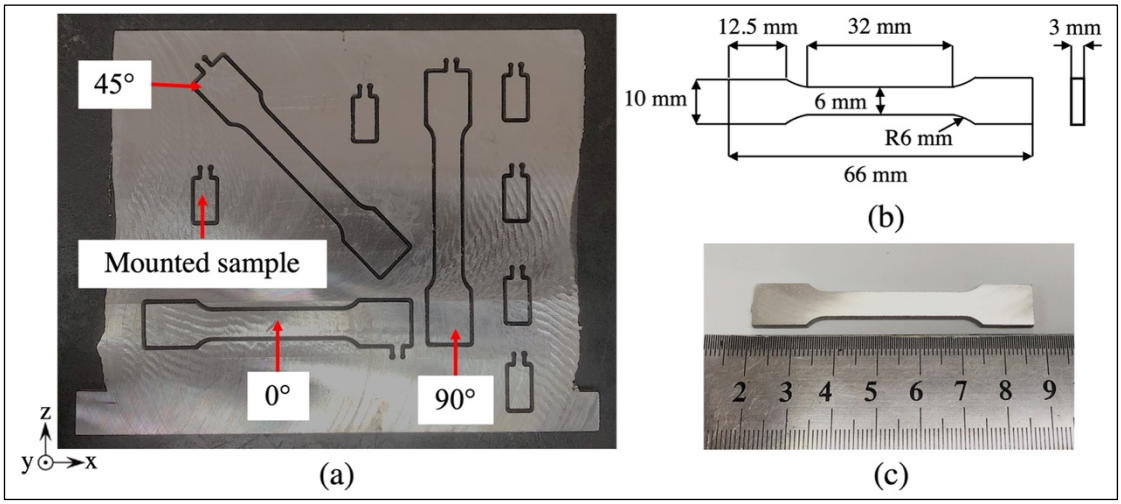

Figure 3.34 (a) Cut Plate using Waterjet, (b) Tensile Sheet Plate Dimension of ASTM E8M Standard, (c) Tensile Sheet Plate

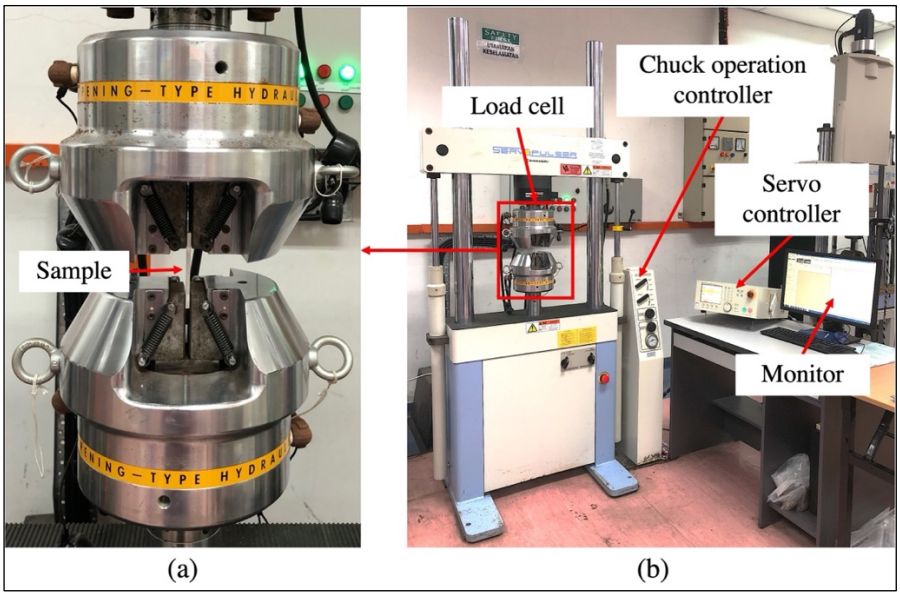

Figure 3.35 (a) Tensile Sample Placement in Cross Head, (b) Tensile Machine

3.6.4 Residual Stress Analysis

To analyze the distribution characteristics of residual stress in WAAM and WAAM-forged aluminium alloy, the residual stress measurements were performed using an X-ray diffractometer, PANanalytical X'Pert Pro, as shown in Figure 3.36 at the Mechanical, Industrial, and Mechatronics Engineering department of Toronto Metropolitan University, Canada. The XRD analysis is performed to assess the residual stress and phase composition of WAAM and WAAM-forged ER5356 by identifying the internal stresses that may Influence material performance and phase stability transformation. The XRD residual stress measurements were performed on the weld

and weld-forging surface. The collimator was used to facilitate the specimen positioning for stress measurement. The incident radiation area is equal to 0.5 mm x 2 mm, which is smaller than the curvature radius weld bead. In this research, the $sin^2\psi$ method which is based on strain analysis of elasticity theory and diffraction theory was used to determine the residual stress.

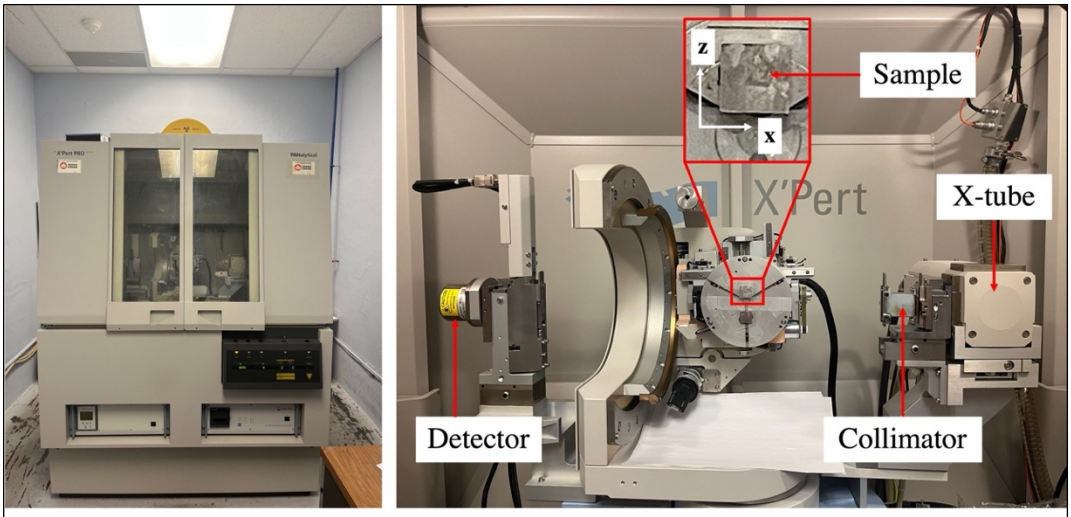

Figure 3.36 (a) XRD machine (b) XRD experimental setup

3.6.5 Compressive Properties in WAAM and WAAM-Forging Process

To investigate the material compressive behavior and determine the effects of strain rate on yield strength, flow stress and the material's capacity to withstand plastic deformation especially of the hybrid WAAM-forging process, the compression testing is performed to evaluate the mechanical properties of both processes. The samples are extracted by from the WAAM and WAAM-forging thin wall by CNC cutting with the dimensions of 4 mm (x-axis), 4 mm (y-axis), and 6 mm (z-axis); see Figure 3.37 (a). To minimise the frictional effects and achieve uniform deformation, a lubricating powder (graphite powder) is applied to the top and bottom surfaces at the z-axis of each of the samples. The test is performed using a computerized United STM-50kN testing system at room temperature, as depicted in Figure 3.37 (c). At four different strain rates, 0.0001 s^{-1}, 0.001 s^{-1}, 0.01 s^{-1}, and 0.01 s^{-1} are performed on each sample by following standardized procedures to ensure the consistency of data acquisition. The sample is carefully aligned with the compression platens to avoid eccentric loading. The test is conducted at the specified strain rate up to 50% height reduction for WAAM and

WAAM-forging samples. The force and displacement are recorded continuously. Figure 3.37 (b) showed the compressed sample after a 50% height reduction was applied along the axis.

The compressive behavior of WAAM and WAAM-forging samples were evaluated through analysis of true stress-strain curves obtained from the compression testing. Strain rate sensitivity was calculated using both common approach and Lindholm's method to cross-validate results, minimise model-specific bias, and strengthen the reliability of the findings.

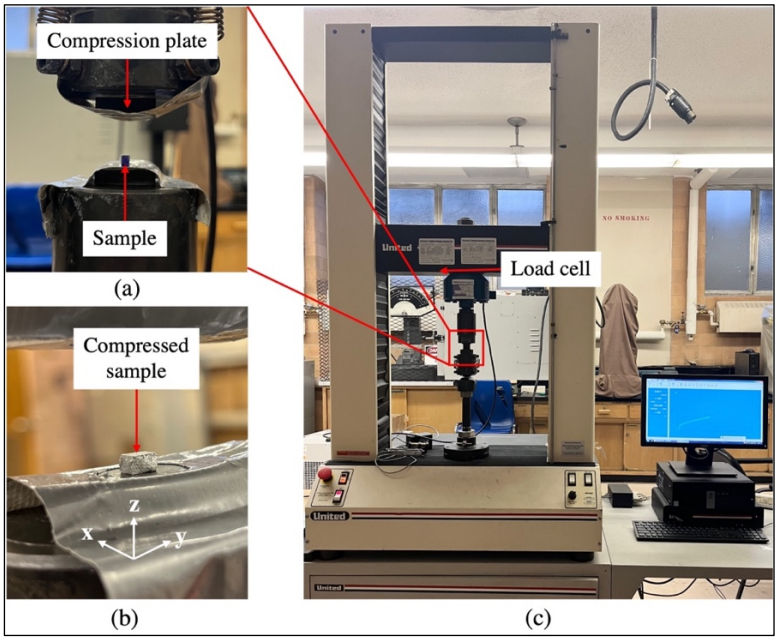

Figure 3.37 Compression Testing Equipment Setup (a) Sample Placement on the Compression Plate before the Test (b) Sample after 50% Compression Loading along z-axis (c) United STM-50kN Testing Machine

CHAPTER 4
RESULTS ON SURFACE INTEGRITY AND MECHANICAL PERFORMANCE WAAM AND HYBRID WAAM-FORGING ER5356 THIN WALL

4.1 Introduction

This chapter presents the discussion of the simulation analyzes and experiments conducted to evaluate the deformation behavior, surface integrity and mechanical properties of WAAM and hybrid WAAM-forging ER5356 aluminium alloy so that a comprehensive understanding of the cold forging process can refine the mechanical and structural performance of WAAM-fabricated components. The surface integrity in this study refers to the geometrical and material quality of the WAAM and WAAM-forged ER5356 thin wall. It is evaluated through dimensional accuracy, deformation behavior, porosity, density, elemental distribution, microstructural condition, and residual stress. The simulation results, such as total displacement, contact pressure, and effective plastic strain, are used to describe the deformation and plastic strain response during WAAM-forging, while the experimental results validate the surface and internal quality through 3D scanning, porosity-density analysis, EDX, SEM/EBSD, and XRD residual stress measurement. The detailed examination of grain morphology, Kernel Average Misorientation (KAM) and local misorientation provides insights into influence of the cold forging process on dislocation rearrangement and grain refinement mechanisms. Finally, the compressive behavior of the WAAM and WAAM-forged samples through strain rates ranging from $0.0001s^{-1}$ to $0.1s^{-1}$ is characterized by serrated flow and stress drop phenomena caused by the PLC effect. The amplitude of stress drops was quantified, and a new equation was developed to describe the relationship between stress-drop amplitude and strain rate sensitivity, extending its applicability to other materials exhibiting the PLC effect.

4.2 Comparative Deformation Analysis of WAAM and WAAM-Forging by Simulation and Experimental

To establish a fundamental understanding of the thermal and mechanical behavior of the WAAM process, FEM simulation was conducted for both GMAW and CMT thin wall depositions. The simulation provides insight into critical parameters such as interpass temperature evolution, stress distribution and total deformation throughout the build. These results offer a valuable comparison of the heat accumulation patterns and structural integrity associated with the two processes. By analyzing the differences in thermal profile, the simulation serves as a predictive tool for evaluating deformation tendencies and potential defect formations during WAAM and WAAM-forging. The outcomes are then correlated with experimental findings, including 3D scanning and microstructural characterization, to validate the simulation's accuracy and enhance the understanding of the process-performance relationship.

4.2.1 Deformation Analysis by Simulation Process

4.2.1.1 Deformation Behavior and Stress Distribution of WAAM

The SW simulation revealed distinct differences in interpass temperature behavior between GMAW and CMT processes. Based on the temperature distribution in Figure 4.1(a) and (c), the top layers experience high heat accumulation and short cooling time. Therefore, the temperature of the uppermost layer of the wall is increases, which is similar to the findings by J. Sun et al. (Sun et al., 2021) for thin wall of Al5356. However, based on the interpass temperature, the highest peak temperature typically appears near mid-height of the deposited wall along the z-axis for both processes as plotted in Figure 4.1(b) and (d). As the layers are deposited sequentially, the heat continuously accumulates within the wall structure from the substrate to the top layer. In the early stages which near the substrate, much of heat can be conducted away into the cold substrate. However, as more layers are deposited, the lower layers are already warm, which reduces the ability to dissipate heat. This causes maximum heat to accumulate around the mid-height. These results are consistent with those reported in the literature by M. Köhler et al. (Köhler et al., 2020) where the highest interpass temperature approximately at the middle height of the wall.

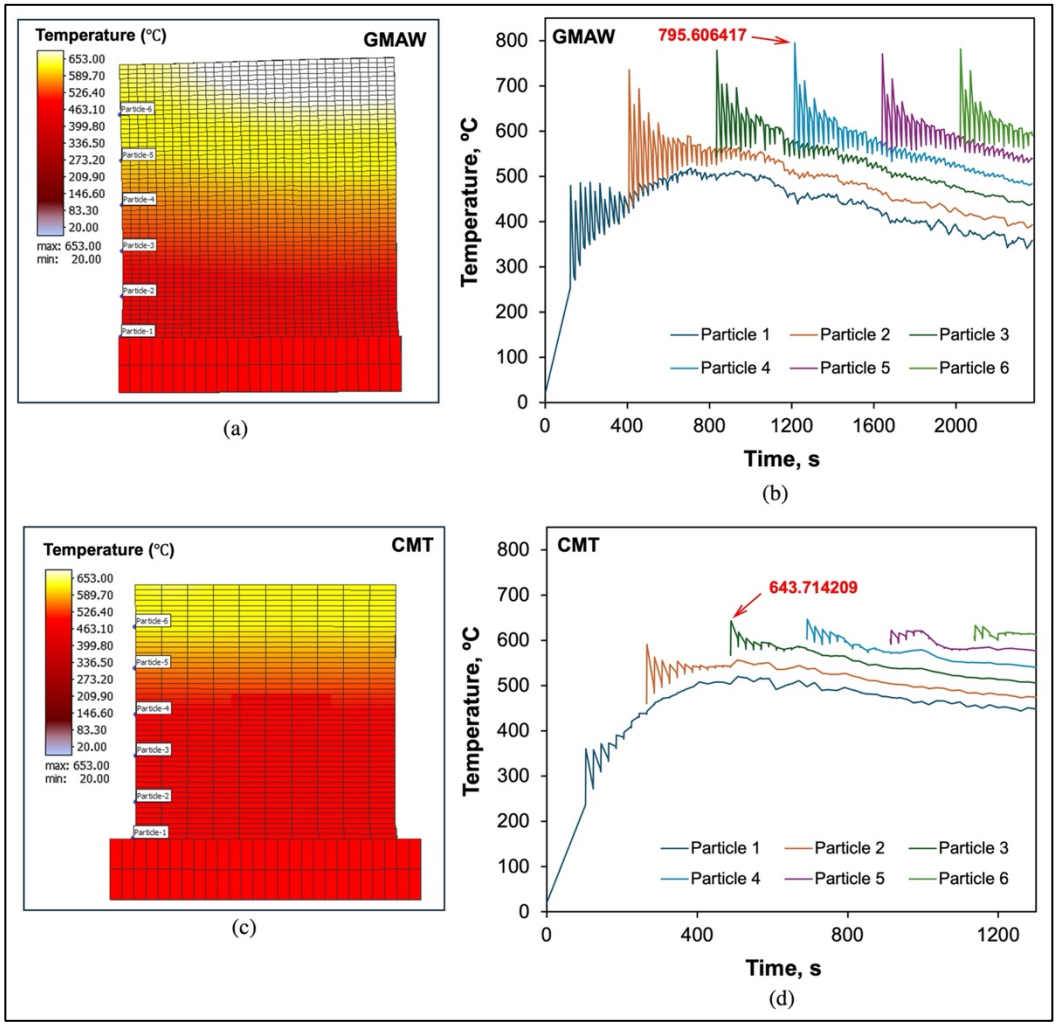

Figure 4.1 Interpass Temperature of Thin Wall Fabricated by ER5356 in SW (a-b) GMAW (c-d) CMT

In Figure 4.1(b), the GMAW wall reached a peak interpass temperature of 795.61 °C, whereas the CMT wall exhibited a significantly lower peak temperature of 643.71 °C, as shown in Figure 4.1(d). The temperature drops represent cooling period between deposition passes. The cooling of GMAW is longer makes it slower cooling rate because of temperature remains longer resulted by higher heat input at each peak in which vice versa with CMT process. The GMAW process employed a constant heat input of around 297.05 J/mm, resulting in a more uniform but continuous energy delivery. The constant heat input resulted in a sustained arc and less adaptive current control. Hence, this leads to broader thermal penetration and more pronounced thermal accumulation. Conversely, the CMT process utilized multi-level heat inputs ranging from 292.47 J/mm to 296.24 J/mm, which were slightly lower by approximately 0.27 % – 1.54 % compared to GMAW. The CMT process resulted more dynamic arc behavior due to intermittent short-circuiting and reduced energy transfer during droplet

detachment. Hence, the peak temperature in CMT process minimized the overall heat input but increases instantaneous localized heating.

Figure 4.2 presents the equivalent distributions where the maximum stress recorded for the GMAW process is 65.10 MPa while CMT process reaches a peak stress of 51.52 MPa. This is because the high temperature in GMAW process cause rapid expansion and plastic deformation in the wall. Conversely, the CMT process shows more uniform stress distribution, which highlight that CMT minimizes displacement and distortion due to better thermal control and induces lower equivalent stress levels compared to GMAW. The combined effect of temperature distribution and stress evolution reflected in the total displacement of the WAAM wall for both processes.

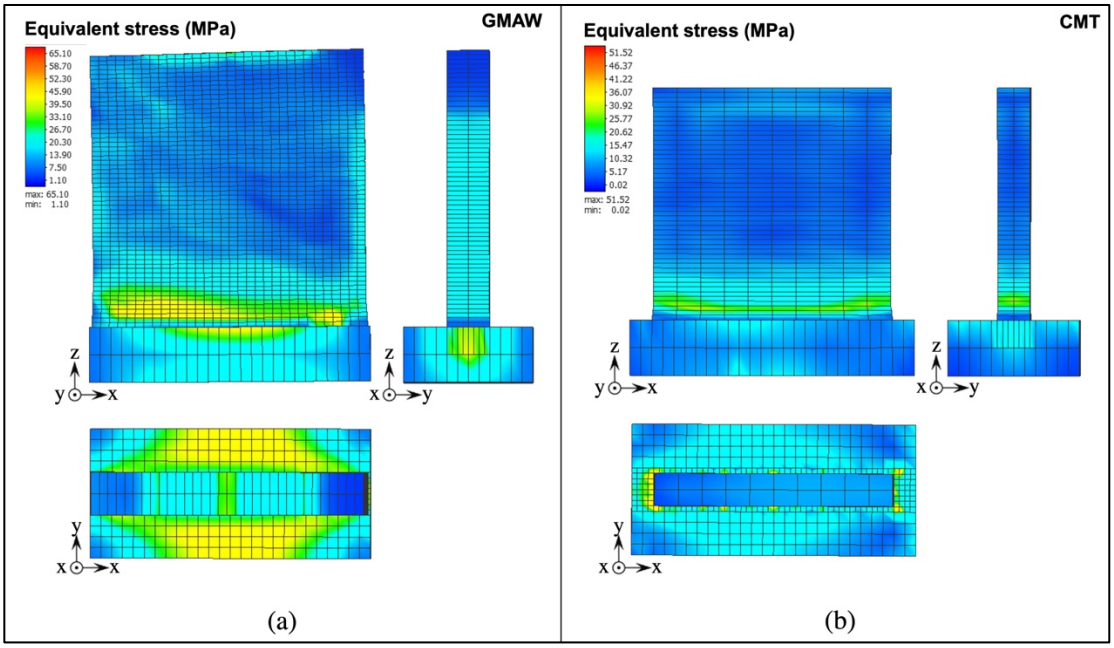

Figure 4.2 Equivalent Stress using SW (a) GMAW (b) CMT

In the simulation for both processes, the total displacement predicted reflects the deformation arising from cyclic heating and cooling during WAAM. The simulation results revealed that the GMAW wall in Figure 4.3(a) exhibited higher total displacement, which is 2.69 mm, compared to CMT wall with 0.88 mm. GMAW produced greater total displacement due to its higher heat input and less controlled metal transfer, resulting distortion in the fabricated wall as shown in the red box. In addition, the corner clamping on GMAW substrate resulted higher distortion compared to the edges clamping in CMT substrate. These findings are consistent with previous studies by R. Israr et al. (Israr et al., 2020) as the edges clamping on substrate resulted less distortion. Therefore, the CMT process resulted reduced displacement and improved bead deposition due to its stable metal transfer and lower thermal input. The short-

circuiting metal transfer and lower overall arc energy inherent in CMT contribute to reduced thermal accumulation and minimized thermal gradients, ultimately resulting better dimensional control as shown in Figure 4.3(b).

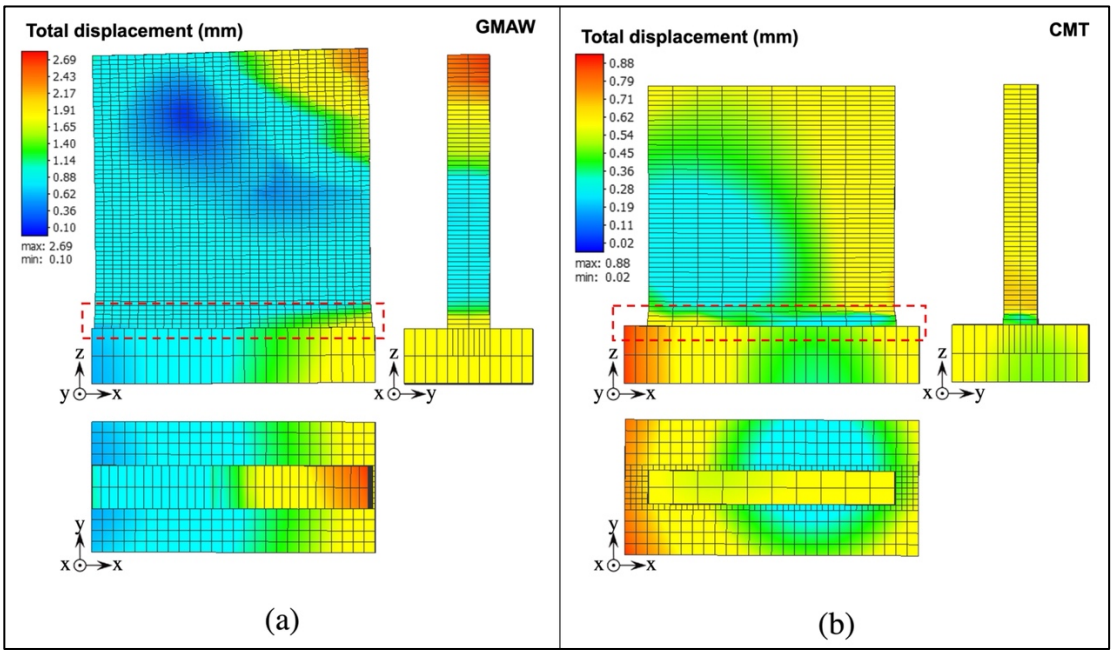

Figure 4.3 Total Displacement using SW Simulation for (a) GMAW (b) CMT

Comprehensive study of the simulation on thermal behavior strongly governs stress distribution and deformation during WAAM deposition. Both processes exhibit heat accumulation along the wall height in which the highest interpass temperature occurred around the mid-height region due to the progressive reduction in heat dissipation as the height of the wall increases. However, the GMAW process generates significantly higher thermal accumulation, leading to greater equivalent stress and larger total displacement compared to the CMT process. The higher and more sustained heat input in GMAW promotes thermal expansion and plastic deformation which consequently increases distortion of the deposited wall. In contrast, the CMT process provides better thermal control through its dynamic metal transfer and slightly lower effective heat input, resulting in lower peak temperature, reduced stress concentration and improved dimensional stability. Therefore, the simulation indicates that CMT is more favourable for producing WAAM structures with lower residual stress and deformation.

4.2.1.2 Forming Behavior and Deformation Characteristics of WAAM-Forging

The integration of SW and SF enables a continuous process-chain analysis that reflects the deformation from WAAM and subsequent cold forging response of ER5356 thin wall structure. The GMAW wall involves higher heat input compared to CMT wall. The higher energy causes uneven expansion and contraction during material deposition, resulting in a distorted and irregular wall structure. Hence, when the irregular GMAW-forged wall is placed in a die for cold forging, the contact between the wall and the die becomes uneven.

The contact pressure shown in Figure 4.4 was measured from the SF simulation at the contact interface between the upper forging die and the top surface of the WAAM thin wall during the upsetting process. The pressure distribution represents the local compressive contact developed as the die pressed the wall in the build direction. The maximum contact pressure was obtained from the region where direct die–wall contact occurred, particularly at the highest local contact zone of the deformed WAAM wall. Therefore, the contact pressure indicates the severity and uniformity of load transfer during cold forging rather than the average pressure over the entire wall surface. Based on the analysis, this geometric irregularity generates localized, high-pressure zones during the upsetting forging, and reaching peak die contact pressure of 259.47 MPa as shown in Figure 4.4(a). In contrast, CMT uses lower heat input, resulting in greater process stability. The stability of CMT wall allows for more symmetric interaction with the forging dies. This results in contact pressure being evenly distributed across the wall thickness, with significantly lower maximum contact pressure of only 0.32 MPa as shown in Figure 4.4(b).

The effective plastic strain shown in Figure 4.5 was measured from the WAAM thin wall material in the SF simulation after the cold upsetting process. The strain was evaluated within the plastically deformed region of the wall, particularly at the area subjected to direct compression between the upper forging die and the lower support surface. The maximum effective plastic strain represents the highest local accumulated plastic deformation in the forged WAAM wall, while the overall distribution indicates the uniformity of deformation introduced during cold forging. Therefore, the effective plastic strain was measured from the deformed WAAM wall and not from the die, substrate, or fixture.

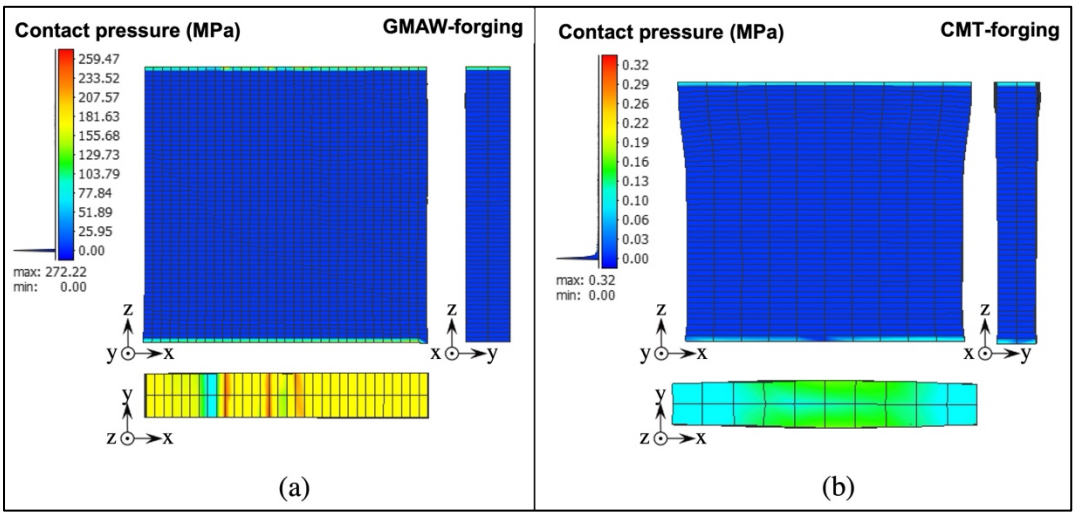

Figure 4.4 Contact Pressure using SF Simulation for (a) GMAW (b) CMT

The difference in contact conditions directly influences the effective plastic distribution within the forged wall. As GMAW leading to high contact pressure, the concentrated pressure forces an inhomogeneous distribution of effective plastic strain within the wall with maximum strain value of 0.04 as presents in Figure 4.5(a). This asymmetric flow confirmed poor utilization of the forging energy, as the strain energy was localized rather than distributed evenly throughout the volume. Instead of promoting bulk formation, the applied load primarily affects localized zones where the contact pressure is highest. Conversely, in CMT-forged wall, the symmetric load resulted homogenous distribution of effective plastic strain, achieving higher effective plastic strain of 0.32 compared to GMAW-forged, refer Figure 4.5(b). The uniform deformation behavior is essential for effective forming as it promotes consistent material flow and reduces premature failure during forging. Therefore, these results revealed that the thermal stability of the WAAM process strongly influences the efficiency of the forming process. Higher heat input during the fabrication of the wall not only increases the distortion but also affected the geometries irregularities that can reduce the forging effectiveness.

Therefore, the integrated process chain simulation of SW and SF on the deposition and forming clearly proved that the superior thermal behavior and stability of CMT wall led to a better geometrical fabrication, which subsequently translates into more uniformly distributed and manageable stress profile during cold forging, unlike the concentrated pressure observed with GMAW wall. Excessive heat input during WAAM developed uneven stress that led to localized pressure concentration and inefficient plastic deformation during forging process. These findings confirmed that

optimization of the WAAM process is a critical procedure for achieving efficient hybrid WAAM-forging, as the thermal and geometric characteristics formed during the deposition influence the deformation behavior, microstructural refinement and defect reduction in the hybrid WAAM-forging.

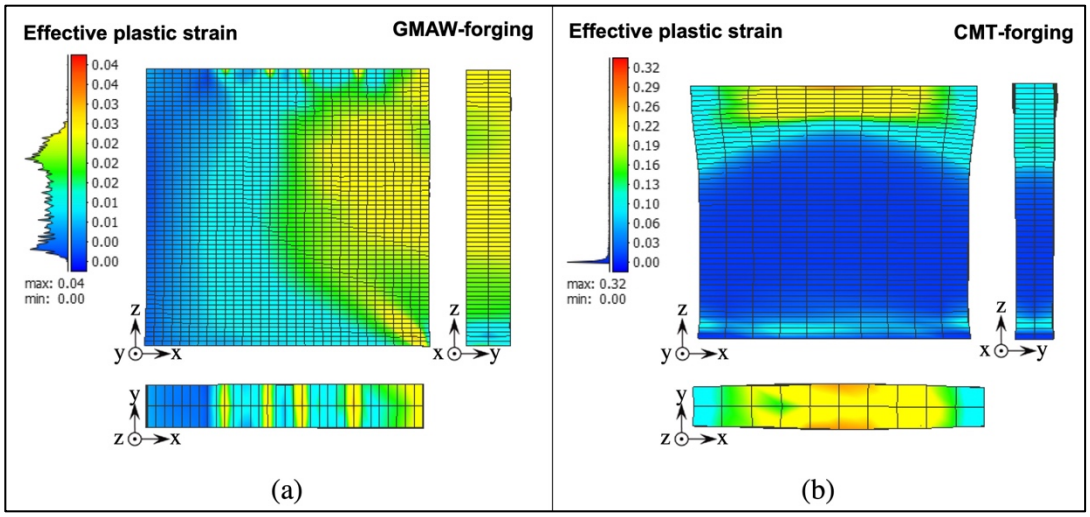

Figure 4.5 Effective Plastic Strain using SF Simulation for (a) GMAW (b) CMT

4.2.2 Dimensional and Geometrical Behavior of Fabricated Wall

While simulation provides predictive insights into thermal behavior, stress and distortion, experimental measurements confirmed the geometrical and dimensional accuracy of fabricated wall is necessary. The macrostructural of the thin walls produced via GMAW and CMT shows difference in wall shape and deformation behavior. In terms of dimensional accuracy as presented in Table 4.1, the GMAW simulated height is 126.80 mm, whereas the height is reduced to 101.50 mm, corresponding to a -24.93% error. This significant height loss reflects macroscopic shrinkage during cooling and wall bending. Similarly, simulated width resulted 19.95 mm is substantially greater than the actual measurement of thin wall, which is 15.00 mm, yielding a -33.00% error. The width reduction happened due to the material contraction and excessive material deposition in the simulation compared to experimental.

Based on the macrostructural of as-deposited wall, the GMAW demonstrated a fan-shaped profile as shown in Figure 4.6(a), where the lower layers exhibited wider deposition that gradually narrows toward the upper region. This behavior is caused by high and continuous heat input in the GMAW process, which resulted heat accumulation at the early stages deposition. The elevated thermal histories as presented

in Figure 4.1(b) reduces the solidification rate and promotes excessive molten pool spreading, which widen beads formation in the lower region of the wall. However, as the built height increases, heat dissipation enhanced to the surrounding and resulted the previous deposited layers to faster solidification, limiting molten pool spreading and produced narrower beads in the upper layers.

Table 4.1
Dimensional of WAAM and WAAM-Forging using Simulation and Experimental

WAAM Type	Side	Dimension (mm)		% error
		Simulated wall	Experimental	
GMAW	Length	127.90	127.00	-0.71
	Height	126.80	101.50	-24.93
	Width	19.95	15.00	-33.00
GMAW-Forged	Length	130.00	127.55	-1.92
	Height	120.80	95.40	-26.62
	Width	19.95	16.88	-25.00
CMT	Length	109.90	114.00	+3.60
	Height	107.10	100.40	-6.67
	Width	15.00	11.30	-32.74
CMT-Forged	Length	121.30	120.00	-1.08
	Height	102.50	85.80	-19.46
	Width	15.64	14.00	-11.71

In contrast, the CMT wall demonstrates a narrower bead formation during the initial layers, with a more uniform wall throughout the build height as presented in Figure 4.6(c). This is because of the controlled and lower heat input characteristic of CMT process stabilizes the molten pool and excessive spreading during early deposition. The controlled droplet transfer and reduced arc energy in CMT promotes rapid solidification and improved dimensional control, in which resulted in a narrower initial layer. As the height increases, the thermal histories remain more stable compared to GMAW, minimizing heat accumulation and enabling consistent bead geometry along

the height direction. The CMT wall also resulted in a less distorted wall with +3.60% error for the fabricated length. The deviation in height is smaller at -6.67%, indicating a closer match between predicted and actual geometry. The CMT length measurements show a slight positive deviation of +3.60% error, implying minimal distortion along the deposition path and high dimensional stability. The width error remains substantial at -32.74%, although less severe than GMAW case.

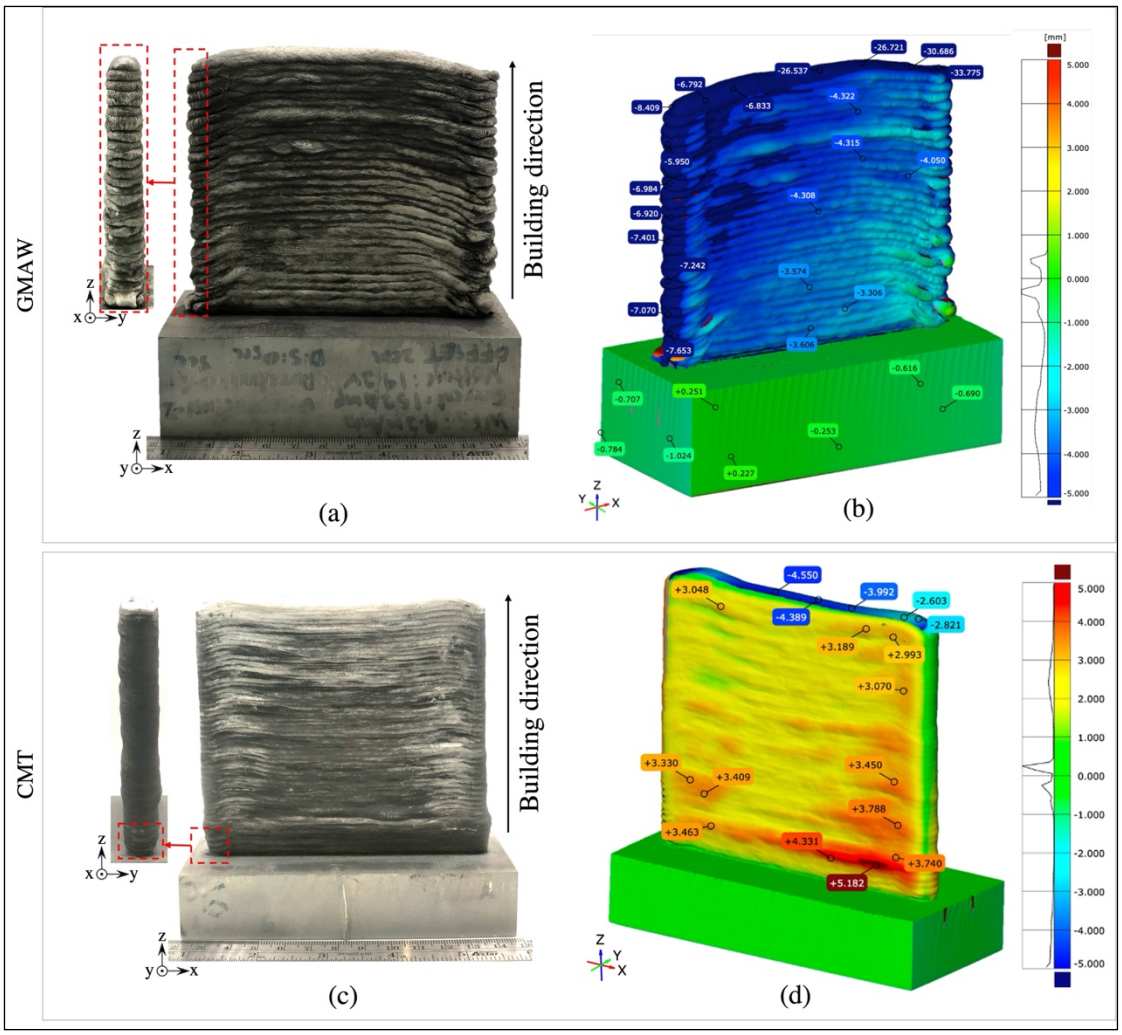

Figure 4.6 Actual and 3D-Scanned Geometries of (a-b) GMAW (c-d) CMT WAAM Walls

According to the thin wall macrostructure analysis, CMT is superior to GMAW in controlling distortion. The lower heat input and improved arc stability in CMT lead to significantly reduce warpage, better vertical accuracy, and more consistent geometry along the wall height. This observation is consistent with previous study, which also reported that the multi heat condition has led to the height increment and decreasing its width size due to the reduction of the penetration of melted material (C. Li et al., 2020). Similar to the review by N. Ana et al (Rosli et al., 2021), the present study also shows

as the heat input is lower, the molten pool does not have enough time to solidified, hence the ratio of width to height tends to be smaller. This consistent width reduction in both processes, GMAW and CMT may attributed to the simulation simplifications in modeling bead cross-sectional geometry. Hence, in future, to ensure the width of the wall more accurate to the actual thin wall, the adjustment of Goldak's heat source dimensions and increment of cooling time should be studied.

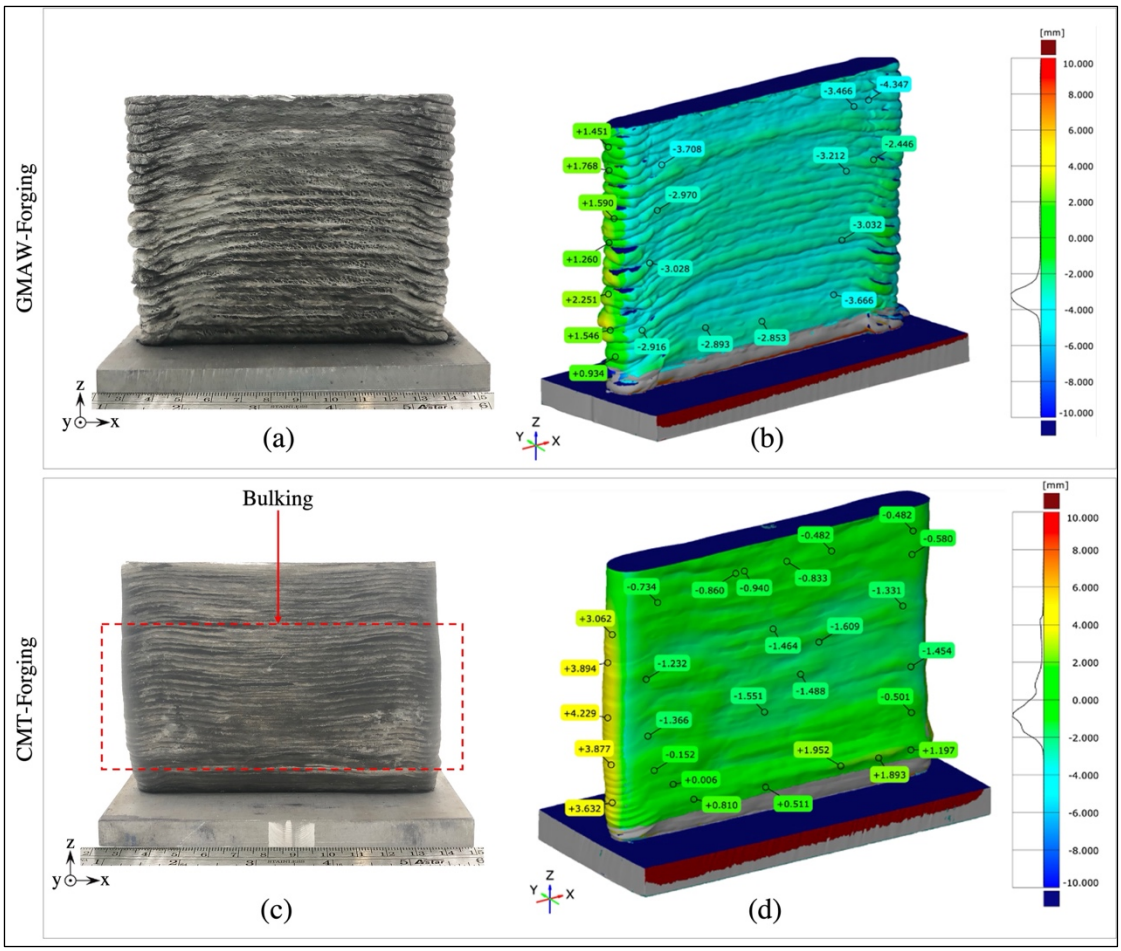

Figure 4.7 Actual and 3D-Scanned Geometries of (a-b) GMAW-Forging (c-d) CMT-Forging

As the WAAM wall subjected to cold forging process, the geometry is modified and changed the deformation characteristics. For the GMAW-forged wall as shown in Figure 4.7(a), the simulated length is 130.00 mm while the experimental measurement is 127.55 mm which corresponding to small error of -1.92%. However, larger deviations are observed in the vertical and lateral dimensions. The simulated height of 120.80 mm decreases to an experimental value of 95.40 mm, caused -26.62% error. Similarly, the simulated width of 19.95 mm is larger than the measured width of 16.88 mm in which resulting -25.00% error. These results caused by the deformation behavior as the distorted wall leads to uneven die contact and localized deformation during upsetting

process as discussed in 4.2.1.2. Hence, accelerated the material flow in specific regions and resulted greater dimensional deviation from the predicted model. According to the scanned analysis in Figure 4.7(b), the deviation map revealed strong asymmetry along the wall height, with negative deviations reaching approximately -3.00 mm to -4.00 mm across the central region, while positive deviations near the edges. The non-uniform color distribution indicates uneven bending toward the upper of the wall.

In contrast, a different trend is observed for CMT-forged where the simulated length of 121.30 mm is very close to the experimental value of 120.00 mm, resulting only -1.08% of error. The height deviation is also reduced compared GMAW-forged wall. The simulated height of 102.50 mm decreases to 85.89 mm, corresponding to -19.46% error. Nevertheless, the width error is significantly improved with simulated of 15.64 mm to 14.00 mm with -11.71% of error. The smaller deviations indicate more stable and uniform geometry is produced. Hence, these observations confirmed the relationship between the deposition stage and the subsequent forming response in hybrid WAAM-forging. Figure 4.7(d) confirmed the deformation behavior of CMT-forging as the deviation distribution appeared more uniform across the wall surface within approximately -1.50 mm to +2.00 mm. However, unlike the GMAW-forged wall, the CMT-forged wall shows bulking profile in the mid-height region as in the red box of Figure 4.7(c), yet still remined balanced material flow across the wall.

Based on the findings, a clear process of geometry and deformation relationship is identified by the strong agreement between simulation, dimensional measurements and 3D scanning for all processes. These analyzes confirmed the validity of the integrated SW-SF process chain modeling. Besides that, the optimization of WAAM deposition parameters is crucial to maximise the efficiency and accuracy of hybrid WAAM-forging processes as the initial geometry directly determines the subsequent deformation behavior of the final component.

4.2.3 Porosity Formation

The geometric deviations are often interrelated with internal defects that resulted during WAAM process. The surface integrity of WAAM thin wall as represented in Figure 4.8 reveals the differences between WAAM and WAAM-forging in terms of porosity distribution and density across all wall regions including bottom, middle, and top. Referring to the result in Figure 4.8(a), the bottom region of GMAW thin wall show

higher porosity than the middle or upper layers. At the beginning of the layer, the substrate temperature was relatively low. The heating started from the substrate which act as strong heat sink, created low heat accumulation and producing rapid solidification of the molten pool. Therefore, the rapid solidification of the melt pool restricts the hydrogen to escape and microvoid is produced due to the entrapment of dissolved hydrogen. As a result, higher porosity is analyzed at the bottom region of the wall. The existence of the porosities may cause by the impurities or contamination of the wire filler and the substrate. As reported by T. Hauser et al. (Hauser et al., 2021) and M. Arana et al (Arana et al., 2021), the moisture, grease or oxides exists during the initial deposition produce atomic hydrogen or oxides, then become trapped as pores in the bottom region. In addition, previous studies have highlighted that during the starting of the thin wall formation, poorer shielding at the earlier phase can cause more spatter and unstable transfer, resulting high pore formation in bottom layers (S. Li et al., 2021).

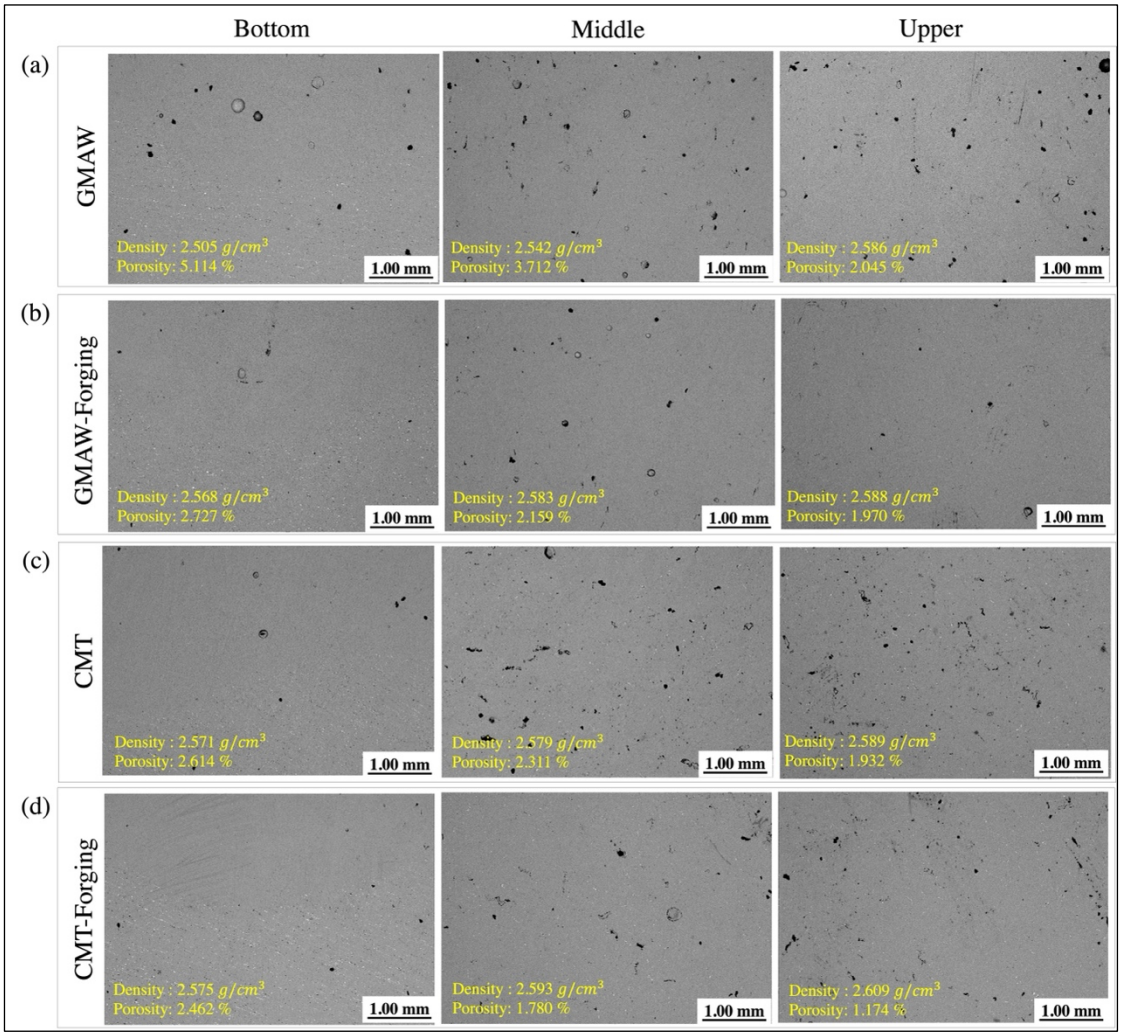

Figure 4.8 Porosity Formation at Different Position of (a) GMAW (b) GMAW-Forging (c) CMT (d) CMT-Forging

As the thin wall height increasing, more heat was accumulated. Hence, the interpass temperature and heat diffusion is high, leading to a slow solidification rate of the molten pool, which able more gases to escape. Thus, gradually decrease of pore formation is observed in the middle region. The middle region resulted moderate to higher porosity due to the typical repeated heating and remelting, continuity from the bottom layers. The hydrogen diffused from the molten pool and promoted growth of pore retention and enlargement of voids in the middle region. The top layer of WAAM thin wall shows the lowest porosity because their solidification rate is low, hence, the gas can escape and prevent subsequent trapping and growth. The hydrogen is more soluble in molten pool, resulting gas nucleated in the molten pool can escape. Once the top layer solidifies, the layers does not undergo reheating cycles, hence, no redissolve hydrogen exsolution and pore growth. However, in GMAW, the porosity produced was in moderate to high porosity compared to CMT process. Therefore, the thermal management capability of CMT resulted more uniform density distribution along the build direction.

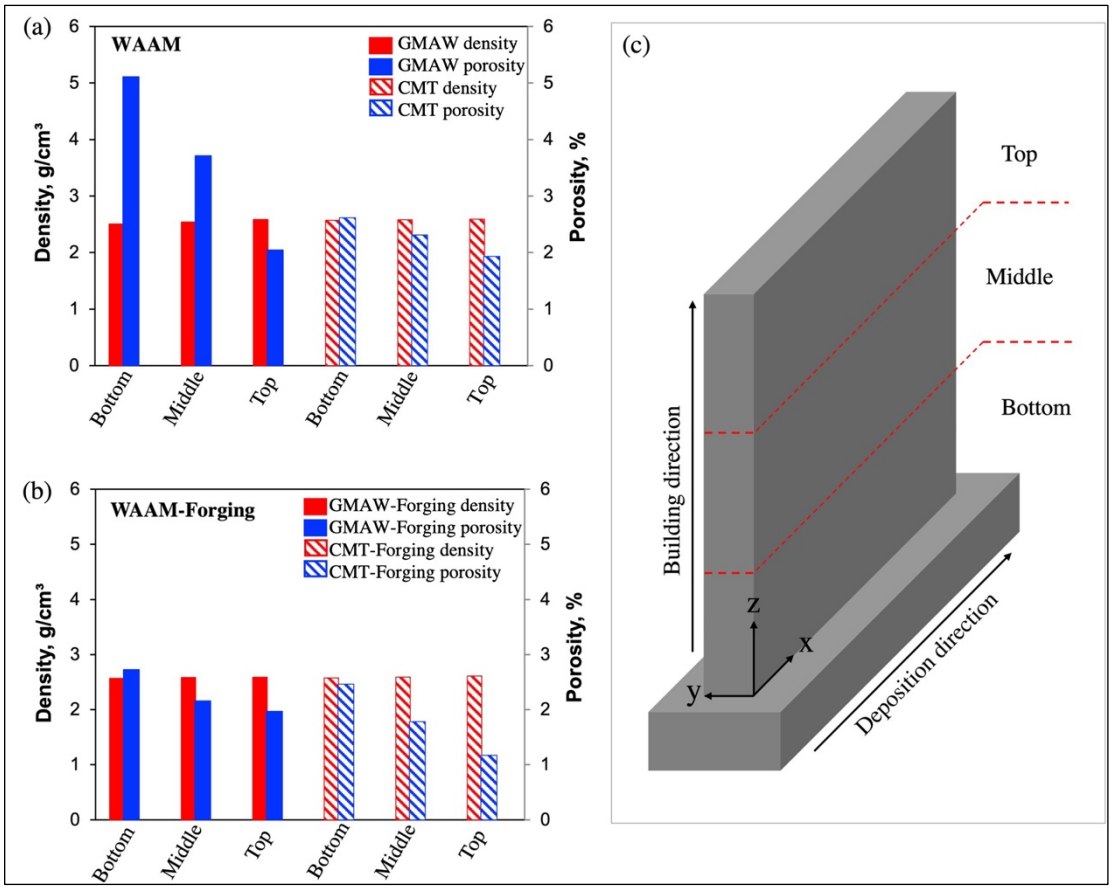

Figure 4.9 Density-Porosity Relationship of Different Process (a) WAAM (b) WAAM-Forging (c) WAAM Wall Observation Position

As the WAAM wall undergo post-processing of cold forging process, the porosity evolution clearly observed in Figure 4.8(b) and (d). Both GMAW-forged and CMT-forged show improved densification compared to as-deposited wall. Referring to Figure 4.9(b), the GMAW-forged shows density increases across all regions (2.568 – 2.588 g/cm^3), while the porosity decreases significantly (1.970 – 2.727%). The largest reduction occurs in the top region where the porosity drops from 5.114% to 2.727% after forging process. Besides that, the CMT-forged wall also improved in densification with the density increasing up to 2.609 g/cm^3 and porosity reduced to as low as 1.174% in the bottom region. This improvement is attributed to compressive plastic deformation during upsetting. Uniform compressive strain enhanced the pressure within the material which is critical for effective pore collapse. This observed trend is in good agreement with previous published studies by S. Kumar et al. (Kumar et al., 2018) where the cold forging reduction drastically decreased the porosity of aluminium alloy.

The porosity formation in WAAM can be associated with the elemental distribution identified through EDX analysis as shown in Figure 4.10. The variation of Mg content between the GMAW and CMT samples can be attributed to the different thermal characteristics of the two WAAM modes. In the GMAW sample, the Mg content decreased slightly from the standard ER5356 value of 5.12 wt% to 5.02 wt%, which may be associated with Mg evaporation during the higher heat input and longer thermal exposure of the arc deposition process. In contrast, the CMT sample showed a higher measured Mg content of 5.46 wt%, which indicates better Mg retention due to the lower heat input, controlled short-circuit transfer, and reduced thermal exposure of the CMT process.

Better Mg retention in CMT may help maintain the solid-solution strengthening potential of the Al-Mg alloy, while the more stable thermal condition reduces melt pool instability and gas entrapment that can contribute to pore formation. Therefore, the improved elemental retention and reduced porosity in the CMT sample support the observed improvement in surface integrity and mechanical performance. The slight increase in Mg content measured by EDX may also be influenced by local elemental distribution and the semi-quantitative nature of EDX analysis, where the measured value depends on the selected scanning region. Hence, the difference in Mg content between GMAW and CMT reflects the combined effect of process-related thermal behavior, Mg evaporation tendency, and local compositional variation within the WAAM deposit.

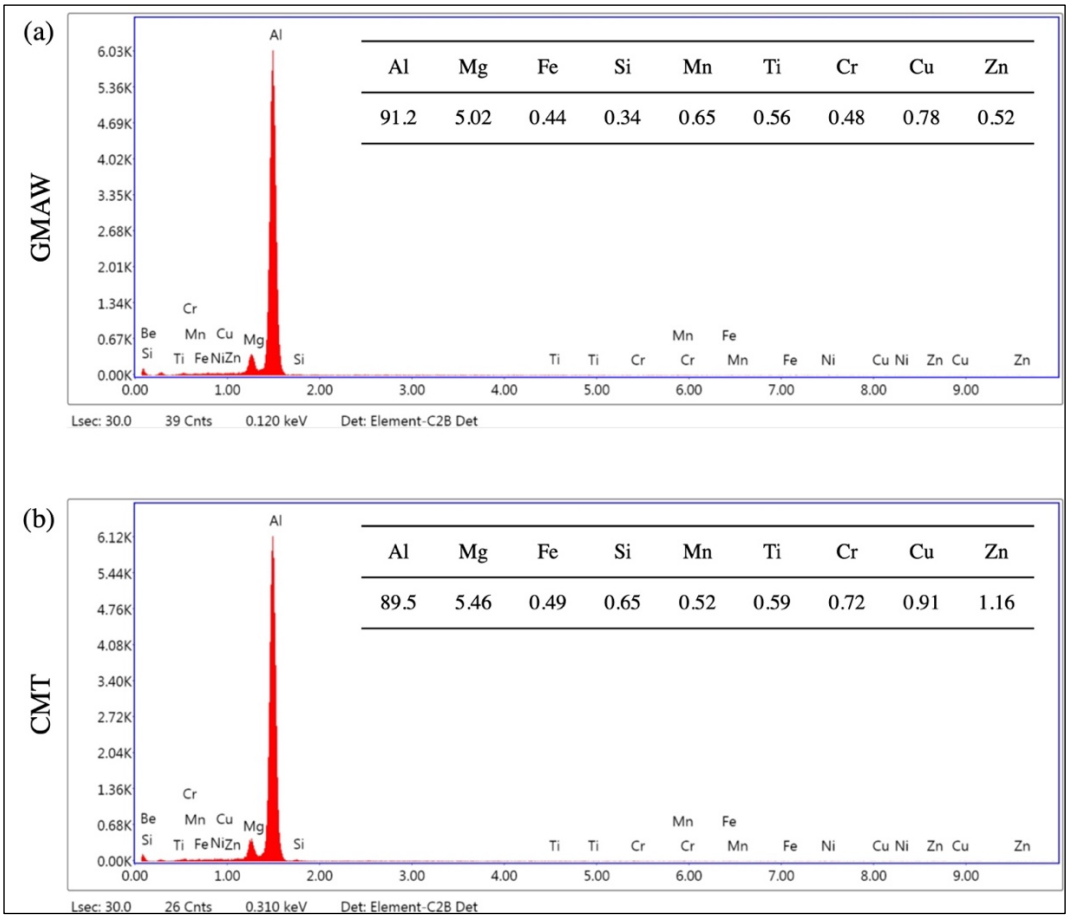

Figure 4.10 Chemical Composition Analysis of Different WAAM Modes (a) GMAW (b) CMT

The characteristics of the process reflecting the WAAM deposition stage which governs the structural integrity and subsequent forging response of ER5356. Since microstructural morphology reflecting the porosity percentage that critically influence the material characteristics, the CMT resulted stable heat input during the fabrication compared to GMAW. Although cold forging enhances densification in both processes through pore elimination, more uniform strain distribution is observed in CMT and better dimensional predictability. Thereby making CMT a more reliable process route compared to conventional GMAW in this research.

4.3 Mechanical Properties of WAAM and WAAM-Forging

4.3.1 Tensile Performance of Thin Wall

The strength enhancement is clearly observed when comparing the WAAM and WAAM-forging for both GMAW and CMT processes. Although extensive tensile repeatability was limited by the available thin-wall geometry, the improvement in

mechanical performance after cold forging was supported by consistent evidence from porosity reduction, density improvement and microstructural observations. Besides that, the reliability of the observed trend was supported through the integrated simulation–experimental approach in this study. Therefore, the tensile results are interpreted as representative trends supported by complementary analyzes rather than as purely statistical comparisons.

The tensile test results for ER5356 WAAM and WAAM-forging were observed at three orientations (0°, 45°, 90°) as shown in Figure 4.11(a), summarized in Table 4.2. Based on the typical stress-strain relationship in Figure 4.11(b-e), all directions presented typical elastic region followed by strain hardening until fracture. In all processes, the tensile performance showed a consistent trend where specimens tested at 0° achieved highest UTS and YS, with a gradual decline at 45° and more pronounced reduction at 90°. As shown in Figure 4.12, the tensile response of the WAAM and WAAM-forged samples demonstrates that the mechanical performance was strongly influenced by both deposition mode and post-forging deformation.

Table 4.2
Tensile Strength of WAAM and WAAM-Forging

Sample	Specimen	YS (MPa)	UTS (MPa)	$A_{\%}$
GMAW	0°	114.0	212.0	13.0
	45°	118.0	202.0	10.9
	90°	148.0	162.0	0.5
Average		127.0	192.0	8.1
CMT	0°	144.0	245.0	21.0
	45°	142.0	222.0	10.6
	90°	124.0	190.0	4.7
Average		136.7	219.0	12.1
GMAW-Forging	0°	168.0	268.0	20.0
	45°	156.0	258.0	19.4
	90°	122.0	230.0	24.2
Average		148.7	252.0	21.2
CMT-Forging	0°	120.0	282.0	28.2
	45°	112.0	248.0	18.8
	90°	108.0	208.0	11.0
Average		113.3	246.0	19.3

Referring to Figure 4.12(a), GMAW at 0° specimen achieved UTS of 212 MPa, while 90° dropped to 162 MPa with low elongation of 0.5%. The severe ductility loss at 90° is directly linked to higher porosity levels which is up to 5.114% as shown in Figure 4.8(a). When loaded perpendicular to the interlayer, pores and defects act as crack-initiation sites. However, the YS increases from 114 MPa (0°) to 148 MPa (90°). As the porosity in GMAW is higher, hence, the porosity restricts the plastic flow. Therefore, higher stress to initiate the yielding is higher to initiate yielding. This behavior has been reported in defect dominated WAAM of Al-Mg alloy by L. Tonelli et. al (Tonelli et al., 2021) where early plastic instability elevates YS while significantly reducing the ductility.

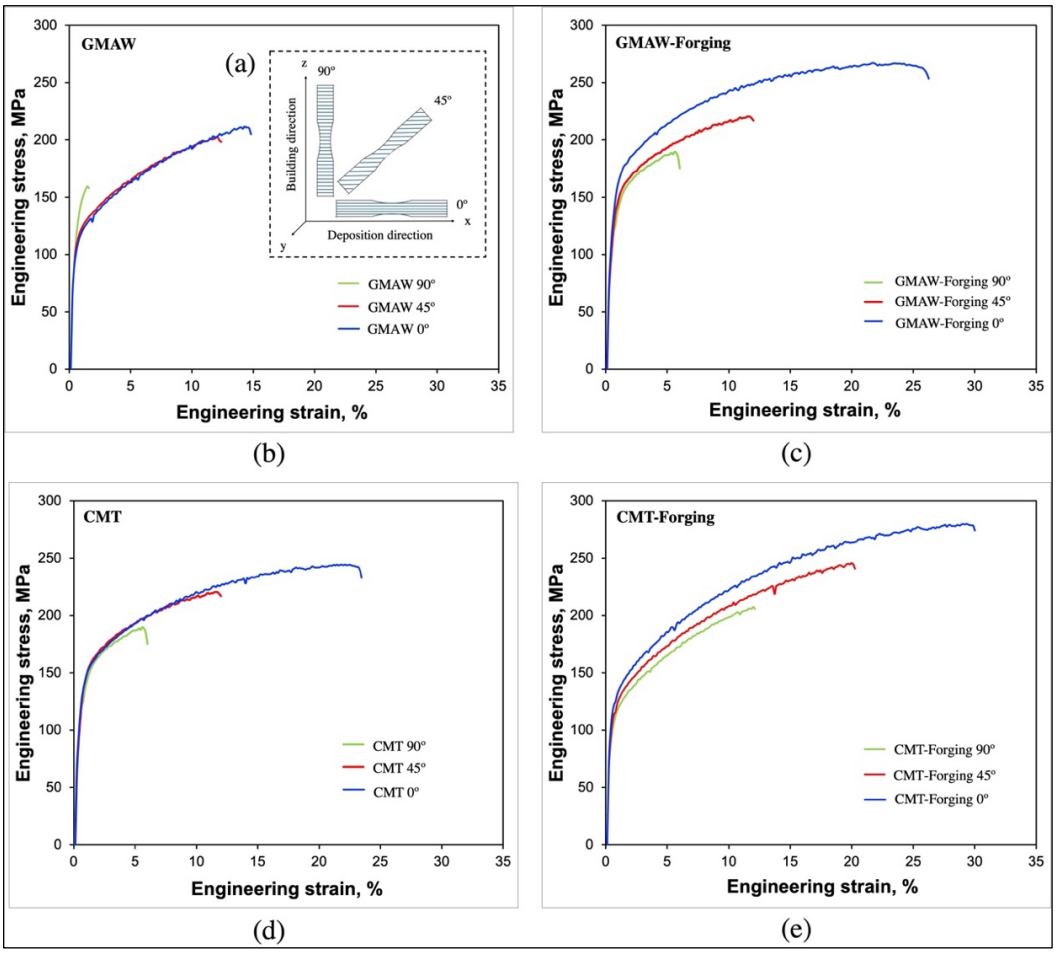

Figure 4.11 Typical Stress-Strain Relationship at Different Orientation (a) Tensile Specimen Orientation (b) GMAW (c) GMAW-Forging (d) CMT (e) CMT-Forging

Based on the analysis, CMT exhibited higher tensile performance than GMAW, particularly at 0° orientation, where the UTS of CMT reached 282 MPa compared with 212 MPa for GMAW. This corresponds to an improvement of approximately 33.0%,

indicating that the lower heat input and controlled droplet transfer in CMT produced a more stable deposit with lower porosity and better load-bearing capability. The CMT 0° specimen also exceeded the wrought ER5356 reference UTS by approximately 4–5%, showing that the deposition quality of CMT was sufficient to produce tensile strength comparable to or higher than the standard material. This improvement is consistent with the reduced porosity, higher density, and more uniform wall geometry observed in the previous analyzes.

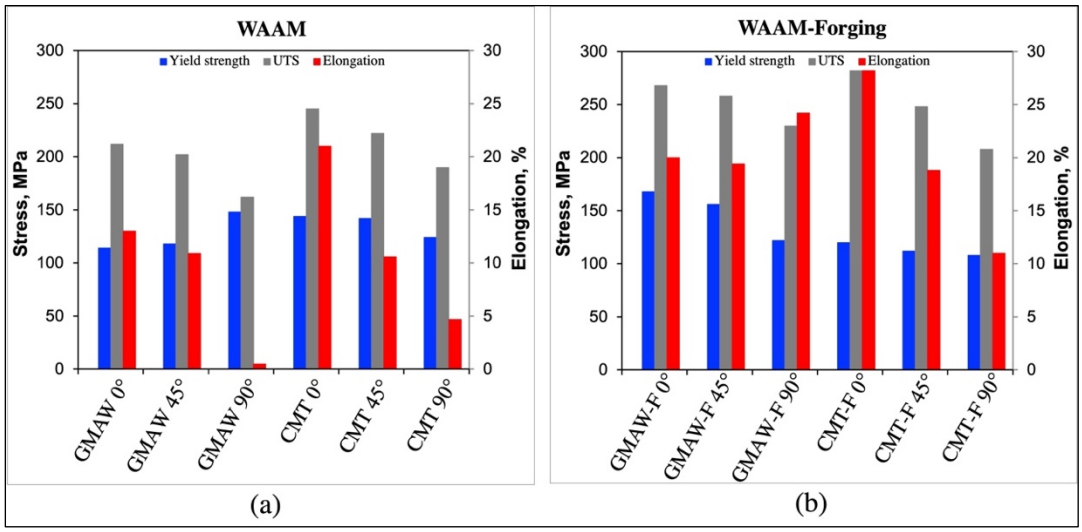

Figure 4.12 Yield Strength, Ultimate Tensile Strength and Elongation for (a) WAAM (b) WAAM-Forging Processes

Next, the tensile behavior of the WAAM-forged samples shows the influence of cold forging on both GMAW and CMT deposited walls as shown in Figure 4.11(c) and Figure 4.11(e). At 0° orientation, the GMAW-forged sample recorded a UTS of 268 MPa, YS of 168 MPa, and elongation of 20%. In comparison, the CMT-forged sample achieved a UTS of 282 MPa, YS of 120 MPa, and elongation of 28.2%. This indicates that CMT-forged exhibited approximately 5.2% higher UTS and 41.0% higher elongation than GMAW-forged, although its yield strength was 28.6% lower. The higher elongation and UTS of CMT-forged suggest better ductility and load-bearing performance, which can be attributed to the more stable CMT deposition condition, lower porosity, and more uniform wall geometry before forging. Although GMAW-forged showed higher yield strength, this may be associated with greater work hardening and localised deformation caused by the less uniform initial GMAW wall condition.

The tensile performance of ER5356 WAAM structures is strongly controlled by deposition stability and internal defect distribution. Due to lower heat input and stable

metal transfer in CMT deposition, CMT showed superior and more consistent mechanical behavior compared with GMAW in both as-deposited and forged conditions. This improvement is consistent with the earlier simulation, porosity, density, and dimensional analyzes, where CMT demonstrated lower deformation, reduced porosity, and better surface integrity. Therefore, CMT was selected as the preferred WAAM condition for subsequent detailed investigation through the hybrid WAAM-forging process.

4.3.2 Residual Stress Performance of Thin Wall

While the tensile results clearly highlight the superiority of CMT over GMAW, these improvements are closely related to the distribution of residual stresses within the wall, as thermal gradients during deposition significantly influence both microstructural integrity and mechanical performance. These stresses can be identified in longitudinal (σ_{xx}), which is parallel to the deposition path (x-axis), and transverse (σ_{yy}) in perpendicular to the deposition path (y-axis). The XRD results in Figure 4.13 shows that both longitudinal and transverse residual stress for WAAM and WAAM-forging of ER5356 alloy are significantly reduced after forging, confirming the beneficial role of plastic deformation in stress relaxation.

In the WAAM condition, the longitudinal residual stress is measure at 82.3 MPa, which is considerably higher than the transverse of 37 MPa. This observation aligns well with the theoretical understanding of stress evolution in WAAM thin walls as studied by J. Sun et al. (Sun et al., 2021). During layer of layer deposition, arc generates intense localised heating along the deposition path and contraction cooling. As illustrated in Figure 4.14, the shrinkage and contraction predominantly occur along the deposition path because the weld bead and deposit extents in this direction, resulting higher longitudinal stress. Moreover, the deposited molten metal solidifies and cools while being constrained by underlying substrate and previously deposited layers, causing differential thermal contraction.

As the region cold, thermal contraction is constrained by the cooler surrounding material and the clamped substrate, leaving a tensile residual stress in the longitudinal direction, refer to Figure 4.14(b). However, during unclamping, the bending distortion occurred, and the residual stress redistributes, but the longitudinal stress remains large to the final state. Hence, the WAAM thin wall exhibit higher longitudinal stress

compared to transverse, which relaxes more during cooling after unclamping. In contrast, in transverse direction, the material contraction is perpendicular to the deposited layers, making the thermal gradient and constrained shrinkage are much smaller, leading to lower transverse residual stresses.

Following cold forging, both longitudinal and transverse residual stresses decrease significantly, with values of 47.7 MPa and 22.9 MPa, respectively. Cold forging after WAAM introduces compressive plastic deformation, which can relieve and redistribute residual stresses (Rodrigues et al., 2019). The compressive loading imposed during upsetting enhances dislocation rearrangement, enabling partial recovery partial recovery processes that reduce internal strain energy. The reduction is more pronounced in the longitudinal direction, where the stress concentration is initially highest, indicating that forging is particularly effective at mitigating the dominant residual stress component. This finding is consistent with literature review that highlight forging and other post deposition thermomechanical treatments as effective strategies to minimize residual stresses and improve mechanical stability in WAAM components.

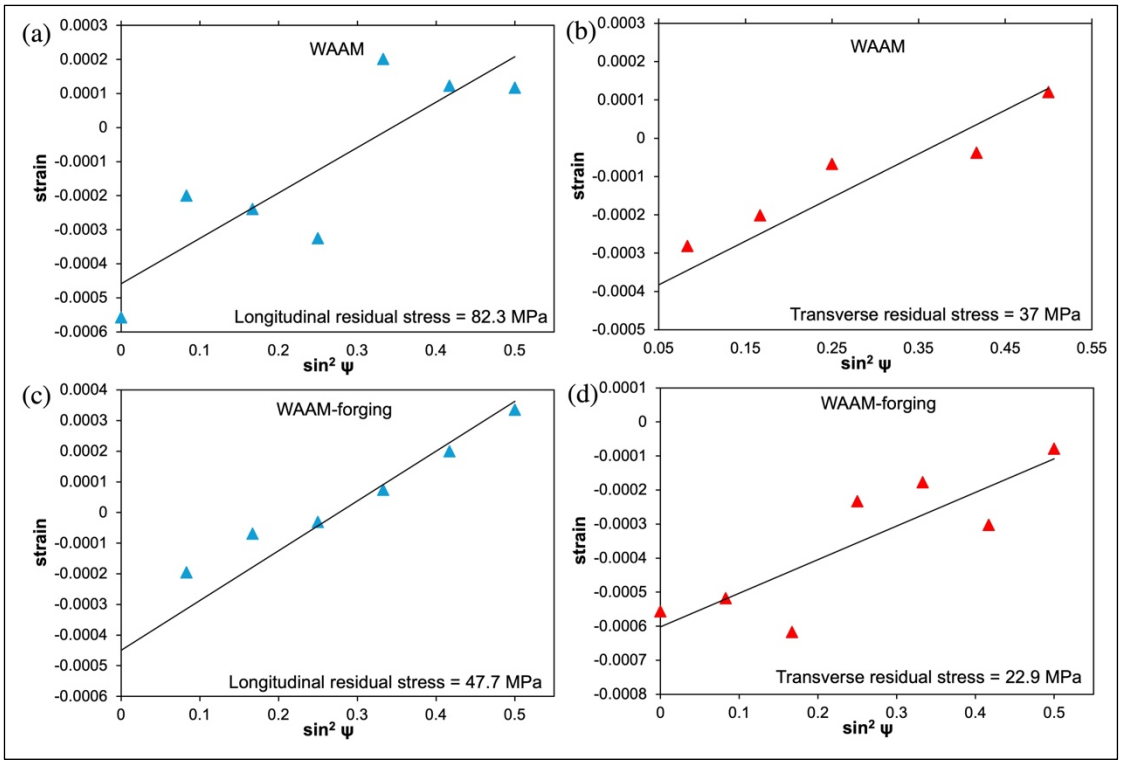

Figure 4.13 Longitudinal and Transverse Residual Stress by XRD Analysis (a-b) WAAM (c-d) WAAM-Forging

The comparison between WAAM and WAAM-forging thus highlights two important points. First, WAAM inherently produces anisotropic residual stress states, with longitudinal stresses exceeding transverse stresses due to the directional nature of

heat flow and contraction. Second, forging not only lowers the overall magnitude of residual stresses but also reduces the degree of anisotropy between the two directions. This more balanced stress distribution is desirable for structural reliability, as it minimizes the risk of distortion, cracking, or premature failure under service conditions. Moreover, the schematic in Figure 4.14(b–c) demonstrates how contraction and shrinkage phenomena are altered by post-deformation, shifting the stress balance from tensile-dominated states towards more relaxed and uniform conditions.

From a processing perspective, these results reinforce the suitability of the hybrid WAAM–forging route. While WAAM alone introduces significant longitudinal stresses that can compromise dimensional accuracy and service performance, the application of cold forging alleviates these stresses, thereby stabilizing the component. In combination with the tensile results, the correlation is clear: the reduction of residual stresses through forging contributes to the improved ductility and reduced anisotropy in mechanical properties, particularly for CMT-processed samples where the microstructure is already refined and porosity minimized. Thus, the integration of WAAM with forging not only enhances microstructural homogeneity but also delivers a dual improvement in residual stress state and mechanical performance.

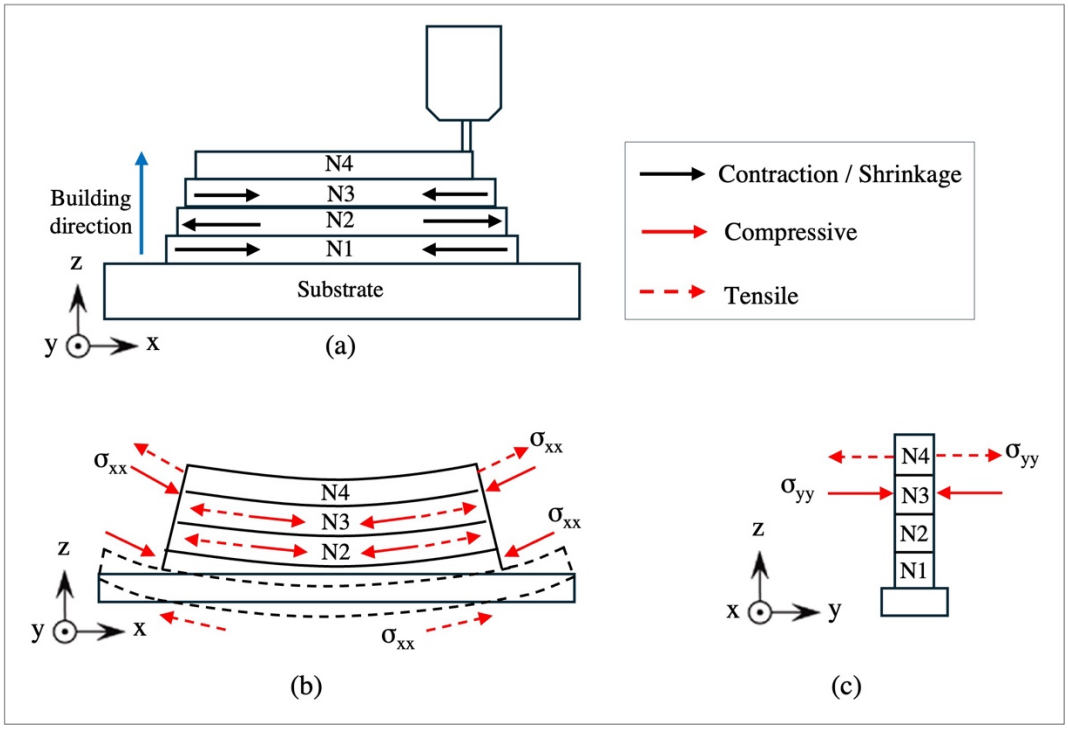

Figure 4.14 Schematic Diagram of Stress in WAAM Thin Wall (a) Contraction and Shrinkage Phenomenon (b)

According to the residual stress, the longitudinal stress is significantly higher than the transverse stress for both conditions with 82.3 MPa and 47.7 MPa for WAAM

and WAAM-forging, respectively. Since the hybrid process proceeds with upsetting cold forging, the stress concentration along z-axis is reduced, resulting lower longitudinal stress. The longitudinal stress for WAAM-forging is reduced via dislocation arrangement and localised plastic flow, which promotes strain hardening.

Since residual stresses affected the mechanical integrity of WAAM and WAAM-forging, the processes also reflected in the phase stress response. The elemental distribution obtained from EDX analysis provides into the origins phase stress in WAAM and WAAM-forging ER5356 alloys. As seen in Figure 4.15, the main peaks with strong intensity were detected in following planes: (111), (200), (220), (311), (222), and (400) which confirms an Al-rich matrix as expected for ER5356 (Al-Mg) wire. The (111) and (200) planes in ER5356 FCC structure are most densely packed where primary growth direction happened due to lower surface energy and greater proportion crystallographic, which equivalent to the findings by Y. Liu et al. (Y. Liu et al., 2022) and Y. Geng et al. (Geng et al., 2022). The growth alignment caused the X-rays to diffract more intense from these planes during the analysis, hence, resulting strong peaks.

Based on the XRD pattern, the intensity between WAAM and WAAM-forging are different. The WAAM pattern resulted high Al peak, with lower peaks of minor intermetallic phase compared to WAAM-forging, see Figure 4.15(a). This finding is consistent with previous studies by M. Wieczorowski et al. (Wieczorowski et al., 2023), which also reported dominant aluminium peak with Al-Mg phases appearing as minor diffraction. In contrast, according to Figure 4.15(a), the $Al_{3.892}Cu_{6.10808}$, $TiCu_2$ and Ti phases are only minor constituents, hence, resulting in negligible XRD signal.

However, the WAAM-forging pattern exhibits change where the XRD pattern revealed that intermetallic compounds (Al_4Cu_9, $Al_{0.65}Mg_{0.35}$, $Al_{0.95}Mg_{0.05}$, $Al_{0.25}Fe_{1.75}Ti$, $Al_{9.75}Fe_3$) produce the highest intensity peaks, while the Al matrix peak significantly decreases, refer Figure 4.15(b). This is because plastic deformation after cold forging process introduces high density dislocations that act as heterogenous nucleation sites for precipitate formation (Zhou et al., 2022). The cold forging process stored strain energy, promoting precipitation of intermetallic compounds.

Besides that, during forging formation, dynamic recrystallization partially occurs in localised regions and intermetallic phases migrate and concentrate at grain boundaries. As a result, the mechanical working breaks up coarse Al dendrites and redistributes second phases, effectively increasing crystalline coherence and peak

intensity relative to the depleted Al matrix. These changes may alter the XRD peak intensity and broadening by changing the preferred orientation and diffraction condition of the material. In addition, the densification effect and partial pore closure after forging may improve the detectability of existing intermetallic particles that were originally formed during WAAM solidification. Hence, the increased intermetallic phase intensity after cold forging is attributed to deformation-induced texture modification, lattice strain, residual stress redistribution, and improved phase detectability, rather than the formation of new intermetallic compounds during room temperature forging.

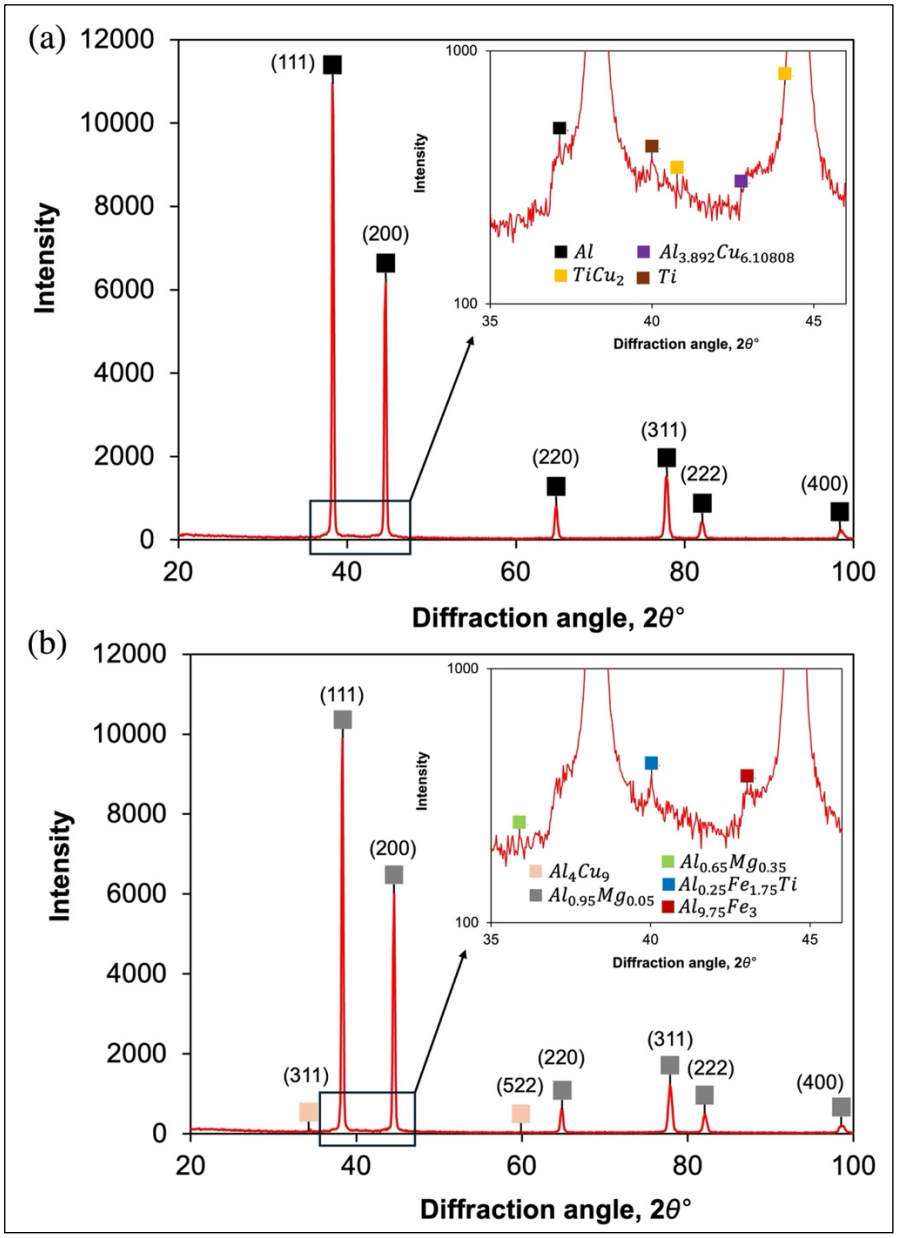

Figure 4.15 XRD pattern of ER5356 sample fabricated by different process (a) WAAM (b) WAAM-forged

4.4 Microstructure Analysis of WAAM and WAAM-Forging of ER5356

Figure 4.16 shows inverse pole figure (IPF) maps for WAAM and WAAM-forging processes of ER5356. The IPF map in Figure 4.16 (b) exhibits a heterogenous grain structure characterized by a mixture of coarse columnar grains and equiaxed grains. The grain size distribution is broad, with notably large grains particularly evident in the interlayer regions. The grain boundary in Figure 4.16(d) reveals high angle grain boundaries (HAGBs) concentrated at specific zones, with red arrows indicating regions of porosity and microcrack initiation, typically located at interlayer boundaries. The microstructure is typical of WAAM due to high heat input and slow cooling rates during layer-by-layer deposition.

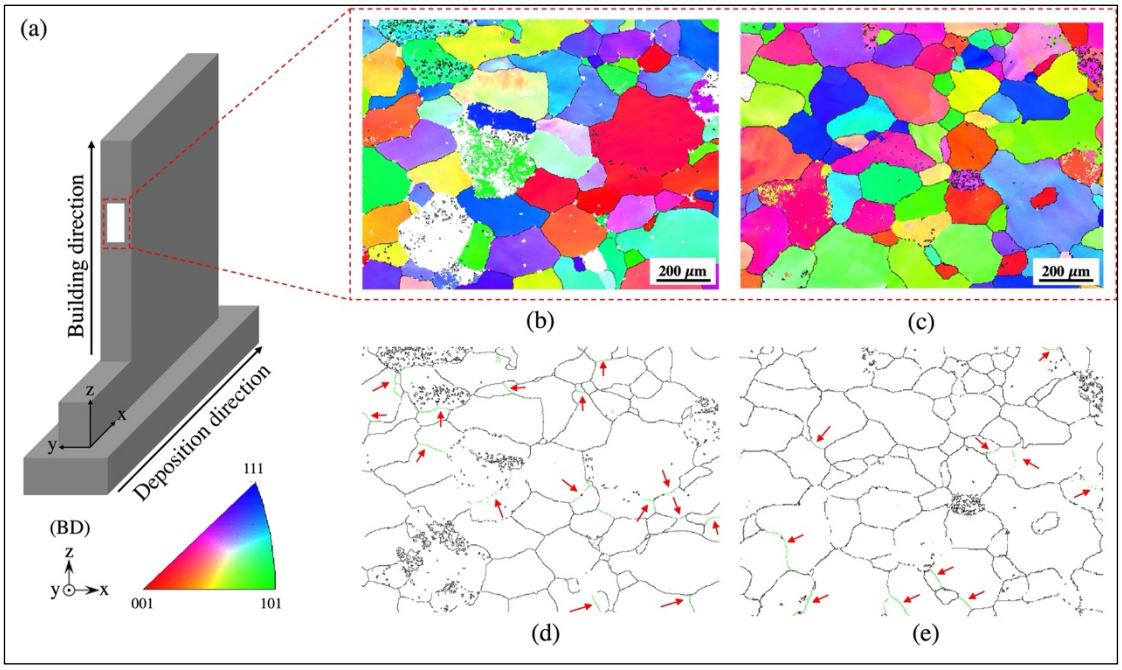

Figure 4.16 Inverse Pole Figure (IPF) maps for ER5356 (a) Scanning Location for on Cross Section (b and d) WAAM (c and e) WAAM-Forging

In contrast, the IPF map of WAAM-forging in Figure 4.16(c) displays a significantly refined and more uniform equiaxed grain structure with substantially reduced average grain size ($51.68\ \mu m$) compared to the WAAM state ($59.30\ \mu m$). The grain exhibit more homogenous coloration, indicating a narrower crystallographic orientation distribution. This is because cold forging induces plastic strain energy stored as dislocation. During deformation, the activation of dislocation multiplication creates geometric necessary dislocation (GNDs) that promote recrystallization. Hence refined equiaxed microstructure and the dislocation acts as nucleation site which forming new

recrystalizes grains with low dislocation density, similar to the microstructure evolution analysis of Al-Mg alloy by S. Zhou et al. (Zhou et al., 2022).

The grain boundary in Figure 4.16(e) shows a higher density of grain boundaries, suggesting dynamic recrystallization during plastic deformation. According to S. Zhou et al. (Zhou et al., 2022), high density dislocations provide preferential trapping sites for hydrogen atoms, effectively removing hydrogen gas from pores. Hence, this mechanism reduces pore stability and facilitates their closure. Notably, the red arrows highlighting defects are fewer and smaller, indicating substantial porosity closure and microcrack healing due to the cold forging process.

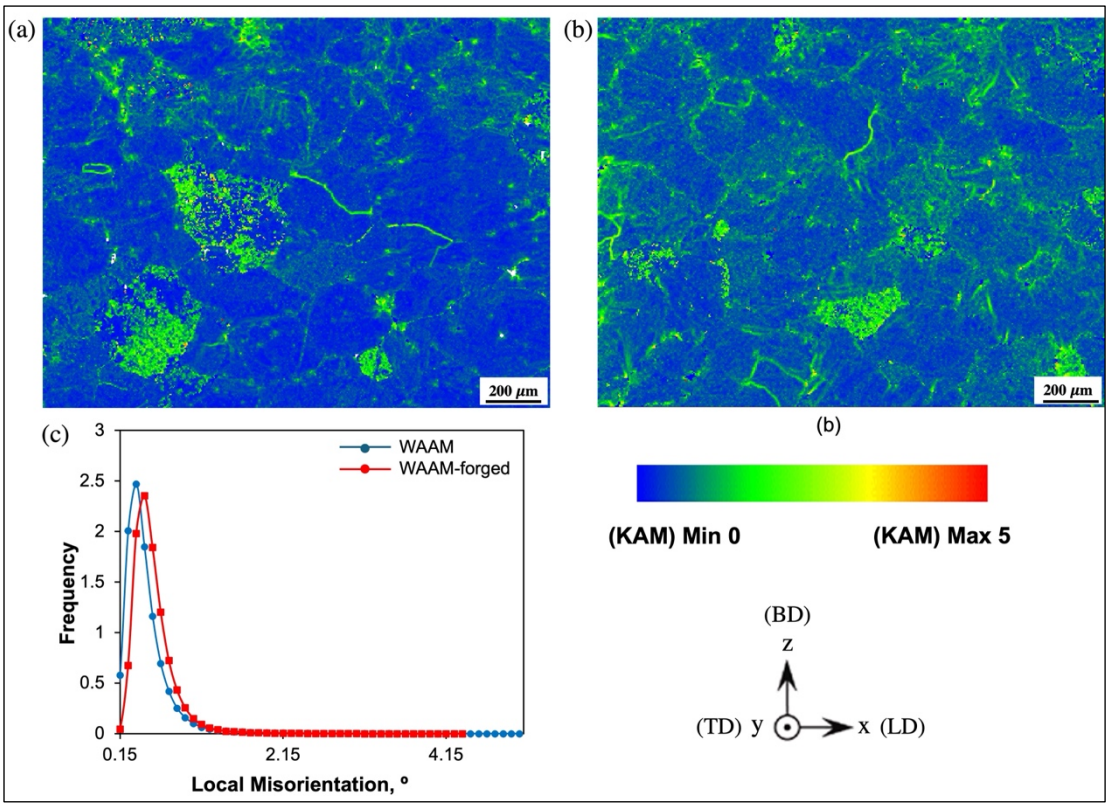

Figure 4.17 Kernel Average Misorientation (KAM) Maps Orientation of ER5356 (a) WAAM (b) WAAM-Forging (c) Frequency Distribution of Local Misorientation

In Figure 4.17, the KAM and local misorientation analyzes strain distribution behaviors between the WAAM and WAAM-forged samples. The WAAM sample exhibits lower KAM but higher frequency (2.471715) at low misorientation angle. These findings indicates that most regions within the microstructure in WAAM experience minimal lattice distortion while localised strain accumulates at specific zones such as interlayer boundaries as shown in Figure 4.17(a). The sharp, concentrated peak in misorientation distribution near 0.35º, reflects a heterogenous strain pattern,

where strain-free regions coexist with highly strained bands, consistent with the heterogenous grain morphology formed, refer Figure 4.16(d).

In contrast, the WAAM-forged sample shows higher KAM and a lower frequency (2.355071). this reflects a more homogeneous strain distribution as the plastic deformation during cold forging redistributes localized strain and increase overall density of GNDs. The strain becomes more evenly dispersed within refined grains, hence, enhanced structural uniformity due to recovery and sub grain boundary formation.

The IPF analysis revealed that cold forging as post deposition process of WAAM fundamentally transforms the ER5356 microstructure from columnar structure into refined equiaxed structure. This mechanism correlates in enhanced phase stability where increases grain boundaries promote intermetallic precipitation, which the XRD shifted from Al-dominant to intermetallic dominant peaks as explained in 4.3.2. These results revealed that cold forging homogenizes the dislocation distribution through recrystallization and boundary formation.

4.5 Compressive Behavior of ER5356 WAAM and WAAM-Forging

4.5.1 Post Compression Texture

The EBSD results highlight the influence of strain rate and cold forging on texture in WAAM and WAAM-forging. The texture pole figures provide visualization of crystallographic arrangements, revealing the degree of preferred orientation associated with the {100}, {110} and {111} planes as shown in Figure 4.18. For the base metal, WAAM shows a higher maximum intensity value, 6.60 (Figure 4.18(a)) than WAAM-forging, 6.05 (Figure 4.18(d)). This indicates that the as-deposited WAAM microstructure possesses a stronger crystallographic alignment, mainly due to directional solidification during layer-by-layer deposition. The slightly lower intensity in WAAM-forging indicated the forging redistributes the orientations, resulting a more uniform and refined grain structure.

At the lowest strain rate ($0.0001s^{-1}$), WAAM exhibits the highest texture intensity (7.62), which reflecting a pronounced strengthening of deformation texture. The larger grains in WAAM (59.3 μm) tend to rotate more under slow compression, resulting in sharper and more concentrated on the pole figures. In contrast, WAAM-

forging shows a much lower maximum intensity (5.16). Despite having smaller grains ($51.68\ \mu m$), the refined microstructure distributes strain more homogenously, preventing the formation of extreme texture peaks. This indicated that lower color intensity in WAAM-forging reflecting more uniform deformation and enhanced microstructural stability.

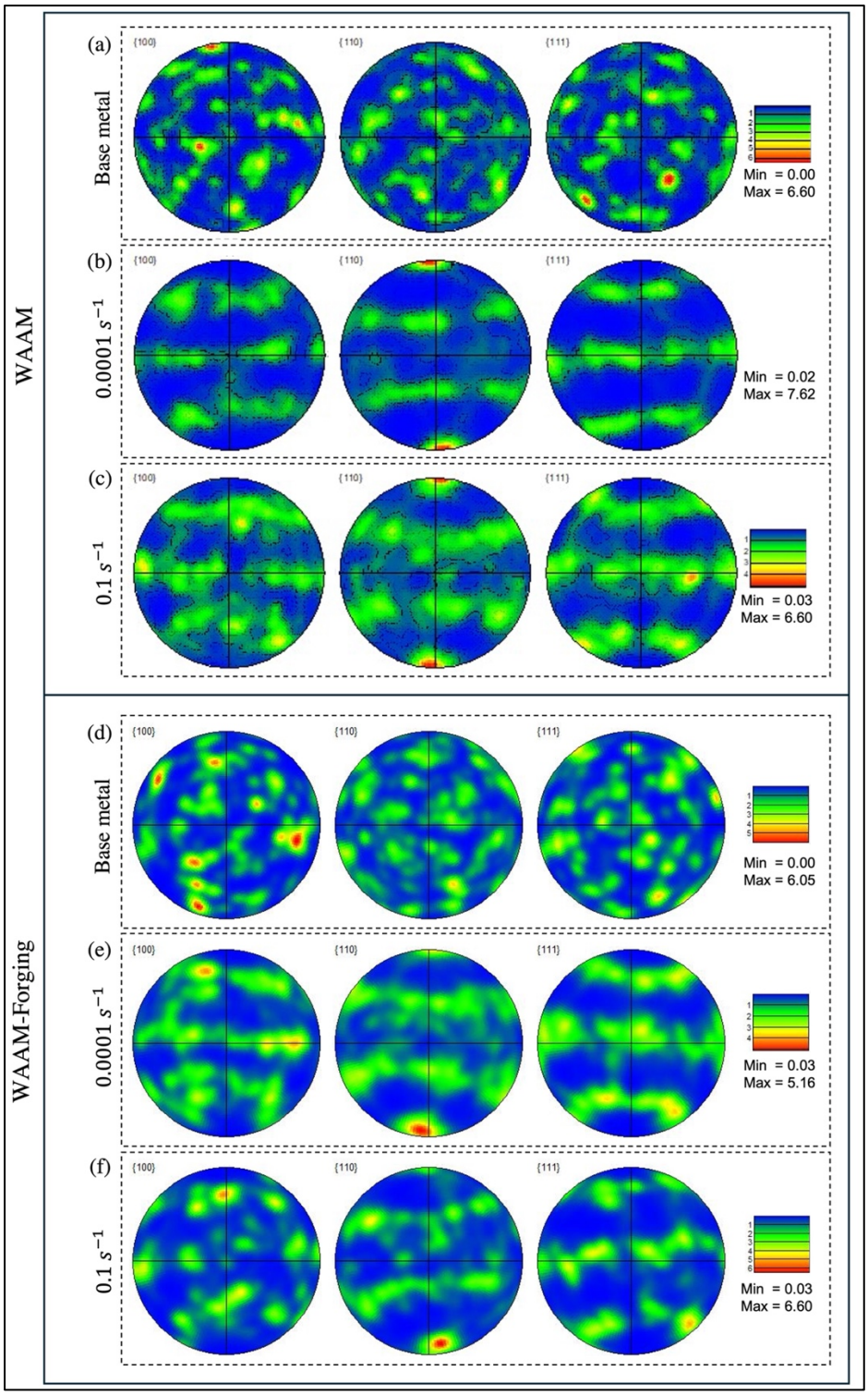

Figure 4.18 Polar Diagram of Al-Mg on Different Planes and Strain Rate (a) Base Metal, (b) $0.0001s^{-1}$, (c) $0.1s^{-1}$

At the highest strain rate ($0.1s^{-1}$), both WAAM and WAAM-forging displayed the same maximum intensity (6.60). This convergence suggests that rapid deformation restricts grain rotation and limits the development of sharp texture peaks. Under high strain rate conditions, both materials behave more similarly because the short deformation time supresses recovery and orientation rearrangement. As a result, differences introduced by grain refinement in WAAM-forging become less dominant at fast loading conditions.

Hence, reporting texture evolution using color intensity clearly shows that WAAM tends to form sharper deformation texture at slow strain rates due to its larger grains and directional solidification microstructure. Meanwhile, WAAM-forging develops more moderate intensities because its refined grains distribute deformation more uniformly. The progression of minimum and maximum color intensities across strain rates confirms that cold forging effectively stabilizes the microstructure, reducing extreme texture peaks while maintaining refined grain morphology. This supports the conclusion that WAM-forging enhances microstructural homogeneity even if the peak color intensity is lower.

4.5.2 Compressive Properties

In Figure 4.19 presents a comparative analysis of compressive mechanical properties of different strain rates ($10^{-4} - 10^{-1}s^{-1}$) for ER5356 processes via WAAM and WAAM-forging. Overall, both conditions exhibit strain rate sensitivity, where yield stress (YS), ultimate compressive stress (UCS) and hardening capacity (H_c) vary with increasing strain rate. The YS of both processes exhibits increased with higher strain rates. Referring to Figure 4.19(a), the yield stress fluctuates irregularly with strain rate. This irregularity from localised deformation and strain heterogeneity within the layered microstructure, which contains columnar grains and residual porosity. At low strain rates ($10^{-4}s^{-1}$), stress relaxation and dislocation rearrangement reduce the YS, while at intermediate rate ($10^{-3}s^{-1}$ to $10^{-2}s^{-1}$), dynamic strain aging (DSA) may temporarily increase it due to solute dislocation interaction, which is associated with the PLC effect. However, in Figure 4.19(d), the WAAM-forged samples show slightly higher and more consistent YS. The cold forging process refines and homogenizes the grains, enhancing dislocation density and eliminating interlayer voids. As a result, stress is distributed more evenly, leading to a more homogenous strain state.

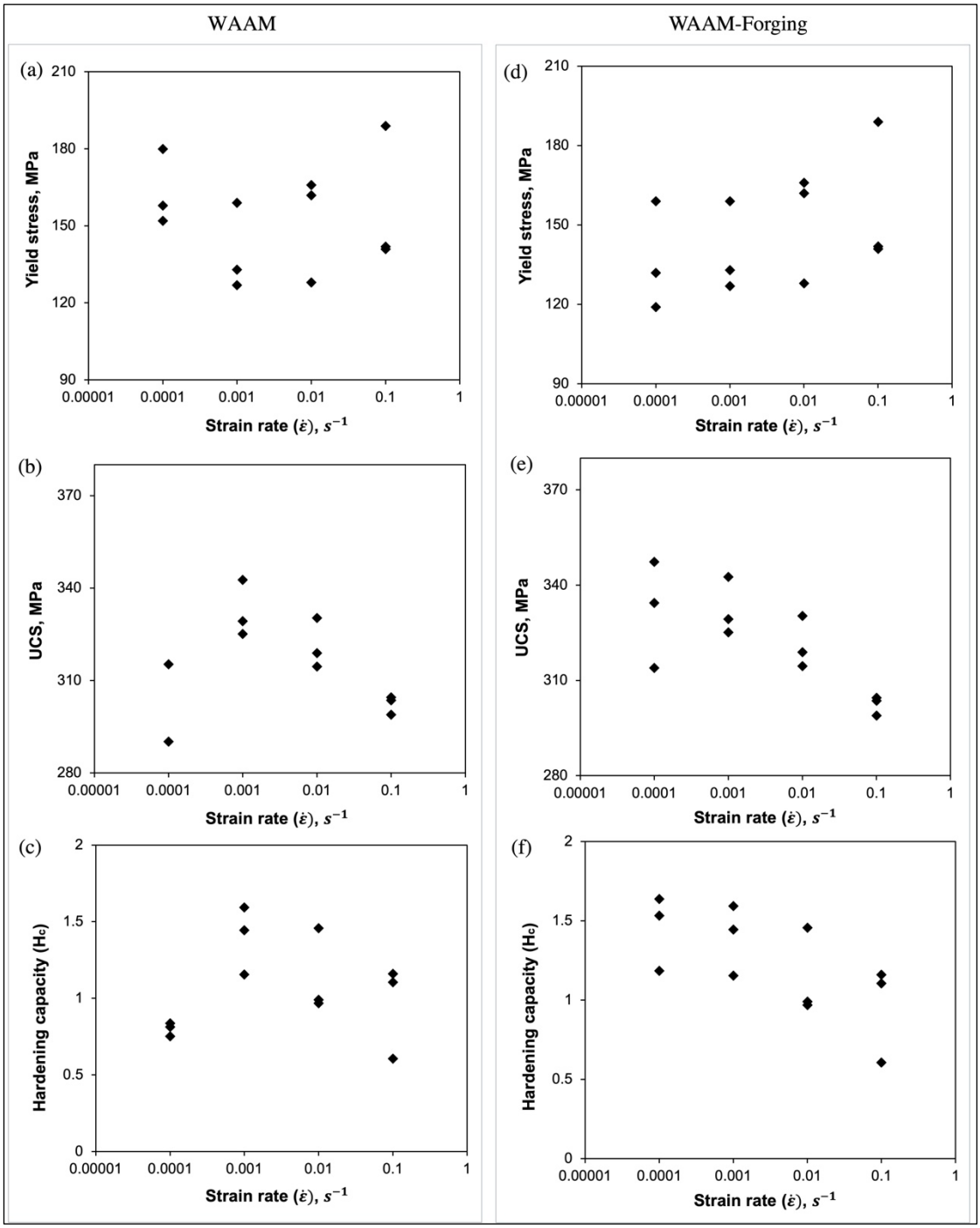

Figure 4.19 Compressive Behavior of WAAM and WAAM-Forging (a and d) Yield Stress (b and d) UCS (c and f) Hardening Capacity

The UCS of WAAM varies between 298 – 347 MPa, showing a clear decrease at higher strain rates, $\geq 10^{-2}s^{-1}$. This trend indicates that under rapid deformation, strain localization occurs more severely in the as-deposited structure, reducing its load bearing capacity. The non-uniform solidification and interlayer boundaries act as preferential sites for early softening. In contrast, the UCS in WAAM-forged samples slightly increasing with strain rate. The reduction of internal porosity and refined

equalized grains improve the material's ability to accommodate deformation, thus maintain higher compressive strength even at elevated strain rates. This reflects the enhanced work-hardening potential induced by the forging process.

Since hardening capacity considered as ratio of UCS to the YS, hardening capacity of WAAM at low strain rates ($10^{-4}s^{-1}$) decreases sharply as strain rate increases, refer Figure 4.19(c). This is attributed to the limited mobility of dislocations at high strain rates and the onset of localized slip bands associated with the heterogenous strain rate. While the WAAM-forging displays more uniform hardening response with reduced scatter. The presence of refined and recrystallized grains promotes stable dislocation interactions and higher strain compatibility among grains. As a result, the overall strain hardening behavior becomes homogenous, indicating structural integrity improvement after forging. Therefore, strain hardening exponent is evaluated to have better understanding of deformation behavior of ER5356.

4.5.3 Strain Hardening Behavior

Figure 4.20 presents the strain rate sensitivity analysis of ER5356 fabricated by WAAM and WAAM-forging processes, evaluated using the Common approach (Figure 4.20(a-b)) and the Lindholm's approach (Figure 4.19(c-d)). The corresponding strain rate sensitivity parameters (m and m_L) as a function of true strain are depicted in Figure 4.20(e-f), enabling direct comparison between the two analytical approaches. Both approaches quantify the material's sensitivity to deformation rate changes, reflecting the extent to which flow stress depends on the applied strain rate under constant temperature conditions.

Based on Figure 4.20(a-d), the trues stress decreases consistently with increasing strain rate at all true strain levels, resulting in a negative strain-rate sensitivity. This inverse relationship indicates that ER5356 or Al-Mg alloy exhibits dynamic strain aging (DSA) behavior, which associated with the Portevin-Le Chatelier (PLC) effect. At lower strain rates, dislocations move slowly, allowing the Mg atoms, which is solute atoms have sufficient time to diffuse and pin mobile dislocations, increasing the flow stress for motion. At higher strain rates, dislocation motion moves rapidly for solute diffusion to occur, inhibiting pinning interactions and reducing the stress. Consequently, the negative m values reveal that the flow stress is rate-dependent and governed by solute dislocation interactions typical of DSA mechanisms.

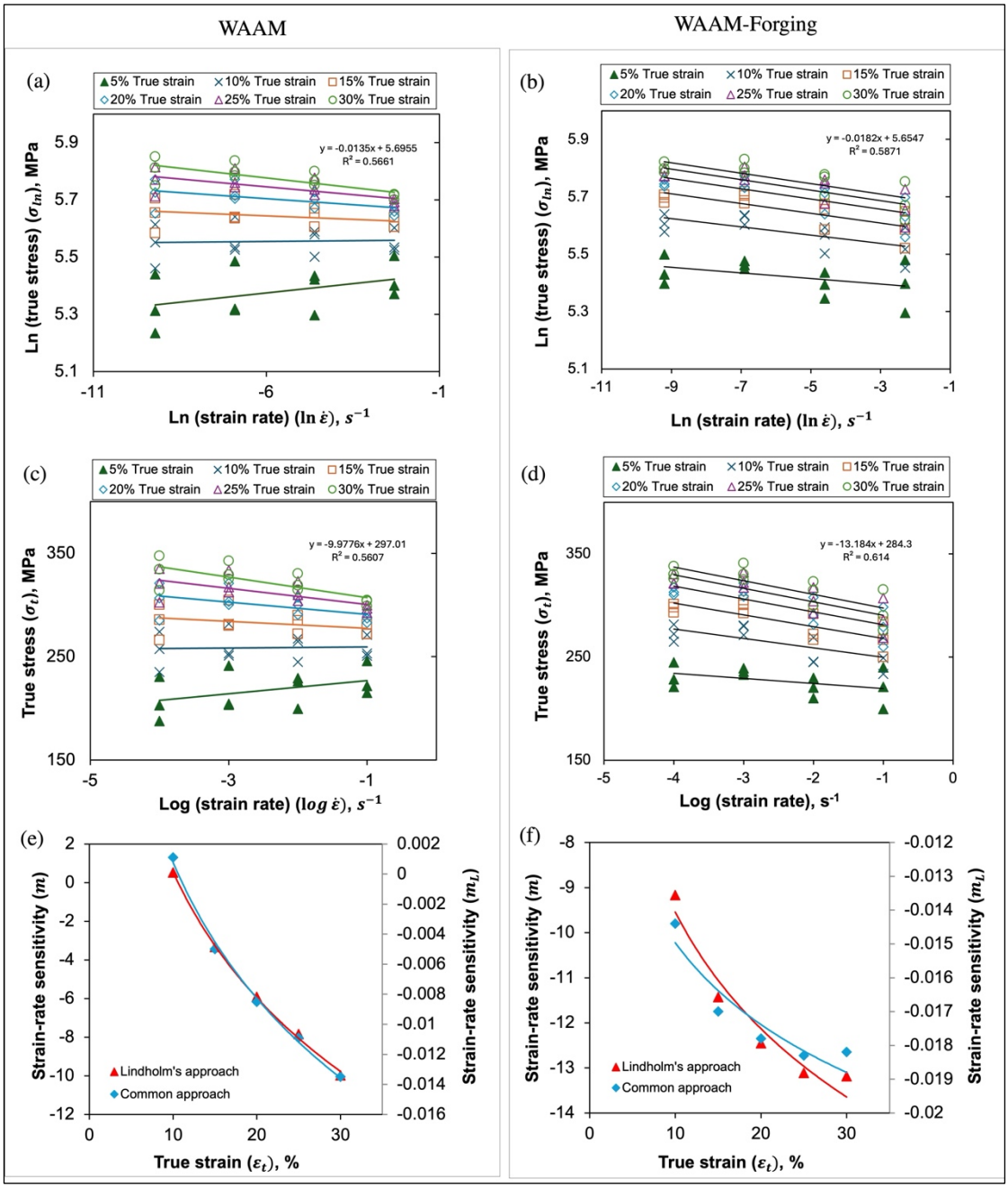

Figure 4.20 Typical Plots Used to Evaluate the Strain Rate Sensitivity at Different True Strain of WAAM and WAAM-Forging via (a-b) Common Approach (c-d) Lindholm's Approach (e-f) Strain Rate Sensitivity

However, comparing both processes, the WAAM-forged samples exhibit a larger magnitude of negative strain rate sensitivity than the WAAM process. From Common approach the slopes changes approximately -0.0135 (Figure 4.20(a)) for WAAM process to -0.0182 (Figure 4.20(b)) for WAAM-forging, while the Lindholm approach yields slopes of -9.98 (Figure 4.20(c)) and -13.184 (Figure 4.20(d)), respectively. This enhanced rate sensitivity following forging indicates that the plastic response of the forged ER5356 is more affected by strain rate variations. The increase

in magnitude is attributed to microstructural refinement and dislocation rearrangement. Hence, the porosity reduction and strain hardening during forging produce a denser and more uniform structure. This will enhance the rate dependent dislocation dynamics that govern PLC behavior.

Based on the analysis, both approaches demonstrate consistent strain rate sensitivity with increasing true strain, refer Figure 4.20 and Table 4.3, where the magnitude of m and m_L become more negative as deformation progresses. This trend signifies that the sensitivity of flow stress to strain rate intensifies with plastic strain, which consistent with the accumulation of dislocation and dynamic evolution of solute atmospheres. As strain increases, the probability of DSA grows, promoting local stress fluctuations and serrations associated with the PLC effect.

Table 4.3
Strain Hardening Sensitivity of WAAM and WAAM-Forging

True Strain, %	**WAAM**		**WAAM-Forging**	
	Common, m	**Lindholm, m_L**	**Common, m**	**Lindholm, m_L**
5	0.013	6.3545	-0.0097	-4.9308
10	0.0011	0.5239	-0.0144	-9.1666
15	-0.005	-3.3297	-0.017	-11.428
20	-0.0085	-5.9107	-0.0178	-12.454
25	-0.0109	-7.8397	-0.0183	-13.112
30	-0.0135	-9.9776	-0.0182	-13.184

Although both methods yield comparable trends, common approach produces higher correlation coefficients ($R^2 \approx 0.55 - 0.61$), suggesting superior fit quality under log-log transformations. This indicates that the power-law relationship captures better nonlinear dependence between stress and strain rate for ER5356 alloy. However, Lindolhm's approach provides alternative visualization that directly relate absolute stress change to rate variation, which provides clearer depiction of material behavior. Although m_L exhibits lower magnitudes, it effectively reflects the same overall trends observed in m, confirming the consistency between the two formulations.

Hence, both analytical approaches confirm that WAAM-forged ER5356 exhibits a stronger negative strain rate sensitivity than WAAM, signifying a more pronounced DSA and PLC effect. The common approach is recommended for parameter extraction due to its superior fitting quality and direct logarithmic

interpretation, whereas the Lindholm's approach serves as a valuable complementary method for visualizing absolute rate dependent stress changes, particularly in materials exhibiting serrated flow. Furthermore, the obtained strain rate sensitivity results provide critical insight into the dislocation processes governing the mechanical behavior of WAAM and WAAM-forging ER5356. These phenomena manifest as serrated flow or stress oscillation in stress-strain response which is associated with the PLC effect.

4.6 PLC Effect and Serrated Stress Flow

As the negative strain rate sensitivity observed in both WAAM and WAAM-forging ER5356 alloys implies DSA, this phenomenon leads to the PLC effect under certain strain-rate regimes. Figure 4.21 and Figure 4.22 present the stress-strain curve that clearly demonstrate the PLC effect in ER5356 or Al-Mg alloy. According to the analysis, both WAAM and WAAM-forging specimens exhibit serrated plastic flow at low strain rate conditions, refer to Figure 4.21(e-f) and Figure 4.22(e-f). As the strain rate lower (10^{-3} and $10^{-4}s^{-1}$), the curves formed repeated and pronounced stress drops. While at intermediate rates ($10^{-2}s^{-1}$), small and low amplitude of stress drop is observed, as presented in Figure 4.21(d) and Figure 4.22(d). In contrast, smooth of distinct serrations is formed at the highest rate ($10^{-1}s^{-1}$) as shown in Figure 4.21(c) and Figure 4.22(c).

The strain rate is a critical external factor that effect the strength, plasticity and flow stability of Al-Mg alloys. According to Zhang et al. (M. Zhang et al., 2024) serrated flow behavior caused by supersaturated solute atoms diffuse and cluster around mobile dislocations at room temperature. Hence, in Al-Mg alloys, Mg atoms act as substitutional solute atoms that distort the aluminium lattice due to Mg larger atomic size. As observed at low strain rates ($10^{-4}s^{-1}$) for both processes (Figure 4.21(f) and Figure 4.22(f)), the external compressed load increases slowly, resulting the dislocation moves slowly. Under this condition, Mg solute atoms become supersaturated around the mobile dislocations, forming pinning strong obstacles as illustrated in Figure 4.24(b-c). During this time, the internal stress accumulates within the grains until it eventually exceeds the pinning resistance, leading to a sudden unpinning as shown in Figure 4.24(d). The unpinning caused large stress drops, which are characteristic of type C serration. Figure 4.23(c) shows type C serration observed in the stress-strain curve.

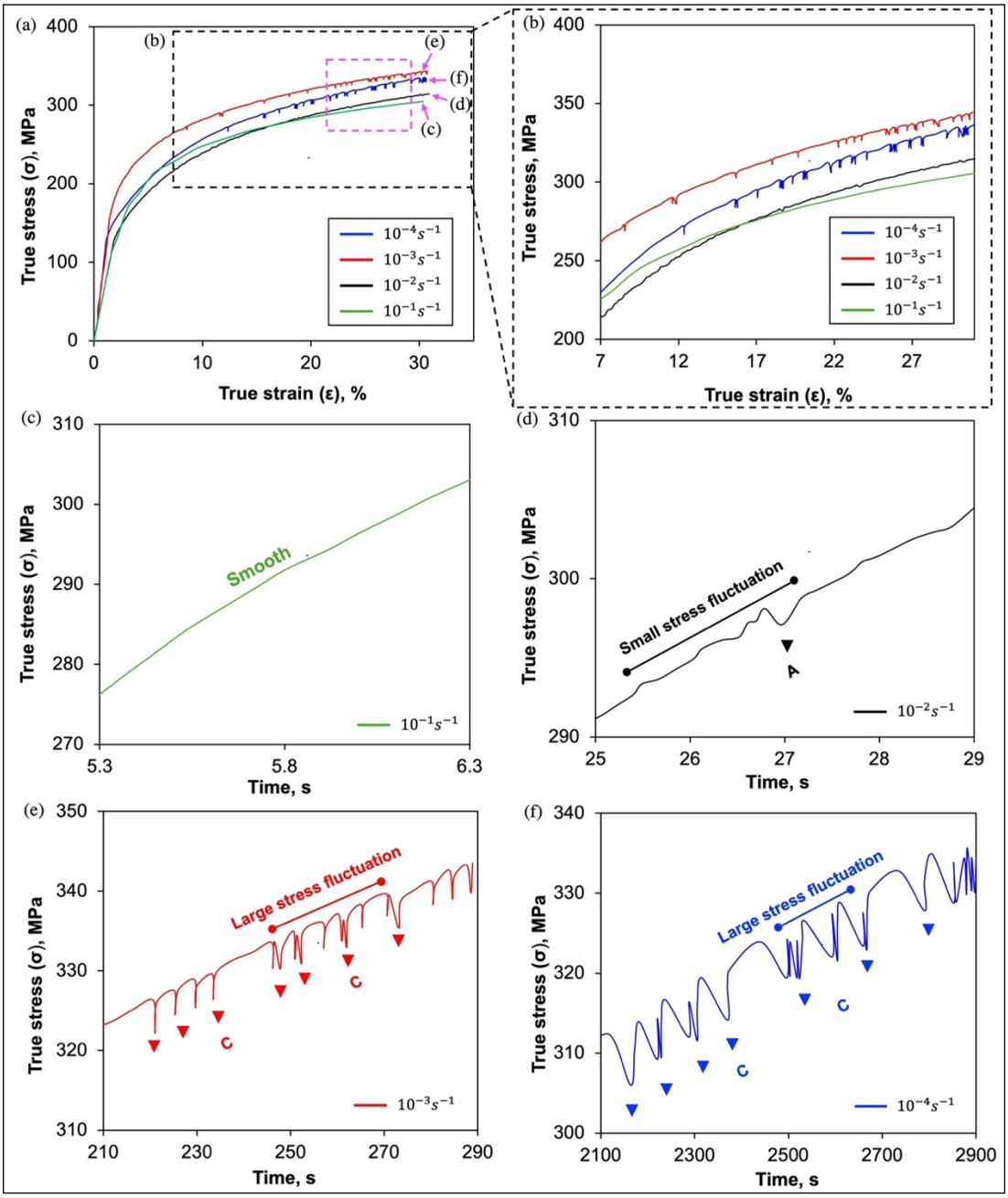

Figure 4.21 (a) Stress-Strain Curves of WAAM at Different Strain Rates (b) Magnified Images of Box Segment (c) $10^{-1}s^{-1}$ Curve (d) $10^{-2}s^{-1}$ Curve (e) $10^{-4}s^{-1}$ Curve (d) $10^{-4}s^{-1}$ Curve

The changes in DSA behavior and dislocation solute interaction are based on the PLC serration pattern that changed from type C to type B and eventually type A as the strain rate increased. Figure 4.23 shows type of serration that can be identified in the stress-strain curves obtained from WAAM and WAAM-forging process. In contrast, when the strain rate increases to 10^{-3} and $10^{-2}s^{-1}$, dislocation moves faster. Although solute atoms can diffuse fast enough to pin dislocations, the pinning becomes partial rather than complete which resulting in intermittent pinning. The partial pinning

resulted repetitive, moderate stress drops which typically formed type B serrations, as illustrated in Figure 4.23(b). While, at high strain rates, dislocation move too rapidly for Mg solute atoms to form strong pinning. As a result, the stress fluctuations become small and nearly continuous, producing serration pattern that defines type A behavior, refer Figure 4.23(a).

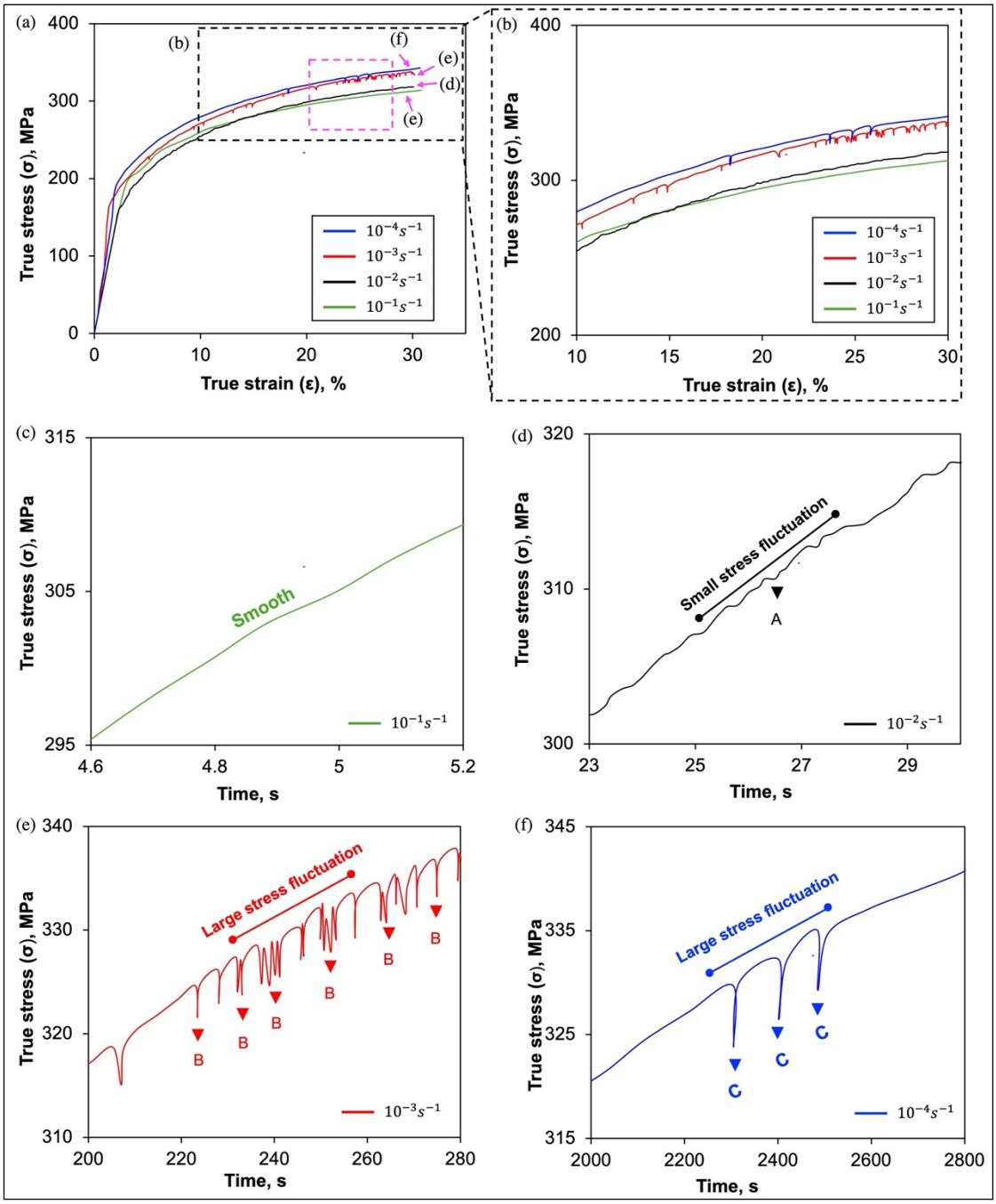

Figure 4.22 (a) Stress-Strain Curves of WAAM-Forging at Different Strain Rates (b) Magnified Images of Box Segment (c) $10^{-1}s^{-1}$ Curve (d) $10^{-2}s^{-1}$ Curve (e) $10^{-4}s^{-1}$ Curve (d) $10^{-4}s^{-1}$ Curve

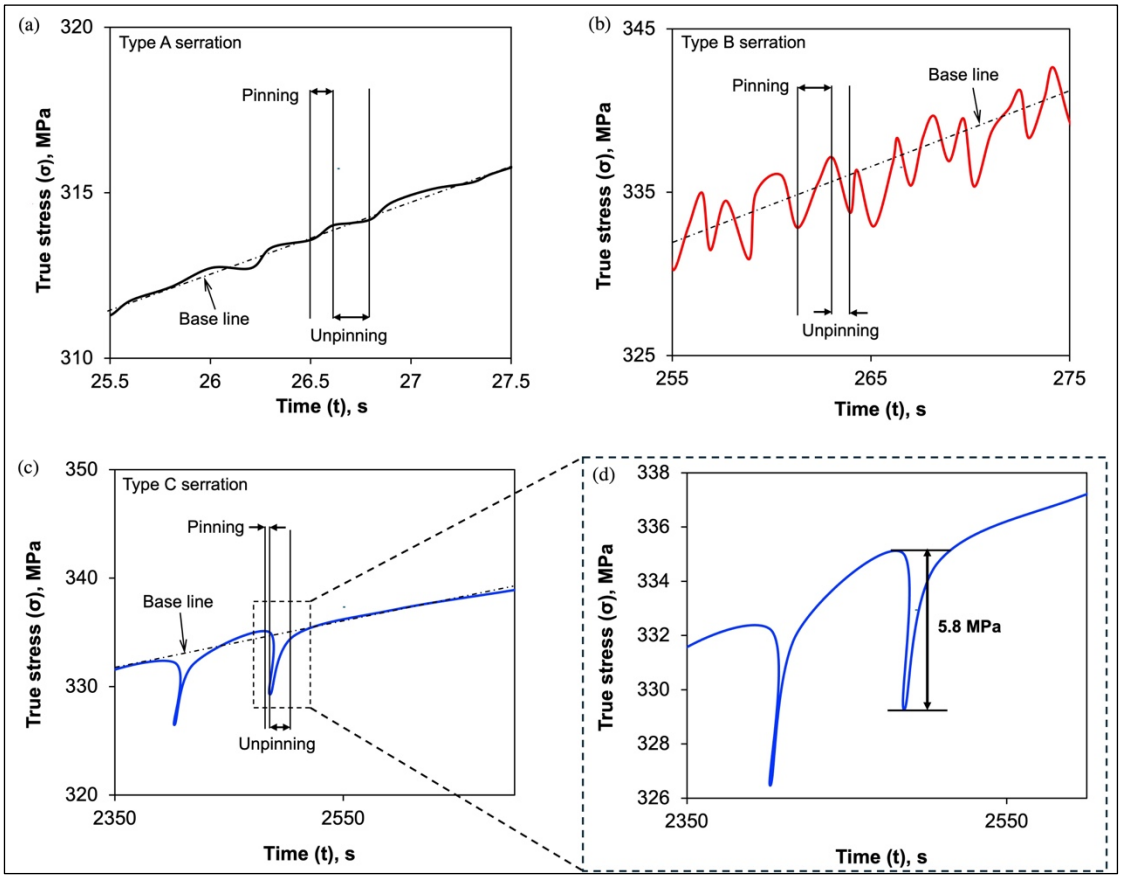

Figure 4.23 Type of Serration in PLC Effect (a) Type A (b) Type B (c) Type C (d) Amplitude of Stress Drop Measurement

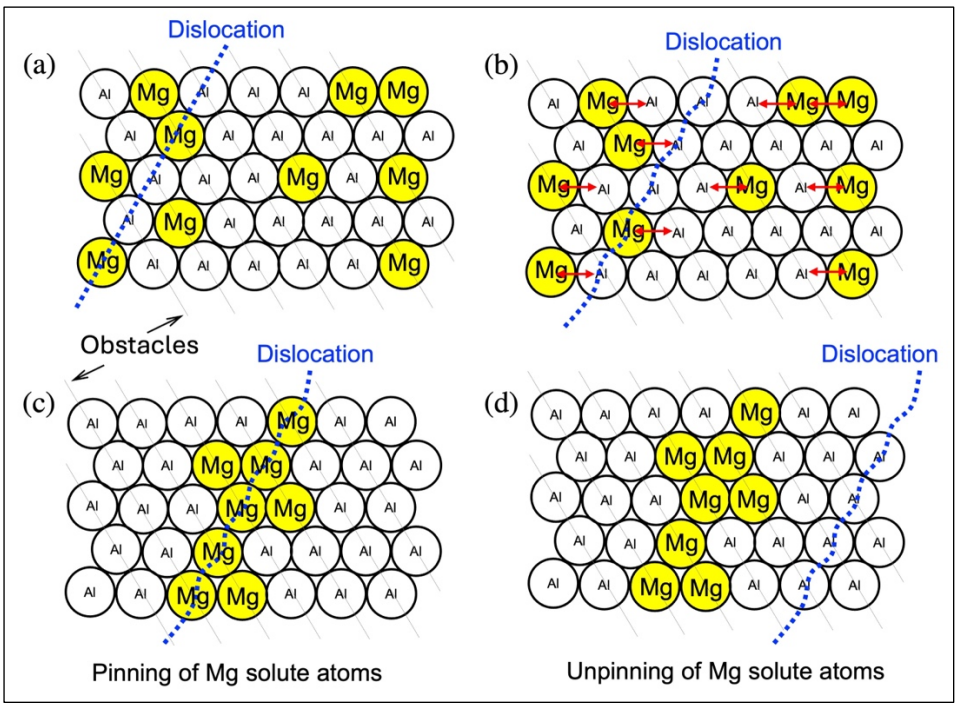

Figure 4.24 Illustrated Cyclic Pinning-Unpinning Mechanism (a-b) Initial Dislocation Motion (c) Pinning Phase (d) Unpinning Phase

Although both processes show similar trends as the strain rate decreases (Figure 4.21 and Figure 4.22), the WAAM-forging exhibits larger stress drops compared to the as-deposited WAAM especially at $10^{-4}s^{-1}$, refer to Figure 4.22(f). The increased PLC severity after cold forging can be further explained by the microstructural changes introduced during plastic deformation. As previously discussed in section 4.4, the cold forging transforms the microstructure from columnar to more equiaxed grains. The refined structure increases the number of grain boundaries where act as obstacle or additional barriers to dislocation motion and serve as nucleation sites for dislocation interactions as reported by R. Kwesi et al (Kwesi Nutor, 2017). These microstructural features provide more obstacles to dislocation motion and promote stronger interaction between mobile dislocations and Mg solute atoms.

At lower strain rates, sufficient time is available for Mg atoms to diffuse and pin the moving dislocations, resulting in a stronger dynamic strain ageing effect. When the dislocations pile up at these boundaries, local stress builds up more rapidly, stored higher energy. Once the dislocation breaks free, the release occurs more abruptly, leading to larger amplitude stress drops. Therefore, the WAAM-forging exhibit higher stress drops amplitude of compared to as-deposited WAAM which indicates that cold forging intensifies the pinning–unpinning process by increasing dislocation accumulation and solute–dislocation interaction within the refined microstructure.

Hence, although cold forging improves the surface integrity and mechanical performance of WAAM ER5356, the refined and plastically deformed microstructure also provides more active sites for solute–dislocation interaction, which increases PLC severity at low strain rates.

4.6.1 Amplitude of Stress Drop

The serrations in PLC effect are directly expressed through stress drops. Therefore, analyzing the amplitude of stress drops as a function of strain rate provides a quantitative method to evaluate the severity of the PLC effect. The amplitude of each stress drop is quantified from the onset of dislocation unpinning to the completion of the unpinning, refer to Figure 4.23(d). Hence, the amplitude stress drops and strain rate relationship is used to compare the deformation instability between WAAM and WAAM-forging ER5356, allowing identification of microstructural refinement changes and dislocation rearrangement influence the PLC behavior.

Figure 4.25 presents the relationship between the amplitude of stress drop and the logarithm of strain rate for WAAM and WAAM-forging Al-Mg alloys. In both conditions, amplitude of stress drop decreases linearly with increasing strain rate. Based on Table 4.4, the amplitude of stress drop at $10^{-4}s^{-1}$ reaches 4.80 MPa and 5.67 MPa for WAAM and WAAM-forging, respectively. It indicates that the severity of the PLC effect is highest under slow deformation. However, WAAM shows a slope of -1.67, while WAAM-forging shows a steeper slope of -1.97. A more negative gradient indicates that the stress-drop amplitude becomes more sensitive to the strain rate changes. It means that the pinning-unpinning mechanism becomes more sudden at lower strain rates. This clearly shows that the forging alters the dynamic interaction behavior by the refined microstructure that enable dislocations to accumulate and leads to pronounced stress drops when Mg solute pinning is overcome.

Table 4.4
Amplitude of Stress Drops at Different Strain Rates

Strain rate, s^{-1}	$\dot{\varepsilon}_{log}$	**Average of stress drops ($\Delta\sigma$), MPa**	
		WAAM	**WAAM-Forging**
0.0001	-4	4.80	5.67
0.0001	-4	4.79	5.31
0.0001	-4	4.52	5.76
0.001	-3	3.25	3.28
0.001	-3	3.55	3.30
0.001	-3	3.33	3.37
0.01	-2	0.86	0.30
0.01	-2	0.94	0.32
0.01	-2	0.61	0.40
0.1	-1	0	0
0.1	-1	0	0
0.1	-1	0	0

Based on the linear relationship, an empirical correlation, referred as Musa Equation is introduced for ER5356 WAAM and WAAM-forging processes to quantify PLC severity. Unlike previous PLC analyzes that primarily examine serration types of qualitative trends, Musa Equation defines a PLC severity index based on the slope of linear relationship between amplitude of stress drop and the logarithm of strain rate. This provides direct relationship to compare the PLC sensitivity between different

manufacturing conditions. The proposed model also enables direct relationship between microstructural refinement due to forging and its impact on DSA behavior. Figure 4.25 shows a contribution linear relationship between amplitude of stress drop and the logarithm of strain rate, even though the fitting method is standard.

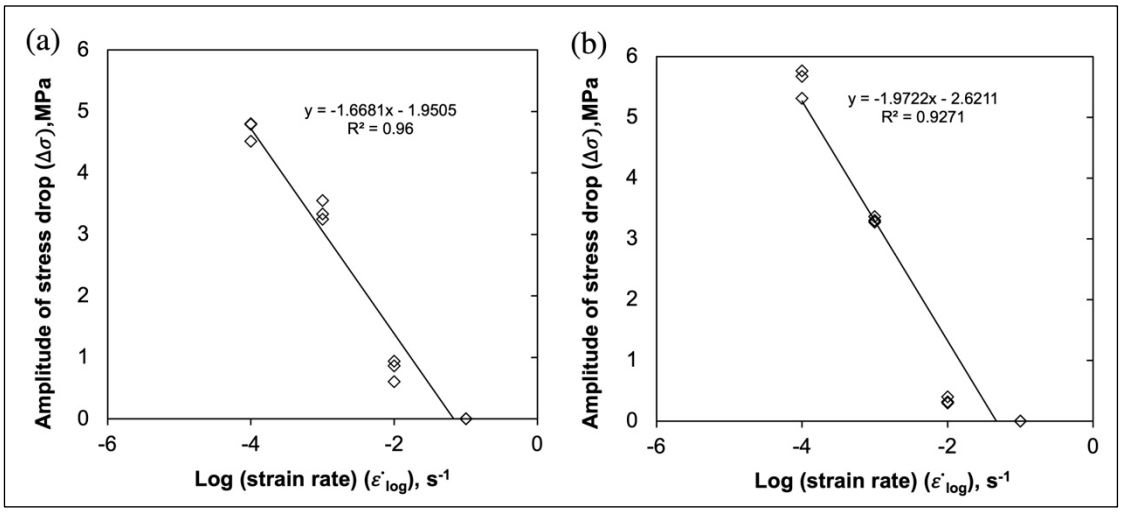

Figure 4.25 Linear Regression between Amplitude of Stress Drop up to 50% True Strain for (a) WAAM (b) WAAM-Forging

Therefore, its applicability is currently limited to the specific experimental conditions of this study, including ER5356 Al-Mg alloy fabricated by WAAM and WAAM-forging, room-temperature compression testing, and strain rates between $0.1s^{-1}$ and $0.0001s^{-1}$. The model is also applicable only to materials that exhibit dynamic strain ageing and PLC-type serrated flow behavior under comparable deformation conditions. Hence, the equation should not be directly generalised to other materials, processing routes, temperatures, strain ranges, or loading modes without further validation. For wider application, additional experimental data involving different Al-Mg compositions, WAAM process parameters, post-processing conditions, and deformation temperatures are required to verify the robustness of the model. This relationship can be expressed as (4.1), where $\Delta\sigma$ is amplitude of stress drop, m_{plc} is severity of PLC effect and $\Delta\sigma_0$ is the extrapolated amplitude at $log\dot{\varepsilon} = 0$.

$$\Delta\sigma = \Delta\sigma_0 + m_{plc}\log(\dot{\varepsilon}) \tag{4.1}$$

Unlike classical strain-rate sensitivity, a new parameter quantifies the solute-dislocation coupling that governs serration magnitude, allowing differentiation between microstructures and processing routes. Its strong linearity approximately $R^2 = 0.9$ demonstrates that is a robust descriptor of PLC behavior. The validity of this equation

is supported by the linearity of the experimental data and the consistent physical mechanism underlying PLC where the DSA serration intensifies at lower strain rates. Therefore, the derived equation captures a genuine material characteristic and can be applied to other materials exhibiting PLC behavior, provide their solute dislocation kinetics that follow similar DSA processes.

In summary, the comparison between WAAM and WAAM-forging ER5356 shows that forging enhances microstructure and mechanical strength but also modified the severity of the PLC effect. The forging condition exhibits stronger sensitivity of stress-drop amplitude to strain rate, indicating more DSA deformation instability at low strain rates. This finding highlight hybrid WAAM-forging process improves material integrity, yet the intrinsic PLC behavior remains active and is expressed differently due to microstructural refinement. The introduced empirical equation therefore provides a useful quantitative tool for characterizing and comparing PLC severity across different processing conditions.

CHAPTER 5
CONCLUSION

The study on WAAM-forging of aluminium alloy ER5356 on microstructural, mechanical properties and PLC behavior achieved based on the objectives stated. The objectives for this research attained and can be concluded as the following three main objectives.

5.1 Objective I: Surface Integrity and Mechanical Properties of Al-Mg using Simulation and Experiment

The process chain of SW-SF and experimental validation able to investigate the thermal stability during WAAM deposition including the surface integrity and mechanical performance of Al-Mg (ER5356) thin walls. SW simulation revealed that GMAW generated higher peak interpass temperatures and greater thermal accumulation compared to CMT, resulting in higher total displacement and residual stress development. These predictions were validated through actual thin-wall fabrication and 3D scanning, where GMAW exhibited larger distortion, while CMT produced a more geometrically stable wall. The dimensional deviation for all investigated conditions, namely GMAW, CMT, GMAW-forged, and CMT-forged, ranged from −33.00% to +3.60%, indicating acceptable predictive capability of the simulation while highlighting the influence of heat input and deposition mode on geometrical stability.

The surface integrity analysis further confirmed that deposition mode strongly influences the defect formation. Porosity measurements and density evaluation showed that GMAW walls contained higher pore fractions up to 5.114% and lower density, whereas CMT maintained lower porosity of 1.932% and more uniform along the build height. The variation across bottom, middle and upper regions was governed by solidification rate, hydrogen entrapment and thermal cycling. SEM observations verified that higher heat input and melt pool instability in GMAW promoted pore growth and interlayer defects. Therefore, within the investigated ER5356 material system, the reduced porosity and improved density in CMT contributed to better surface integrity and mechanical response.

The SF simulation and cold forging analysis showed that room-temperature cold upsetting at approximately 6% reduction improved densification and deformation distribution in the WAAM thin wall. Compared with GMAW-forged, the CMT-forged condition showed more homogeneous effective plastic strain and lower contact pressure, indicating more stable load transfer during forging. Experimentally, cold forging reduced porosity, increased density, and improved geometrical symmetry, particularly in the CMT-forged sample. This suggests that the effectiveness of cold forging was strongly dependent on the initial WAAM deposition quality, where the more stable and lower-defect CMT wall provided a better foundation for post-processing.

The tensile performance of ER5356 WAAM structures was strongly controlled by deposition stability, internal defect distribution, and post-forging deformation. Due to the lower heat input and stable metal transfer in CMT deposition, CMT showed superior and more consistent mechanical behavior compared with GMAW in both as-deposited and forged conditions. In the as-deposited condition, the 0° CMT specimen achieved a UTS of 282 MPa, which was approximately 33.0% higher than the 212 MPa recorded for the 0° GMAW specimen. After cold forging, the GMAW-forged specimen showed an increase in UTS from 212 MPa to 268 MPa, corresponding to approximately 26.4% improvement compared with the as-deposited GMAW condition. Meanwhile, the CMT-forged specimen maintained the highest 0° UTS of 282 MPa and achieved the highest elongation of 28.2%. Compared with GMAW-forged, CMT-forged exhibited approximately 5.2% higher UTS and 41.0% higher elongation, although its YS was 28.6% lower. This indicates that CMT-forged provided the most balanced tensile performance by combining high strength with superior ductility. These findings are consistent with the earlier simulation, porosity, density, and dimensional analyzes, where CMT demonstrated lower deformation, reduced porosity, and better surface integrity. Therefore, within the investigated ER5356 WAAM and WAAM-forging conditions, CMT was selected as the preferred WAAM condition for subsequent detailed investigation through the hybrid WAAM-forging process.

In conclusion, the findings confirmed that optimizing heat input during WAAM with cold forging provides an effective hybrid manufacturing strategy to improve the surface integrity, reducing internal defects and achieve superior mechanical performance in Al-Mg alloys.

5.2 Objective II: Strain Hardening Behavior of Al-Mg WAAM and WAAM-Forging

The research analyzed the influence of strain rate on the compressive strain hardening behavior of ER5356, Al-Mg fabricated by WAAM and hybrid WAAM-forging within the investigated strain-rate range of $0.1s^{-1}$ to $0.0001s^{-1}$. Based on the analysis on compressive behavior, the strain rate is a critical factor governing deformation behavior, texture evolution and strain hardening response in both processes. Through combined EBSD analysis, compressive mechanical testing and strain rate sensitivity, the differences were identified clearly between the as-deposited and forged materials, which highlighting the role of microstructural refinement in controlling plasticity rate.

The EBSD results showed that cold forging refined the WAAM microstructure from larger columnar grains to a more refined and equiaxed structure. The average grain size decreased from 59.30 μm in WAAM to 51.68 μm in WAAM-forged, corresponding to a reduction of approximately 12.8%. This refinement contributed to more homogeneous strain distribution during compression. In terms of texture evolution, the base WAAM sample showed a higher maximum pole figure intensity of 6.60 compared with 6.05 for WAAM-forged, indicating stronger crystallographic alignment in the as-deposited condition. At the lowest strain rate of $0.0001s^{-1}$, WAAM exhibited the highest texture intensity of 7.62, whereas WAAM-forged showed a lower intensity of 5.16, representing approximately 32.3% reduction in maximum texture intensity after forging. This indicates that cold forging suppressed extreme texture development and promoted more stable deformation under slow compression. At the highest strain rate of $0.1s^{-1}$, both WAAM and WAAM-forged showed similar maximum intensity of 6.60, suggesting that rapid deformation limited grain rotation and reduced the influence of initial microstructural differences.

The compressive mechanical response further confirmed that both WAAM and WAAM-forged ER5356 exhibited strain-rate-dependent behavior. Within the investigated strain-rate range, the WAAM-forged samples showed a more stable compressive response, higher and more uniform strain-hardening behavior, and better deformation stability compared with the as-deposited WAAM samples. This improvement is attributed to porosity reduction, grain refinement, and more uniform strain distribution introduced by room-temperature cold forging. In contrast, the as-

deposited WAAM samples showed greater deformation heterogeneity due to columnar grain morphology, interlayer boundaries, and residual defects generated during layer-by-layer deposition.

The SRS analysis using both the common and Lindholm approaches confirmed the presence of negative strain-rate sensitivity, indicating that dynamic strain ageing and PLC deformation instability occurred in the ER5356 WAAM and WAAM-forged samples. The WAAM-forged condition showed a stronger rate-dependent response, which can be related to the refined grain structure, increased dislocation density, and stronger solute–dislocation interaction after cold forging. Therefore, within the specific ER5356 WAAM and WAAM-forging material system, room temperature cold forging condition, and strain-rate range of $0.1s^{-1}$ to $0.0001s^{-1}$, cold forging improved compressive deformation stability and strain-hardening response, but also increased sensitivity to strain-rate-dependent DSA/PLC behavior under low strain-rate conditions.

In conclusion, this research confirms that cold forging significantly modifies the compressive strain hardening behavior of WAAM ER5356 by stabilizing deformation, enhancing strength and increasing sensitivity to strain rate variations. Although forging improves structural integrity, it also intensifies DSA effects under low strain rate conditions. Therefore, the findings are specifically applicable to ER5356 WAAM and WAAM-forged samples tested under room-temperature compression within the strain-rate range of $0.1s^{-1}$ to $0.0001s^{-1}$.

5.3 Objective III: Strain Hardening Relationship Model of PLC Severity in Al-Mg WAAM and WAAM-Forging

This work successfully achieved the third research objective by developing a quantitative strain hardening relationship between stress-drop amplitude and strain rate for WAAM and WAAM-forged ER5356 aluminium alloy. The PLC effect was directly evaluated through the amplitude of stress drops, which represents the intensity of dislocation unpinning during DSA. The developed relationships changed the transition of PLC serration modes from type C to type B and finally to type A with increasing strain rate. A clear and consistent linear decrease in stress-drop amplitude with increasing strain rate was observed for both processes, confirming that PLC severity is highest under slow deformation conditions. The stress-drop amplitude at $0.0001s^{-1}$

increased from 4.80 MPa in WAAM to 5.67 MPa in WAAM-forged, representing an increase of approximately 18.1% after cold forging. This confirms that cold forging intensified the PLC response at low strain rate due to refined microstructure, increased dislocation density, and stronger Mg solute–dislocation interaction, where stronger solute pinning and more abrupt unpinning occur at lower strain rates.

Based on this linear trend, an empirical relationship referred to as Musa equation was established to describe the dependence of stress-drop amplitude on strain rate. The slope (m_{plc}) of this relationship defined as the PLC severity parameter which provides a direct quantitative measure of deformation instability. WAAM-forged samples exhibited a more negative slopes than as-deposited WAAM, indicating higher sensitivity of stress-drop amplitude to strain rate. The WAAM sample recorded a slope of – 1.67 , while the WAAM-forged sample showed a more negative slope of – 1.97. This corresponds to approximately 18.0% higher slope magnitude in the WAAM-forged condition, confirming that cold forging increased the strain-rate sensitivity of PLC behavior. This enhanced sensitivity is attributed to microstructural refinement induced by cold forging, which increases grain boundary density and dislocation storage capacity. Thus, promoting stronger stress accumulation and more pronounced stress release during dislocation unpinning. The high linearity of the model, $R^2 = 0.9$, supports the suitability of the model for describing the tested ER5356 WAAM and WAAM-forged conditions.

However, the Musa Equation should be interpreted within the assumptions and limitations of this study. The model is empirical and assumes a linear relationship between stress-drop amplitude and logarithmic strain rate within the investigated strain-rate range of $0.1s^{-1}$ to $0.0001s^{-1}$. Its current applicability is limited to ER5356 Al-Mg alloy fabricated by WAAM and WAAM-forging, tested under room-temperature compression, and exhibiting dynamic strain ageing or PLC-type serrated flow. Therefore, the equation should not be directly generalised to other aluminium alloys, processing routes, forging reductions, temperatures, strain ranges, or loading modes without further validation.

In conclusion, the developed strain hardening relationship provides a novel and reliable framework for quantifying PLC severity beyond conventional qualitative serration classification. The Musa equation links to microstructural evolution, strain rate, enabling direct comparison of PLC behavior across different manufacturing conditions. Although hybrid WAAM-forging improves microstructural uniformity and

mechanical integrity, the PLC effects remain active and is expressed with greater intensity at low strain rates due to refined microstructure. Therefore, the proposed model offers valuable insight for understanding and controlling deformation instability in Al-Mg alloys and can be extended to other materials governed by similar DSA mechanisms which requires further experimental validation.

5.4 Future Studies

Based on the findings of this thesis, several recommendations can be proposed to further advance hybrid WAAM-forging of ER5356 aluminium alloy. First, optimization studies on multi-stage or interlayer forging strategies could be conducted to investigate whether incremental deformation between selected deposition layers further eliminates porosity and reduces residual stress without extensively intensifying PLC severity at low strain rates. In addition, extending the simulation framework to fully coupled thermomechanical-metallurgical modeling would enable prediction of texture evolution, dislocation density development and dynamic strain ageing behavior directly within the FEM environment. Since the present work focused primarily on compressive strain hardening, future studies should evaluate fatigue performance, fracture toughness and cyclic strain rate sensitivity to assess the applicability of hybrid WAAM-forged ER5356 in structural components subjected to dynamic loading. Besides that, microstructural investigations using advanced techniques such as in-situ EBSD during deformation or TEM analysis could further clarify the solute-dislocation interaction mechanisms responsible for the intensified nSRS after forging. Finally, extending the hybrid strategy to other Al-Mg or heat treatable aluminium alloy would validate the generalisability of the proposed strain hardening relationship and establish broader design guidelines for rate dependent AM applications.

REFERENCES

Abdullah, E., & Jalil, A. (2025). Enhancing Experimental Prediction of Springback in Forming Processes using Advanced Finite Element Modelling. *Journal of Machine Engineering*, *25*(1), 79–101.

Adenan, M. S., Prajadhiana, K. P., Mat, M. F., Manurung, Y. H. P., Ishak, D. P., Adesta, E. T., Colditz, P., Dizon, J. R. C., Mohamed, M. A., & Jamaludin, M. F. (2023). Chained Simulation of the Welding-Forming Process in Analysing Press Force and Geometrical Deformation using Non-Linear Numerical Computation with Experimental Validation. *International Journal of Advanced Manufacturing Technology*, *125*(9–10), 4631–4646.

Afrin, N., Chen, D. L., Cao, X., & Jahazi, M. (2008). Microstructure and Tensile Properties of Friction Stir Welded AZ31B Magnesium Alloy. *Materials Science and Engineering: A*, *472*(1–2), 179–186.

Afteni, C., Paunoiu, V., Afteni, M., & Teodor, V. (2022). Using 3D Scanning in Assessing the Dimensional Accuracy of Mechanically Machined Parts. *IOP Conference Series: Materials Science and Engineering*, *1235*(1), 012071.

Ahmad, S. N., Manurung, Y. H. P., & Mat, M. F. (2020). *FEM Simulation Procedure for Distortion and Residual Stress Analysis of Wire Arc Additive Manufacturing*.

Ait-Amokhtar, H., Fressengeas, C., & Bouabdallah, K. (2015). On the Effects of the Mg Content on the Critical Strain for the Jerky Flow of Al-Mg Alloys. *Materials Science and Engineering: A*, *631*, 209–213.

Albannai, A., & Albannai, A. I. (2022). A Brief Review on The Common Defects in Wire Arc Additive Manufacturing. *Article in International Journal of Current Science Research and Review*.

Aldalur, E., Suárez, A., & Veiga, F. (2021). Metal Transfer Modes for Wire Arc Additive Manufacturing Al-Mg Alloys: Influence of Heat Input in Microstructure and Porosity. *Journal of Materials Processing Technology*, *297*.

Altıparmak, S. C., Yardley, V. A., Shi, Z., & Lin, J. (2021). Challenges in Additive Manufacturing of High-Strength Aluminium Alloys and Current Developments in Hybrid Additive Manufacturing. *International Journal of Lightweight Materials and Manufacture*, *4*(2), 246–261.

Ann, K.-H., Kang, J.-H., Heo, S.-J., Shin, T., & Cho, H.-Y. (2020). Multistage Cold Forging Process Design of Al6082 Considering Forming Limit. *Journal of the*

Korean Society of Manufacturing Process Engineers, *19*(9), 93–99.

Arana, M., Ukar, E., Rodriguez, I., Aguilar, D., & Álvarez, P. (2022). Influence of Deposition Strategy and Heat Treatment on Mechanical Properties and Microstructure of 2319 Aluminium WAAM Components. *Materials & Design*, *221*, 110974.

Arana, M., Ukar, E., Rodriguez, I., & Iturrioz, A. (2021). *Strategies to Reduce Porosity in Al-Mg WAAM Parts and Their Impact on Mechanical Properties*.

Azlin, M. F. A. M., Abdullah, A. B., Yusuf, S. Y. M., Wani, Z. K., & Rajendran, R. (2024). Enhancing the Tribological Performance of Additively Manufactured Aluminium Alloy ER 5356 via the Cold Deformation Process. *Journal of Advanced Research in Applied Mechanics*, *113*(1), 189–206.

Bakare, F., Jiang, L., Langan, T., Weiss, M., & Dorin, T. (2023). Impact of Dispersoids' Distribution on Portevin-Le-Chatelier Effect and Surface Quality in Al–Mg-Sc-Zr Alloys. *Materials Science and Engineering: A*, *875*.

Bambach, M., Sizova, I., Sydow, B., Hemes, S., & Meiners, F. (2020). Hybrid Manufacturing of Components from Ti-6Al-4V by Metal Forming and Wire-Arc Additive Manufacturing. *Journal of Materials Processing Technology*, *282*.

Barannikova, S. A., & Nadezhkin, M. V. (2021). Kinetics of Plastic Deformation Localization Bands in Polycrystalline Nickel. *Metals*, *11*(9).

Barath Kumar, M. D., & Manikandan, M. (2022). Assessment of Process, Parameters, Residual Stress Mitigation, Post Treatments and Finite Element Analysis Simulations of Wire Arc Additive Manufacturing Technique. In *Metals and Materials International* (Vol. 28, Number 1, pp. 54–111). Korean Institute of Metals and Materials.

Baygut, A., Baygut, A., & Çulha, O. (2020). Investigation of the Cold Forging Operation Steps' Effect on Forming Properties. *Celal Bayar University Journal of Science*, *16*(4), 437–443.

Bin, W., Liu, Z., Xu, M., Hong, Y., & Zhu, D. (2024). Numerical Simulation of Efficient Welding for Thick Plates in Shipbuilding using Simufact Welding. *Journal of Physics: Conference Series*, *2760*(1).

Boruah, D., Dewagtere, N., Ahmad, B., Nunes, R., Tacq, J., Zhang, X., Guo, H., Verlinde, W., & De Waele, W. (2023). Digital Image Correlation for Measuring Full-Field Residual Stresses in Wire and Arc Additive Manufactured Components. *Materials*, *16*(4).

Bouquerel, J., Diawara, B., Dubois, A., Dubar, M., Vogt, J., & Najjar, D. (2014). Investigations of the Microstructural Response to a Cold Forging Process of the 6082-T6 Alloy. *Materials and Design*.

Bowen, A. W., & Partridge, P. G. (1974). Limitations of the Hollomon Strain-Hardening Equation Limitations of the Hollomon Strain-Hardening Equation. In *J. Phys. D: Appl. Phys* (Vol. 7).

Bruce, D., Paradise, P., Saxena, A., Temes, S., Clark, R., Noe, C., Benedict, M., Broderick, T., & Bhate, D. (2022). A Critical Assessment of the Archimedes Density Method for Thin-Wall Specimens in Laser Powder Bed Fusion: Measurement Capability, Process Sensitivity and Property Correlation. *Journal of Manufacturing Processes*, *79*, 185–192.

Cai, Y., Yang, S., Fu, S., Zhang, D., & Zhang, Q. (2017). Investigation of Portevin–Le Chatelier Band Strain and Elastic Shrinkage in Al-Based Alloys Associated with Mg Contents. *Journal of Materials Science and Technology*, *33*(6), 580–586.

Cecchel, S., & Cornacchia, G. (2025). Enhancing Aluminum Alloy Properties Through Low Pressure Forging: A Comprehensive Study on Heat Treatments. *Metals*, *15*(7).

Chandra, M., Rajak, S., Vimal, K. E. K., Tanmay, Yadav, V. K., & Rakesh. (2023). Mechanical Properties of Wire Arc Additive Manufactured 5356 Aluminum Alloy Wall Using Robotic-Controlled GMAW. *Metallography, Microstructure, and Analysis*, *12*(6), 999–1008.

Chen, C., Sun, G., Du, W., Liu, J., & Zhang, H. (2023). Effect of Equivalent Heat Input on WAAM Al-Si Alloy. *International Journal of Mechanical Sciences*, *238*.

Cho, C. H., Son, H. W., Lee, J. C., Son, K. T., Lee, J. W., & Hyun, S. K. (2020). Effects of High Mg Content and Processing Parameters on Portevin-Le Chatelier and Negative Strain Rate Sensitivity Effects in Al–Mg Alloys. *Materials Science and Engineering: A*, *779*.

Derekar, K., Lawrence, J., Melton, G., Addison, A., Zhang, X., & Xu, L. (2019). Influence of Interpass Temperature on Wire Arc Additive Manufacturing (WAAM) of Aluminium Alloy Components. *MATEC Web of Conferences*, *269*, 05001.

Derekar, K. S. (2018). A Review of Wire Arc Additive Manufacturing and Advances in Wire Arc Additive Manufacturing of Aluminium. *Materials Science and Technology*, *0*(0), 1–22.

Doumenc, G., Couturier, L., Courant, B., Paillard, P., Benoit, A., Gautron, E., Girault, B., Pirling, T., Cabeza, S., & Gloaguen, D. (2022). Investigation of Microstructure, Hardness and Residual Stresses of Wire and Arc Additive Manufactured 6061 Aluminium alloy. *Materialia*, *25*.

Eimer, E., Ganguly, S., Czink, S., Dietrich, S., Chehab, B., Ding, J., & Williams, S. (2023). Effect of Inter Layer Cold Work on 2024 Aluminium Alloy Produced by Wire Directed Energy Deposition. *Materials Science and Engineering: A*, *880*.

Elka Mehr Kimiya. (2024). *The Ultimate Guide to 5356 Filler Metal: Enhancing Aluminum Welding Performance*.

Fang, X., Chen, G., Yang, J., Xie, Y., Huang, K., & Lu, B. (2021). Wire and Arc Additive Manufacturing of High-Strength Al–Zn–Mg Aluminum Alloy. *Frontiers in Materials*, *8*.

Fisher, C. R., Bechetti, D. H., & Sinfield, M. F. (2021). Comparison of Analytical, Empirical, and Finite-Element Modeling of Weld Metal Cooling as Function of Plate Orientation, Thickness, and Heat input. *Journal of Manufacturing Processes*, *62*, 471–482.

Fuchs, C., Baier, D., Semm, T., & Zaeh, M. F. (2020). Determining the Machining Allowance for WAAM Parts. *Production Engineering*, *14*(5–6), 629–637.

Geng, Y., Panchenko, I., Chen, X., Ivanov, Y., & Konovalov, S. (2022). Wire Arc Additive Manufacturing Al-5.0 Mg alloy: Microstructures and Phase Composition. *Materials Characterization*, *187*.

Gokul KA, & Jose MJ. (2022). *Residual Stress and Distortion in Gas Metal Arc-Based Additive Manufacturing*.

Greebmalai, J., & Warinsiriruk, E. (2020). Multi-Heat Input Technique for Aluminum WAAM using DP-GMAW Process. *AIP Conference Proceedings*, *2279*.

Gu, J., Gao, M., Yang, S., Bai, J., Zhai, Y., & Ding, J. (2020). Microstructure, Defects, and Mechanical Properties of Wire + Arc Additively Manufactured Al-Cu4.3-Mg1.5 Alloy. *Materials and Design*, *186*, 108357.

Guo, C., Chen, F., Liu, H., Shao, X., Zhang, H., Chen, W., Wu, Z., Liu, X., & Nagaumi, H. (2025). Influence of Ag and Processing Routes on the Portevin-Le Châtelier Behavior of Al-Mg based Alloys. *Materials Science and Engineering: A*, *923*.

Guo, H., Fan, C., Yang, S., Wang, J., Pei, W., & Chu, Z. (2023). Numerical Simulation of Layered Bimetallic ZChSnSb8Cu4/Steel TIG-MIG Hybrid Welding Based on Simufact. *Materials*, *16*(15).

Han, X., Chen, W., Hu, X., Hua, L., & Chai, F. (2023). Grain Refinement Mechanism of 5A06 Aluminum Alloy Sheets during Cold Rotary Forging. *Materials*, *16*(7).

Haque, M. S., Nasim Rokon, S. M., & Kaiser, M. S. (2023). Strengthening and Softening Behavior of Non-Heat-treatable Aluminum Alloys Subject to Deformation and Annealing Treatment. *Materials Today: Proceedings*, *82*, 151–157.

Harrington, G. F., & Santiso, J. (2021). Back-to-Basics Tutorial: X-ray Diffraction of Thin Films. *Journal of Electroceramics*, *47*(4), 141–163.

Hauser, T., Reisch, R. T., Breese, P. P., Lutz, B. S., Pantano, M., Nalam, Y., Bela, K., Kamps, T., Volpp, J., Alexander, F., & Kaplan, H. (2021). Porosity in Wire Arc Additive Manufacturing of Aluminium Alloys. *Additive Manufacturing*, *41*(April), 101993.

Hirtler, M., Jedynak, A., Sydow, B., Sviridov, A., & Bambach, M. (2020). A Study on the Mechanical Properties of Hybrid Parts Manufactured by Forging and Wire Arc Additive Manufacturing. *Procedia Manufacturing*, *47*, 1141–1148.

Hu, Y., Deng, X., Kan, Q., Wu, S., Li, Y., Lei, L., Wang, L., & Kang, G. (2023). Influence of Temperature on Deformation and Damage Mechanisms of Wire + Arc Additively Manufactured 2219 Aluminum Alloy. *Engineering Fracture Mechanics*, *292*.

Huang, H., Ma, N., Chen, J., Feng, Z., & Murakawa, H. (2020). Toward Large-Scale Simulation of Residual Stress and Distortion in Wire and Arc Additive Manufacturing. *Additive Manufacturing*, *34*.

Huang, J., Fu, Y., Zhai, W., Li, R., Zhao, X., Lin, H., Zhang, H., & Wang, G. (2024). Hybrid Interlayer Hot Rolling and Wire Arc Additive Manufacturing of Al-Mg Alloy: Microstructure, Mechanical Properties and Strengthening Mechanism. *Journal of Materials Research and Technology*, *30*, 7037–7050.

Huang, J., Li, R., Zhao, X., Lin, H., Zhai, W., Zhang, H., Wang, G., & Fu, Y. (n.d.). *Hybrid In-Situ Hot Rolling and Wire Arc Additive Manufacturing of Al-Si Alloy: Microstructure, Mechanical Properties and Strengthening Mechanism*.

Israr, R., Buhl, J., & Bambach, M. (2020). Numerical Analysis of Different Fixation Strategies in Direct Energy Deposition Processes. *Procedia Manufacturing*, *47*, 1184–1189.

Jiangang, P., Bo, Y., Jinguo, G., yu, R., hongjun, C., Liang, Z., & Hao, L. (2022). Influence of Arc Mode on the Microstructure and Mechanical Properties of 5356

Aluminum Alloy Fabricated by Wire Arc Additive Manufacturing. *Journal of Materials Research and Technology*, *20*, 1893–1907.

Karlina, A. I., Kondratyev, V. V., Balanovskiy, A. E., Astafyeva, N. A., & Yamshchikova, E. A. (2024). Porosity Reduction in Metal with Hybrid Wire and Arc Additive Manufacturing Technology (WAAM). *CIS Iron and Steel Review*, *27*, 91–95.

Kesarwani, S., Yuvaraj, N., & Niranjan, M. S. (2024). Impact of Depositional Direction and Current on Microstructure and Mechanical Properties of the Bimetallic Wall of ER5356/ER4043 Fabricated by Cold Metal Transfer based Wire Arc Additive Manufacturing. *CIRP Journal of Manufacturing Science and Technology*, *53*, 17–33.

Khan, E. A., & Mohan, P. R. (2020). Change in the Mechanical and Electrical Properties of Aluminium 6063 Alloy under Cold Forging Process. *International Research Journal of Engineering and Technology (IRJET)*, 476–478.

Knapek, M., Dobroň, P., Máthis, K., Illková, K., Mortensen, A., & Chmelík, F. (2017). Occurrence of the Portevin Le-Châtelier Effect in Open-Cell Microcellular Al-2 wt% Mg. *Scripta Materialia*, *132*, 13–16.

Köhler, M., Fiebig, S., Hensel, J., & Dilger, K. (2019). Wire and Arc Additive Manufacturing of Aluminum Components. *MDPI Metals*, 1–9.

Köhler, M., Hensel, J., & Dilger, K. (2020). Effects of Thermal Cycling on Wire and Arc Additive Manufacturing of Al-5356 Components. *Metals*, *10*(7), 1–11.

Kumar, S., Singh, G., Sharma, V. S., & Sekar, S. (2024). *Investigation of Process Parameters for Quality Deposition of Al5356 using Cold Metal Transfer Wire Arc Additive Manufacturing (CMT-WAAM)*.

Kumar, S., Singh, R., & Singh, D. (2018). The Influence of Cold Forging Process on the Microstructure, Porosity and Wear Behavior of Spray Formed Al-Si Alloys. In *Materials Today: Proceedings* (Vol. 5).

Kwesi Nutor, R. (2017). Using the Hollomon Model to Predict Strain-Hardening in Metals. *American Journal of Materials Synthesis and Processing*, *2*(1), 1.

Langelandsvik, G., Akselsen, O. M., Furu, T., & Roven, H. J. (2021). Review of Aluminum Alloy Development for Wire Arc Additive Manufacturing. In *Materials* (Vol. 14, Number 18). MDPI.

Lavakumar, A., Sarangi, S. S., Chilla, V., Narsimhachary, D., & Ray, R. K. (2021). A “New” Empirical Equation to Describe the Strain Hardening Behavior of Steels

and Other Metallic Materials. *Materials Science and Engineering: A*, *802*.

Lee, S. Y., Chettri, S., Sarmah, R., Takushima, C., Hamada, J. ichi, & Nakada, N. (2023). Serrated Flow Accompanied with Dynamic Type Transition of the Portevin–Le Chatelier Effect in Austenitic Stainless Steel. *Journal of Materials Science and Technology*, *133*, 154–164.

Li, C., Gu, H., Wang, W., Wang, S., Ren, L., Wang, Z., Ming, Z., & Zhai, Y. (2020). Effect of Heat Input on Formability, Microstructure, and Properties of Al-7Si-0.6Mg Alloys Deposited by CMT-WAAM Process. *Applied Sciences (Switzerland)*, *10*(1).

Li, H., Wang, L., He, W., Cheng, L., Chen, J., & Yi, L. (2023). Effect of Cold Pressing Deformation on Microstructure and Residual Stress of 7050 Aluminum Alloy Die Forgings. *Materials*, *16*(14).

Li, S. S., Yue, X., Li, Q. Y., Peng, H. L., Dong, B. X., Liu, T. S., Yang, H. Y., Fan, J., Shu, S. L., Qiu, F., & Jiang, Q. C. (2023). Development and Applications of Aluminum Alloys for Aerospace Industry. In *Journal of Materials Research and Technology* (Vol. 27, pp. 944–983). Elsevier Editora Ltda.

Li, S., Zhang, L. J., Ning, J., Wang, X., Zhang, G. F., Zhang, J. X., & Na, S. J. (2020). Microstructures and Mechanical Properties of Al-Zn-Mg Aluminium Alloy Samples Produced by Wire + Arc Additive Manufacturing. *Journal of Materials Research and Technology*, *9*(6), 13770–13780.

Li, S., Zhang, L. J., Ning, J., Wang, X., Zhang, G. F., Zhang, J. X., Na, S. J., & Fatemeh, B. (2020). Comparative Study on the Microstructures and Properties of Wire+Arc Additively Manufactured 5356 Aluminium Alloy with Argon and Nitrogen as the Shielding Gas. *Additive Manufacturing*, *34*(December 2019), 101206.

Li, S., Zhang, L. J., Ning, J., Wang, X., Zhang, L. L., Long, J., Zhou, X. R., & Na, S. J. (2021). Microstructures and Properties of Wire-Arc Additively Manufactured 5356 Aluminium Alloy Protected by Different Proportions of Nitrogen and Argon. *Journal of Materials Science*, *56*(31), 17785–17804.

Li, W., Amanov, A., Nagaraja, K. M., Li, B., Ravichander, B. B., Zhang, R., Lu, H., Qian, D., Kumar, G., & Pyun, Y. S. (2023). Processing Aluminum Alloy with Hybrid Wire Arc Additive Manufacturing and Ultrasonic Nanocrystalline Surface Modification to Improve Porosity, Surface Finish, and Hardness. *Journal of Manufacturing Processes*, *103*, 181–192.

Li, Y., Su, C., & Zhu, J. (2022). Comprehensive Review of Wire Arc Additive

Manufacturing: Hardware System, Physical Process, Monitoring, Property Characterization, Application and Future Prospects. In *Results in Engineering* (Vol. 13). Elsevier B.V. https://doi.org/10.1016/j.rineng.2021.100330

Liu, L., Xu, W., Zhao, Y., Lin, Z., Liu, Z., Dong, Y., & Dong, C. (2023). Tailoring the Microstructure and Mechanical Properties of Wire and Arc Additive Manufactured Al–Mg Alloy via Interlayer Friction Stir Processing. *Journal of Materials Research and Technology*, *25*, 1055–1068.

Liu, Y., Liu, Z., Zhou, G., He, C., & Zhang, J. (2022). Microstructures and Properties of Al-Mg Alloys Manufactured by WAAM-CMT. *Materials*, *15*(15).

Manjunath, G. A., Shivakumar, S., Fernandez, R., Nikhil, R., & Sharath, P. C. (2021). A Review on Effect of Multi-Directional Forging/Multi-Axial Forging on Mechanical and Microstructural Properties of Aluminum Alloy. *Materials Today: Proceedings*, *47*(xxxx), 2565–2569.

Manufacturing, A. (2021). *Review of Aluminum Alloy Development for Wire Arc*. 1–26.

Manurung, Y. H. P., Prajadhiana, K. P., Adenan, M. S., Awiszus, B., Graf, M., & Haelsig, A. (2021). Analysis of Material Property Models on WAAM Distortion using Nonlinear Numerical Computation and Experimental Verification with P-GMAW. *Archives of Civil and Mechanical Engineering*, *21*(1).

Maurya, A. K., Yeom, J. T., Kang, S. W., Park, C. H., Hong, J. K., & Reddy, N. S. (2022). Optimization of Hybrid Manufacturing Process Combining Forging and Wire-Arc Additive Manufactured Ti-6Al-4V through Hot Deformation Characterization. *Journal of Alloys and Compounds*, *894*.

Meiners, F., Ihne, J., Jürgens, P., Hemes, S., Mathes, M., Sizova, I., Bambach, M., Hama-Saleh, R., & Weisheit, A. (2020). New Hybrid Manufacturing Routes Combining Forging and Additive Manufacturing to Efficiently Produce High Performance Components from Ti-6Al-4V. *Procedia Manufacturing*, *47*, 261–267.

Mendes, N., Barros, H., Machado, M. A., Oliveira, J. P., Duarte, V. R., & Santos, T. G. (2025). A Novel Robotic Cell for the Hot Forging Wire Arc Additive Manufacturing Process: Vibration Analysis and Process Parameter Investigation. *Measurement: Journal of the International Measurement Confederation*, *245*.

Mohamed, M., Amer, M., Shazly, M., & Masters, I. (2021). Assessment of Different Ductile Damage Models of AA5754 for Cold Forming. *The International Journal of Advanced Manufacturing Technology*, *114*, 1219–1231.

Monine, V. I., Da Cruz Payão Filho, J., Gonzaga, R. S., Passos, E. K. D., & De Assis, J. T. (2018). X-Ray Diffraction Technique for Residual Stress Measurement in NiCrMo Alloy Weld Metal. *Advances in Materials Science and Engineering*, *2018*.

Nawaz, A., & Rani, S. (2021). Fabrication and Evaluation of Percent Porosity and Density Reduction of Aluminium Alloy Foam. *Materials Today: Proceedings*, *47*, 6025–6029.

Oliveira, A. S., Santos, R. O. Dos, Silva, B. C. D. S., Guarieiro, L. L. N., Angerhausen, M., Reisgen, U., Sampaio, R. R., Machado, B. A. S., Droguett, E. L., Da Silva, P. H. F., & Coelho, R. S. (2021). A Detailed Forecast of the Technologies based on Lifecycle Analysis of GMAW and CMT Welding Processes. *Sustainability (Switzerland)*, *13*(7).

P. Ludwik. (1909). *Elemente der Technologischen Mechanik* (1st ed.). Springer Berlin, Heidelberg.

Panchenko, O. V., Zhabrev, L. A., Kurushkin, D. V., & Popovich, A. A. (2019). Macrostructure and Mechanical Properties of Al – Si, Al – Mg – Si, and Al – Mg – Mn Aluminum Alloys Produced by Electric Arc Additive Growth. *Metal Science and Heat Treatment*, *60*(11–12), 749–754.

Pop, M. F., Neag, A. V., & Sas-Boca, I. M. (2023). Experimental and Numerical Study on the Influence of Lubrication Conditions on AA6068 Aluminum Alloy Cold Deformation Behavior. *Materials*, *16*(5).

Pragana, J. P. M., Sampaio, R. F. V., Bragança, I. M. F., Silva, C. M. A., & Martins, P. A. F. (2021). Hybrid Metal Additive Manufacturing: A State–of–the-Art Review. *Advances in Industrial and Manufacturing Engineering*, *2*(December 2020), 100032.

Prajadhiana, K. P., Manurung, Y. H. P., Bauer, A., Adenan, M. S., Syahriah, N. I., Mohamed, M. A., Awiszus, B., Graf, M., & Haelsig, A. (2022). Experimental Verification of Computational and Sensitivity Analysis on Substrate Deformation and Plastic Strain Induced by Hollow Thin-Walled WAAM Structure. *Rapid Prototyping Journal*, *28*(3), 559–572.

Priyadarshini, A., Kiran, C. P., & Suresh, K. (2018). Effect of Friction on Barreling during Cold Upset Forging of Aluminium 6082 Alloy Solid Cylinders. *IOP Conference Series: Materials Science and Engineering*, *330*(1).

Rajesh, K. V. D., Mishra, H., & Buddi, T. (2021). Finite Element Analysis of Chromium

and Molybdenum Alloyed Steel Billets Forged on Multi Step Process using Simufact Forming. *Advances in Materials and Processing Technologies*.

Rathod, D. W. (2025). A Review on Challenges and Opportunities in Wire Arc Additive Manufacturing of Aluminium Alloys: Specific Context of 7xxx Series Alloys. In *Mechanical Engineering for Society and Industry* (Vol. 5, Number 1, pp. 107–124). Universitas Muhammadiyah Magelang.

Rodrigues, T. A., Duarte, V., Miranda, R. M., Santos, T. G., & Oliveira, J. P. (2019). Current Status and Perspectives on Wire and Arc Additive Manufacturing (WAAM). *Materials*, *12*(7).

Rosli, N. A., Alkahari, M. R., bin Abdollah, M. F., Maidin, S., Ramli, F. R., & Herawan, S. G. (2021). Review on Effect of Heat Input for Wire Arc Additive Manufacturing Process. In *Journal of Materials Research and Technology* (Vol. 11, pp. 2127–2145). Elsevier Editora Ltda.

Ryan, E. M., Sabin, T. J., Watts, J. F., & Whiting, M. J. (2018). The Influence of Build Parameters and Wire Batch on Porosity of Wire and Arc Additive Manufactured Aluminium Alloy 2319. *Journal of Materials Processing Technology*, *262*, 577–584.

Sahul, M., Pavlík, M., Ludrovcová, B., Sahul, M., Beránek, L., & Horváth, J. (2025). Influence of Argon Gas Flow Rate on the Porosity of AA5087 Aluminum Alloy Walls Made by Metal Inert Gas Wire and Arc Additive Manufacturing. *Materials Letters*, *399*.

Sahul, M., Pavlík, M., Sahul, M., Kovačócy, P., & Martinkovič, M. (2024). Effect of Travel Speed on the Properties of 5087 Aluminum Alloy Walls Produced by Wire and Arc Additive Manufacturing. *Journal of Materials Engineering and Performance*, *33*(16), 8582–8600.

Saravana Kumar, M., Jeyaprakash, N., & Yang, C. H. (2024). Effect of Combined Parametric Impacts on Collapsing the Wall Quality of WAAM Al5356 Component. *Engineering Failure Analysis*, *166*.

Shah, A., Aliyev, R., Zeidler, H., & Krinke, S. (2023). A Review of the Recent Developments and Challenges in Wire Arc Additive Manufacturing (WAAM) Process. In *Journal of Manufacturing and Materials Processing* (Vol. 7, Number 3). MDPI.

Shanker, H., & Wattal, R. (2023). Comparative Study of Microstructural and Mechanical Properties of Robotic CMT and GMAW Welded 7475-T7351

Aluminium Alloy Joints. *Materials Today Communications*, *37*.

Silveira, F. D., & Schaeffer, L. (2018). Evaluation of Different Levels of Prestressing for Cold Forging Tools by Numerical Simulation Analysis. *International Journal of Advanced Manufacturing Technology*, *98*(9–12), 2487–2495.

Singh, S. R., & Khanna, P. (2020). Wire Arc Additive Manufacturing (WAAM): A New Process to Shape Engineering Materials. *Materials Today: Proceedings*, (xxxx).

Singh, S., Sharma, S., & Rathod, D. W. (2021). A Review on Process Planning Strategies and Challenges of WAAM. *Materials Today: Proceedings*, (xxxx).

Singla, J., Kumar, N., & Bansal, A. (2024). Microstructural and Mechanical Properties of Al-5356 Alloy Structures Fabricated using Direct Energy Deposition (DED): In-Pursuit to Optimizing Deposition Parameters. *Materials Characterization*, *216*.

Song, C. R., Dong, B. X., Zhang, S. Y., Yang, H. Y., Liu, L., Kang, J., Meng, J., Luo, C. J., Wang, C. G., Cao, K., Qiao, J., Shu, S. L., Zhu, M., Qiu, F., & Jiang, Q. C. (2024). Recent Progress of Al–Mg Alloys: Forming and Preparation Process, Microstructure Manipulation and Application. *Journal of Materials Research and Technology*, *31*, 3255–3286.

Srinivasan, D., Sevvel, P., John Solomon, I., & Tanushkumaar, P. (2022). A review on Cold Metal Transfer (CMT) Technology of Welding. *Materials Today: Proceedings*, *64*, 108–115.

Srivastava, M., Rathee, S., Tiwari, A., & Dongre, M. (2023). Wire Arc Additive Manufacturing of Metals: A Review on Processes, Materials and Their Behaviour. *Materials Chemistry and Physics*, *294*.

Su, C., Chen, X., Gao, C., & Wang, Y. (2019). Effect of Heat Input on Microstructure and Mechanical Properties of Al-Mg Alloys Fabricated by WAAM. *Applied Surface Science*, *486*, 431–440.

Sun, J., Hensel, J., Köhler, M., & Dilger, K. (2021). Residual Stress in Wire and Arc Additively Manufactured Aluminum Components. *Journal of Manufacturing Processes*, *65*, 97–111.

Sutrimo, Azmy, I., Koeshardono, F., & Winarta, R. (2023). Effect of Welding Speed on Residual Stress and Distortion of AISI 1045 Plate Using the Finite Element Method (FEM). *International Journal of Advances in Scientific Research and Engineering*, *09*(01), 01–08.

Swift, H. W. (1952). Plastic Instability under Plane Stress. In *Journal of the Mechanics*

and Physics of Solids (Vol. 1). Pcrgamon Press Ltd.

Tahreen, N., Chen, D. L., Nouri, M., & Li, D. Y. (2014). Effects of Aluminum Content and Strain Rate on Strain Hardening Behavior of Cast Magnesium Alloys during Compression. *Materials Science and Engineering: A*, *594*, 235–245.

Tao, L., Feng, Z., Jiang, Y., & Tong, J. (2023). Analyzing Forged Quality of Thin-Walled A-286 Superalloy Tube under Multi-Stage Cold Forging Processes. *Materials*, *16*(13), 4598.

Tian, N., Liu, H., Zhang, Z., Liu, J., Zhang, Y., Zhou, Y., Zhao, G., & Qin, G. (2024a). Portevin-Le Chatelier Characterization of Annealed Al-Mg Alloy Sheets with Different Mg Contents. *Materials Science and Engineering: A*, *893*.

Tian, N., Liu, H., Zhang, Z., Liu, J., Zhang, Y., Zhou, Y., Zhao, G., & Qin, G. (2024b). Portevin-Le Chatelier characterization of annealed Al-Mg alloy sheets with different Mg contents. *Materials Science and Engineering: A*, *893*. https://doi.org/10.1016/j.msea.2024.146118

Tonelli, L., Laghi, V., Palermo, M., Trombetti, T., & Ceschini, L. (2021). AA5083 (Al–Mg) Plates Produced by Wire-and-Arc Additive Manufacturing: Effect of Specimen Orientation on Microstructure and Tensile Properties. *Progress in Additive Manufacturing*, *6*(3), 479–494.

Treutler, K., & Wesling, V. (2021). The Current State of Research of Wire Arc Additive Manufacturing (WAAM): A Review. *Applied Sciences*.

Truppel, G. H., Angerhausen, M., Pipinikas, A., Reisgen, U., & dos Santos Paes, L. E. (2019). Stability Analysis of the Cold Metal Transfer (CMT) Brazing Process for Galvanized Steel Plates with ZnAl4 Filler Metal. *International Journal of Advanced Manufacturing Technology*, *103*(5–8), 2485–2494.

Uvarov, S., & Efremov, D. (2019). Critical Phenomena in Portevin-Le Chatelier Effect during Compression of Aluminium-Magnesium Alloy and Stored Energy Evolution. *Procedia Structural Integrity*, *18*, 309–313.

Vazquez, L., Iturrioz, A., Lopez de Uralde, P., & Alvarez, P. (2023). Maximising the Deposition Rate of 5356 Aluminium Alloy by CMT-Twin-Based WAAM While Reducing Segregation-Related Problems by Local IR Thermography. *Metals*, *13*(11).

Vijayakumar, M. D., Dhinakaran, V., Sathish, T., Muthu, G., & Ram, P. M. B. (2020). Experimental Study of Chemical Composition of Aluminium Alloys. *Materials Today: Proceedings*, *37*(Part 2), 1790–1793.

Vimal, K. E. K., Naveen Srinivas, M., & Rajak, S. (2019). Wire Arc Additive Manufacturing of Aluminium Alloys: A Review. *Materials Today: Proceedings*, *41*, 1139–1145.

Wang, C., Li, Y., Tian, W., Hu, J., Li, B., Li, P., & Liao, W. (2022). Influence of Ultrasonic Impact Treatment and Working Current on Microstructure and Mechanical Properties of 2219 Aluminium Alloy Wire Arc Additive Manufacturing Parts. *Journal of Materials Research and Technology*, *21*, 781–797.

Wang, W. H., Wu, D., Shah, S. S. A., Chen, R. S., & Lou, C. S. (2016). The Mechanism of Critical Strain and Serration Type of the Serrated Flow in Mg-Nd-Zn Alloy. *Materials Science and Engineering: A*, *649*, 214–221.

Wang, Y., Xia, L., Zhang, H., Cao, Y., Pan, A., & Wu, W. (2022). The Serration Behavior and Mechanical Properties of Al0.1CoCrFeNi High-Entropy Alloy under Coupled Electron-Heat Field. *Journal of Alloys and Compounds*, *898*.

Wieczorowski, M., Pereira, A., Carou, D., Gapinski, B., & Ramírez, I. (2023). Characterization of 5356 Aluminum Walls Produced by Wire Arc Additive Manufacturing (WAAM). *Materials*, *16*(7).

William D. Callister, & David G. Rethwish. (2018). *Materials Science and Engineering An Introduction: 10th Edition*.

Wu, Q., Mukherjee, T., De, A., & DebRoy, T. (2020). Residual Stresses in Wire-Arc Additive Manufacturing – Hierarchy of Influential Variables. *Additive Manufacturing*, *35*.

Xiong, J., Li, Y., Li, R., & Yin, Z. (2018). Influences of Process Parameters on Surface Roughness of Multi-Layer Single-Pass Thin-Walled Parts in GMAW-Based Additive Manufacturing. *Journal of Materials Processing Technology*, *252*, 128–136.

Xu, J., Holmedal, B., Hopperstad, O. S., Mánik, T., & Marthinsen, K. (2022). Dynamic Strain Ageing in an AlMg Alloy at Different Strain Rates and Temperatures: Experiments and Constitutive Modelling. *International Journal of Plasticity*, *151*.

Xu, J., Yu, H., Xiao, R., Liu, Q., & Chen, S. (2023). Features Detection of Al Alloy Porosity during GTAW Process based on Arc Spectrum and Improved Porosity-Focus Decision Tree. *Journal of Manufacturing Processes*, *88*, 71–83.

Xu, M., Zhang, H., Yuan, T., Yan, Z., & Chen, S. (2023). Microstructural Characteristics and Cracking Mechanism of Al-Cu Alloys in Wire Arc Additive

Manufacturing. *Materials Characterization*, *197*.

Yelamasetti, B., Kumar, D., Saxena, K. K., & G, R. (2022). Experimental Investigation on Temperature Profiles and Residual Stresses in GTAW Dissimilar Weldments of AA5052 and AA7075. *Advances in Materials and Processing Technologies*, *8*(sup2), 352–365.

Zhang, M., Gu, K., Pan, R., Liu, B., Weng, Z., & Wang, J. (2024). Cryogenic Deformation Behavior of Al–Zn–Mg–Cu alloy and its Sensitivity to Temperature and Strain Rate. *Materials Science and Engineering: A*, *893*.

Zhang, S., Gong, M., Cen, L., Lu, Y., & Gao, M. (2023). Differences in Properties between Hybrid Wire Arc Additive-Milling Subtractive Manufactured Aluminum and Magnesium Alloys. *Applied Sciences (Switzerland)*, *13*(4).

Zhang, T., Li, H., Gong, H., Ding, J., Wu, Y., Diao, C., Zhang, X., & Williams, S. (2022). Hybrid Wire - Arc Additive Manufacture and Effect of Rolling Process on Microstructure and Tensile Properties of Inconel 718. *Journal of Materials Processing Technology*, *299*.

Zhang, Y., Gao, M., Lu, Y., & Du, W. (2022). Deposition Geometrical Characteristics of Wire Arc Additive-Manufactured AA2219 Aluminium Alloy with Cold Metal Transfer Pulse Advance Arc Mode. *International Journal of Advanced Manufacturing Technology*.

Zhao, D. S., Long, D. F., Niu, T. R., Zhang, T. F., Hu, X., & Liu, Y. J. (2022). Effect of Mg Loss and Microstructure on Anisotropy of 5356 Wire Arc Additive Manufacturing. *Journal of Materials Engineering and Performance*, *31*(10), 8473–8482.

Zhao, Y., Chen, F., Cao, S., Chen, C., & Xie, R. (2022). Effect of CMT Welding Heat Input on Microstructure and Properties of 2A14 Aluminum Alloy Joint. *Metals*, *12*(12).

Zhou, S., Wang, J., Yang, G., Wu, B., Xie, H., Wu, K., & An, D. (2022). Periodic Microstructure of Al–Mg Alloy Fabricated by Inter-Layer Hammering Hybrid Wire Arc Additive Manufacturing: Formation Mechanism, Microstructural and Mechanical Characterization. *Materials Science and Engineering: A*, *860*.

Zhu, K., Wang, J., Zhang, W. chen, Zhu, X. lei, & Lu, X. feng. (2024). Effect of Deposition Strategies on Microstructures, Defects and Mechanical Properties of 5356 Aluminum Alloy by Wire Arc Additive Manufacturing. *Transactions of Nonferrous Metals Society of China (English Edition)*, *34*(2), 423–434.

Zhu, X. (2024). Effect of Post-Welding Coating Process on the Organization and Properties of MIG-Welded T-Joints of 6063-T6 Aluminum Alloy. *Applied Mathematics and Nonlinear Sciences*, *9*(1).

Zhu, Z., Hu, Z., Seet, H. L., Liu, T., Liao, W., Ramamurty, U., & Ling Nai, S. M. (2023). Recent Progress on the Additive Manufacturing of Aluminum Alloys and Aluminum Matrix Composites: Microstructure, Properties, and Applications. In *International Journal of Machine Tools and Manufacture* (Vol. 190). Elsevier Ltd.

Zuo, X., Lv, Z., Wang, Y., Chen, X., & Qi, W. (2025). Microstructural Organization and Mechanical Properties of 5356 Aluminum Alloy Wire Arc Additive Manufacturing Under Low Heat Input Conditions. *Metals*, *15*(2).

APPENDICES

APPENDIX 1

Procedure of Calibration Process in GOM Software 2022

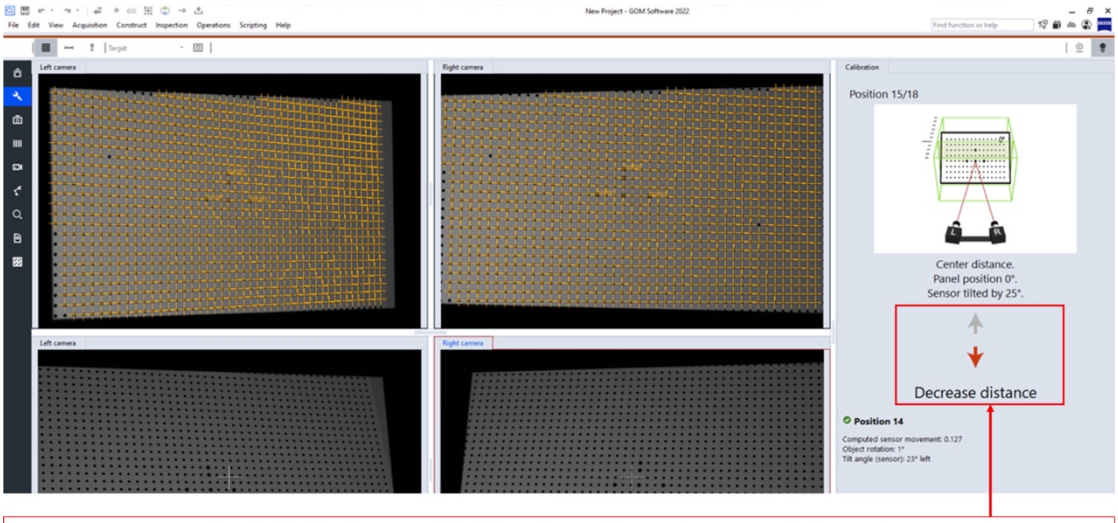

Step 1: Calibration panel is adjusted according to the automatic instruction

Appendix 1 (a) Calibration Process in GOM Software 2022

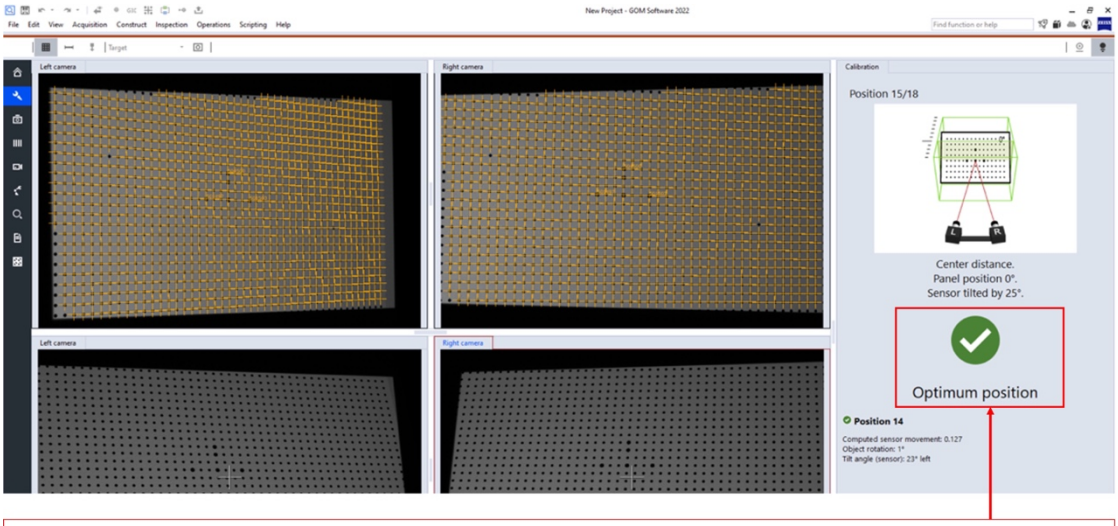

Step 2: The calibration panel is adjusted until optimum position achieved

Appendix 1 (b) Optimum Position Achieved during Calibration Process

Calibration results

Calibration deviation

Current calibration info

General

Calibration date	Mon Jan 16 10:56:12 2023

Calibrated sensor

Sensor name	GOM Scan 1
Measuring volume	MV200 (200x125x150)
Serial number	210919

Calibration object

Object type	Panel (Triple Scan)
Name	CPA30/210/10028
Certification date	21/3/2021
Certification ID	CPA30/210/10028/2021-03-21
Calibration points	1910 points
Certified lengths	250.399 / 250.296 mm
Certification temperature	20.0 °C
Expansion coefficient	22.40 x 10^{-6} K^{-1}
Calibration temperature	24.0 °C

Calibration settings

Camera lenses	16.00 mm
Snap mode	Double snap
Max. ellipse residual	0.05 (gray value adjustment)

Calibration Result

Calibration deviation	0.039 Pixels
Calibration deviation (optimized)	0.017 Pixels
Calibration deviation (check)	OK (limit value: 0.075 Pixels)
Camera angle	26.6°
Height variance	145 mm
Measuring volume	190 / 110 / 155 mm

Appendix 1 (c) Calibration Results

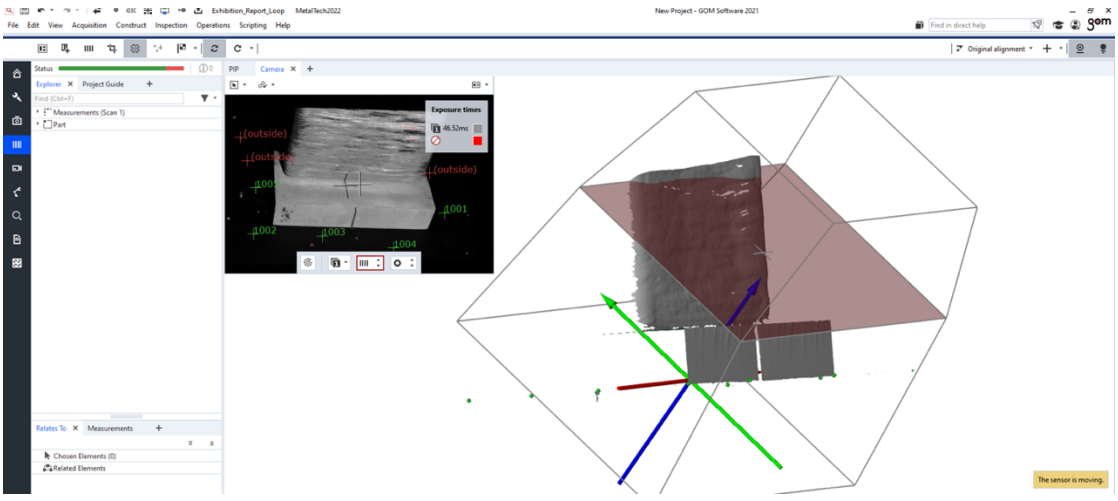

Appendix 1 (d) Overexposed Areas during Scanning Process

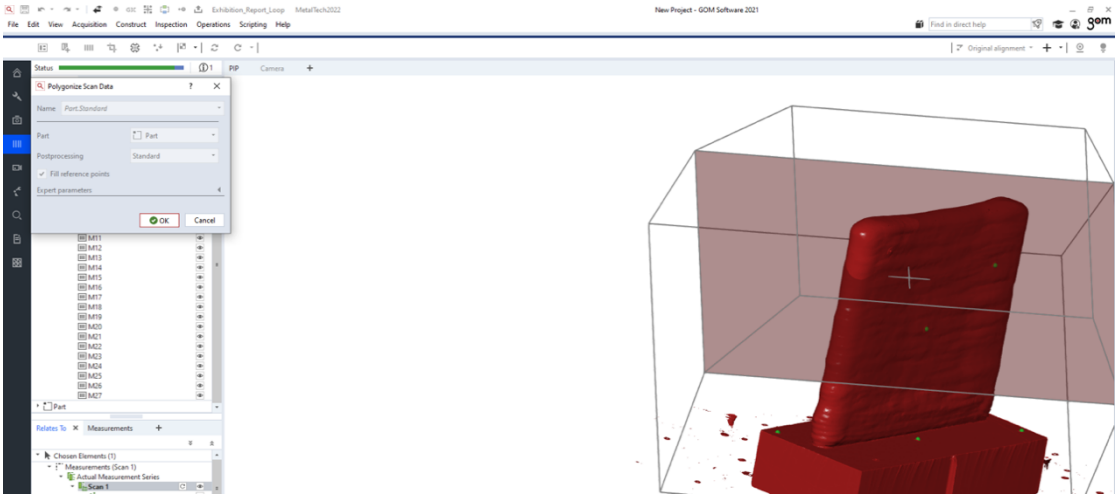

Appendix 1 (e) Assembled of Polygonise Scan Data

AUTHOR'S PROFILE



Nornisaadila binti Musa obtained Bachelor of Manufacturing Engineering (Hons.) in 2017 from Universiti Kebangsaan Malaysia (UKM), MSc in Mechanical Engineering (2020) from Universiti Teknologi Mara and PhD in Mechanical Engineering (2026) from the Univeristi Teknologi Mara, Shah Alam. Her PhD thesis involves several methods in microstructural characterization, mechanical properties performance and FEM analysis in additive manufacturing.

LIST OF PUBLICATION:

Musa, N., Adenan, M. S., & Saedon, J., (2026). Microstructural refinement and texture enhancement of ER 5356 Aluminium Alloy by Hybrid WAAM-Forging. Journal of Mechanical Engineering, 23(1), 116 – 131.

Musa, N., Adenan, M. S., Manurung, Y. H. P., & Mat, M. F., (2025). Wire-Arc Additive Manufacturing – Forging Process Chain Simulation Analysis of Aluminium Alloy. Nigerian Journal of Technological Development, 22(1), 148 – 158.

Musa, N., Saedon, J., & Adenan, M. S. (2020). An Investigation on the Surface Integrity of Grade 5 Titanium Alloy Proceeding the Wire Electro-Discharge Machining (WEDM) Process. Applied Mechanics and Materials, 899, 144 – 155.

Musa, N., Saedon, J., & Adenan, M. S., (2019). Surface Topography and Biocompatibility of Ti-6Al-4V after Wire Electro-Discharge Machining (WEDM). Journal of Mechanical Engineering, 8(1), 130 – 139.